BERGISCHE
UNIVERSITÄT
WUPPERTAL

Advancing FeNi Nanocatalyst Production for Green Hydrogen using Multi-Beam Pulsed Laser Ablation in Liquid

Dissertation

to obtain the doctoral degree

Dr.-Ing.

in the

School of Mechanical and Safety Engineering

University of Wuppertal

Submitted by

Inna Yusnila Khairani

from Surakarta, Indonesia

Wuppertal 2025

This thesis was conducted at the Chair of Materials Science and Additive Manufacturing, University of Wuppertal, under the supervision of Prof. Dr. Bilal Gökce. It has been approved for publication by the University of Wuppertal.

Location and date of the doctoral disputation:

Wuppertal, 14.02.2025 (14:00, Room: VW.09.002)

Chairman:

Prof. Dr.-Ing. Uwe Janoske

University of Wuppertal

Referees:

Prof. Dr. Bilal Gökce

University of Wuppertal

Prof. Dr.-Ing. Arne Röttger

University of Wuppertal

Dr. Carlos Donate Buendia

University Jaume I

Prof. Dr.-Ing. Axel Schumacher

University of Wuppertal

Curiosity and a passion for learning,

The desire to improve ourselves,

Are the driving forces that lead us

Toward a more advanced civilization and technology—

Whether for better or for worse.

But as long as we continue along the straight path,

We will not forget what is important

Or why we want to learn in the first place.

I believe that we learn to live,

And we live to learn.

Thus, once we stop learning,

It is the moment we truly cease to exist.

Never stop learning.

Inna Y. Khairani

Golm, 26.06.2025

Abstract

Hydrogen technology, specifically green hydrogen, holds an irreplaceable role in achieving net zero carbon by 2050. Capacity increase (higher hydrogen production volume), longer stack lifetime, and cost reduction of electrolysers are some of the key strategies to lower the green hydrogen production costs, which will accelerate the industrial implementation of this technology. One approach to lower green hydrogen production costs is to use abundant and affordable catalysts, free of rare and precious elements, to facilitate water splitting in the electrolyser. Among the abundant elements catalysts being investigated, FeNi alloys are believed to be the key due to the reported high catalytic activity for the kinetically more sluggish OER in the water-splitting process. To further enhance the catalytic activity of FeNi-based catalysts, size reduction is a common strategy to increase the surface area of the catalyst, leading to more active sites for the reactions to take place.

The key global goal of achieving net zero carbon by 2050 through the production of cost-effective and catalytically active FeNi-based nanocatalysts on a large scale should be accompanied by a production method that also complies with the green chemistry principle. Pulsed laser ablation in liquid (PLAL) is a straightforward and versatile green synthesis method to produce nanoparticles (NPs). It employs a high-power pulsed laser to ablate a target immersed in a liquid media. The liquid in PLAL, although mainly used to capture and carry the generated NPs, plays a significant role in the NPs' properties. The liquid defines the composition, particle size, oxidation, and morphology of the generated NPs, affecting the catalytic activity. Moreover, liquid properties also influence NPs production rate, which is an important parameter for our goal of industrial-scale production of catalysts. Hence, it is crucial to investigate which liquid is the most fitting for our application.

In this dissertation, three different ablation liquids, namely water, acetone, and dried acetone (acetone with reduced water impurity), which are economically viable for the industrial-scale production of FeNi NPs via the PLAL method, were explored. Key properties such as morphology, oxidation, catalytic activity, and productivity were examined through analytical methods, namely transmission electron microscopy (TEM), energy dispersive X-ray (EDX), X-ray diffraction (XRD), and electrochemical analysis, resulting in a smaller NPs size, less oxidation, and slightly more active catalytic activity of FeNi in dried acetone compared to FeNi in water and acetone. However, the productivity of FeNi in dried acetone was only one-third compared to water. Considering the sustainability issue, hazard risk, and marginal improvement when using dried acetone as an ablation liquid, water was chosen as the ablation liquid to produce FeNi NPs through PLAL as it complies with green chemistry principles and has higher productivity.

Nonetheless, PLAL suffers from low productivity, inhibiting its industrial use. PLAL productivity ranges from tens to a few hundred milligrams per hour depending on various experimental conditions. Scaling up the production of FeNi NPs through PLAL is therefore crucial to fulfilling the industrial need for abundant and catalytically active nanocatalysts for the water-splitting process. In this dissertation, a cost-effective approach using static diffractive optical elements (DOE) is introduced to achieve parallel ablation, termed multi-beam PLAL (MB-PLAL). With this method, a higher interpulse distance was achieved, increasing nanoparticle productivity without the need to increase the scanning speed. The

larger interpulse distance is a direct consequence of pulse frequency adjustment to compensate for pulse energy splitting by the DOE. MB-PLAL with 11 beams improved the productivity of FeNi NPs in water by a factor 4 compared to the single beam PLAL (0.4 g/h to 1.6 g/h). MB-PLAL scalability, efficiency, and versatility were confirmed by the ablation of Au and $Fe_{50}Ni_{50}$ targets using 1, 6, and 11 beams, resulting in a linear productivity increase.

Implementing our laser-generated FeNi NPs as OER catalysts was the final objective of this work. The goal is to produce catalysts completely free of precious and rare elements on a large scale and with high catalytic activity. The MB-PLAL-produced FeNi NPs in water were deposited on the surface of rGO, resulting in smaller particle sizes. An investigation of different supporting methods, i.e., downstream and in situ PLAL, was performed to find the most efficient one-step production method to generate FeNi-rGO composites. Downstream PLAL produces FeNi-rGO with similar properties as the in situ PLAL but offers higher efficiency and productivity. The produced FeNi-rGO were then sprayed on FeNi layered double hydroxide (FeNi LDH) grown on Ni foam substrate to produce a hybrid catalyst, FeNi-rGO/FeNi/Ni foam, for oxygen evolution reaction (OER) in alkaline media. The prepared hybrid catalyst requires an overpotential of only 234 mV at a current density of 10 mA/cm^2, which is 37 mV lower than the tested commercial RuO_2 catalyst on Ni foam substrate. Besides, the hybrid catalyst is extremely robust; it stands 10,000 cycles of accelerated deterioration and runs for more than 1,300 h at a current density of 10 mA/cm^2 without performance decay.

In summary, the investigations presented in this dissertation significantly contribute to the advancement of both PLAL and OER catalyst fields. It offers insights related to the influence of the ablation liquid on FeNi NPs properties, a newly proposed MB-PLAL method to upscale productivity to the industrial requirements, and the combination of both approaches for the production of a hybrid catalyst free of rare and precious elements with low overpotential and long-term stability.

Keywords: *green chemistry, water-splitting catalyst, laser processing, optical diffraction, iron nickel equimolar*

Zusammenfassung

Die Wasserstofftechnologie, insbesondere der grüne Wasserstoff, spielt eine unersetzliche Rolle bei der Verwirklichung der Kohlenstofffreiheit bis 2050. Kapazitätssteigerung (höheres Wasserstoffproduktionsvolumen), längere Stack-Lebensdauer und Kostensenkung bei Elektrolyseuren sind einige der Schlüsselstrategien zur Senkung der Produktionskosten für grünen Wasserstoff, was die industrielle Umsetzung dieser Technologie beschleunigen wird. Ein Ansatz zur Senkung der Wasserstoffproduktionskosten besteht darin, reichlich vorhandene und erschwingliche Katalysatoren, die frei von seltenen und wertvollen Elementen sind, zu verwenden, um die Wasserspaltung im Elektrolyseur zu erleichtern. Unter den untersuchten Katalysatoren mit reichlich vorhandenen Elementen gelten FeNi-Legierungen aufgrund ihrer hohen katalytischen Aktivität im Wasserspaltungsprozess als der Schlüssel. Um die katalytische Aktivität von Katalysatoren auf FeNi-Basis weiter zu verbessern, ist die Verkleinerung eine gängige Strategie, um die Oberfläche des Katalysators zu vergrößern, was zu mehr aktiven Stellen für die stattfindenden Reaktionen führt.

Das wichtige globale Ziel, bis 2050 durch die Herstellung kostengünstiger und katalytisch aktiver Nanokatalysatoren auf FeNi-Basis in großem Maßstab eine kohlenstofffreie Atmosphäre zu erreichen, sollte mit einer Produktionsmethode einhergehen, die auch dem Prinzip der grünen Chemie entspricht. Die gepulste Laserablation in Flüssigkeit (PLAL) ist eine unkomplizierte und vielseitige grüne Synthesemethode zur Herstellung von Nanopartikeln (NP). Dabei wird ein gepulster Hochleistungslaser verwendet, um ein in ein flüssiges Medium eingetauchtes Ziel abzutragen. Obwohl die Flüssigkeit bei PLAL hauptsächlich dazu dient, die erzeugten NP einzufangen und zu transportieren, spielt sie eine wichtige Rolle für die Eigenschaften der NP. Die Flüssigkeit bestimmt die Zusammensetzung, die Partikelgröße, die Oxidation und die Morphologie der erzeugten NPs und wirkt sich auf die katalytische Aktivität aus. Darüber hinaus beeinflussen die Flüssigkeitseigenschaften auch die NP-Produktionsrate, die ein wichtiger Parameter für die angestrebte großtechnische Produktion von Katalysatoren ist. Daher ist es von entscheidender Bedeutung, zu untersuchen, welche Flüssigkeit für unsere Anwendung am besten geeignet ist.

In dieser Dissertation wurden drei verschiedene Trägermedien für die Ablation untersucht, nämlich Wasser, Aceton und getrocknetes Aceton (Aceton mit reduzierter Wasserverunreinigung), die für die großtechnische Herstellung von FeNi NPs mittels der PLAL-Methode wirtschaftlich sind. Schlüsseleigenschaften wie Morphologie, Oxidation, katalytische Aktivität und Produktivität wurden mit Hilfe von Analysemethoden wie Transmissionselektronenmikroskopie (TEM), energiedispersiver Röntgenstrahlung (EDX), Röntgendiffraktometrie (XRD) und elektrochemischer Analyse untersucht. Das Ergebnis war, dass FeNi in getrocknetem Aceton im Vergleich zu FeNi in Wasser und Aceton eine kleinere NP-Größe, weniger Oxidation und eine etwas aktivere katalytische Aktivität aufweist. Die Produktivität von FeNi in getrocknetem Aceton betrug jedoch nur ein Drittel im Vergleich zu Wasser. In Anbetracht der Nachhaltigkeitsproblematik, des Gefahrenrisikos und der geringfügigen Verbesserung bei der Verwendung von getrocknetem Aceton als Ablationsflüssigkeit wurde Wasser als Ablationsflüssigkeit für die Herstellung von FeNi-NP durch PLAL gewählt, da es mit den Prinzipien der grünen Chemie übereinstimmt und eine höhere Produktivität aufweist.

Dennoch leidet die PLAL unter ihrer geringen Produktivität, was ihre industrielle Nutzung behindert. Die PLAL-Produktivität reicht von einigen Dutzend bis zu einigen hundert Milligramm pro Stunde, je nach den verschiedenen Versuchsbedingungen. Die Steigerung der Produktion von FeNi NPs durch PLAL ist daher von entscheidender Bedeutung, um den industriellen Bedarf an reichlich vorhandenen und katalytisch aktiven Nanokatalysatoren für den Wasserspaltungsprozess zu decken. In dieser Dissertation wird ein kosteneffizienter Ansatz unter Verwendung statischer diffraktiver optischer Elemente (DOE) vorgestellt, um eine parallele Ablation zu erreichen, die als Multi-Beam PLAL (MB-PLAL) bezeichnet wird. Mit dieser Methode wurde ein größerer Interpulsabstand erreicht, der die Produktivität der Nanopartikel erhöht, ohne dass die Scangeschwindigkeit erhöht werden muss. Der größere Impulsabstand ist eine direkte Folge der Anpassung der Impulsfrequenz, um die Aufteilung der Impulsenergie durch die DOE zu kompensieren. MB-PLAL mit 11 Strahlen verbesserte die Produktivität von FeNi NPs in Wasser um den Faktor 4 im Vergleich zu PLAL mit einem Strahl (0,4 g/h bis 1,6 g/h). Die Skalierbarkeit, Effizienz und Vielseitigkeit von MB-PLAL wurde durch die Ablation von Au- und $Fe_{50}Ni_{50}$-Targets mit 1, 6 und 11 Strahlen bestätigt, was zu einer linearen Produktivitätssteigerung führte.

Die Umsetzung unserer lasergenerierten FeNi NPs als Katalysatoren war das letzte Ziel dieser Arbeit. Ziel ist es, Katalysatoren in großem Maßstab und mit hoher katalytischer Aktivität herzustellen, die völlig frei von wertvollen und seltenen Elementen sind. Die mit MB-PLAL in Wasser hergestellten FeNi NPs wurden auf der Oberfläche von rGO abgeschieden, was zu kleineren Partikelgrößen führte. Um die effizienteste einstufige Produktionsmethode zur Herstellung von FeNi-rGO-Verbundwerkstoffen zu finden, wurden verschiedene unterstützende Methoden untersucht, d. h. nachgeschaltete und in situ PLAL. Die nachgeschaltete PLAL produziert FeNi-rGO mit ähnlichen Eigenschaften wie die in situ PLAL, bietet aber eine höhere Effizienz und Produktivität. Die hergestellten FeNi-rGO wurden dann auf FeNi-Doppelschichthydroxid (FeNi LDH) aufgesprüht, das auf einem Ni-Schaumsubstrat gewachsen ist, um einen Hybridkatalysator, FeNi-rGO/FeNi/Ni-Schaum, für die Sauerstoffentwicklungsreaktion (OER) in alkalischen Medien herzustellen. Der hergestellte Hybridkatalysator benötigt eine Überspannung von nur 234 mV bei einer Stromdichte von 10 mA/cm^2, was 37 mV niedriger ist als der getestete kommerzielle RuO_2-Katalysator auf Ni-Schaumsubstrat. Außerdem ist der Hybridkatalysator extrem robust; er übersteht 10.000 Zyklen beschleunigter Verschlechterung und läuft mehr als 1.300 Stunden bei einer Stromdichte von 10 mA/cm^2 ohne Leistungsabfall.

Zusammenfassend lässt sich sagen, dass die in dieser Dissertation vorgestellten Untersuchungen einen bedeutenden Beitrag zur Weiterentwicklung der Bereiche PLAL und Katalysatoren leisten. Sie bietet Einblicke in den Einfluss der Ablationsflüssigkeit auf die Eigenschaften von FeNi NPs, eine neu vorgeschlagene MB-PLAL-Methode, um die Produktivität auf die industriellen Anforderungen hochzuschrauben, und die Kombination beider Ansätze für die Herstellung eines Hybridkatalysators, der frei von seltenen und wertvollen Elementen ist, eine niedrige Überspannung aufweist und langfristig stabil ist.

Schlüsselwörter: *Grüne Chemie, Katalysator für Wasserspaltung, Laserprozessierung, Optische Beugung, Äquimolares Eisen-Nickel*

Table of Contents

List of Figures and Tables

List of Abbreviation

AOM	Acousto-Optic Modulators
ADT	Accelerated Durability Test
CB	Cavitation Bubble
CLAL	Continuous Wave Laser Ablation in Liquid
CVD	Chemical Vapor Deposition
DAC	Diamond Anvil Cell
DOE	Diffractive Optical Element
E^0	Standard Reduction Potential
EDX	Energy Dispersive X-Ray
EIS	Electrochemical Impedance Spectroscopy
EOM	Electro-Optic Modulators
EU	European Union
FCC	Face Centered Cubic
FeNi	Iron Nickel Alloy
F_{thr}	Threshold Fluence
HAADF	High-Angle Annular Dark-Field Imaging
HCP	Hexagonal Closed Packed
HER	Hydrogen Evolution Reaction
HTHPHD	High Temperature, High Pressure, and High Density
ICP-MS	Inductively Coupled Plasma Mass Spectrometry
ICSD	Inorganic Crystal Structure Database
IR	Infrared
LAL	Laser Ablation in Liquid
LDH	Layered Double Hydroxide
LIPSS	Laser-Induced Periodic Surface Structures
LSV	Linear Sweep Voltammetry
M(H)	Magnetic Field-Dependent Magnetization
MB-PLAL	Multi-Beam Pulsed Laser Ablation in Liquid
Nd:YAG	Neodymium-Doped Yttrium Aluminum Garnet
NIR	Near Infrared
NPs	Nanoparticles
OER	Oxygen Evolution Reaction
PDI	Poly Dispersity Index
PGM	Platinum Group Metal
PLAL	Pulsed Laser Ablation in Liquid
PLD	Pulsed Laser Deposition
PPMS	Physical Property Measurement System
PSD	Particle Size Distributions
PVP	Polyvinylpyrrolidone
Rct	Charge-Transfer Resistance
RDE	Rotating Disk Electrode
RHE	Reversible Hydrogen Electrode
SEM	Scanning Electron Microscopy

SLM	Spatial Light Modulators
SDS	Sodium Dodecyl Sulfate
SXRD	Synchrotron X-Ray Diffraction
TEM	Transmission Electron Microscopy
UV	Ultraviolet
XPS	X-Ray Photoelectron Spectroscopy
XRD	X-Ray Diffraction

Preface

This thesis covers a general introduction and discussion related to the topic of iron nickel generation via pulsed laser ablation in liquid and its productivity increase, as well as its potential use as electrocatalyst for oxygen evolution reaction (OER) in water splitting process for the generation of green hydrogen. The thesis contains four peer-reviewed articles published in international scientific journals, including three original research papers and one perspective paper (short review paper). My contributions as a first author of the following publications are also listed below.

(I) Khairani, I. Y., Lin, Q., Landers, J., Salamon, S., Doñate-Buendía, C., Karapetrova, E., Wende, H., Zangari, G., & Gökce, B. (2023). Solvent Influence on the Magnetization and Phase of Fe-Ni Alloy Nanoparticles Generated by Laser Ablation in Liquids. *Nanomaterials*, *13*(2), 227. https://doi.org/10.3390/nano13020227
CRediT Authorship Contribution of I.Y.K.: Conceptualization, methodology, investigation, visualization, writing – original draft preparation, writing – review and editing.

(II) Khairani, I. Y., Spellauge, M., Riahi, F., Huber, H. P., Gökce, B., & Doñate-Buendía, C. (2024). Parallel Diffractive Multi-Beam Pulsed-Laser Ablation in Liquids Toward Cost-Effective Gram Per Hour Nanoparticle Productivity. Advanced Photonics Research, 5(5), 2300290. https://doi.org/10.1002/adpr.202300290
CRediT Authorship Contribution of I.Y.K.: Conceptualization, methodology, investigation, visualization, writing – original draft preparation, writing – review and editing.

(III) Khairani, I. Y., Jin, B., Palardonio, S. M., Hagemann, U., Alonso, B., Ortega, A., Doñate-Buendía, C., Martorell, J., Ros, C., Kallio, T., & Gökce, B. (2024). FeNi nanoparticle-modified reduced graphene oxide as a durable electrocatalyst for oxygen evolution. Journal of Catalysis, 439(September), 115771. https://doi.org/10.1016/j.jcat.2024.115771
CRediT Authorship Contribution of I.Y.K.: Conceptualization, methodology, investigation, visualization, writing – original draft preparation, writing – review and editing.

(IV) Khairani, I. Y., Mínguez-Vega, G., Doñate-Buendía, C., & Gökce, B. (2023). Green nanoparticle synthesis at scale: a perspective on overcoming the limits of pulsed laser ablation in liquids for high-throughput production. Physical Chemistry Chemical Physics, 25(29), 19380–19408. https://doi.org/10.1039/D3CP01214J
CRediT Authorship Contribution of I.Y.K.: Conceptualization, literature research, visualization, writing – original draft preparation, writing – review and editing.

1 General Introduction

This section introduces the topics of the thesis, including the background of the study (1.1), a short review of relevant literatures on the topics (1.2), and the thesis framework (1.3), including the aim (1.3.1), the scope (1.3.2), as well as the research questions (1.3.3).

1.1 Background

Achieving net zero emissions by 2050 is a key global goal to avoid the impacts of climate change and preserve a habitable planet (United Nations, 2023). Many countries are now taking measures to achieve this goal (Donohoo-Vallett et al., 2023; European Commission, 2021; Ministry of Economy Trade and Industry Japan, n.d.; Office of the Federal Chief Sustainability, n.d.), including the European Union which pledged to reduce greenhouse emissions to at least 55% by 2030 through the European Green Deal (European Commission, 2021), the United States to reduce emission by 50-52% compared to 2005 level before 2030 (Office of the Federal Chief Sustainability, n.d.) and achieve the clean electricity by 2035 (Donohoo-Vallett et al., 2023), and Japan to reduce emission by 26% from the 2013 level before 2030 and retroactively reduce CO_2 emission through the Beyond Zero initiative (Ministry of Economy Trade and Industry Japan, n.d.). Through the 28th United Nations Climate Change Conference (COP28) where 198 nations gathered in Dubai to discuss the world's climate trajectory, the importance of transitioning away from fossil fuel was highlighted as a primary element to achieve net zero emissions by 2050, to avoid the increase of global temperature of more than 1.5°C which can subsequently lead to climate change and extreme weather events (United Nations, 2023).

Hydrogen, in particular green hydrogen, is projected as one of the key solutions to substitute carbon-based energy sources. However, producing green hydrogen is still comparably expensive, at approximately 4-6 USD per kg, which is 2-3 times higher than the grey hydrogen production (Miranda et al., 2021) through methane reformation (Arcos & Santos, 2023; Incer-Valverde et al., 2023; Panić et al., 2022). Reducing green hydrogen production cost to 2 USD per kg requires the decrease of renewable electricity price to 20 USD per MWh and the electrolyser cost to 130 USD per kW (Miranda et al., 2021). Fortunately, the cost to produce renewable energy steadily decreases, thanks to the global efforts to increase installations and enhance production efficiency (IRENA, 2022b). Henceforth, the strategy to lower green hydrogen prices should be focused on suppressing electrolyser prices and expanding its capacity (IRENA, 2020, 2022a). One of the main cost drivers of an electrolyser originates from its stacks (IRENA, 2020). The electrodes in the stacks are covered by precious metals or rare elements belonging to the platinum-group metals (PGM) which act as catalysts for the water-splitting process. Some of the most studied catalysts include ruthenium (Ru) and iridium (Ir)-based catalysts, as they show excellent catalytic performances for both oxygen evolution reaction (OER) and hydrogen evolution reaction (HER) (Y. Lee et al., 2012; C. Li & Baek, 2020; C. C. L. L. McCrory et al., 2015; C. Wang et al., 2023; S. Wang et al., 2021; Y. Zhao et al., 2011). Platinum is also highly considered as HER catalyst due to its exceptionally low overpotential (C. Li & Baek, 2020; C. C. L. L. McCrory et al., 2015; L. Zhang et al., 2019; F. Zhou et al., 2021).

The employment of precious or rare elements as water-splitting catalysts for green hydrogen significantly increases electrolyser cost. Hence, abundant and affordable catalysts with high catalytic performance comparable to the PGM elements are necessary to facilitate large production of electrolysers at a lower cost (IRENA, 2020).

The research direction to obtain more affordable catalysts for OER, which is a considerably slower reaction than HER due to the four electrons transfer, focuses on finding catalysts from abundant and non-precious elements, such as manganese (C. Hu et al., 2019; Zaharieva et al., 2012; Z. Zhao et al., 2022), cobalt (Kanan & Nocera, 2008; Liang et al., 2011; Meng et al., 2018), nickel (Y. Chen et al., 2019; Kauffman et al., 2016; Y. Li et al., 2020; Vij et al., 2017), and iron (Bai et al., 2019; Bandal et al., 2018; Feng et al., 2020; Han et al., 2018; Y. Wei et al., 2020). Among these materials, nickel (Ni)-based catalysts are deemed the most promising alternative to PGM catalysts for OER reaction (Tsubonouchi et al., 2024). Ni-based catalysts for OER in the water-splitting process earned their popularity thanks to their low overpotentials (Y. Chen et al., 2019; C. C. L. McCrory et al., 2013; Roger et al., 2017), in addition to their high conductivity, thermal stability, and multivalent property (-1 to +4) to undertake various electronic transitions (Vij et al., 2017; J. Zhang et al., 2024). In particular, adding a small amount of iron to nickel-based catalysts is found to increase the OER catalytic activity in alkaline conditions (Corrigan, 1987; Klaus et al., 2015; Ros et al., 2021; Trotochaud et al., 2014; Twight et al., 2024). This phenomenon is attributed to the modification of electronic structure, possible additional active sites, conductivity increase, and Ni's higher oxidation state stabilization (J. S. Kim et al., 2018; N. Li et al., 2017; Salmanion & Najafpour, 2023; Smith et al., 2013; Spanos et al., 2021; Trotochaud et al., 2014). Using Fe and Ni-based catalysts for OER is a key strategy to overcome price and availability issues associated with precious and rare element catalysts, not only due to FeNi's high catalytic activity but also to the abundance of these elements on earth (Cui et al., 2018; Frey & Reed, 2012). In particular, the equiatomic $Fe_{50}Ni_{50}$ alloy catalysts gained popularity for the OER, thanks to their low overpotential (Acharya et al., 2019; Corrigan, 1987; Friebel et al., 2015; J. Jiang et al., 2016), and better OER catalytic performance at higher current densities (Acharya et al., 2019), which is related to the purpose of industrial application. It is therefore crucial to concentrate on developing FeNi-based OER electrocatalyst, specifically the equiatomic FeNi, to accelerate the hydrogen transition and achieve net zero emission by 2050.

In general, the development of catalysts mostly focuses on increasing the number of active sites, and areas on the surface of catalysts where reactions take place. One way to increase the number of active sites is by increasing catalysts' specific surface area, for example through the particle size reduction to nano dimension (X. Zhang et al., 2016). There are two approaches to producing nanosized materials: top-down and bottom-up. The top-down approach is done through the breaking of bulk material into smaller particles until nanomaterials are produced. Some methods such as mechanical grinding, ball-milling, and lithography are included in this approach. Meanwhile, the bottom-up approach involves building nanomaterials through the joining of their atoms, for example through chemical vapor deposition and chemical synthesis, such as hydrothermal, co-precipitation, and sol-gel.

Nanomaterials' synthesis method plays a significant role in their catalytic performance, since catalysts' purity, specific surface area, and active sites are the main aspects that determine catalysts' activity. Pulsed laser ablation in liquid (PLAL) generates nanosized particles that fulfil these aspects, allowing the synthesis of various types of nanomaterials (Frias Batista et al., 2022; Khairani, Mínguez-Vega, et al., 2023; Nag et al., 2023) dispersed in a wide variety of solvents depending on the intended application (Frias Batista et al., 2023; Fromme et al., 2024). Firstly introduced in 1987 by Patil et al. (Patil et al., 1987) and in 1993 by Fojtik and Henglein (Anton Fojtik and Arnim Henglein, 1993; Henglein, 1993), it is considered a modern technique to produce nanoparticles (NPs) and is mostly classified as a top-down approach, due to its principle of ablating bulk materials using a high-intensity laser ($>10^9$ W/cm^2) to create NPs. PLAL can be performed simply by shooting the pulsed laser beam onto a target which is immersed in a liquid media. The ablated matters in the form of NPs are collected by the liquid instead of dispersed in air, avoiding inhalation and health risks. This method gained popularity in terms of catalyst production, due to the reported high catalytic activity (Forsythe et al., 2021; Hunter et al., 2014; Reichenberger et al., 2019; D. Zhang, Liu, et al., 2017) which outperforms NPs produced through wet chemical synthesis (Blakemore et al., 2013; Hunter et al., 2014). The excellent catalytic activity of PLAL-generated NPs is attributed to the bare-surface NPs due to the absence of ligand or capping agent and defect-rich (Manshina et al., 2024) property as a result of a rapid quenching, offering more active sites (Shankar Naik et al., 2023; G. W. Yang, 2007). PLAL can also produce complex structures which are difficult to obtain in other methods (Jia et al., 2014; J. Zeng et al., 2007), such as hollow NPs (Alheshibri et al., 2021; Desarkar et al., 2013) and core-shell NPs (Khairani, Lin, et al., 2023; Tymoczko et al., 2019). This technique also works at ambient temperature and atmosphere, uses no hazardous chemicals, and generates no or only a small fraction of waste, proving its compliance with the green chemistry principle (Amendola et al., 2020).

One of the most important parameters in PLAL which directly affects the generated NPs is the liquid media. By changing the liquid employed for PLAL, properties such as the composition, size, morphology, and phase of the produced NPs can be modified (D. Zhang & Wada, 2021a). As an example of phase modification, a study by Choi's group found that the PLAL of Ni in water produces NiO and FCC Ni, while only FCC Ni is produced in methanol. Changing the liquid to hexane and acetonitrile increased the complexity of the phases found, where the HCP phase was also present in addition to FCC Ni and NiO (Jung & Choi, 2014). The structure or morphology of the generated NPs also changes depending on the liquid, as the liquid reacts differently with different targets. For example, PLAL of Pt, Ag, and Pd in acetone tend to form core-shell of their metals with an outer carbon layer, while Ti, Mo, and Nb produce metal carbide with carbon encapsulation (D. Zhang et al., 2019). The oxidation level of the generated NPs is also an interesting property which is affected by the liquid (D. Zhang & Wada, 2021a) and the target material (M.-R. Kalus et al., 2019). Due to NPs' large surface area, they are susceptible to oxidation upon exposure to oxidizing agents. For example, PLAL of Ti in water generates almost 100% of TiO_x, meanwhile, gold's surface is oxidized less than 5% (M.-R. Kalus et al., 2019). Oxidation of PLAL-generated NPs might be intentionally done depending on the application, such as the production of TiO_2 from the PLAL of Ti target in water. But when oxidation is not desired, organic solvents can be used to

reduce the oxidation of PLAL-generated NPs (D. Zhang et al., 2019). These reports tell us how versatile PLAL is to produce NPs of a certain target material with different properties, simply by changing the liquid.

Despite PLAL's versatility, straightforward procedure, and compliance with the green chemistry principle, its practical use in industry barely exists. One critical drawback of PLAL is the low production rate (productivity) of the generated NPs which cannot fulfil the demand of industrial applications. The productivity of PLAL using an oxide target is typically measured in milligrams per hour range (Amendola et al., 2020; Chemin et al., 2019; Schmitz et al., 2017). Recent advances in strategies to achieve g/h productivity have been reported for metallic (Streubel, Bendt, et al., 2016) and ceramic NPs (Sajti et al., 2010), with a world record of 8 g/h for Pt NPs (Waag et al., 2021). In comparison to chemical methods to produce iron oxide NPs which have achieved a yield value of 40 g per batch (Park et al., 2004), PLAL is far from achieving this number. Although indeed a direct comparison between these two methods is not possible, as each of them has its own advantages and disadvantages, increasing PLAL productivity to gram per hour will reduce the production cost, lowering the NPs' market price and possibly increasing market demand for PLAL for industry (Jendrzej et al., 2017). Hence, it is necessary to find strategies to increase the productivity of PLAL.

1.2 Literature Review

In this sub-chapter, the influence of various factors on productivity will be discussed. The aim is to critically review the state-of-the-art of PLAL productivity and provide strategies to continue upscaling the process. Following the productivity discussion, liquid influence on the properties of the generated NPs will be elaborated. It is aimed to give better understanding of how different liquids in PLAL greatly affect the structure, phase, composition, oxidation, morphology, size, and stability of the generated NPs. It is important to consider the best liquid in PLAL to achieve the desired macroscopic properties of the NPs, thus potential applications. At the end of this sub-chapter, the fundamentals of water-splitting and FeNi-based OER catalyst will also be elaborated to lay the groundwork of the OER catalysis part, which is the main application of this study.

1.2.1 The Fundamentals of PLAL

Pulsed laser is used in the PLAL as the energy source to ablate the target material and produce NPs. It sends its laser energy in packages (pulses) with a certain pulse duration or pulse width (τ_{pulse}). The peak power is inversely proportional to the pulse width, hence, the shorter the laser pulse duration the larger the peak power. In comparison to continuous wave lasers, pulsed lasers with the same average power can reach a significantly higher peak power, making laser ablation with pulsed laser more efficient by reducing material heating.

The process of material removal and nanoparticle formation in PLAL involves a series of complex physical and chemical interactions between the material, the laser, and the liquid (Barcikowski, S., Amendola, V., Lau, M., Marzun, G., Rehbock, C., Reichenberger, S., Zhang,

D., Gökce, 2019; Chaudhary et al., 2016; Lahaye et al., 2013; X. Li & Guan, 2020; C.-Y. Shih et al., 2018). The interaction between the laser beam and the target induces a fast phase transition between the target-liquid boundary, leading to the formation of high pressure, temperature, and density plasma containing ionized and atomized species (Dell'Aglio et al., 2015; Kanitz et al., 2019; D. Zhang, Gökce, et al., 2017). As the plasma decays at a fast-cooling rate, the surrounding liquid absorbs the energy and it is transformed into a layer of supercritical vapor containing the evaporated and dissociated species from the liquid, namely the cavitation bubble (J. Long et al., 2020). The cavitation bubble is presumed to be the reservoir of solid crystallization, i.e., the formation of the atomic cluster, and primary and secondary particles (Ibrahimkutty et al., 2015; Jendrzej et al., 2016; C.-Y. Shih et al., 2017). The cavitation bubble might undergo expansion and shrinkage (Ibrahimkutty et al., 2015) before its final collapse, which releases the NPs to the surrounding liquid (C.-Y. Shih et al., 2018).

Depending on the operating laser pulse duration τ_{pulse}, the ablation mechanism differs (Kanitz et al., 2019). When a nanosecond laser is employed, the bulk target absorbs the energy and transfers it to the lattice, inducing energy release by heating the target, which causes melting, vaporization, bond-breaking, or defects formation that leads to material removal. All these processes take place while the laser is still irradiating the target. Meanwhile, when ultrashort pulses are employed (in pico- or femtosecond regime), the heating, melting, and material removal occur at a different time frame due to the electron-phonon coupling time being longer than the laser pulse duration. These differences due to the pulse duration influence the lifetime and cooling rate of the plasma, which leads to a unique plasma-liquid interaction (Kanitz et al., 2019), thus influencing nanoparticle phase, size, composition, as well as productivity.

1.2.2 Defining Nanoparticle Productivity

The amount of NPs produced within a certain period of time is defined as the production rate or productivity. Its value commonly lies within the milligrams per hour range, meanwhile, it is important to achieve NPs productivity in gram per hour scale to popularize this technology, reduce cost and move toward industrial applications. There are several strategies that can be employed to measure the ablated mass as gravimetric, optical extinction, or the use of analytical chemistry techniques approaches (Haiss et al., 2007). In the gravimetric approach, the mass difference of a target before and after PLAL is measured to be the total mass of NPs produced. The advantage of this approach is the easy and undemanding labor, but is not suitable for low productivities below the balance detection range, and the target mass difference can differ from the amount of colloidal nanoparticles produced if larger fractions of the target are ablated. This is especially relevant for powder-pressed targets where the compactness and porosity facilitate the detachment of larger particles by the laser action. The optical extinction approach employs a spectrophotometer to measure the intensity difference of light passed through the liquid used as a reference compared to the colloidal NPs. Based on the Lamber-Beer law, the absorbance of a dissolved substance is correlated with the colloid concentration (Hendel et al., 2014). It should be noted, however, that the concentration determination could only be applied if extinction (which consists of

absorbance and scattering) is dominated by absorbance and the scattering effect is insignificant. If the scattering effect is significant, for example, in the case of big NPs sizes, the absorbance and scattering elements should be separated before one can determine the concentration through the extinction method. The drawback of this approach is the unreliability for colloids at extreme concentrations (too high or too low) and materials which easily agglomerate and sediment, such as magnetic NPs (Golas et al., 2010; Phenrat et al., 2007; Yeap et al., 2017). In the case of highly concentrated colloids where the high absorption obscures the characterization, dilution of the colloid can be employed to reduce agglomeration effects and increase colloidal stability while bringing the absorption value to the linear regime of the concentration calibration curve without reducing the resolution of the concentration determination. The use of analytical chemistry techniques approach, for instance, as the inductively coupled plasma mass spectrometry (ICP-MS) usually requires a dilution of the sample, as the system is well suited for very low concentrations. These techniques can be used to provide the calibration curve required for optical extinction spectroscopy. The drawback of this approach comes from the high price of the equipment and the possible inaccuracies in the dilution process.

1.2.3 Strategies to Increase PLAL Productivity

A first thought on the possibilities for increasing productivity in PLAL immediately leads to the study of laser-matter interaction. The first approach that can come to mind is to optimize laser parameters by increasing laser power and repetition rate, and find the optimum irradiation wavelength for the employed material. Nowadays, there exist commercial laser systems operating at wavelengths from the UV to the IR able to achieve mean power values of hundreds of Watts that allow obtaining huge fluence values at the focal spot even operating at repetition rates in the order of the MHz. However, above a fluence threshold, limitations that depend on the scanning velocity (Streubel, Bendt, et al., 2016), repetition rate (Sajti et al., 2010), pulse width (C. Y. Shih et al., 2020), focusing conditions (Menéndez-Manjón et al., 2011), interaction with the liquid media (Doñate-Buendía et al., 2019), and target geometry appear (Kohsakowski et al., 2016). Consequently, several parameters are involved, and their optimization turns into a difficult task that even varies depending on the material, liquid, and pulse duration.

1.2.3.1 Choosing the Laser Pulse Duration

Depending on the pulse duration, the ablation mechanism differs. In the case where pulse duration is shorter than the electron cooling time, typically pulses shorter than 1 ps, the strong evaporation regime is produced and material removal is associated with the direct solid-vapor or solid-plasma transition, avoiding melting of the material. If the pulse duration exceeds the electron cooling time, the released heat causes first the melting of the material surface and its posterior vaporization or solidification. This results in some energy being used for melting rather than material removal.

Based on the above discussion, we might consider using ultrashort pulse lasers (femtosecond lasers) over picosecond and nanosecond lasers for a higher production rate.

Nevertheless, the influence of pulse width on NP productivity by PLAL is not only the ablation threshold reduction as in air, but also peak power and intensity-dependent interaction of the pulses with the liquid (S. Kudryashov et al., 2019; Nastulyavichus, Kudryashov, et al., 2022; Nastulyavichus, Smirnov, et al., 2022; Smirnov et al., 2022). Picosecond lasers are found to provide a suitable subcritical peak pulse power for the ablation process in the liquid medium, thus, generating the highest NPs yield per pulse and per unit energy (Nastulyavichus, Smirnov, et al., 2022). The ultrashort femtosecond lasers, on the other hand, trigger non-linear optical absorption, self-focusing, and filamentation effects in the liquid medium as it reaches supercritical peak pulse power, which affects the beam spatial profile and generates energy losses, decreasing the overall productivity (Barcikowski et al., 2007; Nastulyavichus, Smirnov, et al., 2022). The same trend is also observed for longer pulse duration in the nanosecond regime, in which plasma screening is attributed to be the main cause of productivity reduction, besides the energy loss from thermal processes such as localized heating and melting (Nastulyavichus, Smirnov, et al., 2022). It has been suggested that the use of picosecond lasers is advantageous compared to femtosecond lasers if the generated thermal energy can be redistributed, i.e., by using a liquid flow ablation chamber (Barcikowski et al., 2007).

1.2.3.2 Laser Wavelength Selection

Another important laser parameter which influences both target and liquid is the laser wavelength. Linear interactions such as absorption, reflection, and scattering occurring both in the liquid and the target need to be accounted for to maximize PLAL NPs yield. The laser wavelength defines these processes, as each material's absorption, reflectance, and scattering depend on the wavelength of the incident light (Berkmanns & Faerber, 2008; Bunaziv et al., 2021; Nakano, 2021). Higher absorption of the target at the laser wavelength leads to a higher energy density delivered to the sample and so the ablated volume increases. For example, for laser ablation in air, if a material has a low absorptivity at 1064 nm, the amount of ablated material with an Nd:YAG 1064 nm laser will be lower (Berkmanns & Faerber, 2008).

The optimum processing wavelength of the material can be determined by spectrophotometry, hence defining the most suitable wavelength for laser ablation in air. Nevertheless, the absorption of the liquid and generated nanoparticles in the laser ablation in liquid produce energy losses, requiring a laser wavelength with low liquid absorption and high material absorption (Tsuji, 2002; Tsuji et al., 2001). This key difference with ablation in air is shown in materials such as Au and Ag where the laser wavelength with maximum ablation efficiency differs from ablation in air (Mafuné et al., 2001; Tsuji et al., 2008). Scattering and inter- and intra-pulse absorption are commonly found as the main hurdles to increasing PLAL productivity. Intra-pulse absorption is related to the laser pulse width, which is found for longer pulses in the ns regime and above, as the pulse tail can be absorbed by the generated NPs and plasma plume from the pulse front (Tsuji et al., 2001). The scattering and inter-pulse absorption, on the other hand, are associated with the extinction coefficient of the liquid and the generated colloidal NPs, which affect the laser energy delivered to the target.

As reported by Intartaglia et al. (2014) (Intartaglia et al., 2014), the ablation of Si in water using a UV laser (355 nm) resulted in lower productivity compared to the ablation using a NIR laser (1064 nm). They observed two different regimes in the UV laser ablation, termed transient and steady-state regimes, where the productivity is higher during the transient regime (smaller number of pulses, shorter ablation time) compared to the steady-state regime (larger number of pulses, longer ablation time). TEM analysis shows that the smaller Si NPs size is obtained with increasing ablation time, proving the photo-fragmentation phenomenon (Intartaglia et al., 2014). Meanwhile, the ablation using a NIR laser shows a steady ablation yield and the particle size is also bigger than the UV-ablated Si NPs. These effects are especially prominent if a batch chamber is used in PLAL, where the generated NPs stay in the chamber after generation and shield the laser beam. The employment of a flow chamber is thus recommended to reduce scattering and absorption related to the generated NPs and to improve productivity. Selecting the laser wavelength with minimum absorption and scattering by the generated NPs is crucial to maximizing the laser energy delivered to the target. While UV laser is more beneficial to produce smaller NPs due to the fragmentation effect, the NIR laser is the most ideal choice to obtain high ablation yield due to the low absorption by generated NPs.

1.2.3.3 Bypassing the Cavitation Bubble

The optical phenomena occurring in the liquid are not the only difference between laser ablation in air and PLAL. The presence of the liquid and the laser interaction promotes the formation of a cavitation bubble for each pulse interacting with the target. This vapor bubble is formed when the local pressure drops below the liquid's vapor pressure; hence, the inside of the bubble is filled with vapor. The cavitation bubble in PLAL is formed due to the instant vaporization of the liquid exposed to the heat of the plasma plume. After the cavitation bubble formation and expansion up to the maximum height, the cavitation bubble undergoes a shrinkage process and finally collapses, releasing a shockwave to the surrounding liquid. The cavitation bubble's lifetime and size strongly constrain PLAL productivity. In continuous ablation PLAL, the first bubble generated by the first laser pulse can shield the subsequent pulses, hindering the laser energy that reaches the target material. Two strategies have been proposed to bypass the cavitation bubble. The first one is to temporally bypass the cavitation bubble, which means that the subsequent pulse is sent when the previous cavitation bubble already collapsed (Wagener et al., 2010). This approach is only suitable for low repetition rate laser sources, for example, if the lifetime of the cavitation bubble is 100 µs, the maximum repetition rate that can be employed is 10 kHz to temporally bypass the cavitation bubble (Doñate-Buendia et al., 2023). Nevertheless, high repetition rate lasers with high pulse energy are desired to increase PLAL productivity. Hence, the second proposed mechanism, i.e., spatially bypassing the cavitation bubble, represents a more feasible way to achieve industrial-scale PLAL production.

Spatial bypassing of the cavitation bubble can be achieved by a high scanning speed of the processing pattern. The distance between pulses has to be at least equal to the cavitation bubble radius so the subsequent pulse does not interact with the bubble formed by the previous pulse. In a real NP production scenario, the laser power and repetition rates are

maximized while keeping the optimum fluence in order to deliver the larger number of pulses and maximize the ablated volume. In this scenario, a fast-scanning system is required to increase the inter-pulse distance and increase the ablated area to ensure that the target has enough time between successive scanning patterns to cool down. The scanning speed becomes a fundamental parameter together with the repetition rate and the cavitation bubble size for each specific system to ensure cavitation bubble bypass. As an example, for a cavitation bubble with an average radius of 100 μm produced with a laser source operating at a 100 kHz repetition rate, the minimum scanning speed required to completely bypass the cavitation bubble is 10 m/s. The galvanometer scanner technology can reach 10 m/s. Nevertheless, if the repetition rate is further increased to the MHz range, scanning speeds of at least 100 m/s are required. As the number of delivered pulses per second is critical for PLAL productivity, the required scanning speeds reach the current technological limitations. In 2013, De Loor introduced a new scanning technology based on the rotation of mirrors fixed on a polygon wheel (De Loor, 2013). This polygon scanning technology offers a beam deflection speed of up to ~1000 m/s (De Loor, 2013; Schille et al., 2016). However, since the corner of the polygon wheel will deflect the beam at uncontrolled angles, the laser beam is shut off during this time and the laser beam only irradiates the target within a certain percentage of the duty cycle. This effect is more pronounced for small processing patterns, requiring large patterns with lower spatial resolution than the galvanometric scanners (Franz et al., 2022).

In conclusion, PLAL upscaling requires faster scanning technologies. Using high-speed polygon scanners is one of the easiest ways to enhance NPs production (S. Kudryashov et al., 2021). However, their high prices, low precision demanding large scanning patterns, and their duty cycle that reduces the initial laser power employed in the target processing by a 50% factor, make it difficult the implementation of this technology in every PLAL system. Consequently, generally galvanometric scanners still represent are more economical and repost alternative for PLAL, especially when fast galvanometric scanners reaching 30 m/s are employed.

1.2.3.4 Avoiding Persistent Microbubbles

The productivity of PLAL can be adversely affected not only by cavitation bubbles and NPs in the laser path but also by the formation of so-called persistent microbubbles during the process. Persistent microbubbles are spherical and stable gas bubbles, generated from the collapse of the cavitation bubbles. While a cavitation bubble lifetime is approximately 0.1–1 ms (M. R. Kalus et al., 2017), persistent microbubbles can stay even as long as seconds (Sasaki & Takada, 2010). Consequently, it is critical to understand the liquid, target, and laser processing parameters related to the lifetime of the persistent microbubbles in order to avoid their presence that shields the laser beam and can even become a safety issue when they stick to the chamber window, increasing reflectivity and even leading to glass breakage by the high-intensity laser source. Unlike cavitation bubbles, which can be spatially and temporally located, allowing the implementation of bypassing strategies, persistent microbubbles exhibit an unpredictable evolution that limits their bypass. Consequently, liquid flow strategies such as a high flow rate and good laminar flow represent the best

approach to remove the detached persistent bubbles. Controlling the liquid flow by the chamber design becomes a fundamental factor for PLAL upscaling since turbulence would extend the retention time of these shielding bubbles inside the chamber, resulting in a reduction of the process efficiency.

1.2.3.5 Optimizing the Ablation Chamber Design

The simplest ablation chamber design in PLAL is a glass beaker or a cuvette where the target is placed either laying or standing depending on the direction of the incoming beam. This setup is sufficient for the production of NPs in a small batch, but for larger production, the employment of these chambers is no longer feasible. Due to the limited volume of the chamber, the colloid becomes concentrated more rapidly, which hinders the ability of the incoming laser beam to reach the target. In addition, the NPs and persistent bubbles that are formed scatter the incoming laser beam since there is no liquid flow to remove them. (Charee et al., 2015). Hence, different chamber designs have been proposed to improve the PLAL production rate. Barcikowski et al. (2007) (Barcikowski et al., 2007) presented a type of batch chamber with a magnetic stirrer to make the liquid flow inside the chamber. The liquid flow inside the chamber is aimed to induce target cooling during ablation and displace the generated NPs away from the target to reduce laser shielding.

A different approach includes the liquid flow within the chamber produced by the rotation of the cylindrical target attached to a brushless motor (Resano-Garcia et al., 2016). At the same time, the rotating target drives away the generated NPs from the vicinity of the target and increases the inter-pulse distance reducing cavitation bubble shielding (Resano-Garcia et al., 2016). The influence of the rotation speed on the ablation rate was evaluated by the colloidal optical extinction approach. The highest PLAL productivity was found at the lowest rotation speed (300 rpm), decreasing with the increasing rotation speed. Based on the flow simulation results, increasing the rotation speed leads to the formation of unsteady flows and vortices in front of the target's surface, which traps the bubbles produced during PLAL increasing laser shielding (Resano-Garcia et al., 2016).

The next evolution in chamber design is a flow-through chamber that allows PLAL with a continuous feed of fresh liquid and collection of the generated colloid (Marzun, Levish, et al., 2017). The liquid is pumped through the chamber where ablation takes place, and the generated NPs are carried out of the ablation chamber so that laser shielding is avoided. An optimum liquid flow rate is achieved when the generated NPs are completely removed from the ablation area, confirmed by monitoring the productivity with increasing flow rates (Sajti et al., 2010). An advantage of this chamber is the capacity to extend PLAL without a colloid concentration saturation and is only limited by the target drilling which allows processing times of several hours even for thin (1 mm) targets (Streubel, Bendt, et al., 2016).

Many ablation chamber designs are proposed to increase productivity and improve the efficiency of the PLAL process, nevertheless, the discussion related to the fluid dynamics inside the chamber is limited. As the design of the chamber strongly influences the liquid flow, an ineffective chamber produces fluid turbulences which increases the retention time of the NPs inside the chamber, giving rise to the NPs shielding effect of the incoming laser beam.

Producing ablation chambers with a laminar flow is needed in order to increase ablation efficiency and productivity. To produce a laminar flow, a fluid dynamic simulation of the newly designed chamber should be done prior to the production step, to analyze the formation of turbulences and vortices. Studying different liquid viscosities and the influence of species and effects generated by the PLAL process, including the persistent gas, nanoparticles, heat transfer, and the collapse of the cavitation bubbles, are some further stages that can be done in this regard. In summary, the design of an ablation chamber should be accompanied by an engineering approach of fluid mechanical design, which addresses the shortcomings of the inefficient chamber in order to produce laminar flow with minimum turbulence and vortices.

1.2.4 Liquid Influence on Properties of PLAL-Generated NPs

In previous chapters, the fundamentals of PLAL, the definition of productivity, and the strategies to increase productivity have been discussed. The influence of liquid on productivity has also been reviewed, such as viscosity, where bubble dwell time is longer during the PLAL in a more viscous liquid, reducing productivity. Yet, the influence of liquid in PLAL is broader than that, as the ablated matters undergo chemical reactions with the liquid vapour inside the cavitation bubble (D. Zhang, Gökce, et al., 2017). In this sub-section, we discuss the liquid's role in the properties of the generated NPs, such as the morphology, structure, size, and phase.

1.2.4.1 Atomic Composition and Oxidation

In most cases, PLAL generates NPs with atomic compositions that are almost identical to the target materials (D. Zhang, Gökce, et al., 2017). This is indeed true for noble metals such as Au, Ag, and Pt, as they possess higher resistance to oxidation, or alloys with miscible constituting elements which can form monophase crystalline structures, such as AgAu (Neumeister et al., 2014). However, metals or alloys composed of easily oxidized elements, typically characterized by their negative standard reduction potential, E^0, may produce unidentical atomic composition to the target materials, and form nonstoichiometric and segregated alloys (Jakobi et al., 2010; Wagener et al., 2016), for example, PLAL of Cu (Marzun, Bönnemann, et al., 2017), AgCu (Malviya & Chattopadhyay, 2014), and FePt (Ishikawa et al., 2006) in water. Alloys consisting of elements with a large difference in reduction potential may produce doped oxides through a one-step synthesis method, such as the PLAL of AgTi alloy in DI water, generating Ag-TiO_2 (Hamad, Li, Liu, et al., 2015). If stoichiometric alloying is desired for these types of metals and alloys, the use of water as the liquid in PLAL is unfavourable, as its decomposition produces oxygen species which react with the non-noble metals (D. Zhang, Gökce, et al., 2017), organic solvents can be used instead to reduce the oxidation and segregation effect (Jakobi et al., 2010; T. B. Nguyen et al., 2015; Wagener et al., 2016). However, the formation of carbides, instead of oxides, can be observed while performing PLAL in organic solvents, such as in the PLAL of Cr in toluene and acetone that produce Cr_3Cr_{2-x}. In addition, some organic solvents still contain molecular oxygen in their structures, which can be transformed into reactive oxygen species during the ablation process and contribute to oxidation, for example in the case of $Al@Al_2O_3$ core-shell formation

in H_2-purged ethanol (Viau et al., 2011). The exact control of atomic composition and oxidation of the generated NPs requires a deeper understanding of the chemical reactions, kinetics, and thermodynamics during the whole process of PLAL, from the laser pulses reaching the liquid and target to the storing of the NPs themselves. Although tuning the oxidation degree of the generated NPs remains a challenge, PLAL is capable of producing these diverse oxides with interesting properties, which may potentially be useful for specific applications. Hence, it all comes back to the final application of the generated NPs themselves; if oxide NPs are desired as they provide interesting properties, then PLAL of metals in water can be done, for example, the PLAL of Ti in water has been reported to form defect rich TiO_x showing ferromagnetism at room temperature (S. C. Singh et al., 2015) and TiO_x with smaller bandgap (C. N. Huang et al., 2010). Therefore, a thorough understanding of the liquid influence to the oxidation and atomic composition should be done to achieve the best possible results of the desired NPs.

1.2.4.2 Morphology

Nanomaterials that are produced through PLAL are mostly spherical, as this form offers the smallest surface area to volume ratio and, thus the lowest surface tension, as compared to other shapes. However, other shapes such as core-shell, nanosheets, spindle-like, hollow, and flower-like, can actually be formed during PLAL of some materials by changing liquid parameters (D. Zhang, Gökce, et al., 2017), for example, the formation of nanorods Co_3O_4 and nanosheets $Co(OH)_2$ in aqueous KOH solution at pH 14 (S. Hu et al., 2014), or the formation nanosheets and flower-like morphology of α-$Ni(OH)_2$ doped with Mn in the PLAL of Mn in $NiCl_2$ solution (H. Zhang et al., 2013). The liquid used in PLAL can vary from water, solution of salts, surfactants, or polymers, and organic solvents (D. Zhang, Gökce, et al., 2017), but PLAL in different polymers or surfactants can still generate different shapes of NPs, as they react differently with the atoms of the target material. For example, PLAL of Ag in polyvinylpyrrolidone (PVP) (Tsuji et al., 2008) and sodium dodecyl sulfate (SDS) (Mafuné et al., 2001) solutions result in Ag nanospheres, but PLAL of Ag in polysorbate 80 (Tween 80) aqueous solution generates Ag_2O nanocubes and nanorods, in addition to Ag nanospheres (Z. Yan et al., 2011). Adding ethanol to the aqueous polysorbate 80 produces Ag nanonetworks (Z. Yan et al., 2011). These results show us that changing the liquid in PLAL could completely change the morphology of the generated NPs.

1.2.4.3 Phase

Phase and shape (morphology) occasionally correlate to each other, as different phases tend to grow into a certain shape, as in the case of nanorods Co_3O_4 and nanosheets $Co(OH)_2$ (S. Hu et al., 2014) and nanocubes Ag_2O and nanosphere Ag, discussed in the above section. However, in this section, the discussion is heightened to the distinct, metastable phases that can be generated straightforwardly in the PLAL than in other methods.

In the formation of NPs, the nucleated atoms and ions from the plasma come into contact with the liquid at the liquid-plasma interface, which results in the formation of a cavitation bubble due to the evaporation of the surrounding liquid, indicating that chemical reactions that drive the formation of NPs' phases may take place in this time scale (nanosecond). Due

to the rapid quenching after the ions and atoms encounter the comparatively colder liquid, "freezing" of metastable phases is sometimes observed in PLAL. Nanomaterials consisting of metastable phases are one of the most remarkable outcomes of PLAL, as they can bring forth these metastable phases to ambient conditions, which are difficult or even impossible to be synthetically produced in the laboratory. For example, a method called diamond anvil cell (DAC) produces metastable phases by applying extremely high pressure to the material using two colliding diamonds (Boehler, 2005). However, after the pressure is released, the metastable phase cannot be preserved. PLAL, on the other hand, keeps these metastable phases at ambient conditions after the synthesis without the use of external pressure or temperature.

The liquid, including the dissolved gas in the liquid, plays an important role in the formation of these metastable phases, for example in the formation of metastable Cr_3C_{2-x} phase in the PLAL of Cr in ethanol, acetone, and toluene (Semaltianos et al., 2014), β-$Co(OH)_2$ phase in the PLAL of Co in N_2-purged water where most of the dissolved O_2 gas were removed (S. Hu et al., 2014), and HCP Ni in the PLAL of Ni in acetonitrile and hexane (Jung & Choi, 2014). The mechanism, as to why certain liquid produces certain metastable phases, is not yet fully understood, other than the postulated high temperature, high pressure, and high density (HTHPHD) condition which is formed at the interface between the plasma plume and the liquid (P. Liu et al., 2008). Finding metastable phases in PLAL at the present moment is purely coincidental, as we cannot predict which metastable phases will be formed in a certain experimental condition. Tuning the amount or ratio of these metastable phases also remains a challenge. Understanding how the liquid influences the formation of metastable phases in the PLAL will contribute tremendously to the advancement of materials science.

1.2.4.4 Ageing and Stability

Oxides in the laser-generated NPs are formed due to the reaction of ablated matter with reactive oxygen species from the evaporated liquid (Lam et al., 2014). Nevertheless, prolonged storage of NPs in the liquid, especially water, may cause further oxidation and ripening (growth) effects, termed ageing. Ageing was observed in the prolonged storage of Al NPs in water, as observed in the shift of surface plasmon resonance peak from 225 nm to 264 nm just 2 hours after storage, indicating the formation of an Al_2O_3 shell (R. Singh & Soni, 2014). Ripening and growth of the NPs are also observed after prolonged storage, for example in the PLAL of Ag in water, where the peak size distribution is shifted to a larger size within 4 months of storage (Oseguera-Galindo et al., 2012). Meanwhile, PLAL of Ag in propanol does not show this trend of size increase (Oseguera-Galindo et al., 2012). The use of diluted electrolytes, such as sodium hydroxide, phosphate and carbonate buffers, at low concentrations was also found to increase colloidal stability of Pd NPs to 14 days, as compared to 1 day only in water (Marzun et al., 2015). This phenomenon is attributed to the change of surface charge after ion adsorption on the surface of NPs, increasing their electrostatic stability (Rehbock et al., 2013; Sylvestre et al., 2004). Nevertheless, not all electrolytes have the same effect. A study found that ionic kosmotropes, ions that promote water-to-water bonding, result in lower stability of the NPs in an aqueous solution, as they hydrate and interact with water molecules (Merk et al., 2014). Meanwhile, chaotropes, ions that are large and have a low charge, increase the

stability after their adsorption onto the NPs surface (Merk et al., 2014). However, this effect should be further investigated, as different types of NPs, depending on their oxidation potential, react differently with these electrolytes. For example, Pd NPs, which are more prone to oxidation than Au NPs, show that the stabilization effect from electrolytes is less pronounced, as Pd's surface is readily more oxidized than Au (Marzun et al., 2015).

1.2.4.5 Size distribution

The size distribution of NPs generated through PLAL is directly influenced by the liquid. Although the target material, laser parameters, chamber design, and storage time also affect the size distribution, one can adjust the NPs' size and prevent agglomeration by changing the liquid. PLAL of Ag in acetone and propanol result in average NPs' sizes of less than 10 nm, while in water, ethanol, and methanol NPs generated have an average size of more than 10 nm (Oseguera-Galindo et al., 2012). Meanwhile, Ag ablation in PVP results in a lower average size compared to water, but varying PVP concentration from 2 mM to 18 mM does not change the size nor the particle distribution much (Tsuji et al., 2008). Another report, however, found that increasing SDS concentration from 3 mM to 50 mM offers a size-quenching effect on Ag NPs (Mafuné et al., 2001). The use of 1mM of phosphate buffer as a liquid in the PLAL of Pd avoids the bimodality and lowers the polydispersity index (PDI) compared to water from 1.03 to 0.36 (Marzun et al., 2015). Meanwhile, the influence of kosmotropes and chaotropes is not only limited to the stability as discussed in the previous section but also to the size distribution, since these two properties are usually related to each other, as bigger NPs and more agglomeration reduce the stability of NPs in the liquid. Rehbock et al. (Rehbock et al., 2013) found that chaotropes ions, i.e., Br^- and I^- lead to the reduction of NPs size, due to the electrostatic stability provided by these large ions after their adsorption to the Au NPs' surface.

Size distribution, as well as atomic composition, morphology, and phase of the generated NPs, are strongly influenced by the liquid in PLAL. However, these NPs' properties also play important roles in the NPs' final applications. For example, smaller NPs are usually proposed in catalysis, but they are also more prone to oxidation. Finding the balance between an affordable, environmentally friendly, and safe liquid to produce NPs with the best catalytic performance is therefore important.

1.2.5 OER in Water Splitting Process

In the previous chapter, we have discussed PLAL to a great extent, as to how productivity in PLAL can be defined, measured, and improved, and how liquid in PLAL influences NPs' properties. All of this information provides the groundwork needed to underline the aim of this work, which is to produce OER nanocatalysts from a green synthesis method and to scale up the production rate in order to fulfil industrial demand. In this sub-chapter, the discussion is more focused on the PGM-free FeNi-based catalyst for OER reaction in the water splitting process, which is envisioned to lower the production cost of green hydrogen by lowering electrolysers price, accelerating the hydrogen energy transition and net zero emission by 2050.

1.2.5.1 Mechanism

In the water-splitting process, two reactions happen, hydrogen evolution reaction (HER) in the cathode, and oxygen evolution reaction (OER) in the anode. Both of these processes require the transfer of electrons to produce the respective molecules, but generating one molecule $O_{2\,(g)}$ requires the transfer of 4 e^-, meanwhile, only 2 e^- are needed to generate $H_{2\,(g)}$. Due to this, the water-splitting process is usually limited by the kinetically more sluggish OER than HER, therefore, a significant amount of research in this field is focused on the development of OER catalyst (Kawashima et al., 2023). Ruthenium and iridium oxide catalysts are usually used for OER catalysts due to their low overpotentials (~ 200–300 mV for thin films) and ability to work in a wide range of pH (F. Song et al., 2018), but they are scarce and expensive, rendering them impractical for large-scale applications (Kawashima et al., 2023). Hence, the focus has shifted to developing and improving the performance of abundant and cheap catalysts with high catalytic activity, such as transition metal catalysts. Nevertheless, transition metals are easily dissolved in acidic solutions, thus, most research on transition metal OER catalysts is focused on alkaline conditions (F. Song et al., 2018). These different pH values result in different half-reactions, influencing the standard reduction potential, E^0, of each half-reaction, as shown in Table 1 (Hunter et al., 2016). Nevertheless, the overall cell potential needed for the water-splitting process remains the same, which is 1.23 V.

Table 1. Water splitting reactions in different pH conditions (F. Song et al., 2018).

In acid condition			
$2\,H_2O\,(l)$	$\rightarrow$	$O_2(g) + 4\,H^+ + 4\,e^-$	$E^0 = -1.23\,V$
$4\,H^+ + 4\,e^-$	$\rightarrow$	$2\,H_2\,(g)$	$E^0 = 0\,V$
$2\,H_2O\,(l)$	$\rightarrow$	$O_2(g) + 2\,H_2\,(g)$	$E^0 = -1.23\,V$
In basic condition			
$4\,OH^-$	$\rightarrow$	$O_2(g) + 2\,H_2O\,(l) + 4\,e^-$	$E^0 = -0.40\,V$
$4\,H_2O\,(l) + 4e^-$	$\rightarrow$	$2\,H_2\,(g) + 4\,OH^-$	$E^0 = -0.83\,V$
$2\,H_2O\,(l)$	$\rightarrow$	$O_2(g) + 2\,H_2\,(g)$	$E^0 = -1.23\,V$

In the alkaline condition, the electron transfer process for OER on a catalyst with active site M may happen under these mechanisms (S. Chen et al., 2023):

$$\mathrm{OH}^- + M \rightarrow MOH + e^- \quad (1)$$

$$MOH + OH^- \rightarrow MO + H_2O + e \quad (2)$$

$$MO + OH^- \rightarrow MOOH + e \quad (3)$$

$$MOOH + OH^- \rightarrow M + O_2 + H_2O + e \quad (4)$$

It should be noted that this mechanism is a step-by-step single electron transfer route, hence, MO and MO cannot be combined to produce O_2. Each step is influenced by the activation energy to bind and release the intermediate to and from the active site M (S. Chen et al., 2023).

1.2.5.2 Electrochemical Analysis

The equilibrium potential needed to drive the overall water-splitting reaction is 1.23 V, Table 1. Nevertheless, the experimental value cannot be as ideal as the theoretical value, due to reactant transport limitation, bubble formation, resistance, kinetic barriers, etc. The additional potential required to start the reaction is termed overpotential (η, unit mV). Lower overpotential means higher catalytic activity, as only smaller additional energy is needed to drive the reaction spontaneously. The overpotential needed to reach a specific current density, i.e., at 10 mA/cm^2, is commonly used to compare the electrical performance of different catalysts.

In general, the performance of a catalyst is mainly controlled by four factors: (1) intrinsic activity, (2) mass loading (thus active sites), (3) surface structure (thus area), and (4) synergistic effect between the catalyst and the substrate (Kawashima et al., 2023). Intrinsic activity is the chemistry of the catalyst itself, independent of the number of active sites and surface area, yet many reports define the intrinsic activity based on the overpotential to reach 10 mA/cm^2. This overpotential value, however, does not reflect the intrinsic activity of the catalyst itself, since it is not normalized to the surface area and active sites of the catalyst (C. Wei & Xu, 2018). It means that two catalysts with the same loading mass may have different surface areas or active sites, making them less or more catalytically active. It is therefore important to avoid using the overpotential value to define the intrinsic activity of a catalyst. Alternatively, intrinsic activity can be analyzed using turnover frequency (TOF), where the number of electrons transferred per active site every second is measured. Yet, quantifying active sites is a difficult task, making it hard to accurately measure TOF (Kawashima et al., 2023; C. Wei & Xu, 2018). Using the value of overpotential to reach current density at 10 mA/cm^2 is fine, as long as it is not used to define the intrinsic activity and instead the overall performance of the electrode (catalyst and substrate).

Overpotential is measured through cyclic voltammetry (CV) or linear sweep voltammetry (LSV) which can be done in a three-electrode system. The three-electrode system consists of:

(1) A working electrode: an electrode where the catalysts are deposited and reactions occur. Some examples include glassy carbon electrodes (GCE), carbon paper, and metal foams (Fe or Ni foams).
(2) A reference electrode: an electrode that is used as a reference throughout the catalysis process, hence, it must remain stable (by reading the potential before and after the experiment). Commonly employed reference electrodes are Ag/AgCl, Hg/HgO, and Hg/Hg_2Cl_2 (saturated calomel electrode), and should be chosen based on the electrolyte.
(3) A counter electrode: an electrode which is used to balance the current in the working electrode and does not affect the electrochemical reaction. This type of electrode is commonly made out of inert materials, such as graphite, glassy carbon, Pt, and Au.

The kinetics of a catalyst can be defined by the Tafel slope (unit mV/dec) from the Tafel equation, $\eta = a + b \log(j)$, where η is overpotential, a is an equilibrium constant, b is the Tafel

slope, and j is the current density. Tafel slope simplified definition is the overpotential (in mV) needed to increase the current density by an order of magnitude, hence, smaller Tafel slopes indicate better catalyst performance (van der Heijden et al., 2024). In addition, Tafel slope values can also be used to determine the slowest step in the mechanism, meaning the rate-determining step (RDS). Tafel slope ~118 mV/dec indicates that the first single-electron transfer, for example as shown in Equation (1), is the RDS. Tafel slope at ~59 mV/dec signifies the RDS to be the chemical reaction after the single electron transfer, while ~29.5 mV/dec implies that the third electron transfer is the RDS (D. Li et al., 2020). Another measurement of reaction kinetic can be performed using electrochemical impedance spectroscopy (EIS). A Nyquist plot can be obtained from the EIS and its diameter represents the charge transfer resistance (R_{ct}) value (Lazanas & Prodromidis, 2023). R_{ct} is the resistance value against electron transfer from one phase to another, i.e., from the electrode to the electrolyte (D. Li et al., 2020). A smaller R_{ct} represents a faster electron transfer, thus, a faster reaction kinetic.

Catalyst stability is an important parameter for long-term applications such as electrolysers. Electrochemical approaches to measure catalyst stability can be done via dynamic and/or steady-state approaches (D. Li et al., 2020). Dynamic stability is measured by CV at a high scan rate, i.e., accelerated degradation test (ADT), and the plot before and after certain cycles are compared. A current density lower than 20 mA is recommended, as a higher current density produces a lot of gas which can hinder mass transfer, i.e., reactants cannot diffuse or reach the electrode (D. Li et al., 2020). Meanwhile, steady-state stability can be performed through chronoamperometry (current density as a function of time) or chronopotentiometry (potential as a function of time). Catalysts that show stable performance after a long duration of applied current density or potential have good stability (Kawashima et al., 2023).

1.2.5.3 FeNi-based OER Catalyst

FeNi-based OER catalysts are promising candidate to replace PGM catalysts for the water-splitting process in alkaline conditions due to their high electrocatalytic activity (Corrigan, 1987; Klaus et al., 2015; Ros et al., 2021; Trotochaud et al., 2014; Twight et al., 2024). It is reported that the combination of Fe and Ni forms a synergistic effect, due to the change of electronic structure, more active sites available, and stabilization of higher oxidation states (J. S. Kim et al., 2018; N. Li et al., 2017; Salmanion & Najafpour, 2023; Smith et al., 2013; Spanos et al., 2021; Trotochaud et al., 2014; Xiao et al., 2018). At first, Ni oxyhydroxides (γ-NiOOH phase) was known as the phase responsible for the high activity of Ni for OER. Nevertheless, further studies reported that the removal of Fe impurities in the electrolyte lowers NiOOH catalytic activity (Trotochaud et al., 2014) while adding Fe increases NiOOH catalytic activity (Stevens et al., 2017). Following this observation, Xiao et al. (Xiao et al., 2018) found that the responsible steps for OER are the formation of O radicals and the O-O coupling, but NiOOH is poor at generating O radicals. Using quantum mechanics methods, they discovered that the high spin in the d^4 orbital of Fe(IV) stabilizes the O radical via exchange interaction while the d^6 Ni(IV) catalyzes the coupling of O-O. This phenomenon results in a lower Tafel slope as the O-O coupling precedes the steps for two-electron transfer (Xiao et al., 2018).

Other forms of FeNi catalysts are also explored, such as FeNi-layered double hydroxides (LDH). This structure exhibits exceptional OER performance (Gong et al., 2013; Z. Lu et al., 2014) than other PGM-free catalysts (Y. Liu et al., 2018). The reason behind its high performance is most likely due to the increased surface area, the multivalence states (S. Jiang et al., 2024), and Fe atoms integration into α-$Ni(OH)_2$/γ-NiOOH lattice (Tang et al., 2015). Growing FeNi LDH on the Ni foam substrate via the hydrothermal method to produce FeNi LDH/Ni foam produces a catalyst with a lower overpotential to reach a current density of 30 mA/cm^2 than Ir/C catalysts, requiring only 280 mV, while commercial Ir/C requires 390 mV (Z. Lu et al., 2014). FeNi LDH on the Ni foam increases the electrode's surface area by factor 4 from 0.06 m^2/cm^2 to 0.24 m^2/cm^2 (Z. Lu et al., 2014). In Table 2, the electrochemical performances of various FeNi-based catalysts, especially those with LDH structures and/or Ni foam supports as substrate material, are presented, showing the possibility of producing PGM-free catalysts with overpotential lower than 300 mV and stability even up to 6000 h. Indeed, among the explored non-PGM oxide (Burke et al., 2015) and hydroxide (X. Li et al., 2011) species, Fe-Ni is the most active catalyst for OER in alkaline media.

Table 2. Literature review of FeNi-based catalysts for OER

Catalyst	Support	Electrolyte	η (mV)	*j* (mA/cm^2)	Tafel slope (mV/dec)	Stability (h)	*j* (mA/cm^2)	Ref
NiFe-LDH/rGO	**Ni foam**	1 M KOH	150	10	35	24	10	(C. Li et al., 2019)
FeNi-LDH/rGO	**Ni foam**	1 M NaOH	195	10	40	8	10	(X. Long et al., 2014)
FeNi-LDH	**Fe foam**	1 M KOH	300	500	n/a	6000	1000	(Y. Liu et al., 2018)
FeNi-LDH	**Fe plate**	1 M KOH	269	10	48	100	100	(Y. Liu et al., 2018)
FeNi-LDH/Phospide NPs	**Ni foam**	1 M NaOH	224	10	72	20	20	(Q. Yan et al., 2018)
$NiFe_2O_4$@N-doped/rGO	**Ni foam**	1 M KOH	252	20	49.7	12	20	(L. Cao et al., 2021)
NiFe-LDH intercalated NO_3 & H_2O	**flat pyrolytic graphite**	1 M KOH	280	10	47.6	5	2	(Hunter et al., 2014)
NiFe Nanosheets	**Glassy carbon disk**	1 M KOH	300	10	40	13	10	(F. Song & Hu, 2014)
rGO	**Ni foam**	1 M KOH	350	10	170	n/a	n/a	(J. Wang & Lian, 2023)
Sulfated NiFe LDH nanosheet	**Glassy carbon disk**	1 M KOH	219	10	39.5	24	10	(Qiao et al., 2021)
FeNi-LDH with carboxyl ligands	**Ni foam**	1 M KOH	273	500	34.8	1000	1000	(Y. Chen et al., 2024)

1.3 Thesis Framework

1.3.1 Aim

This dissertation addresses the property analysis and production of NPs through the PLAL method and their use as OER catalysis. Particularly, the dissertation is focused on the generation of abundant and catalytically active FeNi-based catalysts for OER as an alternative to precious and rare catalysts. The use of abundant elements such as Fe and Ni as catalysts is crucial to lower the cost of the catalyst needed to accelerate sluggish OER reaction in the water-splitting process. In addition, the NPs production method, PLAL, complies with the green chemistry principle as it avoids the use of hazardous chemicals and operates in an ambient atmosphere. The knowledge gained from this dissertation is therefore hoped to bring PLAL into the industry as a green synthesis method to produce abundant and catalytically active FeNi NPs, lowering the catalysts cost and accelerating the production of green hydrogen to achieve net zero carbon by 2050.

1.3.2 Scope of the Thesis

The solvent influence and the production rate of the PLAL method are evaluated and the optimum strategies to maximize productivity while controlling the composition and reducing the oxidation are proposed. The schematic illustration of the dissertation's scope is presented in Figure 1. First of all, a general introduction to the topic in Chapter 1, including the state-of-the-art, specifically on the scaling-up strategies in PLAL, liquid influence on the generated NPs, and OER catalyst in water splitting, is elaborated. The scope of the dissertation and the research questions are also provided at the end of the introduction section. After building the foundation, results and discussions related to the experimental investigations and results are presented in Chapters 2 and 3.

The results of the first study, presented in Chapter 2.1, is related to the liquid media influence on PLAL. PLAL is a method that requires a liquid media to capture and carry the generated NPs, thus, the selected liquid affects the properties of the produced FeNi NPs. In addition, it is important to find a balance between the cost-effectiveness of the liquid and the properties of the generated FeNi NPs. As our goal is to produce catalysts on a large scale for the industry, the investigated liquids are limited to affordable and abundant solvents which are more economically viable, such as water and acetone. Nevertheless, water is a liquid that can oxidize the produced FeNi NPs, hence, organic solvents such as acetone are usually used to lower the oxidation. Yet, acetone contains some water impurities, which contribute to the oxidation of the NPs. To reduce the water content in acetone, cheap and reusable molecular sieves can be used to capture the water molecules, producing "dried" acetone (acetone with reduced water content, obtained after treatment with molecular sieves). Hence, we investigate these liquids, namely water, acetone, and dried acetone, and their influence on key properties of FeNi NPs for the catalytic performance such as morphology, phase, size distribution, and catalytic activity. Due to the importance of high throughput production to aim for the industrial application, it is also crucial to consider a balance between high

catalytic activity and production rate. Therefore, FeNi NPs productivity measurements as a function of the solvent employed were also conducted in this chapter, in addition to the property analysis of the produced FeNi NPs.

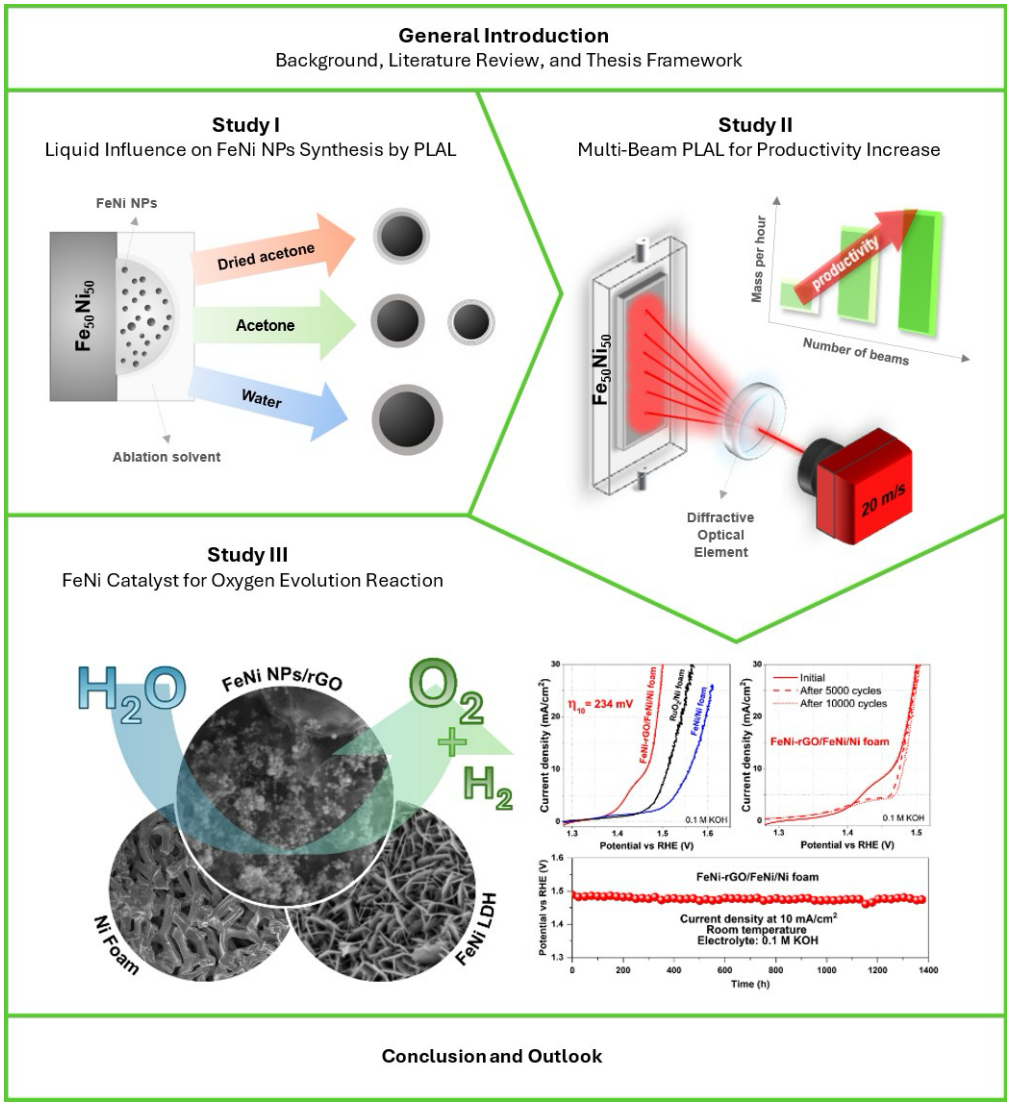

Figure 1. Schematic illustration of the scope of the dissertation. Chapter 1 introduces the topic, state-of-the-art, scope, and research questions. Chapter 2 summarizes the results from Study I, Study II, and Study III. Chapter 3 discussed the results presented in Chapter 2. Chapter 4 concludes the dissertation and Chapter 5 elaborates the outlook for further studies.

Chapter 2.2 highlights a proposed new method to increase the productivity of FeNi NPs through PLAL, termed MB-PLAL. This novel method promotes the use of PLAL as a green synthesis method to produce NPs in industry, as MB-PLAL addresses one critical drawback of PLAL's low productivity. MB-PLAL integrates a beam splitter DOE in the PLAL system, resulting in a jump in productivity during the production of FeNi NPs without the need to increase the scanning speed requiring more expensive scanners. The use of beam splitter DOE is significantly more cost-effective, power-efficient, and could be easily implemented in existing PLAL systems. Beam splitter DOE with configurations of 1:6 and 1:11 are used to generate 6 and 11 beams, respectively. The selected liquid is water after considering the results and discussion in Chapter 2 (the sustainability, the compliance to green chemistry

principle, and high productivity compared to other liquids). Productivity measurements through the gravimetric method, followed by a discussion on the principle and mechanism to explain the productivity jump of FeNi NPs through MB-PLAL are systematically discussed in this chapter. Besides, a comparative study of MB-PLAL on Au target as benchmark material highlights the differences compared to FeNi. A literature comparison to the world-record PLAL productivity to emphasize MB-PLAL cost-effectiveness is performed, in addition to CAPEX, OPEX, and production costs to evaluate the economical perspectives for the implementation of PLAL as a standard catalysts production technique in the industry.

After investigating the solvents in Chapter 2.1 and increasing the production rate in Chapter 2.2, the final application of FeNi NPs as OER catalysts is presented in Chapter 2.3. Our goal is to produce catalysts that are abundant, free from precious and rare elements, and catalytically active. In order to achieve this goal, a hybrid catalyst consisting of the produced FeNi NPs dispersed on rGO microflakes and deposited on FeNi LDH/Ni foam substrate is assembled and investigated. Here, the highly conductive rGO microflakes are used at low amounts to quench the size of the generated FeNi NPs, act as supporting materials to disperse the NPs, and increase conductivity. There are two approaches to directly synthesis and support FeNi NPs on supporting materials, namely downstream and in situ PLAL, and both are compared to find the most efficient one-step synthesis and supporting method to produce FeNi-rGO composite. The FeNi LDH/Ni foam serves as both a substrate for the deposition of FeNi-rGO and as an electrode for electrochemical analysis. Ruthenium oxide, RuO_2, is chosen as a benchmark catalyst to compare the electrocatalytic activity with our hybrid catalyst.

Chapter 4 condenses the dissertation into a few pages summary of the advances achieved in bringing laser-generated FeNi NPs with high production rates for the practical application as abundant and catalytically active OER catalysts. Finally, Chapter 5 concludes the dissertation with an outlook and further studies that can be done to develop the knowledge gained from this dissertation and achieve a better understanding of various topics related to this work. The complete work in a form of published articles can be found in the Appendix.

1.3.3 Research Questions

Overall, the dissertation and its related work are aimed to answer the following research questions:

1. What are the strategies to increase the productivity of PLAL?
2. How do different liquids affect the productivity, properties, and catalytic performance of the PLAL-generated FeNi NPs?
3. Can PLAL NPs productivity be increased through optical methods to reduce nanoparticle catalysts production costs?
4. Can PLAL-produced FeNi NPs be used to produce an FeNi-based OER electrocatalyst with high catalytic activity?

1.3.4 Studies

The thesis contains four peer-reviewed articles published in international scientific journals, including three original research papers and one perspective paper (short review paper). Each of the studies focuses on different but relevant topics, as extensively explained in subchapter 1.3.1. Aim. The studies were specifically designed to achieve our ultimate goal to produce green hydrogen at large scale and lower its production cost.

(V) Khairani, I. Y., Lin, Q., Landers, J., Salamon, S., Doñate-Buendía, C., Karapetrova, E., Wende, H., Zangari, G., & Gökce, B. (2023). Solvent Influence on the Magnetization and Phase of Fe-Ni Alloy Nanoparticles Generated by Laser Ablation in Liquids. *Nanomaterials*, *13*(2), 227. https://doi.org/10.3390/nano13020227

(VI) Khairani, I. Y., Spellauge, M., Riahi, F., Huber, H. P., Gökce, B., & Doñate-Buendía, C. (2024). Parallel Diffractive Multi-Beam Pulsed-Laser Ablation in Liquids Toward Cost-Effective Gram Per Hour Nanoparticle Productivity. Advanced Photonics Research, 5(5), 2300290. https://doi.org/10.1002/adpr.202300290

(VII) Khairani, I. Y., Jin, B., Palardonio, S. M., Hagemann, U., Alonso, B., Ortega, A., Doñate-Buendía, C., Martorell, J., Ros, C., Kallio, T., & Gökce, B. (2024). FeNi nanoparticle-modified reduced graphene oxide as a durable electrocatalyst for oxygen evolution. Journal of Catalysis, 439(September), 115771. https://doi.org/10.1016/j.jcat.2024.115771

(VIII) Khairani, I. Y., Mínguez-Vega, G., Doñate-Buendía, C., & Gökce, B. (2023). Green nanoparticle synthesis at scale: a perspective on overcoming the limits of pulsed laser ablation in liquids for high-throughput production. Physical Chemistry Chemical Physics, 25(29), 19380–19408. https://doi.org/10.1039/D3CP01214J

The authors' contributions are explained in each articles in a format of CRediT Authorship Contributions. In the first study published in *Nanomaterials*, I, Inna Yusnila Khairani (IYK), conceptualized the research idea and planned for the methodology together with my supervisors, Carlos Doñate-Buendía (CDB) and Bilal Gökce (BG). Sample production, investigation, data collection, visualization of the data were mostly done by IYK, with small parts of the data collection and visualization using instruments that were available in the project partners were done by our project partners. The writing of original draft were done by IYK, while review and editing part was done by most authors.

In the second study published in *Advanced Photonics Research*, IYK worked closely with supervisors, CDB and BG, to generate research idea and plan for the methodology. Sample production, data collection, investigation, and writing of the original draft were conducted by IYK. Review and editing of the draft were done by all authors.

In the third study published in the *Journal of Catalysis*, IYK, supervised by CDB and BG, generated research idea and planned for the methodology. Sample production, data collection, investigation, and writing of the original draft were mostly done by IYK, with some parts of investigation and data collection done by project partners who provide a certain analytical method. Original draft was written by IYK with some small parts written by the respective project partners. Review and editing of the draft were done by all authors.

In the fourth study (perspective paper), published in the *Physical Chemistry Chemical Physics,* IYK prepared the original draft, investigated the literatures, and prepared the visualizations almost solely by herself, while CDB and GMV contributed to a short subchapter and the conclusion part of the original draft, respectively. All authors contributed to the review and editing of the final draft before submission.

2 Summary of the Studies

2.1 Study I

Khairani, I. Y.; Lin, Q.; Landers, J.; Salamon, S.; Doñate-Buendía, C.; Karapetrova, E.; Wende, H.; Zangari, G.; Gökce, B. Solvent Influence on the Magnetization and Phase of Fe-Ni Alloy Nanoparticles Generated by Laser Ablation in Liquids. Nanomaterials 2023, 13 (2), 227, doi:10.3390/nano13020227.

CRediT Authorship Contribution of I.Y.K.: Conceptualization, methodology, investigation, visualization, writing – original draft preparation, writing – review and editing.

2.1.1 Aim

In the previous chapter, we have discussed the importance of NPs produced via PLAL, the mechanisms involved, the definition of productivity, and how to increase productivity via target geometry, scanning and laser parameters. The influence of liquid on productivity was also discussed, for example, how viscosity affects the formation and dwell time of persistent microbubbles, which scatter the incoming laser pulses and lowers the productivity.

However, the influence of the liquid is not only limited to the productivity, but also to the properties of the generated NPs, including oxidation, carbonization, elemental ratio, shape, and size (D. Zhang et al., 2021). These microscopic properties greatly impact the macroscopic properties of NPs, such as the catalytic activity, and it is therefore important to control them in parallel to upscaling productivity.

In this chapter, we investigated the influence of several ablation liquids, namely water, acetone, and dried acetone (acetone with lower water content) on the properties and productivity of $Fe_{50}Ni_{50}$ NPs. The liquids were chosen based on the economic viability and abundance for large-scale production. Similarly, the reason for choosing $Fe_{50}Ni_{50}$ lies in the elemental abundance of Fe and Ni, in addition to its high performance as an OER catalyst in the alkaline electrolysers among non-PGM elements. Not only that, $Fe_{50}Ni_{50}$ might be the key to finding the $L1_0$-phase FeNi, which is sought for its high coercivity and potential application as a rare-earth-free permanent magnet. Accordingly, the magnetic properties of this material were also studied on top of electrocatalytic performance, productivity, and general NPs properties, such as crystalline phase, morphology, particle size, elemental composition, and oxidation level.

2.1.2 Method

A picosecond laser Nd:YAG with a wavelength of 1064 nm, a pulse duration of 10 ps, a power of 8 W, a repetition rate of 100 kHz, a raw beam diameter of 2 mm, and a pulse energy of 80 µJ was employed to produce nanoparticles by PLAL. The laser beam was focused on the immersed equiatomic FeNi alloy target by a galvanometric scanner coupled with an f-theta

lens (focal length of 100 mm) following an Archimedean spiral pattern (6 mm diameter) with a speed of 2 m/s. The beam radius and peak fluence were calculated to be 65 µm at the focal length (based on the Gaussian beam profile) and 1.2 J/cm^2, respectively. A $Fe_{50}Ni_{50}$ (FeNi) alloy target was fixed in a flow chamber, where the liquid of interest was pumped using a peristaltic pump at a flow rate of 150 mL/min (calibrated before the experiments of each liquid). The investigated liquids are distilled water, acetone, and "dried" acetone (obtained by immersing molecular sieves type 3 Å for 24 h to capture water molecules in acetone). The FeNi samples ablated in different liquids will be further referred to as FeNi in water, FeNi in acetone, and FeNi in dried acetone, respectively. To dry the colloids and obtain nanopowders suitable for characterization, we performed magnetic separation using a permanent magnet (NdFeB) followed by liquid evaporation using an exhaust fan.

2.1.3 Results

The FeNi NPs generated in water, show the diffraction peaks of the face-centered cubic (FCC) FeNi and the spinel $NiFe_2O_4$ structure. Meanwhile, the FeNi NPs generated in acetone and dried acetone consist of the hexagonal closed-packed (HCP) FeNi phase in addition to the FCC FeNi phases and the spinel $NiFe_2O_4$ phases. The NPs in dried acetone consist of 35.2 ± 1.0 wt% of the HCP phase, while the NPs in acetone account for 38.4 ± 0.2 wt% of the HCP phase, and the NPs in water contain no HCP phase.

For the FeNi in dried acetone, morphology observed through TEM indicates the formation of core-shell structures with two layers of shell, independent of the particle size. The thickness of the first layer (inner shell) ranges from 1.5 to 2.9 nm and has an average of 1.9 nm, whereas the average thickness of the second layer (outmost shell) was measured to be 2.4 nm, with a size range of 1.1–4.2 nm. The core part shows a darker contrast in comparison to the shell, which can be explained as the change of electron scattering due to the electron density.

Contrarily to the FeNi NPs in dried acetone, which exhibit the same core-shell structure for both small and large nanoparticle sizes, the sample in acetone has two types of core-shell structures. Large NPs (d > 50 nm) form a core-shell structure, and the small NPs (d ~20 nm) lean towards the formation of a core with outer graphitic carbon layers. Regarding the ablation of FeNi NPs in water, the formation of a core and a single shell structure for all NPs sizes was found. The formation of a single layer (without the carbon layer) is expected as water decomposes to H_2 and O_2 (M. R. Kalus et al., 2017). Based on the standard reduction potential, O_2 acts as an oxidizing agent in the reaction with Fe and Ni, hence, the shell is most likely to be composed of oxides as supported by the XRD data.

The particle size distribution of each sample was measured for at least 400 particles. All the histograms of the particle size distribution fit the log-normal distribution, which is common in PLAL-produced NPs. The average particle size of the sample is defined based on the center value of the log-normal fitting curve (x_c) and the polydispersity index (PDI) is calculated from the square of standard deviation divided by the square of the mean value (σ^2/μ^2). The PDI is used to define whether the NPs are monodisperse or polydisperse, where a value of less than 0.3 is considered monodisperse (Barcikowski, S., Amendola, V., Lau, M., Marzun, G.,

Rehbock, C., Reichenberger, S., Zhang, D., Gökce, 2019). The NPs size in dried acetone shows the lowest average particle size (x_c) of 10.2 ± 0.3 nm, followed by NPs in acetone (12.0 ± 0.2 nm), and NPs in water (17.7 ± 0.6 nm). The PDI values of NPs in dried acetone, acetone, and water are found to be 0.28, 0.28, and 0.91, respectively.

To determine the elemental composition of the NPs' core and shell, elemental scans using EDX-TEM were performed. The EDX line scans show that the Fe intensity is generally higher than the Ni intensity on the NPs surface. This signal difference between Ni and Fe represents the composition of the shell, where Fe is present in a higher percentage compared to Ni. The oxygen intensity in all samples increases from the start of the shell where Fe is detected, then the value is constant throughout the particle. This shows that oxidation only occurs on the surface of the particle but not in the core, where the $Fe_{50}Ni_{50}$ composition of the initial target is preserved.

Mössbauer spectroscopy was employed to quantify the total oxide fraction of the FeNi NPs and their aging behavior for longer oxidation times. From the spectrum at 5 K, where the sub-spectra can be well resolved, 26% of the spectral area is assigned to the oxide fraction, which would suggest that further oxidation of this sample takes place following drying and storage before the measurement was completed. For the dried acetone colloid 4 months after production, the $NiFe_2O_4$ sub-spectra contains roughly 27% of the spectral area. To evaluate the effect of reducing water content on the total oxide fraction as well as the stability of the prepared nanoparticles, the oxide spectral area in aged, and dried acetone colloid is compared to fresh dried acetone (14%) and fresh acetone colloid (22%). The results clearly show a lower oxide fraction after preparation in dried acetone and minor ongoing oxidation upon a longer aging time.

Clear differences are apparent when regarding the 1 T magnetization values. When comparing the acetone and dried acetone samples, the effect of the drying process becomes clear, as the dried acetone sample has a higher magnetization of ca. 59 Am^2/kg compared to the 52 Am^2/kg of the untreated acetone sample, which can presumably be attributed to the lower oxidation of the former. However, the sample produced in water shows an even higher magnetization at 68 Am^2/kg. Additional magnetometry measurements were performed, up to higher fields of 9 T and in a wide range of temperatures from 4.3 K up to 300 K, for the dried acetone and water-based samples. Here, two aspects can be discussed: on the one hand, the low temperature and high field measurements show that the water-based sample still retains a slightly higher magnetization value at 9 T of 82 Am^2/kg compared to 76 Am^2/kg for the dried acetone sample.

The following subsections related to the OER catalytic activity and productivity in different solvents are unpublished results.

The abundance, affordability, and high OER catalytic performance of FeNi catalysts increase the popularity of this material as an alternative to precious and rare element catalysts such as RuO_2. An initial evaluation of the performance of the prepared FeNi NPs in different solvents is discussed in this chapter to select the best-performing samples for the productivity study in Chapter 2.2 and the developed electrode in Chapter 2.3. The PLAL-

generated FeNi NPs in different ablation liquids, along with commercial RuO_2 NPs as a benchmark OER catalyst, were prepared and tested for the OER catalytic activity according to reference (Jin et al., 2024). All 4 samples were deposited on carbon nanotubes (CNTs) as a support material and were tested in a standard three-electrode cell using a rotating disk electrode (RDE) at room temperature. The electrolyte used was 0.1 M KOH, while the reference and the counter electrodes were commercial Hg/HgO electrode and a graphite rod, respectively.

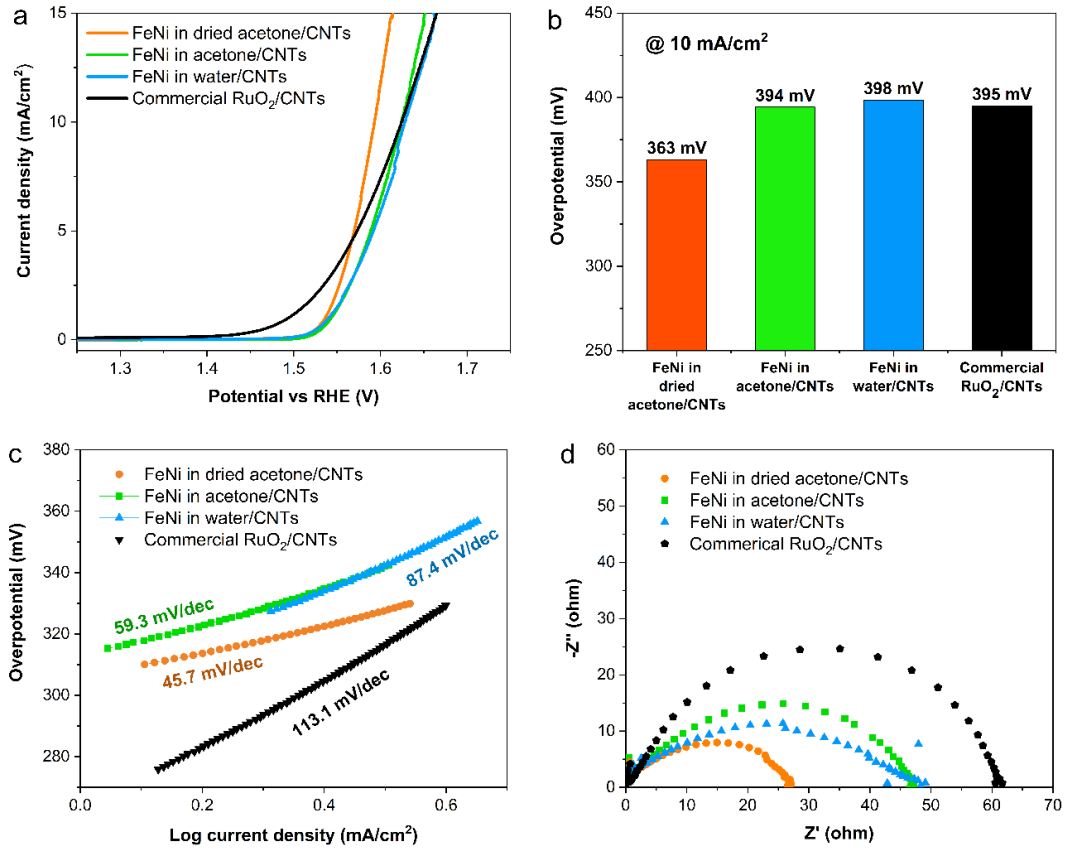

Figure 2. Electrochemical performances of FeNi NPs catalyst in different ablation liquids as compared to commercial RuO_2. (a) Linear sweep voltammetry, (b) required overpotential at a current density of 10 mA/cm^2, (c) Tafel slopes, and (d) Nyquist plot from electrochemical impedance spectroscopy.

The onset potential of a catalyst is the voltage where there is a sudden increase of measured current. It indicates the initially required potential to start the reaction. Lower onset potential means that the catalyst works at a smaller overpotential to start the reaction and is usually important if the catalyst is used at low current density applications. Based on the results in Figure 2 (a), commercial RuO_2 NPs have a lower onset potential at 1.49 V_{RHE} compared to the laser-generated FeNi NPs in the investigated ablation liquids, 1.54 V_{RHE}. Nevertheless, the overpotentials needed for laser-generated FeNi NPs catalysts to reach a current density of 10 mA/cm^2 are similar to or even smaller than the tested commercial RuO_2 NPs, which are at around 390–400 mV, except for FeNi in dried acetone with only 363 mV, Figure 2 (b). In industrial applications, electrolyzers operating at a larger current density are preferred as they have a higher production rate (the amount of gas produced from the water splitting process in an electrolyzer per unit of time) (IRENA, 2020), indicating that a lower overpotential at a larger current density value is preferred in a big scale system. Thereby, FeNi in dried

acetone/CNTs catalyst is preferred for industrial applications compared to RuO_2 NPs/CNTs. In addition, the Tafel slopes of FeNi in water/CNTs at 45.7 mV/dec, FeNi in acetone/CNTs at 59.3 mV/dec, and FeNi in dried acetone/CNTs at 87.4 mV/dec are smaller than commercial RuO_2/CNTs at 113 mV/dec, Figure 2 (c), indicating a faster kinetics with smaller overpotential. The Nyquist plot from the electrochemical impedance spectroscopy (EIS) represents the charge-transfer resistance (R_{ct}) between the electrode and the electrolyte. The value is obtained from the diameter of the semicircle plot, Figure 2 (d). The smaller the R_{ct} value, the faster the kinetics of the charge-transfer. From Figure 2 (d), it can be seen that the commercial RuO_2/CNTs have the biggest R_{ct} value at approximately 62 Ω, followed by FeNi in water/CNTs at 49 Ω, FeNi in acetone/CNTs at 47 Ω, and FeNi in dried acetone/CNTs at 27 Ω.

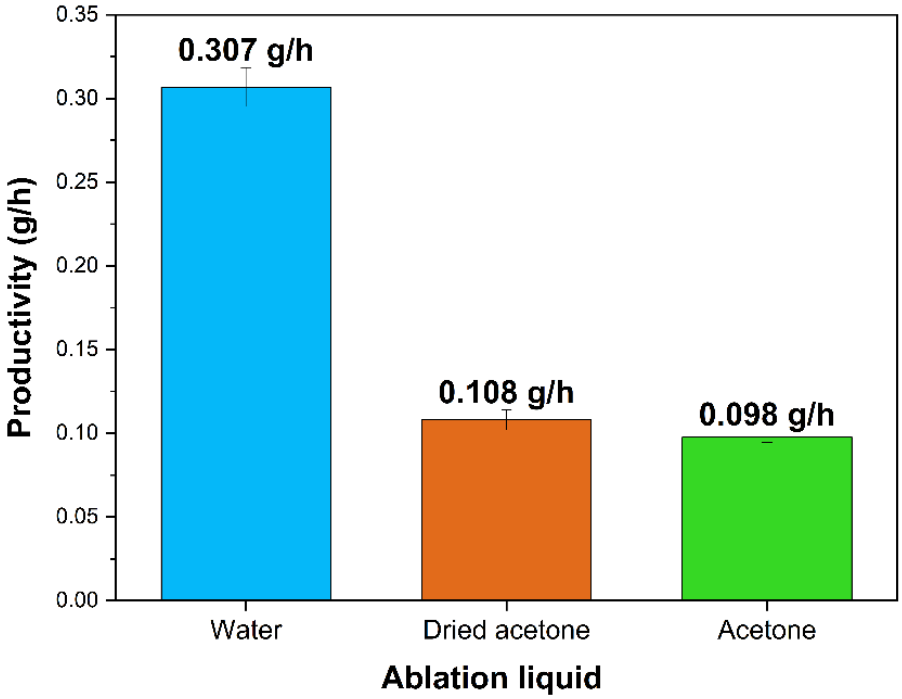

Figure 3. Productivity of laser-generated FeNi NPs in different ablation liquids (water, dried acetone, and acetone) with error bar from three repetitions.

The NPs productivity in PLAL is not only dependent on the properties of the target itself, but also the properties of the ablation liquid (Khairani, Mínguez-Vega, et al., 2023). PLAL in organic solvents typically has lower productivity than in water due to the formation of bigger and persistent bubbles (M. R. Kalus et al., 2021), which shield the incoming laser pulses. The same phenomenon is observed in the studied ablation liquids, i.e., water, acetone, and dried acetone. The PLAL of FeNi target in water resulted in a production rate of 307 mg/h, which is almost 3 times higher compared to the PLAL in dried acetone and acetone with 108 mg/h and 98 mg/h, respectively, Figure 3. During the experiment, bubble formation was indeed more pronounced in the case of acetone and dried acetone compared to water, because the C–C bond (3.6 eV) in acetone is considerably weaker than the H–O bond (4.8 eV) in water. A related study reported that the gas formation in acetone is 30 times more efficient than in water (M. R. Kalus et al., 2021). Therefore, it is not surprising that the productivity values in acetone and dried acetone are much lower than the productivity in water.

2.2 Study II

Khairani, I. Y.; Spellauge, M.; Riahi, F.; Huber, H. P.; Gökce, B.; Doñate-Buendía, C. Parallel Diffractive Multi-Beam Pulsed-Laser Ablation in Liquids Toward Cost-Effective Gram Per Hour Nanoparticle Productivity. Adv. Photonics Res. 2024, 5 (5), 2300290, doi:10.1002/adpr.202300290.

CRediT Authorship Contribution of I.Y.K.: Conceptualization, methodology, investigation, visualization, writing – original draft preparation, writing – review and editing.

2.2.1 Aim

Study I in chapter 2.1 discusses how different ablation liquids, namely water, acetone, and dried acetone, influence the properties of the generated FeNi NPs by PLAL. Based on the results, FeNi in dried acetone performs slightly better than FeNi in water; yet its productivity is only one-third of the productivity in water. Moreover, acetone possesses higher health, hazard, and environmental risks compared to water, making it less safe and less sustainable in large-scale production. Due to these reasons, our investigation to increase the productivity of PLAL is performed in water.

Increasing NPs productivity in the PLAL to gram-per-hour range represents a demand for industrial applications of the NPs. Using a high-power picosecond laser with high scanning speed and a liquid flow ablation chamber is up to now the best approach to achieve gram-per-hour productivity. Nevertheless, not all PLAL systems can offer such sophisticated specifications due to the large capital investment and unavailability of those lasers and scanning equipment (including inaccessibility to custom-made products). It is therefore important to study approaches to achieve gram-per-hour productivity with simpler and more affordable approaches that could be easily installed in the already established PLAL systems.

In this chapter, we propose an optical approach to increase productivity in most PLAL systems. The approach is based on the addition of a beam-splitter diffractive optical element (DOE) to a picosecond laser to generate several beams and perform a parallel, multi-beam PLAL process, which is abbreviated as MB-PLAL. Despite the constant scanning speed of our galvanometer scanner, we were able to improve the productivity of FeNi NPs by factor 4 (an increase of 300 %), from 400 mg/h to 1.6 g/h, achieving gram-per-hour productivity.

2.2.2 Methods

A 10 picosecond Nd:YAG laser with a wavelength of 1064 nm, an average power of 120 W, a tunable repetition rate of 400–4000 kHz, a raw beam diameter ($1/e^2$ criteria) of 5 mm, and a beam quality of 1.11 was employed. The laser beam was directed on the $Fe_{50}Ni_{50}$ (FeNi) or Au target by a galvanometer scanner coupled with an f-theta lens (focal length of 167 mm) describing an Archimedean spiral pattern (10 mm diameter) with a marking speed of 20 m/s. Distilled water (18.2 MΩ•cm at 25 °C ultrapure Mili-Q water) was used as the liquid source and pumped by a peristaltic pump at 500 mL/min. A quartz window (2 mm thickness) with an

anti-reflective coating at laser wavelength (R < 0.25%) was employed, and the liquid layer thickness, defined as the distance between the inner side of the glass and the surface of the target, was approximately 6 mm. The splitting of the initial laser beam into 6 and 11 equivalent beams is achieved by the use of beam-splitting diffractive optical elements (DOEs), a 1:6 beam splitter DOE (HOLOEYE Photonics AG) and a 1:11 beam splitter DOE (LIMO Lissotschenko Mikrooptik GmbH), respectively. To simplify the naming, standard single-beam PLAL without any DOE will be further addressed as "standard PLAL", while the PLAL process with 1:6 and 1:11 beam splitter DOE will be referred to as "6-beam MB-PLAL" and "11-beam MB-PLAL", respectively. Parameters such as repetition rate and working distance were independently optimized for each material and the number of beams produced by the DOE. The DOE is placed after the f-theta lens of the scanner to accommodate the use of a large scanning pattern. The characterizations of the generated FeNi and Au colloidal nanoparticles were performed by a high-resolution transmission electron microscopy (HR-TEM, JEOL JEM-2200FS, 200 kV, ZrO_2/W emitter) and powder X-ray diffraction (PXRD, Bruker D8 Advance Powder Diffractometer, Bragg-Brentano geometry, CuKα radiation 1.5418 Å, 40 kV, and 40 mA).

2.2.3 Results

The FeNi NP productivity using the standard PLAL configuration was 0.4 g/h. After placing the 6-beam DOE, the repetition rate was reduced to 500 kHz (one-sixth of the repetition rate of standard PLAL) to employ a similar pulse energy value. With the 6-beam splitter, we obtained a productivity jump from 0.4 g/h to 1.24 g/h, which represents a factor 3 increase. The 11-beam MB-PLAL, on the other hand, was performed at 400 kHz due to the impossibility of further reducing the repetition rate of our laser source, hence, the pulse energy and fluence in this setup was half of the standard PLAL and 6-beam MB-PLAL. Nevertheless, the increase in productivity is still observed, obtaining productivity as high as 1.6 g/h with an increasing factor of 4 compared to the standard PLAL. To the best of our knowledge, this is the first time a productivity value of 1.6 g/h has been reported for PLAL of $Fe_{50}Ni_{50}$ in water. The power-specific productivities of 6-beam and 11-beam MB-PLAL were increased 3.5 and 4 times compared to the standard PLAL, respectively. The increasing trend of power-specific productivity is also similar to the trend of mass productivity, which confirms the enhanced laser power delivery to the target for the MB-PLAL configuration. We further measured the productivity of the FeNi target at the same fluence and repetition rate by changing the laser power. From the standard PLAL to 6-beam and 11-beam MB-PLAL, the productivity increase factors are 3.6 and 6.4, respectively.

The particle size distribution of the generated FeNi NPs was measured to investigate the influence of MB-PLAL setup on the morphology and size of the resulting nanoparticles. Based on the TEM analysis, FeNi NPs are formed as core-shell. The median values (x_c) of the log-normal fitting of all the samples are similar, 14.3 ± 7.3 nm for the standard PLAL (1 beam), 11.5 ± 9.1 nm for the 6-beam MB-PLAL, and 14.4 ± 13.0 nm for the 11-beam MB-PLAL. The polydispersity index (PDI) shows a value of 0.26 for the single-beam ablation, which is smaller than the samples with beam splitting with respective values of 0.44 and 0.53 for 6 and 11 beam processing.

Based on the XRD results, two phases are formed in the standard PLAL of FeNi in water: face-centered cubic (FCC) FeNi and spinel $NiFe_2O_4$. The FCC FeNi occupies the core part of the NPs, while spinel nickel ferrite ($NiFe_2O_4$) can be found in the shell part as a result of oxidation (Khairani, Lin, et al., 2023). Based on the diffractograms of FeNi NPs generated with different number of beams, there is no formation of new peaks or disappearance of peaks as compared to the single beam diffractogram, which indicates the crystalline structure of the FeNi NPs remains constant for MB-PLAL, finding the FCC and spinel nickel ferrite composition.

The productivity comparison of FeNi with a benchmark material such as Au is essential to help us understand the influence of the material's property on the MB-PLAL productivity. The standard PLAL productivity of Au and FeNi is similar, 0.32 and 0.40 g/h, respectively. The productivity increase factors of Au from the standard PLAL to 6-beam and 11-beam MB-PLALs are found to be 2.1 and 3, which is lower than FeNi increase factors of 3.1 and 4, respectively.

With an aim to upscale and introduce MB-PLAL to the industry, we present the economical perspective of Au NPs production using MB-PLAL. We performed a cost-benefit analysis related to the labour and electricity costs that are needed to produce 1 k g of Au NPs, as well as the daily and yearly production rate. The calculations of labour and electricity costs to produce Au NPs are based on the highest Au productivity achieved in our laser system. Several assumptions are considered, such as the gross salary assumption of the working staff at 21 €/h and the labour time which considers 2 hours daily initial set up and adjustment for every 8 hours ablation. The electricity consumption is measured for the whole PLAL system, which is approximately 3 kWh.

Based on the calculation, using the 11-beam MB-PLAL, the total labour working hours are reduced by one-third compared to the standard PLAL, which saves approximately 54,000 € of labour cost for every 1 kg of Au NPs produced. In addition, the electricity consumption could be trimmed down by 66% and it is possible to save around 2,500 € per 1 kg of Au NPs when using the 11-beam splitter. As also calculated by Jendrzej et al. (2017) in their cost comparison to produce one gram of Au NPs (Jendrzej et al., 2017), the energy cost (electricity) to produce the Au NPs is much smaller compared to the labour cost to operate the laser. Hence, the main advantage of using the MB-PLAL is the labour cost reduction.

Meanwhile, for the time-based production rate, we focus on the daily and annual production as well as the percentage increase of production when using the DOE compared to the standard PLAL. By assuming the 16 hours daily ablation time and 350 days of annual working days, the percentage increase of the daily and annual production rate using the 11-beam MB-PLAL compared to the standard PLAL is almost 200%, where the daily production is increased from 3 g to 8 g per day, and the annual production is increased from 640 g to 1,800 g per year. The most important point based on these calculations is that we can achieve this jump in production and cost reduction just by increasing the capital investment by 1.3% to acquire the 11-beam splitting DOE. As for the case of the 6-beam DOE, the price is more affordable and the increase in capital investment is only 0.5%. The minuscule addition of capital

investment and the low implementation time of the DOE in the PLAL setup are insignificant compared to the benefits achieved by the proposed MB-PLAL system.

2.3 Study III

Khairani, I. Y.; Jin, B.; Palardonio, S. M.; Hagemann, U.; Alonso, B.; Ortega, A.; Doñate-Buendía, C.; Martorell, J.; Ros, C.; Kallio, T.; Gökce, B. FeNi Nanoparticle-Modified Reduced Graphene Oxide as a Durable Electrocatalyst for Oxygen Evolution. J. Catal. 2024, 439 (September), 115771, DOI: 10.1016/j.jcat.2024.115771.

CRediT Authorship Contribution of I.Y.K.: Conceptualization, methodology, investigation, visualization, writing – original draft preparation, writing – review and editing.

2.3.1 Aim

In Chapter 2.2, we discuss how MB-PLAL increases FeNi NPs productivity by a 300 % factor while retaining the properties of the generated NPs. As PLAL generally suffers from low productivity, MB-PLAL helps to overcome the barrier of implementing this method in the industry. Specifically, we have shown that MB-PLAL pushes forward the large-scale production of FeNi NPs catalysts for OER via this green synthesis method. Despite the possibility of increasing PLAL productivity, MB-PLAL still cannot address the issue of the broad size distribution of NPs produced via the PLAL method.

In catalysis, size distribution is one of the most important factors determining the catalytic activity. It is generally accepted that smaller particle sizes and larger surface areas result in more active sites for the catalytic reaction to take place, hence, a higher catalytic activity. To better control the particle size in PLAL, a surfactant or capping agent is usually added to the ablation liquid. Yet, these additional functional groups or layers hinder the attachment of reactants to the catalyst' active sites. Another method to quench NPs size in PLAL is to use supporting materials, such as high surface area materials with high conductivity that are used to support the catalysts, by mixing them directly in the ablation liquid used for PLAL. This is a one-step catalyst synthesis and supporting process that promotes the size quenching of the produced NPs. Nevertheless, the presence of these supporting materials in the ablation liquid scatters and/or absorbs the incoming laser pulses, hindering the ablation of the target material and reducing productivity. Hence, in this chapter, we propose downstream PLAL, where the support materials are mixed with the PLAL-produced NPs directly after the synthesis procedure. The catalysts employed are FeNi NPs generated through the MB-PLAL method, and the support materials are reduced graphene oxide (rGO) microflakes. In our study, we chose Fe:Ni ratio of 50:50 due to several reasons: (1) former reports of its low overpotential (Acharya et al., 2019; Corrigan, 1987; Friebel et al., 2015; J. Jiang et al., 2016), (2) PLAL of $Fe_{50}Ni_{50}$ in water forms minor $NiFe_2O_4$ phase (Khairani, Lin, et al., 2023), which is presumed to improve OER catalytic activity (J. Jiang et al., 2016; Landon et al., 2012), and (3) better OER performance at higher current densities (100 and 150 mA/cm^2) (Acharya et al., 2019), which is essentially related to our purpose for industrial application.

rGO is chosen due to its high conductivity, large surface area, and the formerly reported size-quenching effect on the PLAL-generated NPs (Haxhiaj et al., 2019; Torres-Mendieta et al., 2016). The produced FeNi-rGO composite is deposited on the substrate material, an FeNi LDH/Ni foam, to build a hybrid catalyst, where we observe exceptional stability and low overpotential values under OER tests.

2.3.2 Methods

A 1064 nm Nd:YAG laser with a pulse width of 10 ps, repetition rate of 400 kHz, and average power of 100 W was employed for the PLAL of a $Fe_{50}Ni_{50}$ target. A galvanometer scanner with a scanning speed of 20 m/s was coupled with an f-theta lens (focal length 167 mm) to focus and steer the laser beam into the desired pattern. A static diffractive optical element (DOE) with a 1:11 matrix was placed closely in front of the f-theta lens to split the laser beam into 11 and increase the production rate of the FeNi NPs (Khairani et al., 2024). PLAL was performed in a flow chamber where the liquid was pumped through with a flow rate of 400 mL/min.

We investigated two different techniques for the direct synthesis and support of FeNi NPs on rGO. In the in situ PLAL, rGO powder was dispersed in distilled MiliQ water with a concentration of 15 mg/L and then pumped through the chamber where PLAL happens. In this setup, the supporting of FeNi NPs on the rGO surface took place inside the ablation chamber directly after the NPs formation. The produced sample is further referred to as “in situ FeNi-rGO”. Meanwhile, in the second method, downstream PLAL, distilled MiliQ water was used as NPs carrier and was pumped through the ablation chamber. The rGO dispersion with a concentration of 30 mg/L was placed in the collecting reservoir at the end of the system. In this method, the supporting process was delayed by several seconds until the FeNi NPs colloid reached the collecting reservoir (where rGO was present). The sample is further denoted as “downstream FeNi-rGO”. Note that we kept the final concentration of rGO at 15 mg/L and the final colloid volume of 2 L for both samples. A comparative study with graphene oxide (GO), as the support material was also performed in the downstream PLAL to investigate the influence of supporting materials on this process. The sample will be further referenced as “downstream FeNi-GO”.

The preparation of the iron nickel-layered double hydroxide (FeNi-LDH) nanoplates on Ni foam followed the hydrothermal procedure previously reported (P. Li et al., 2020; Z. Lu et al., 2014). The reactants $Ni(NO_3)_2{\cdot}6H_2O$ (0.67 mmol), $Fe(NO_3)_3{\cdot}9H_2O$ (0.33 mmol), and $CO(NH_2)_2$ (5 mmol) were mixed with 35-38 mL of distilled water and stirred until a clear solution was formed. The Ni foam electrode with a dimension of 3 cm × 4 cm was cleaned in an ultrasound bath for 5 min using HCl solution (32 wt%) to remove the oxidized surface layer. It was later rinsed with deionized water. The Ni foam was then placed in the 40 mL Teflon-lined stainless-steel autoclave and the as-prepared aqueous solution was added. The autoclave was sealed and heated at 120 °C for 12 h and subsequently cooled down naturally. The formation of a thin film on the Ni foam was observed and the substrate was rinsed subsequently with distilled water and absolute ethanol in the ultrasonic bath for 5 min each. The prepared FeNi-LDH/Ni foam was dried naturally and stored in a plastic container.

The FeNi-rGO/FeNi/Ni foam electrode was prepared according to a typical procedure. 24 µL of FeNi-rGO suspension with a concentration of 68 mg/mL were mixed with 16 µL Nafion (5 wt% Nafion-117 solution, purchased from Aldrich). The mixture was stirred overnight and sprayed on the FeNi LDH/Ni foam electrode with an area of 1 cm^2 using an airbrush. Then, the samples were transferred into a tube furnace and calcinated at 400 °C for 2 h under N_2 flow. The FeNi-rGO/FeNi/Ni foam was obtained after cooling down to room temperature. The benchmark OER catalyst, RuO_2, was also spray-coated on Ni foam as a comparative study to our FeNi-based catalyst. In a typical procedure (D. Wang et al., 2019), 1.6 mg of commercial RuO_2 (25-30 nm, purchased from Sigma) was dissolved in 24 µL isopropanol with sonication and 16 µL Nafion (5 wt%) was added into the solution. The mixture was sprayed on Ni foam with an area of 1 cm^2 using an airbrush. The RuO_2/Ni foam was obtained after drying in air.

Transmission electron microscopy (TEM) and energy dispersive X-ray (EDX) measurements were performed to analyse the morphology, size distribution, and elemental distribution of the generated FeNi NPs supported on the rGO (HR-TEM, JEOL JEM-2200FS, 200 kV, ZrO_2/W emitter). The nanoparticle size distribution was characterized using ImageJ software (Rasband, 1997). X-ray diffraction (XRD) analysis was done to confirm the crystalline structure of the FeNi-rGO/FeNi/Ni foam hybrid catalyst before and after the 1300 h stability test. XRD patterns were captured by PANalytical X` Pert Powder XRD operating at the voltage of 40 kV and the current of 40 mA with Cu K radiation. The scanning electron microscopes (SEM) were obtained by Tescan Mira3.

The electrochemical experiments were conducted at room temperature. A commercial Hg/HgO electrode and a graphite rod were used as a reference and counter electrode, respectively. The Ni foam-based samples were used as work electrodes directly and the electrolyte is 0.1 M KOH. The measured potentials were calibrated to a reversible hydrogen electrode (RHE) by the following equation: $E_{RHE} = E_{Hg/HgO} + 0.098\ V + 0.059 \times pH$ (pH=13). The accelerated durability tests (ADT) of the catalysts were assessed by cyclic voltammetry (CV) at a scan rate of 100 mVs^{-1} between 1.2 V and 1.65 V vs RHE for 10,000 continuous cycles. The electrochemical experiments were performed in a standard three-electrode cell using an Autolab potentiostat (PGSTAT128N, Metrohm Autolab B.V.). The electrochemical impedance spectroscopy (EIS) was performed at 1.64 V vs RHE with an amplitude of 8 mV from 100 kHz to 0.1 Hz.

Raman spectroscopy was performed on 30 µL of FeNi-rGO suspension dropcast on 4 mm cavity glass slides and then dried at 60º C vacuum oven to prevent oxidation in air. Raman spectra of the dried samples were obtained by Renishaw inVia spectrometer, using a 532 nm wavelength laser and 50x objective. To avoid laser-induced reduction (Mehta et al., 2017), the laser was limited to 0.5% power, 1 s exposure time, and 30 acquisitions. The intensities of Raman scattering were corrected by taking the fluorescence as the baseline and then fitted to sums of functions using peak-o-mat 1.2.9 software, using three pseudo-Voigt functions (for D, G and D' bands) and two Gaussian functions (for D* and D'' bands) (Claramunt et al., 2015; Pinilla-Sánchez et al., 2022).

XPS measurements were performed on a VersaProbe II system. The commercial rGO powder and FeNi-rGO/FeNi/Ni foam sample were put on carbon tape, and the colloidal solutions of

in situ and downstream FeNi-rGO were dropcast on Si substrates. All samples did not undergo the sputtering step. Secondary x-ray-induced electron imaging (SXI) was used to make sure the X-ray beam was properly focused on the particles. Data evaluation was done using CasaXPS (Fairley et al., 2021).

2.3.3 Results

Prior to the assembly of the hybrid catalyst, we explored how different supporting techniques, i.e., in situ and downstream PLAL, influence the supporting efficiency and properties of the FeNi-rGO composite. Based on our investigation, a reduction of the FeNi NPs productivity from 909 mg/h in the downstream FeNi-rGO to 854.4 mg/h in the in situ PLAL is observed. At larger rGO concentrations, the productivity of in-situ PLAL suffers even more. To reduce the laser shielding effect observed in the in situ PLAL, we propose another approach which is termed downstream PLAL. We compared the influence of downstream and in situ PLAL methods on the supporting of FeNi NPs on rGO and studied the properties of the produced composites, including the FeNi NPs dispersion on the rGO surface, the FeNi NPs' size distribution, the OER catalytic activity, the oxidation state of Fe and Ni, and the defect state of the rGO. The aim is to find the most efficient method to directly synthesise and support the produced FeNi NPs on the rGO while achieving high catalytic activity.

Based on the TEM images, the in situ PLAL shows a more uniform dispersion of small nanoparticles ($d \leq 10$ nm) throughout the surface of the rGO sheet. Meanwhile, more clustered and agglomerated particles can be seen in the downstream PLAL sample. Similar dispersion results were also observed through EDX-mapping and high-angle annular dark-field imaging (HAADF).

The particle size distributions (PSD) of the supported NPs are compared. While in situ PLAL is known to produce smaller nanoparticles due to the size-quenching effect of the support materials (Haxhiaj et al., 2019; Torres-Mendieta et al., 2016), we observed only a slight difference between in-situ and downstream FeNi-rGO. The centre value (x_c) of the particle diameter in the log-normal distribution shows that the downstream FeNi-rGO ($x_c = 11.3 \pm 6.9$ nm) exhibits a similar size distribution compared to the in situ FeNi-rGO ($x_c = 10.6 \pm 9.2$ nm). Meanwhile, downstream FeNi-GO has a smaller peak value ($x_c = 7.9 \pm 5.0$ nm) compared to downstream FeNi-rGO ($x_c = 11.3 \pm 6.9$ nm) despite the same supporting technique used. It can be assumed that GO facilitates NP support due to its good dispersibility in water and less wrinkling structure than rGO, making smaller NPs more easily dispersed on the surface of GO.

If no support material is employed, the peak size of unsupported FeNi NPs in water by PLAL is found to be $x_c = 14.4 \pm 13.0$ nm (Khairani et al., 2024). Compared to this value, we observe a particle size shift towards smaller values by 3.1 nm, 3.8 nm, and 6.5 nm for in situ FeNi-rGO, downstream FeNi-rGO, and downstream FeNi-GO, respectively. Meanwhile, the polydispersity index (PDI) (Khairani, Lin, et al., 2023) values of each sample are 0.50 (in situ FeNi-rGO), 0.30 (downstream FeNi-rGO), and 0.30 (downstream FeNi-GO), which are smaller than the PDI of unsupported FeNi NPs (PDI = 0.53) (Khairani et al., 2024). It confirms that both

in situ and downstream PLAL could provide a size quenching effect compared to the ex situ and standard PLAL methods.

The OER electrocatalytic activities of in situ FeNi-rGO, downstream FeNi-rGO, and downstream FeNi-GO with the same NPs loading were investigated using CV in 0.1 M KOH. The CVs of in situ FeNi-rGO and downstream FeNi-rGO are almost overlapping, indicating that they have similar OER activity, meanwhile, the activity of downstream FeNi-GO is much lower than the FeNi-rGO samples. Extracting these overpotential data at 10 mA/cm^2 shows that downstream FeNi-rGO has the lowest overpotential at approximately 418 mV, followed closely by in situ FeNi-rGO at 432 mV, and downstream FeNi-GO with the highest overpotential of almost 500 mV.

Meanwhile, the corresponding Tafel slopes of these samples are all lower than 120 mV/dec, indicating that the rate-determining step happens after one-electron transfer reaction (Shinagawa et al., 2015). Electrochemical impedance spectroscopy (EIS) was evaluated to assess the charge transfer rate for the three electrodes. The diameter of the semicircle EIS plot represents the resistance of charge transfer (R_{ct}), whereas the smaller diameter shows a higher charge diffusion rate. The in situ FeNi-rGO and downstream FeNi-rGO have similar R_{ct} values, which are smaller than that of downstream FeNi-GO.

Surface elemental analysis of as-prepared FeNi-rGO is important to unveil their catalytic response and to elucidate the influence of supporting techniques. The XPS results of pristine commercial rGO show the carbon and oxygen 1s spectra, which are the only detectable elements (90 at% C, 10 at% O). The carbon signal is then best described by an asymmetric graphitic C-C peak (asymmetry parameters in CasaXPS LA(0.95,1.9,50)) and a minor contribution of non-graphitic carbon (about 10% of the carbon signal), which possibly can be attributed to carbon contaminations on the surface of the rGO. Meanwhile, the XPS results of the dropcast in situ FeNi-rGO and downstream FeNi-rGO samples show that the atomic ratio of Fe to Ni is roughly 2:1 for both in situ and downstream FeNi-rGO, which might verify the formation of the $NiFe_2O_4$ layer on the surface of FeNi NPs (Khairani, Lin, et al., 2023). Nevertheless, in situ FeNi-rGO shows a higher oxygen content than the downstream FeNi-rGO (35 at% to 29 at%), presumably due to the presence of rGO during the PLAL process leading to further oxidation and higher O content, or due to surface contamination.

Comparing the C 1s signals of in situ FeNi-rGO and downstream FeNi-rGO to that of pristine rGO, the main difference is that both samples, especially the in situ FeNi-rGO, show a slightly higher non-graphitic C-C and also C-O content compared to that of pristine rGO. The contribution to the total C 1s spectrum increases from 25% in pristine rGO to about 45% for the in situ FeNi-rGO. This could be an effect of the laser interaction with the rGO during the synthesis in the in situ setup, inducing pyrolysis and the formation of non-graphitic carbon, or carbon contamination during the PLAL process.

Raman spectroscopy is employed as an effective tool to quantify the structural changes in the carbon network of the rGO. Raman spectra of all samples show a similar peak profile, the presence of the rGO. After baseline correction and performing peak-fitting, the signature D and G bands were deconvoluted into five interbands (Ciammaruchi et al., 2019; Delfino et al., 2024; Pinilla-Sánchez et al., 2022). The D peak (~1350 cm^{-1}) is correlated to the breathing

mode of the hexagonal sp^2 carbon lattice of the rGO. The broad and faint D* (~1200 cm^{-1}) is related to the breathing of the lattice disorder by sp^2-sp^3 bonds and, consequently, interlayer distance. The G peak signature (~1600 cm^{-1}), associated with the vibration of graphitic sp^2 domains, shows a D' peak shoulder (~1625 cm^{-1}) originating from structurally defective graphene, and another D" peak shoulder (~1550 cm^{-1}) attributed to the amorphization of the rGO. These peaks can shift in intensity and position depending on the structure and functionalization (Claramunt et al., 2015).

The produced downstream FeNi-rGO was chosen as the constituent of the Ni foam-based electrode. The FeNi LDH grown on Ni-foam was found to lose its LDH structure after undergoing calcination at 400 °C. For the downstream FeNi-rGO spray-coated on FeNi LDH/Ni foam substrate, we could not confirm whether the LDH is ruptured or sustained after the calcination as the LDH is not visible behind the FeNi NPs-rGO. Hence, we conducted XRD measurements of FeNi LDH/Ni foam and FeNi-rGO/FeNi LDH/Ni foam before and after calcination. FeNi LDH peaks (Trotochaud et al., 2014; Y. Wang et al., 2023) in our XRD data are located at 2θ = 34.86° (012), 39.17° (015), 46.05° (018), 60.07° (110), and 61.31° (113), which are visible in both FeNi LDH/Ni foam and FeNi-rGO/FeNi LDH/Ni foam before the calcination step, confirming the presence of FeNi LDH. After the calcination, however, we found those peaks diminishing from the XRD data and there was the formation of new peaks at 2θ = 29.24°, 44.13°, 47.31°, and 63.20° which might correspond to oxides of iron and nickel, such as $NiFe_2O_4$, NiO, and Fe_3O_4. Thereby we suppress the descriptor of "LDH" in the FeNi LDH/Ni-foam and FeNi-rGO/FeNi LDH/Ni foam and will further refer to them as FeNi/Ni foam and FeNi-rGO/FeNi/Ni foam, respectively.

In this part onward, we are focusing on the electrocatalytic activity results of 3 samples: (1) calcinated downstream FeNi-rGO spray-coated on the FeNi LDH grown on Ni foam, referred to as FeNi-rGO/FeNi/Ni foam, (2) calcinated FeNi LDH/Ni-foam electrode substrate, referred to as FeNi/Ni-foam, and (3) commercial ruthenium oxide spray-coated on Ni-foam as the benchmark electrocatalyst, referred to as RuO_2/Ni-foam.

The resulting linear sweep voltammetry (LSV) polarization curves performed in O_2-saturated 0.1 M KOH of the aforementioned samples shows that the OER polarization curves of the FeNi-rGO/FeNi/Ni foam exhibit smaller onset potentials and higher current densities at a fixed potential compared to RuO_2/Ni foam and FeNi/Ni foam, suggesting a better OER activity. FeNi/Ni foam requires the highest overpotential of 330 mV, presumably due to the rupture of the FeNi LDH structure by calcination, thus less active surface area is available for the OER. Meanwhile, an overpotential of only 234 mV was required for FeNi-rGO/FeNi/Ni foam, which is lower than the benchmark material RuO_2/Ni foam at 271 mV. The Tafel slopes of FeNi-rGO/FeNi/Ni foam (76.0 mV/dec), RuO_2/Ni foam (237.7 mV/dec), and FeNi/Ni foam (377.5 mV/dec) explain several things. FeNi/Ni foam and RuO_2/Ni foam with Tafel slope values higher than 120 mV/dec indicate that surface species are formed just before the rate-determining step (RDS) is predominant (Shinagawa et al., 2015), which is similar to a single electron transfer reaction. Meanwhile, FeNi NPs-rGO/FeNi/Ni foam results in a Tafel slope lower than 120 mV/dec, at approximately 70-80 mV/dec, indicating that the adsorbed surface

species are produced in the earlier stage of the predominant OER step (Shinagawa et al., 2015), hence the rate-determining step happens after one-electron transfer reaction.

The stability of the OER catalyst is critical from a practical viewpoint. The electrochemical durability was investigated by ADT and chronopotentiometry in N_2-saturated 0.1 M KOH. The degradation of OER activity is negligible after running 10,000 cycles, indicating its superior durability. The chronopotentiometry result, indicating the potential required to achieve a current density of 10 mA/cm^2, remains relatively constant even after 1300 h of testing.

3 General Discussion

3.1 Liquid Influence on the Properties of PLAL-generated FeNi NPs

Variation of ablation liquid in the generation of $Fe_{50}Ni_{50}$ nanoalloys by PLAL influences the phases, core-shell structure, oxidation, magnetic and electrocatalytic properties, as well as the productivity of the produced NPs. Hereby we discuss how water, acetone, and dried acetone liquids impact the aforementioned characteristics of the FeNi NPs and the underlying hypotheses and reasonings.

3.1.1 Phase, Oxidation, and Morphology

It is interesting to observe that the ablation in acetone and dried acetone produced a mixture of the metastable HCP and stable FCC phases in the NP core, while only the FCC phase was formed in water. Different arguments were postulated regarding the formation of stable and metastable phases during PLAL: (i) The specific heat capacity of the solvent, which influences the cooling rate of the ablation plasma plume generated during PLAL (Jung & Choi, 2014), (ii) Shorter cavitation bubble lifetime compared to the theoretical lifetime according to the Rayleigh-Plesset theory (S. J. Lee et al., 2022), and (iii) the confinement of the cavitation bubble by the surrounding liquid, which induces the high temperature, high pressure, and high density (HTHPHD) state and shorter quenching time of the plasma plume in the liquid (P. Liu et al., 2008). The above-mentioned hypotheses all pointed to the freezing of the metastable phase during the cooling (quenching), which preserves the metastable phases.

For FeNi alloy, the formation of metastable FeNi HCP phase is usually associated with high pressure and high-temperature conditions, such as in the earth's core (E. Huang et al., 1988; J.-F. Lin et al., 2002; Shen et al., 1998; Tateno et al., 2012; Torchio et al., 2020). It has been produced synthetically using a diamond anvil cell (DAC) from the bulk FeNi with face-centered cubic (FCC) phase (E. Huang et al., 1988; Komabayashi et al., 2012; Kuwayama et al., 2008). Laser ablation in liquid also a provides high-pressure and high-temperature state to the nuclei inside the cavitation bubble (CB) and its collapse (Soliman et al., 2010). The bubble pressure during laser ablation might provide a suitable environment for the formation of the HCP phase, however, this cannot be the sole reason since the ablation in water does not produce HCP phases. The cavitation bubble dynamic study from the Choi group also showed that the cavitation bubble size was larger for hexane and acetonitrile compared to water (S. J. Lee et al., 2022). The larger cavitation bubble and longer lifetime indicate lower pressure inside the bubble, as formerly reported from the laser ablation of aluminium oxide in ethanol, water, and isopropanol (Lam et al., 2016). Hence, the pressure effect related to the cavitation bubble geometry would favour the HCP formation in water, however, it is only observed in organic solvents. Consequently, the liquid composition seems to be a significant factor influencing the FeNi NP's phase. We have observed that the HCP phase does not scale with the fraction of water content in the organic solvent, consequently, this factor can be ruled out. However, the fact that the ablation in acetone (and dried acetone) produced an

HCP phase, while the ablation in water only provided the FCC phase, suggests that the carbon-based solvent plays a significant role in the HCP phase formation. During PLAL, the presence of carbon species in the cavitation bubble generated from the interaction of the high-intensity laser with the organic solvent can influence the nucleation kinetics of the HCP and FCC phases. Hence, not only the FCC phase forms but also the HCP phase. When the cavitation bubble finally collapses, the fast temperature quenching freezes this metastable phase. Nevertheless, many factors related to the liquid and the laser ablation dynamics might form a complex system that contributes to the formation of the HCP phase in the FeNi NPs.

Besides HCP and FCC phases, some surface oxidation is also observed. Oxidation of NPs, either partially or completely, changes the NP properties such as catalytic activity (Cuenya, 2010) and magnetization (Rebodos & Vikesland, 2010). Controlling the oxidation level of laser-generated NPs is therefore important to produce NPs with the desired functionality. Based on the XRD results, formations of minor amounts of spinel iron-nickel oxide $NiFe_2O_4$ (ICSD No. 241661) are observed in all studied samples, which shows that oxidation occurs even in dried acetone where most of the water molecules are captured by molecular sieves. Nevertheless, the amount of crystalline oxides in all samples is significantly low, approximately 0.7 wt% for FeNi in water, while the quantities are lower than the quantification error of the measurement/device for FeNi synthesized in acetone and dried acetone, hence, the values are not of significance. Based on the study by Marzun et al., the ablation of a Cu target in water with an inert Ar atmosphere still resulted in oxidized species, due to the splitting of water molecules to reactive OH species. To avoid water impurities in acetone, we used molecular sieves. It was formerly reported that using the molecular sieve with the size of 4 Å for 21 hours reduced the water content from 0.45% to 0.001% (w/w) (Meeker et al., 1962). Meanwhile, the water molecule has a diameter of 2.8 Å, hence, molecular sieves with a pore size of 3 Å were used to capture the water molecules in acetone and produce the “dried acetone”. Nadarajah et al. have investigated the influence of 3 Å molecular sieves to capture water molecules in acetone and reduce the oxidation level of the laser-ablated FeRh NPs. They reported that the use of molecular sieves resulted in less nanoparticle oxidation compared to NPs produced in untreated acetone (Nadarajah, Tahir, et al., 2020) and they suggest that the bound oxygen atoms in acetone contribute to NP oxidation. The dissolved oxygen gas in the liquid is also found to partially oxidize NPs due to aging (Marzun, Bönnemann, et al., 2017), which means that the oxidation occurs also due to the possibly prolonged NPs storage in the liquid before the analysis. Hence, the surface oxidation of FeNi NPs into spinel $NiFe_2O_4$ was likely caused by the NPs’ exposure to the oxygen species generated from the pyrolysis of the ablation liquid and later followed by the dissolved gas due to aging.

Based on the TEM results, the FeNi NPs in dried acetone and acetone can be considered monodisperse, while the FeNi NPs produced in water are polydisperse. The FeNi NPs in dried acetone and acetone are smaller than the FeNi in water due to the carbon coating on the NPs surface, which prevent the growth and coalescence of the NPs (Amendola et al., 2011). This layer was formed due to the pyrolysis of organic solvent by the high-intensity pulses (D. Zhang et al., 2019), which then become the building block of the outer NP layer. Nevertheless, it

should be noted that further growth and oxidation during storage cannot be completely ruled out (D. Zhang et al., 2018). The reduced oxidation of the sample is lost again after extended storage time, and results in a similar oxide fraction as the fresh colloid made from the commercial, untreated acetone. This means that the carbon shell and the $NiFe_2O_4$ shell on the NPs did not completely stop further oxidation of the NPs during longer storage time. Oxidation might occur from the presence of molecularly bound O atoms in acetone or the dissolved O_2 gas. Therefore, it is important to use fresh colloids in the posterior intended catalysis or magnetic application to avoid further oxidation that can detriment the produced FeNi NPs performance.

3.1.2 Magnetic and Electrocatalytic Properties

M(H) curves comparison of three different samples shows that the FeNi in water exhibits the highest magnetization. It would be prudent to assume that this difference stems from the fact that the particle size of the water-based sample is significantly higher than that of the two acetone-based ones, which would lead to a lower surface-to-volume ratio and thus a reduced amount of surface spin canting. To discern this difference, M(H) curves were also taken at a lower temperature and a higher magnetic field. Interestingly, the slightly more pronounced shape of the M(H) curves for the water-based sample indicates that full saturation has not yet been reached at 9 T, which would suggest that the higher magnetization value compared to the acetone-based samples is not solely due to a reduced occurrence of spin canting due to the larger average particle size. An explanation can be provided by the paramagnetic HCP phase being present in the acetone-based samples, but not in the water-based one, leading to a reduction of the overall measured magnetization. Additionally, the previously mentioned carbon shell formation can also contribute to this effect. However, despite this slight decrease relative to the water-based sample, the difference in magnetization visible between the sample formed in dried and regular acetone clearly shows the viability of the method presented here to prevent undesired oxidation of the FeNi NPs.

Based on the electrochemical performance results, FeNi in dried acetone/CNTs is the best catalyst among the studied materials, even better than the commercial RuO_2 NPs/CNTs. This might be due to the fact that FeNi NPs produced in dried acetone have the smallest average particle size and, thus a larger surface area, which increases the number of active sites for the reaction to occur. Nevertheless, NPs size should not be the sole reason for this high catalytic activity, since FeNi in water and FeNi in acetone have similar overpotential despite the 5 nm difference in average particle size. In addition, although it was reported that HCP NiFe encapsulated in N-doped carbon has a superior OER electrocatalytic activity compared to the FCC one (C. Wang et al., 2019), the overpotential of FeNi in acetone and dried acetone, with similar HCP content, is different by almost 30 mV. This could mean that the smaller particle size, along with the reduced oxidation as reported by Mössbauer spectroscopy, of FeNi in dried acetone might explain the higher OER catalytic activity.

3.1.3 PLAL Productivity in Different Liquids

PLAL in water shows the highest productivity, which is a factor of 3, compared to PLAL in acetone and dried acetone. High NPs production rates are needed to fulfil the demand for catalysts for industrial use. PLAL in water is therefore better in terms of scalability, despite the catalytic activity being slightly lower than dried acetone. In addition, the use of organic solvents such as acetone as an ablation liquid, especially in a large quantity, does not comply with the green chemistry principles (Anastas & Eghbali, 2010), apart from the safety and health hazards it possesses such as fire and inhalation risks. It is, therefore, more advantageous to use water as an ablation liquid for industrial applications, where productivity in the scale of gram per hour is crucial for large-scale production. Hence, water is the selected liquid for the following chapters related to the further increase of the NPs production rate and the application of FeNi NPs as an OER catalyst.

3.2 Productivity Increase through Multi-Beam PLAL (MB-PLAL)

MB-PLAL has been shown as a feasible and practical technique to increase nanoparticle productivity by only integrating a static DOE into the PLAL system, improving the efficiency and economic viability of colloidal NPs production. Hereby we discuss how the proposed MB-PLAL increases PLAL productivity, how the NPs properties are effected, and the comparative study to MB-PLAL of gold and its economical perspective.

3.2.1 Principle of Productivity Increase in MB-PLAL

The employed 6-beam and 11-beam DOE increased the productivity of FeNi PLAL in water by factors 3 and 4, respectively, with a maximum FeNi NPs productivity of 1.6 g/h. The underlying reason for this lies in the achieved interpulse distance increase from approximately 7 µm (single beam) to 50 µm (11-beam) due to the repetition rate reduction. The larger interpulse distance reduces the laser beam interaction with the cavitation bubble generated by the previous laser pulse. The advantage of using the beam splitter is the ability to increase the interpulse distance while keeping the same number of pulses delivered to the target. In the standard PLAL system without the beam splitter (and a fixed scanning speed), one might need to reduce the repetition rate value to achieve the desired interpulse distance. However, the reduction of the number of pulses irradiating the target would highly reduce productivity. Besides, the cavitation bubble would be enlarged due to the increase of the pulse energy (Reich et al., 2017; Tomko et al., 2015) resulting in the subsequent increase of the laser pulse shielding. If the repetition rate and fluence are kept constant, the compromise would be to lower the laser power, which means that the maximum outcome of the laser source is not fully utilized to achieve the highest productivity. Productivity measurement at the same fluence and repetition rate was also done by adjusting the laser power according to the number of beams. Even though the laser power is increased, the productivity is not increased 6 and 11 times. The non-linear scale-up is probably due to the energy lost as shock waves (Z. Yang et al., 2023), in addition to turbulences and backflow inside the ablation chamber, promoting laser shielding by the NPs, cavitation bubbles, and persistent

microbubbles. Based on the linear fitting, it is possible to infer that increasing the number of beams with other DOEs could result in even higher productivity if a laser with a higher power and higher repetition rate is used.

The energy splitting into multiple beams achieved by the DOEs has been shown to require the reduction of the repetition rate by a factor equal to the number of beams generated in order to keep the same optimum processing fluence per beam produced by the DOE compared to the single beam PLAL. This fact allows us to increase the interpulse distance from 7 µm to 50 µm without the use of expensive high-speed scanners, reducing the beam shielding by the cavitation bubble, while the number of pulses delivered to the target is not affected. In the case of reducing the repetition rate without the use of the DOEs, the high pulse energy promotes nonlinear interactions with the liquid and induces optical breakdown, lowering the productivity due to the extra energy losses. The proposed MB-PLAL system thus enables us to employ the optimal pulse energy and fluence to achieve the highest productivity while increasing the interpulse distance without modifying the scanning parameters. This is further confirmed by the trend observed for increasing power-specific productivity as well as mass productivity, indicating that the MB-PLAL system causes a reduction of the factors affecting the energy delivery to the target as pulse shielding due to the cavitation bubble.

3.2.2 Properties of the MB-PLAL-Generated NPs

Ensuring consistent properties of the produced NPs in the MB-PLAL is a crucial consideration for the scalability of the process and the prospective industrial use. The properties of the produced NPs, including FeNi and Au, do not change for MB-PLAL compared to single beam PLAL, based on the HR-TEM, XRD, and UV-Vis results, indicating that the MB-PLAL with repetition rate compensation to keep the same processing fluence as single beam PLAL does not modify the ablation mechanism or chemical processes during the NPs generation. The only parameter modified from the standard PLAL to the MB-PLAL is the interpulse distance (due to the repetition rate compensation), while the pulse energy, delivered number of pulses to the target's surface, and pulse width are kept approximately the same. The increase in the interpulse distance reduces cavitation bubble shielding, thus increasing NP productivity. Meanwhile, pulse energy and the number of delivered pulses in our setup are kept approximately constant, which is only possible due to the use of the DOE and repetition rate compensation. Hence, the properties of the generated NPs in the MB-PLAL are not modified compared to the single-beam PLAL system.

3.2.3 Comparative Study to MB-PLAL of Gold and its Economical Perspective

A comparative study with Au productivity was also performed to investigate the material's influence on the MB-PLAL system and the possibility of extending the MB-PLAL technique to any material processable by PLAL. Productivity increase factors of 2.1 and 3 were observed for the 6-beam and 11-beam MB-PLAL of Au in water, respectively, with a maximum productivity value of 0.94 g/h for the 11-beam MB-PLAL. Although usually material-dependent productivity has been reported to be linked to the trend of material

density (M.-R. Kalus et al., 2019), other underlying reasons might have influenced the productivity differences observed between FeNi and Au in our case. (1) Larger bubble half-width of Au than FeNi, which contributes to a larger pulse shielding. The temporal distance between two pulses in the 11-beam MB-PLAL of Au and FeNi is 2.5 µs, as the employed repetition rate was 400 kHz. At this time range, the cavitation bubble half-width of Au is larger than FeNi, resulting in a larger energy shielding. Hence, even for the achieved larger interpulse distance, pulse shielding from the cavitation bubble is expected to further influence Au nanoparticle production. (2) The steady-state optical absorptance of Au at our laser wavelength (1064 nm) is 3% (G. Zhu et al., 2019), lower compared to the FeNi which is 35%. The higher the optical absorptance of the material at the irradiation laser wavelength, the higher the energy absorbed by the target material (Berkmanns & Faerber, 2008; Bunaziv et al., 2021; Nakano, 2021), leading to a higher ablation volume. (3) The intrinsic chemical disorder of alloy materials as FeNi (He et al., 2019) contributes to a stronger electron-phonon coupling and lower thermal conductivity (He et al., 2019), resulting in a lower threshold fluence than elemental materials, such as Au. Hence, Au's higher threshold fluence, the weaker electron-phonon coupling, and higher conductivity of Au compared to FeNi, leading to energy thermal dissipation, which lower productivity.

A comparison of MB-PLAL and PLAL employing the same laser source allows us to conclude that MB-PLAL can achieve an annual production of approximately 1800 g of colloidal Au NPs, which is almost a 200% production increase compared with the PLAL system. A decreased labour cost and electricity consumption of 54,000 € and 20,000 kWh are expected for every 1000 g of Au NPs produced with the 11-beam MB-PLAL compared to the PLAL using the same laser source and scanning system. Prospectively, the proposed MB-PLAL system can be integrated into the current high-productivity PLAL systems available worldwide to further boost achievable productivity with a minimum cost and low experimental effort. Furthermore, the employment of the MB-PLAL system with higher laser power systems with repetition rates in the MHz range or higher would allow to employ beam splitters to generate a larger number of beams. Consequently, the repetition rate reduction factor would be higher and so the increase of the interpulse distance, further lowering pulse shielding and reaching even higher production rates, enhancing the efficiency and economic viability of PLAL for industrial applications.

3.3 MB-PLAL-Generated FeNi NPs as Electrocatalyst

A hybrid catalyst completely free of precious metals or rare elements has been synthesized and investigated as an OER catalyst in the alkaline water splitting process. The hybrid catalyst consisting of laser-generated FeNi NPs dispersed on rGO microflakes and spray-coated on a FeNi/Ni foam substrate, FeNi-rGO/FeNi/Ni foam, shows an outstanding performance in terms of catalytic activity and stability. Hereby we discuss the preparation process, the characterization, and hypothesis of the resulting properties of the hybrid catalyst.

3.3.1 FeNi-rGO Composite Formation

To produce FeNi-rGO/FeNi/Ni foam catalyst, FeNi-rGO composites were first generated and supported on rGO sheets through the PLAL method. Two techniques to directly synthesise and support the FeNi NPs to rGO were compared, namely in situ and downstream PLAL. NPs dispersion is more uniform in the case of in situ FeNi-rGO than in downstream FeNi-rGO. Based on these results, it seems that the in situ PLAL offers a benefit, where rGO flakes in the liquid carrier act as a capping agent, thus NPs are more easily anchored within the wrinkles of rGO and their growth and coalescence are avoided (Torres-Mendieta et al., 2016). On the other hand, downstream FeNi-rGO shows a less uniform distribution as the wrinkling structure of rGO prevents the NPs from reaching the central area, and the NPs accumulate on the perimeter of rGO microflakes. A previous study also reported a similar phenomenon where more Au NPs are found at the wrinkles of GO compared to rGO, suggesting that the higher defect density, electrostatic interactions such as van der Waals, and overlapping of GO's π-orbitals with metal NPs' d-orbitals promote the accrued NPs at the wrinkles (Rance et al., 2010; Torres-Mendieta et al., 2016). In our case, however, replacing the rGO with GO in the downstream PLAL resulted in a more uniform distribution of FeNi NPs; probably due to a lower wrinkling structure observed in our pristine GO. It proves the possibility of getting a uniform distribution of NPs via the downstream PLAL by changing the support material. The difference in the NPs dispersion on the rGO surface compared to the GO in the downstream PLAL in our case could be caused by (1) the higher wrinkling morphology of rGO, causing NPs to be accumulated already at the perimeter area during the mixing, and (2) the loss of some oxygen functional groups in rGO compared to GO, resulting in a more hydrophobic and less dispersible support material. The distribution of the nanoparticles on the rGO or GO microflakes is therefore not only related to the technique but also to the property of the supporting materials, i.e. morphology and electronic structure.

As for the size quenching effect, both in situ and downstream PLAL show a size-quenching effect on the generated FeNi NPs, resulting in size reductions of approximately 3-4 nm compared to unsupported FeNi NPs. But the presence of light-absorbing or light-scattering matters in the liquid carrier during in situ PLAL results in lower production rate; which was 50 mg/h productivity reduction in this study at rGO concentration of only 15 mg/L. At a higher concentration of rGO, FeNi NPs productivity will be reduced even further due to laser shielding by rGO microflakes. Hence, downstream PLAL was investigated as a more productive approach to synthesizing and supporting FeNi NPs on rGO without the optical shielding effect.

Based on these electrochemical performances, FeNi-rGO prepared by in situ and downstream PLAL have higher OER catalytic activities and charge transfer rates than the downstream FeNi-GO. Despite the more uniform distribution of the FeNi NPs on the surface of GO flakes, GO has more oxygen functional groups which leads to increasing defects and the sp^3 carbon hybridization (Qiu et al., 2023). This reduces the π electrons conjugation and hinders the electron transfer process, lowering its electrical conductivity (Qiu et al., 2023). Hence, the performance of FeNi-GO is significantly worse than the FeNi-rGO samples. Similar performance between in situ and downstream FeNi-rGO shows that the supporting mechanism of FeNi on the rGO does not significantly influence its electrochemical

performance. In addition, Raman spectroscopy reveals ten-fold increases of $I_{D''}/I_G$ and I_{D*}/I_G of in situ FeNi-rGO compared to downstream FeNi-rGO, implying to loss of crystallinity and an increase in rGO sheets' interlayer spacing in the case of in situ FeNi-rGO. Consequently, due to the higher FeNi NP productivity achievable by downstream PLAL, the downstream FeNi-rGO sample is selected for further testing.

3.3.2 FeNi-rGO/FeNi/Ni foam Electrode

Combining the downstream FeNi-rGO composite with FeNi/Ni foam substrate, the hybrid FeNi-rGO/FeNi/Ni foam catalyst achieved high OER catalytic activity which requires an overpotential of only 234 mV at a current density of 10 mA/cm^2, in addition to exceptional durability and stability, depicted from the stable chronopotentiometry results for over 1300 h at a current density of 10 mA/cm^2.

The high catalytic activity of the hybrid catalyst may be attributed to the formation of a thin oxidized layer of $NiFe_2O_4$ on the surface of laser-generated FeNi NPs (Khairani, Lin, et al., 2023), which was found to enhance the OER activity (Dalai et al., 2019; Gong & Dai, 2014; J. Jiang et al., 2016; Landon et al., 2012). In addition, the dispersion of these FeNi NPs on FeNi/Ni foam may form a synergistic effect between the $NiFe_2O_4$ layer, FeNi core, and FeNi/Ni foam, as the metal-oxide surface could host reaction intermediates, which then may migrate to the more active area for the reaction to complete (Chang et al., 2018; Pan et al., 2017). Besides the aforementioned hypothesis, the high catalytic activity of FeNi-rGO/FeNi/Ni foam may also be attributed to the following factors, (1) the high conductivity of rGO as support material, (2) dispersion of FeNi NPs on rGO surface, reducing NPs overlapping and obstruction or shielding of the active sites, (3) synergistic interaction between FeNi and rGO which induces charge redistribution and electron transfer between the metal-support at the interface (Pan et al., 2017), and (4) hybrid catalyst providing more cations' valence state suitable for wide range bonding with intermediate species (Chang et al., 2018). In addition, while we cannot completely rule out the contribution of the ruptured FeNi LDH to the increased surface area and overall current, and it complicates direct comparisons of intrinsic catalytic activity between FeNi-rGO alone and RuO_2, our primary goal was to develop a catalyst using only abundant elements—specifically Fe and Ni—without relying on rare elements. We achieved this by combining FeNi-rGO with FeNi LDH (which is ruptured after calcination) and utilizing Ni foam. This hybrid catalyst system, referred to as FeNi-rGO/FeNi/Ni foam, demonstrates promising performance with low overpotential for the OER.

The hybrid FeNi NPs, rGO, and FeNi/Ni foam catalysts are confirmed to have outstanding stability. XRD results before and after 1300 h of testing show no considerable structural changes in the hybrid catalyst. Based on the electrocatalytic performance, the FeNi-rGO/FeNi/Ni foam hybrid catalyst is proven as a high-performance catalyst in both activity and stability.

4 Conclusion

Pulsed laser ablation in liquid is a green synthesis method to produce various types of NPs such as oxides, alloys, and composites. However, despite its versatility and sustainability in producing NPs, PLAL is rarely found in industrial applications, mainly due to its low productivity compared to conventional chemical synthesis methods. Various parameters play big roles in the productivity of PLAL, including the laser, scanner, ablation chamber, liquid, and the target material itself, hence, optimizing these parameters will greatly improve PLAL productivity. Several key strategies to optimize them and to answer our first research question, "What are the strategies to increase the productivity of PLAL?" are as follow:

1. Low productivity in PLAL is commonly caused by species that scatter or absorb the incoming laser pulses, including cavitation bubbles, persistent microbubbles, and the generated NPs themselves, which hinder the incoming laser pulses from reaching the target material. By-passing the cavitation bubbles, changing the laser wavelength to reduce the interaction with the NPs, as well as fast removal of persistent microbubbles and NPs from the ablation area, are keys to boosting productivity. Several methods such as designing a laminar flow chamber, employing a high-speed scanner, integrating a beam-splitter, and using a liquid with low viscosity and/or low vapor pressure, can improve productivity.
2. Finding the optimal fluence is crucial, as each target material has its optimal fluence value. To reach the optimal fluence, fine adjustments of laser power, repetition rate, focal length, and working distance are needed.
3. A shorter pulse duration (ps or fs) is usually preferred to avoid energy dissipation through heating, such as in the case of ns and continuous-wave lasers. Nevertheless, fs-lasers trigger non-linear, self-focusing, and filamentation effects in the liquid, resulting in energy losses and lower productivity. Hence, ps-lasers are usually the first choice to reach high productivity in PLAL.
4. Target morphology such as a wire tip can increase productivity due to the spring-like movement that reduces the cavitation bubble lifetime. Nevertheless, precise laser positioning to such a small area is difficult, prolonging the adjustment time and reducing productivity. Therefore, the use of plate targets is still preferred.
5. Ablation chamber design with flow mechanisms, less turbulence, a thin liquid layer, and fast removal of shielding species is expected to increase productivity. The utilization of fluid dynamics simulation coupled with iterative design is believed to be the fastest way to obtain the desired ablation chamber design.
6. Automatization and continuous production are critical for industrial applications to reduce laser idle time and human error during the adjustment process, increasing the production rate.

These key strategies can increase PLAL productivity and will surely drive forward its potential use in the industry as a greener alternative to conventional chemical synthesis methods. It is especially important to push PLAL into a larger scale production, particularly to supply nanocatalysts, as PLAL is known to produce NPs with a higher defect density, which can act as active sites for catalytic reactions. One of the most popular ideas regarding PLAL is the

capability of producing “bare surface” NPs, meaning that the outer layer of the NPs is free from surfactant or capping agents. Nevertheless, this is mostly true only for noble metals such as Pd, Pt, and Au, which are generally more resistant to oxidation. Materials such as Mn and Cu, when ablated in the presence of water or oxygen-containing liquid, i.e., acetone, will form oxide counterparts in addition to the metal parts, for example, Mn and MnO during ablation of Mn in acetone (D. Zhang et al., 2019), and Cu, CuO, and Cu_2O during ablation of Cu in water (Marzun, Bönnemann, et al., 2017).

Our material of interest for the OER catalyst is composed of Fe and Ni, elements that could be easily oxidized, hence, it is important to first examine the phases of generated FeNi NPs in different liquids before working on increasing the productivity of this catalyst. Organic solvents usually pose hazards, health, and environmental risks, yet they are commonly used as ablation liquid in PLAL if oxidation is not desired. For this work, we investigated acetone as an option for the PLAL of FeNi due to its affordability and availability. However, acetone contains water impurities which may oxidize the produced FeNi NPs, thus a prior treatment of the commercial acetone with molecular sieves to capture water molecules and produce dried acetone is needed. The PLAL of FeNi in dried acetone and commercial acetone are compared. In addition, we also perform PLAL of FeNi in a green and sustainable solvent, water, as a comparison to acetone. Based on our results, our second research question, “How do different liquids affect the productivity, properties, and catalytic performance of the PLAL-generated FeNi NPs?”, can be answered as follows:

1. The three investigated liquids produce FeNi NPs with different phases and core-shell structures: FCC/HCP FeNi@$NiFe_2O_4$ and FCC/HCP FeNi@graphitic carbon in commercial acetone, FCC/HCP FeNi@$NiFe_2O_4$@amorphous carbon in dried acetone, and FCC FeNi@$NiFe_2O_4$ in water.
2. A lower total oxide fraction of 8 % is measured by Mössbauer spectroscopy for FeNi in dried acetone compared to FeNi in acetone.
3. The average NPs size of FeNi in water is 17 nm, larger than FeNi in acetone (12 nm) and FeNi in dried acetone (10 nm).
4. The magnetization value of the dried acetone sample (59 Am^2/kg) is higher than the acetone sample (52 Am^2/kg) due to the lower degree of oxidation. While FeNi in water exhibits the highest magnetization (68 Am^2/kg) as the largest average NPs size.
5. FeNi in dried acetone requires the lowest overpotential (363 mV) than FeNi in acetone, FeNi in water, and benchmark catalyst RuO_2 (390 – 400 mV) at a current density of 10 mA/cm^2.
6. FeNi in water has the highest productivity at 307 mg/h compared to FeNi in dried acetone at 108 mg/h and FeNi in acetone at 98 mg/h.

Although FeNi in dried acetone offers better OER catalytic activity and smaller particle size, its productivity is only one-third of FeNi in water. Hence, considering the sustainability, compliance to the green synthesis method, lower hazard and health risks, and our aim to produce large-scale FeNi NPs for OER catalyst, water is chosen as the ablation liquid and for the study of productivity and hybrid catalyst formation.

The decision to use water to generate FeNi NPs via PLAL leads to the next investigation on productivity study. An approach by integrating a static DOE into the PLAL system, termed multi-beam PLAL (MB-PLAL), has been done to answer our third research question, "Can PLAL NPs productivity be increased through optical methods to reduce nanoparticle catalysts production costs?". Our MB-PLAL approach using a DOE to obtain spatial beam splitting is found to improve the efficiency and economic feasibility of NPs production via the PLAL method without altering NPs properties. MB-PLAL is a practical technique which can be easily installed in existing PLAL systems. DOE with beam-splitting configurations of 1:6 and 1:11 increase the productivity of FeNi PLAL in water by factors 3 and 4, respectively, with the highest FeNi NPs productivity of 1.6 g/h. By adjusting the repetition rate according to the splitting number, to keep the same pulse energy and fluence to the single beam PLAL, allows us to improve the interpulse distance by factor 7 (from 7 µm to 50 µm), without the use of expensive high-speed scanners. As the interpulse distance increases, shielding by the cavitation bubble decreases, while the number of pulses delivered to the target is kept almost constant. Other interesting key findings of MB-PLAL are as follows:

1. Productivity increase factors using 6-beam and 11-beam for the FeNi target in water are 3 and 4, while they are slightly lower for the Au target, at 2.1 and 3.
2. The properties of the generated FeNi and Au NPs via MB-PLAL are similar to single beam PLAL, according to HR-TEM, XRD, and UV-Vis results.
3. Compared to the world record PLAL productivity using a 500-W ps-laser coupled with a polygon scanner, MB-PLAL offers higher power-specific productivity at 9.5 mg/(h·W), in addition to the capability of reaching the same 50-µm interpulse distance despite only using a galvanometer scanner, and requires only one-third of the initial investment.

In summary, MB-PLAL enables us to use the optimal pulse energy and fluence to reach the highest productivity while increasing the interpulse distance without using a sophisticated PLAL system, reducing the capital expenditure and improving the affordability and accessibility of this method.

With the success of increasing the productivity of PLAL via MB-PLAL, the work continued to the final application of FeNi NPs as OER catalysts in the alkaline water splitting process to answer our final research question, "Can PLAL-produced FeNi NPs be used to produce an FeNi-based OER electrocatalyst with high catalytic activity?". We have assembled a hybrid catalyst, completely free of precious metals or rare elements, and have investigated its properties. The hybrid catalyst, consisting of FeNi NPs dispersed on rGO and sprayed on a FeNi/Ni foam substrate, named FeNi-rGO/FeNi/Ni foam, performs satisfactorily in terms of catalytic activity and stability. Before constructing our hybrid catalyst, we also investigated one-step techniques to synthesise FeNi NPs and directly support them on rGO microflakes, namely in situ PLAL and downstream PLAL, and compared the properties of produced NPs. Several key findings of this study include:

1. Both in situ and downstream PLAL successfully quench the size of the generated FeNi NPs by approximately 3-4 nm compared to unsupported FeNi NPs.

2. Based on Raman spectroscopy results, loss of crystallinity and an increase in rGO sheets' interlayer spacing are observed in the in situ FeNi-rGO.
3. FeNi NPs from the in situ PLAL are more uniformly dispersed on the rGO surface than downstream FeNi-rGO, however, both samples show similar average particle size (10 nm) and overpotential (400 mV at 10 mA/cm^2). As there is not much difference between in situ and downstream FeNi-rGO in terms of catalytic activity, downstream FeNi-rGO is chosen for the hybrid catalyst as it has higher productivity.
4. The hybrid FeNi-rGO/FeNi/Ni foam catalyst shows promising catalytic activity, requiring an overpotential of only 234 mV and exceptional durability and stability for over 1300 h at a current density of 10 mA/cm^2.

With this final work of investigating and applying the laser-generated FeNi NPs as a catalyst, the dissertation is concluded. This dissertation covers the production of FeNi NPs in different ablation liquids via the PLAL method, increasing productivity through a newly proposed MB-PLAL, and finally producing a hybrid catalyst, FeNi-rGO/FeNi/Ni foam; all with the hope of this knowledge being further used toward the advancement of science: (1) Fostering the utilization and advancement of PLAL, a method to produce NPs that complies with green chemistry principle, (2) increasing PLAL productivity to push this method into the industry, thereby improving the sustainability of NPs production on a large scale, and (3) the construction of hybrid catalyst free of precious and rare elements for OER, with high stability and low overpotential, to suppress the production cost and increase the lifetime of alkaline electrolysers, accelerating the transitioning towards hydrogen energy to reach net zero carbon by 2050.

5 Outlook

The dissertation has been summarized in the previous chapter, where advances, discoveries, and knowledge obtained through the course of this study are envisioned to open new pathways and potentials in PLAL, catalyst, and hydrogen technology. Nevertheless, there are limitations in this study which can be further studied and explored, especially related to methodological and data limitations that could not be addressed due to constraints.

Firstly, in terms of solvent influence on the properties of the PLAL-generated FeNi NPs, water content analysis using Karl Fischer titration can be sought to accurately determine the water content in acetone. If Karl Fischer titration is available, the water content in the acetone can also be varied depending on the duration of treatment using molecular sieves. Changing to other organic solvents with varying carbon chain length, i.e., methanol, ethanol, propanol, butanol, type of carbon bonds, i.e., hexane, hexene, hexyne, or functional groups, i.e., hexene, hexanol, hexanoic acid, hexanal, can also be done to find the reason of metastable phase formation. The synthesis of metastable NPs via PLAL will surely unlock many potentials related to unexplored materials, which are not possible to be characterized except they stay in high-temperature and high-pressure conditions. Using artificial intelligence through machine learning by feeding reactions of metals with different solvents at various temperatures (up to the temperature achievable by PLAL) will also give an interesting perspective of possible phases which could be formed. This method reduces the number of experiments needed to find the most suitable solvent for PLAL of a certain target material to obtain the desired NPs.

The second work on the productivity increase via MB-PLAL offers valuable insight into further tuning laser parameters after the integration of an additional optical element, increasing PLAL productivity. Constraints related to the laser and scanner parameters, as well as chamber design were faced. For example, the lowest repetition rate value of our laser is at 400 kHz. Nevertheless, the highest productivity obtained without the DOE at 100 % laser power uses a repetition rate of 3000 kHz. With our 11-beam setup, a repetition rate of 270 kHz should have been employed to get the optimal pulse energy, instead of 400 kHz. Hence, further study using a high-power laser (>100 W) set at a low repetition rate and coupled with DOE with a high beam-splitting number can be sought. For industrial applications, it is also important to consider a ps laser system with a low repetition rate, instead of a high repetition rate, when building an MB-PLAL system. During the experiment, we also limit the scanning pattern to the Archimedean spiral. Studying the scanning pattern's influence on PLAL productivity may provide insight into the most productive scanning pattern that is synergistic with the galvanometer scanner’s working principle. In addition, the scanning pattern used in this work is limited to approximately 10 mm in diameter due to the size of the DOE, which limits the scanning speed to only 20 m/s. A scanning speed of 50 m/s can be performed when the scanning pattern occupies approximately 75% of the lens area, approximately a spiral with a diameter of 150 mm. But to do PLAL in such a large area, a new flow chamber should be built and an extremely large DOE should be custom-produced. For a long-term investment, this might be worth pursuing, but to suppress the capital investment and avoid time delay, purchasing readily available products is more efficient. In terms of target material influence

on MB-PLAL, it is important to find the right laser parameters for each target. For example, our laser system (10 ps 1064 nm laser) is more suitable for the FeNi target instead of Au, thus a higher FeNi productivity is observed despite Au's higher density. Deciding which NPs are desired before building the laser system is important for large-scale production.

Our last work on the assembly of FeNi-rGO/FeNi/Ni foam for the OER catalyst investigates the downstream and in situ PLAL where we observe the influence of the supporting materials on the produced composite. For further study, it might be interesting to change the supporting materials, for example to monomers that polymerize in certain laser wavelength, and compare the downstream and in situ PLAL. There is a possibility that NPs are trapped inside the polymer structure instead of just mixed or attached on the surface through weak interactions. These might reduce the leaching of NPs for example in the anti-bacterial packaging or membrane for water purification. The concentration of the supporting materials can also be varied to see the changes in the ratio of NPs to supporting materials, morphology, elemental ratio, and size distribution of the PLAL-generated NPs, which might influence the OER catalytic activity. It might also be interesting to find a way where FeNi LDH structure can be maintained after the calcination step, which will surely increase the surface area and catalytic activity. The OER performance of the hybrid catalyst presented in this study is exceptional, with an overpotential required of only 234 mV and stability of more than 1300 h, but the exact mechanism of the interactions between materials, i.e., FeNi NPs, rGO, FeNi layer, and Ni foam, is not yet fully understood. Finding this mechanism may open pathways in building hybrid catalysts with an even lower overpotential and longer stability. Testing hybrid catalysts' performance and durability at higher current densities (0.5-2 A/cm^2) is crucial to match industrial needs for stacks with lower energy demand and longer lifetime.

6 References

Acharya, P., Nelson, Z. J., Benamara, M., Manso, R. H., Bakovic, S. I. P. P., Abolhassani, M., Lee, S., Reinhart, B., Chen, J., & Greenlee, L. F. (2019). Chemical Structure of Fe-Ni Nanoparticles for Efficient Oxygen Evolution Reaction Electrocatalysis. *ACS Omega*, *4*(17), 17209–17222. https://doi.org/10.1021/acsomega.9b01692

Alheshibri, M., Akhtar, S., Al Baroot, A., Elsayed, K. A., Al Qahtani, H. S., & Drmosh, Q. A. A. (2021). Template-free single-step preparation of hollow CoO nanospheres using pulsed laser ablation in liquid enviroment. *Arabian Journal of Chemistry*, *14*(9), 103317. https://doi.org/10.1016/j.arabjc.2021.103317

Amendola, V., Amans, D., Ishikawa, Y., Koshizaki, N., Scirè, S., Compagnini, G., Reichenberger, S., & Barcikowski, S. (2020). Room-Temperature Laser Synthesis in Liquid of Oxide, Metal-Oxide Core-Shells, and Doped Oxide Nanoparticles. *Chemistry – A European Journal*, *26*(42), 9206–9242. https://doi.org/10.1002/chem.202000686

Amendola, V., Riello, P., & Meneghetti, M. (2011). Magnetic nanoparticles of iron carbide, iron oxide, iron@iron oxide, and metal iron synthesized by laser ablation in organic solvents. *Journal of Physical Chemistry C*, *115*(12), 5140–5146. https://doi.org/10.1021/jp109371m

Anastas, P., & Eghbali, N. (2010). Green Chemistry: Principles and Practice. *Chemical Society Reviews*, *39*(1), 301–312. https://doi.org/10.1039/b918763b

Anton Fojtik and Arnim Henglein. (1993). Laser ablation of films and suspended particles in a solvent: formation of cluster and colloid solutions. *Berichte Der Bunsen-Gesellschaft*, *97*(2), 252–254.

Arcos, J. M. M., & Santos, D. M. F. (2023). The Hydrogen Color Spectrum: Techno-Economic Analysis of the Available Technologies for Hydrogen Production. *Gases*, *3*(1), 25–46. https://doi.org/10.3390/gases3010002

Bai, L., Duan, Z., Wen, X., & Guan, J. (2019). Bifunctional atomic iron-based catalyst for oxygen electrode reactions. *Journal of Catalysis*, *378*, 353–362. https://doi.org/10.1016/j.jcat.2019.09.009

Bandal, H., Reddy, K. K., Chaugule, A., & Kim, H. (2018). Iron-based heterogeneous catalysts for oxygen evolution reaction; change in perspective from activity promoter to active catalyst. *Journal of Power Sources*, *395*(February), 106–127. https://doi.org/10.1016/j.jpowsour.2018.05.047

Barcikowski, S., Amendola, V., Lau, M., Marzun, G., Rehbock, C., Reichenberger, S., Zhang, D., Gökce, B. (2019). *Handbook of Laser Synthesis & Processing of Colloids* (Second Edi). Duisburg-Essen Publication Online. https://doi.org/https://doi.org/10.17185/duepublico/70584

Barcikowski, S., Meńndez-Manjón, A., Chichkov, B., Brikas, M., & Račiukaitis, G. (2007). Generation of nanoparticle colloids by picosecond and femtosecond laser ablations in liquid flow. *Applied Physics Letters*, *91*(8). https://doi.org/10.1063/1.2773937

Berkmanns, Dr.-Ing. J., & Faerber, Dr.-Ing. M. (2008). *Laser basics - LASERLINE Technical*.

Blakemore, J. D., Gray, H. B., Winkler, J. R., & Müller, A. M. (2013). Co3O4 Nanoparticle Water-Oxidation Catalysts Made by Pulsed-Laser Ablation in Liquids. *ACS Catalysis*, *3*(11), 2497–2500. https://doi.org/10.1021/cs400639b

Boehler, R. (2005). Diamond cells and new materials. *Materials Today*, *8*(11), 34–42. https://doi.org/10.1016/S1369-7021(05)71158-5

Bunaziv, I., Akselsen, O. M., Ren, X., Nyhus, B., Eriksson, M., & Gulbrandsen-Dahl, S. (2021). A review on laser-assisted joining of aluminium alloys to other metals. *Metals*, *11*(11). https://doi.org/10.3390/met11111680

Burke, M. S., Zou, S., Enman, L. J., Kellon, J. E., Gabor, C. A., Pledger, E., & Boettcher, S. W. (2015). Revised Oxygen Evolution Reaction Activity Trends for First-Row Transition-Metal (Oxy)hydroxides in Alkaline Media. *The Journal of Physical Chemistry Letters*, *6*(18), 3737–3742. https://doi.org/10.1021/acs.jpclett.5b01650

Cao, L., Li, Z., Su, K., Zhang, M., & Cheng, B. (2021). Rational design of hollow oxygen deficiency-enriched NiFe2O4@N/rGO as bifunctional electrocatalysts for overall water splitting. *Journal of Energy Chemistry*, *54*, 595–603. https://doi.org/10.1016/j.jechem.2020.06.053

Chang, C., Zhang, L., Hsu, C. W., Chuah, X. F., & Lu, S. Y. (2018). Mixed NiO/NiCo2O4 Nanocrystals Grown from the Skeleton of a 3D Porous Nickel Network as Efficient Electrocatalysts for Oxygen

Evolution Reactions. *ACS Applied Materials and Interfaces*, *10*(1), 417–426. https://doi.org/10.1021/acsami.7b13127

Charee, W., Tangwarodomnukun, V., & Dumkum, C. (2015). Laser ablation of silicon in water under different flow rates. *International Journal of Advanced Manufacturing Technology*, *78*(1–4), 19–29. https://doi.org/10.1007/s00170-014-6625-6

Chaudhary, K., Rizvi, S. Z. H., & Ali, J. (2016). Laser-Induced Plasma and its Applications. In *Plasma Science and Technology - Progress in Physical States and Chemical Reactions*. InTech. https://doi.org/10.5772/61784

Chemin, A., Lam, J., Laurens, G., Trichard, F., Motto-Ros, V., Ledoux, G., Jarý, V., Laguta, V., Nikl, M., Dujardin, C., & Amans, D. (2019). Doping nanoparticles using pulsed laser ablation in a liquid containing the doping agent. *Nanoscale Advances*, *1*(10), 3963–3972. https://doi.org/10.1039/c9na00223e

Chen, S., Wang, Y., Wang, Z., & Zhang, K. (2023). Advances in nonprecious metal catalysts for efficient water oxidation in alkaline media. *Ionics*, *29*(1), 9–32. https://doi.org/10.1007/s11581-022-04774-2

Chen, Y., Li, Q., Lin, Y., Liu, J., Pan, J., Hu, J., & Xu, X. (2024). Boosting oxygen evolution reaction by FeNi hydroxide-organic framework electrocatalyst toward alkaline water electrolyzer. *Nature Communications*, *15*(1). https://doi.org/10.1038/s41467-024-51521-4

Chen, Y., Rui, K., Zhu, J., Dou, S. X., & Sun, W. (2019). Recent Progress on Nickel-Based Oxide/(Oxy)Hydroxide Electrocatalysts for the Oxygen Evolution Reaction. *Chemistry – A European Journal*, *25*(3), 703–713. https://doi.org/10.1002/chem.201802068

Ciammaruchi, L., Bellucci, L., Castillo, G. C., Sánchez, G. M. D., Liu, Q., Tozzini, V., & Martorell, J. (2019). Water splitting for hydrogen chemisorption in graphene oxide dynamically evolving to a graphane character lattice. *Carbon*, *153*, 234–241. https://doi.org/10.1016/j.carbon.2019.06.087

Claramunt, S., Varea, A., López-Díaz, D., Velázquez, M. M., Cornet, A., & Cirera, A. (2015). The importance of interbands on the interpretation of the raman spectrum of graphene oxide. *Journal of Physical Chemistry C*, *119*(18), 10123–10129. https://doi.org/10.1021/acs.jpcc.5b01590

Corrigan, D. A. (1987). The Catalysis of the Oxygen Evolution Reaction by Iron Impurities in Thin Film Nickel Oxide Electrodes. *Journal of The Electrochemical Society*, *134*(2), 377–384. https://doi.org/10.1149/1.2100463

Cuenya, B. R. (2010). Synthesis and catalytic properties of metal nanoparticles: Size, shape, support, composition, and oxidation state effects. *Thin Solid Films*, *518*(12), 3127–3150. https://doi.org/10.1016/j.tsf.2010.01.018

Cui, J., Kramer, M., Zhou, L., Liu, F., Gabay, A., Hadjipanayis, G., Balasubramanian, B., & Sellmyer, D. (2018). Current progress and future challenges in rare-earth-free permanent magnets. *Acta Materialia*, *158*, 118–137. https://doi.org/10.1016/j.actamat.2018.07.049

Dalai, N., Mohanty, B., Mitra, A., & Jena, B. (2019). Highly Active Ternary Nickel–Iron oxide as Bifunctional Catalyst for Electrochemical Water Splitting. *ChemistrySelect*, *4*(27), 7791–7796. https://doi.org/10.1002/slct.201901465

De Loor, R. (2013). Polygon Scanner System for Ultra Short Pulsed Laser Micro-Machining Applications. *Physics Procedia*, *41*, 544–551. https://doi.org/10.1016/j.phpro.2013.03.114

Delfino, F., Ros, C., Palardonio, S. M., Carretero, N. M., Murcia-López, S., Morante, J. R., Martorell, J., Fthenakis, Z. G., Sgroi, M. F., Tozzini, V., & Bellucci, L. (2024). Multi-methodological analysis of hydrogen desorption from graphene. *Carbon*, *227*(May), 119211. https://doi.org/10.1016/j.carbon.2024.119211

Dell'Aglio, M., Gaudiuso, R., De Pascale, O., & De Giacomo, A. (2015). Mechanisms and processes of pulsed laser ablation in liquids during nanoparticle production. *Applied Surface Science*, *348*, 4–9. https://doi.org/10.1016/j.apsusc.2015.01.082

Desarkar, H. S., Kumbhakar, P., & Mitra, A. K. (2013). One-step synthesis of Zn/ZnO hollow nanoparticles by the laser ablation in liquid technique. *Laser Physics Letters*, *10*(5), 055903. https://doi.org/10.1088/1612-2011/10/5/055903

Doñate-Buendía, C., Fernández-Alonso, M., Lancis, J., & Mínguez-Vega, G. (2019). Overcoming the barrier of nanoparticle production by femtosecond laser ablation in liquids using simultaneous spatial and temporal focusing. *Photonics Research*, *7*(11), 1249. https://doi.org/10.1364/PRJ.7.001249

Doñate-Buendia, C., Spellauge, M., Streubel, R., Riahi, F., Barcikowski, S., Huber, H. P., & Gökce, B. (2023). Double-pulse laser ablation in liquids: nanoparticle bimodality reduction by sub-nanosecond interpulse delay optimization. *Journal of Physics D: Applied Physics*, *56*(10), 104001. https://doi.org/10.1088/1361-6463/acbaaa

Donohoo-Vallett, P., Ryan, N., & Wiser, R. (2023). *On The Path to 100% Clean Electricity* (Issue May).

European Commission. (2021). *Delivering the European Green Deal*. https://commission.europa.eu/strategy-and-policy/priorities-2019-2024/european-green-deal/delivering-european-green-deal_en

Fairley, N., Fernandez, V., Richard-Plouet, M., Guillot-Deudon, C., Walton, J., Smith, E., Flahaut, D., Greiner, M., Biesinger, M., Tougaard, S., Morgan, D., & Baltrusaitis, J. (2021). Systematic and collaborative approach to problem solving using X-ray photoelectron spectroscopy. *Applied Surface Science Advances*, *5*(May), 100112. https://doi.org/10.1016/j.apsadv.2021.100112

Feng, C., Faheem, M. B., Fu, J., Xiao, Y., Li, C., & Li, Y. (2020). Fe-Based Electrocatalysts for Oxygen Evolution Reaction: Progress and Perspectives. *ACS Catalysis*, *10*(7), 4019–4047. https://doi.org/10.1021/acscatal.9b05445

Forsythe, R. C., Cox, C. P., Wilsey, M. K., & Müller, A. M. (2021). Pulsed Laser in Liquids Made Nanomaterials for Catalysis. *Chemical Reviews*, *121*(13), 7568–7637. https://doi.org/10.1021/acs.chemrev.0c01069

Franz, D., Häfner, T., Kunz, T., Roth, G. L., Rung, S., Esen, C., & Hellmann, R. (2022). Characterization of a hybrid scanning system comprising acousto-optical deflectors and galvanometer scanners. *Applied Physics B: Lasers and Optics*, *128*(3), 1–9. https://doi.org/10.1007/s00340-022-07782-2

Frey, P. A., & Reed, G. H. (2012). The ubiquity of iron. *ACS Chemical Biology*, *7*(9), 1477–1481. https://doi.org/10.1021/cb300323q

Frias Batista, L. M., Kaplan, E., Weththasingha, C., Cook, B., Harris, S., Nag, A., & Tibbetts, K. M. (2023). How Pulse Width Affects Laser Ablation of Organic Liquids. *The Journal of Physical Chemistry B*, *127*(29), 6551–6561. https://doi.org/10.1021/acs.jpcb.3c03708

Frias Batista, L. M., Nag, A., Meader, V. K., & Tibbetts, K. M. (2022). Generation of nanomaterials by reactive laser-synthesis in liquid. *Science China Physics, Mechanics & Astronomy*, *65*(7), 274202. https://doi.org/10.1007/s11433-021-1835-x

Friebel, D., Louie, M. W., Bajdich, M., Sanwald, K. E., Cai, Y., Wise, A. M., Cheng, M.-J., Sokaras, D., Weng, T.-C., Alonso-Mori, R., Davis, R. C., Bargar, J. R., Nørskov, J. K., Nilsson, A., & Bell, A. T. (2015). Identification of Highly Active Fe Sites in (Ni,Fe)OOH for Electrocatalytic Water Splitting. *Journal of the American Chemical Society*, *137*(3), 1305–1313. https://doi.org/10.1021/ja511559d

Fromme, T., Reichenberger, S., Tibbetts, K. M., & Barcikowski, S. (2024). Laser synthesis of nanoparticles in organic solvents – products, reactions, and perspectives. *Beilstein Journal of Nanotechnology*, *15*, 638–663. https://doi.org/10.3762/bjnano.15.54

Golas, P. L., Louie, S., Lowry, G. V, Matyjaszewski, K., & Tilton, R. D. (2010). Comparative Study of Polymeric Stabilizers for Magnetite Nanoparticles Using ATRP. *Langmuir*, *26*(22), 16890–16900. https://doi.org/10.1021/la103098q

Gong, M., & Dai, H. (2014). A mini review of NiFe-based materials as highly active oxygen evolution reaction electrocatalysts. *Nano Research*, *8*(1), 23–39. https://doi.org/10.1007/s12274-014-0591-z

Gong, M., Li, Y., Wang, H., Liang, Y., Wu, J. Z., Zhou, J., Wang, J., Regier, T., Wei, F., & Dai, H. (2013). An Advanced Ni–Fe Layered Double Hydroxide Electrocatalyst for Water Oxidation. *Journal of the American Chemical Society*, *135*(23), 8452–8455. https://doi.org/10.1021/ja4027715

Haiss, W., Thanh, N. T. K., Aveyard, J., & Fernig, D. G. (2007). Determination of Size and Concentration of Gold Nanoparticles from UV−Vis Spectra. *Analytical Chemistry*, *79*(11), 4215–4221. https://doi.org/10.1021/ac0702084

Hamad, A., Li, L., Liu, Z., Zhong, X. L., Liu, H., & Wang, T. (2015). Generation of silver titania nanoparticles from an Ag-Ti alloy via picosecond laser ablation and their antibacterial activities. *RSC Advances*, *5*(89), 72981–72994. https://doi.org/10.1039/c5ra16466d

Han, B., Grimaud, A., Giordano, L., Hong, W. T., Diaz-Morales, O., Yueh-Lin, L., Hwang, J., Charles, N., Stoerzinger, K. A., Yang, W., Koper, M. T. M., & Shao-Horn, Y. (2018). Iron-Based Perovskites for Catalyzing Oxygen Evolution Reaction. *The Journal of Physical Chemistry C*, *122*(15), 8445–8454. https://doi.org/10.1021/acs.jpcc.8b01397

Haxhiaj, I., Tigges, S., Firla, D., Zhang, X., Hagemann, U., Kondo, T., Nakamura, J., Marzun, G., & Barcikowski, S. (2019). Platinum nanoparticles supported on reduced graphene oxide prepared in situ by a continuous one-step laser process. *Applied Surface Science*, *469*, 811–820. https://doi.org/10.1016/j.apsusc.2018.10.257

He, M., Wu, C., Shugaev, M. V., Samolyuk, G. D., & Zhigilei, L. V. (2019). Computational Study of Short-Pulse Laser-Induced Generation of Crystal Defects in Ni-Based Single-Phase Binary Solid-Solution Alloys. *Journal of Physical Chemistry C*, *123*(4), 2202–2215. https://doi.org/10.1021/acs.jpcc.8b09922

Hendel, T., Wuithschick, M., Kettemann, F., Birnbaum, A., Rademann, K., & Polte, J. (2014). In situ determination of colloidal gold concentrations with uv-vis spectroscopy: Limitations and perspectives. *Analytical Chemistry*, *86*(22), 11115–11124. https://doi.org/10.1021/ac502053s

Henglein, A. (1993). Physicochemical properties of small metal particles in solution: "microelectrode" reactions, chemisorption, composite metal particles, and the atom-to-metal transition. *The Journal of Physical Chemistry*, *97*(21), 5457–5471. https://doi.org/10.1021/j100123a004

Hu, C., Zhang, L., Huang, Z., Zhu, W., Zhao, Z.-J., & Gong, J. (2019). Facet-evolution growth of Mn3O4@CoxMn3-xO4 electrocatalysts on Ni foam towards efficient oxygen evolution reaction. *Journal of Catalysis*, *369*, 105–110. https://doi.org/10.1016/j.jcat.2018.10.034

Hu, S., Melton, C., & Mukherjee, D. (2014). A facile route for the synthesis of nanostructured oxides and hydroxides of cobalt using laser ablation synthesis in solution (LASIS). *Physical Chemistry Chemical Physics*, *16*(43), 24034–24044. https://doi.org/10.1039/c4cp03018d

Huang, C. N., Bow, J. S., Zheng, Y., Chen, S. Y., Ho, N. J., & Shen, P. (2010). Nonstoichiometric titanium oxides via pulsed laser ablation in water. *Nanoscale Research Letters*, *5*(6), 972–985. https://doi.org/10.1007/s11671-010-9591-4

Huang, E., Bassett, W. A., & Weathers, M. S. (1988). Phase relationships in Fe-Ni alloys at high pressures and temperatures. *Journal of Geophysical Research*, *93*(B7), 7741. https://doi.org/10.1029/JB093iB07p07741

Hunter, B. M., Blakemore, J. D., Deimund, M., Gray, H. B., Winkler, J. R., & Müller, A. M. (2014). Highly Active Mixed-Metal Nanosheet Water Oxidation Catalysts Made by Pulsed-Laser Ablation in Liquids. *Journal of the American Chemical Society*, *136*(38), 13118–13121. https://doi.org/10.1021/ja506087h

Hunter, B. M., Gray, H. B., & Müller, A. M. (2016). Earth-Abundant Heterogeneous Water Oxidation Catalysts. *Chemical Reviews*, *116*(22), 14120–14136. https://doi.org/10.1021/acs.chemrev.6b00398

Ibrahimkutty, S., Wagener, P., Rolo, T. D. S., Karpov, D., Menzel, A., Baumbach, T., Barcikowski, S., & Plech, A. (2015). A hierarchical view on material formation during pulsed-laser synthesis of nanoparticles in liquid. *Scientific Reports*, *5*(1), 16313. https://doi.org/10.1038/srep16313

Incer-Valverde, J., Korayem, A., Tsatsaronis, G., & Morosuk, T. (2023). "Colors" of hydrogen: Definitions and carbon intensity. *Energy Conversion and Management*, *291*(June), 117294. https://doi.org/10.1016/j.enconman.2023.117294

Intartaglia, R., Bagga, K., & Brandi, F. (2014). Study on the productivity of silicon nanoparticles by picosecond laser ablation in water: towards gram per hour yield. *Optics Express*, *22*(3), 3117. https://doi.org/10.1364/OE.22.003117

IRENA. (2020). Green Hydrogen Cost Reduction: Scaling up Electrolysers to Meet the 1.5^{0}C Climate Goal, International Renewable Energy Agency. In *Irena*. International Renewable Energy Agency.

IRENA. (2022a). *Electrolyser costs*. International Renewable Energy Agency. https://www.irena.org/Energy-Transition/Technology/Hydrogen/Electrolyser-costs

IRENA. (2022b). Renewable Generation Costs in 2022. In *International Renewable Energy Agency*.

Ishikawa, Y., Kawaguchi, K., Shimizu, Y., Sasaki, T., & Koshizaki, N. (2006). Preparation of Fe-Pt alloy particles by pulsed laser ablation in liquid medium. *Chemical Physics Letters*, *428*(4–6), 426–429. https://doi.org/10.1016/j.cplett.2006.07.076

Jakobi, J., Petersen, S., Menéndez-Manjón, A., Wagener, P., & Barcikowski, S. (2010). Magnetic alloy nanoparticles from laser ablation in cyclopentanone and their embedding into a photoresist. *Langmuir*, *26*(10), 6892–6897. https://doi.org/10.1021/la101014g

Jendrzej, S., Gökce, B., Amendola, V., & Barcikowski, S. (2016). Barrierless growth of precursor-free, ultrafast laser-fragmented noble metal nanoparticles by colloidal atom clusters – A kinetic in situ study. *Journal of Colloid and Interface Science*, *463*, 299–307. https://doi.org/10.1016/j.jcis.2015.10.032

Jendrzej, S., Gökce, B., Epple, M., & Barcikowski, S. (2017). How Size Determines the Value of Gold: Economic Aspects of Wet Chemical and Laser-Based Metal Colloid Synthesis. *ChemPhysChem*, *18*(9), 1012–1019. https://doi.org/10.1002/cphc.201601139

Jia, Y., Sun, T.-Y. Y., Wang, J.-H. H., Huang, H., Li, P., Yu, X.-F. F., & Chu, P. K. (2014). Synthesis of hollow rare-earth compound nanoparticles by a universal sacrificial template method. *CrystEngComm*, *16*(27), 6141–6148. https://doi.org/10.1039/c4ce00440j

Jiang, J., Zhang, C., & Ai, L. (2016). Hierarchical iron nickel oxide architectures derived from metal-organic frameworks as efficient electrocatalysts for oxygen evolution reaction. *Electrochimica Acta*, *208*, 17–24. https://doi.org/10.1016/j.electacta.2016.05.008

Jiang, S., Zhang, M., Xu, C., Liu, G., Zhang, K., Zhang, Z., Peng, H. Q., Liu, B., & Zhang, W. (2024). Recent Developments in Nickel-Based Layered Double Hydroxides for Photo(-/)electrocatalytic Water Oxidation. *ACS Nano*, *18*(26), 16413–16449. https://doi.org/10.1021/acsnano.4c03153

Jin, B., Wang, Q., Sainio, J., Saveleva, V. A., Jiang, H., Shi, J., Ali, B., Kallio, A.-J., Huotari, S., Sundholm, D., Han, N., & Kallio, T. (2024). Amorphous carbon modulated-quantum dots NiO for efficient oxygen evolution in anion exchange membrane water electrolyzer. *Applied Catalysis B: Environment and Energy*, *358*(May), 124437. https://doi.org/10.1016/j.apcatb.2024.124437

Jung, H. J., & Choi, M. Y. (2014). Specific solvent produces specific phase Ni nanoparticles: A pulsed laser ablation in solvents. *Journal of Physical Chemistry C*, *118*(26), 14647–14654. https://doi.org/10.1021/jp503009a

Kalus, M. R., Bärsch, N., Streubel, R., Gökce, E., Barcikowski, S., & Gökce, B. (2017). How persistent microbubbles shield nanoparticle productivity in laser synthesis of colloids - Quantification of their volume, dwell dynamics, and gas composition. *Physical Chemistry Chemical Physics*, *19*(10), 7112–7123. https://doi.org/10.1039/c6cp07011f

Kalus, M. R., Lanyumba, R., Barcikowski, S., & Gökce, B. (2021). Discrimination of ablation, shielding, and interface layer effects on the steady-state formation of persistent bubbles under liquid flow conditions during laser synthesis of colloids. *Journal of Flow Chemistry*. https://doi.org/10.1007/s41981-021-00144-7

Kalus, M.-R., Lanyumba, R., Lorenzo-Parodi, N., Jochmann, M. A., Kerpen, K., Hagemann, U., Schmidt, T. C., Barcikowski, S., & Gökce, B. (2019). Determining the role of redox-active materials during laser-induced water decomposition. *Physical Chemistry Chemical Physics*, *21*(34), 18636–18651. https://doi.org/10.1039/C9CP02663K

Kanan, M. W., & Nocera, D. G. (2008). In Situ Formation of an Oxygen-Evolving Catalyst in Neutral Water Containing Phosphate and Co 2+. *Science*, *321*(5892), 1072–1075. https://doi.org/10.1126/science.1162018

Kanitz, A., Kalus, M. R., Gurevich, E. L., Ostendorf, A., Barcikowski, S., & Amans, D. (2019). Review on experimental and theoretical investigations of the early stage, femtoseconds to microseconds processes during laser ablation in liquid-phase for the synthesis of colloidal nanoparticles. *Plasma Sources Science and Technology*, *28*(10). https://doi.org/10.1088/1361-6595/ab3dbe

Kauffman, D. R., Alfonso, D., Tafen, D. N., Lekse, J., Wang, C., Deng, X., Lee, J., Jang, H., Lee, J. S., Kumar, S., & Matranga, C. (2016). Electrocatalytic Oxygen Evolution with an Atomically Precise Nickel Catalyst. *ACS Catalysis*, *6*(2), 1225–1234. https://doi.org/10.1021/acscatal.5b02633

Kawashima, K., Márquez, R. A., Smith, L. A., Vaidyula, R. R., Carrasco-Jaim, O. A., Wang, Z., Son, Y. J., Cao, C. L., & Mullins, C. B. (2023). A Review of Transition Metal Boride, Carbide, Pnictide, and Chalcogenide Water Oxidation Electrocatalysts. *Chemical Reviews*, *123*(23), 12795–13208. https://doi.org/10.1021/acs.chemrev.3c00005

Khairani, I. Y., Lin, Q., Landers, J., Salamon, S., Doñate-Buendía, C., Karapetrova, E., Wende, H., Zangari, G., & Gökce, B. (2023). Solvent Influence on the Magnetization and Phase of Fe-Ni Alloy Nanoparticles Generated by Laser Ablation in Liquids. *Nanomaterials*, *13*(2), 227. https://doi.org/10.3390/nano13020227

Khairani, I. Y., Mínguez-Vega, G., Doñate-Buendía, C., & Gökce, B. (2023). Green nanoparticle synthesis at scale: a perspective on overcoming the limits of pulsed laser ablation in liquids for high-throughput production. *Physical Chemistry Chemical Physics*, *25*(29), 19380–19408. https://doi.org/10.1039/D3CP01214J

Khairani, I. Y., Spellauge, M., Riahi, F., Huber, H. P., Gökce, B., & Doñate-Buendía, C. (2024). Parallel Diffractive Multi-Beam Pulsed-Laser Ablation in Liquids Toward Cost-Effective Gram Per Hour Nanoparticle Productivity. *Advanced Photonics Research*, *5*(5), 2300290. https://doi.org/10.1002/adpr.202300290

Kim, J. S., Kim, B., Kim, H., & Kang, K. (2018). Recent Progress on Multimetal Oxide Catalysts for the Oxygen Evolution Reaction. *Advanced Energy Materials*, *8*(11), 1702774. https://doi.org/10.1002/aenm.201702774

Klaus, S., Cai, Y., Louie, M. W., Trotochaud, L., & Bell, A. T. (2015). Effects of Fe Electrolyte Impurities on Ni(OH) 2 /NiOOH Structure and Oxygen Evolution Activity. *The Journal of Physical Chemistry C*, *119*(13), 7243–7254. https://doi.org/10.1021/acs.jpcc.5b00105

Kohsakowski, S., Gökce, B., Tanabe, R., Wagener, P., Plech, A., Ito, Y., & Barcikowski, S. (2016). Target geometry and rigidity determines laser-induced cavitation bubble transport and nanoparticle productivity-a high-speed videography study. *Physical Chemistry Chemical Physics*, *18*(24), 16585–16593. https://doi.org/10.1039/c6cp01232a

Komabayashi, T., Hirose, K., & Ohishi, Y. (2012). In situ X-ray diffraction measurements of the fcc-hcp phase transition boundary of an Fe-Ni alloy in an internally heated diamond anvil cell. *Physics and Chemistry of Minerals*, *39*(4), 329–338. https://doi.org/10.1007/s00269-012-0490-3

Kudryashov, S., Danilov, P., Schneider, L., Schille, J., Loeschner, U., Nastulyavichus, A., Smirnov, N., Kuchmizhak, A., & Vitrik, O. (2021). Polygon-facilitated generation of colloidal gold nanoparticles by multi-MHz ultrashort-pulse laser trains: key optical factors. *Laser Physics Letters*, *18*(1). https://doi.org/10.1088/1612-202X/abd171

Kudryashov, S., Samokhvalov, A., Nastulyavichus, A., Saraeva, I., Mikhailovskii, V., Ionin, A., & Veiko, V. (2019). Nanosecond-Laser Generation of Nanoparticles in Liquids: From Ablation through Bubble Dynamics to Nanoparticle Yield. *Materials*, *12*(4), 562. https://doi.org/10.3390/ma12040562

Kuwayama, Y., Hirose, K., Sata, N., & Ohishi, Y. (2008). Phase relations of iron and iron-nickel alloys up to 300 GPa: Implications for composition and structure of the Earth's inner core. *Earth and Planetary Science Letters*, *273*(3–4), 379–385. https://doi.org/10.1016/j.epsl.2008.07.001

Lahaye, N. L., Harilal, S. S., Diwakar, P. K., & Hassanein, A. (2013). The effect of laser pulse duration on ICP-MS signal intensity, elemental fractionation, and detection limits in fs-LA-ICP-MS. *Journal of Analytical Atomic Spectrometry*, *28*(11), 1781–1787. https://doi.org/10.1039/c3ja50200g

Lam, J., Amans, D., Chaput, F., Diouf, M., Ledoux, G., Mary, N., Masenelli-Varlot, K., Motto-Ros, V., & Dujardin, C. (2014). γ-Al2O3 nanoparticles synthesised by pulsed laser ablation in liquids: A plasma analysis. *Physical Chemistry Chemical Physics*, *16*(3), 963–973. https://doi.org/10.1039/c3cp53748j

Lam, J., Lombard, J., Dujardin, C., Ledoux, G., Merabia, S., & Amans, D. (2016). Dynamical study of bubble expansion following laser ablation in liquids. *Applied Physics Letters*, *108*(7), 1–6. https://doi.org/10.1063/1.4942389

Landon, J., Demeter, E., İnoğlu, N., Keturakis, C., Wachs, I. E., Vasić, R., Frenkel, A. I., & Kitchin, J. R. (2012). Spectroscopic Characterization of Mixed Fe–Ni Oxide Electrocatalysts for the Oxygen Evolution Reaction in Alkaline Electrolytes. *ACS Catalysis*, *2*(8), 1793–1801. https://doi.org/10.1021/cs3002644

Lazanas, A. C., & Prodromidis, M. I. (2023). Electrochemical Impedance Spectroscopy–A Tutorial. *ACS Measurement Science Au*, *3*(3), 162–193. https://doi.org/10.1021/acsmeasuresciau.2c00070

Lee, S. J., Theerthagiri, J., & Choi, M. Y. (2022). Time-resolved dynamics of laser-induced cavitation bubbles during production of Ni nanoparticles via pulsed laser ablation in different solvents and their electrocatalytic activity for determination of toxic nitroaromatics. *Chemical Engineering Journal*, *427*(March 2021), 130970. https://doi.org/10.1016/j.cej.2021.130970

Lee, Y., Suntivich, J., May, K. J., Perry, E. E., & Shao-Horn, Y. (2012). Synthesis and Activities of Rutile IrO2 and RuO2 Nanoparticles for Oxygen Evolution in Acid and Alkaline Solutions. *The Journal of Physical Chemistry Letters*, *3*(3), 399–404. https://doi.org/10.1021/jz2016507

Li, C., & Baek, J.-B. (2020). Recent Advances in Noble Metal (Pt, Ru, and Ir)-Based Electrocatalysts for Efficient Hydrogen Evolution Reaction. *ACS Omega*, *5*(1), 31–40. https://doi.org/10.1021/acsomega.9b03550

Li, C., Chen, J., Wu, Y., Cao, W., Sang, S., Wu, Q., Liu, H., & Liu, K. (2019). Enhanced oxygen evolution reaction activity of NiFe layered double hydroxide on nickel foam- reduced graphene oxide interfaces. *International Journal of Hydrogen Energy*, *44*(5), 2656–2663. https://doi.org/10.1016/j.ijhydene.2018.11.167

Li, D., Liu, H., & Feng, L. (2020). A Review on Advanced FeNi-Based Catalysts for Water Splitting Reaction. *Energy & Fuels*, *34*(11), 13491–13522. https://doi.org/10.1021/acs.energyfuels.0c03084

Li, N., Bediako, D. K., Hadt, R. G., Hayes, D., Kempa, T. J., von Cube, F., Bell, D. C., Chen, L. X., & Nocera, D. G. (2017). Influence of iron doping on tetravalent nickel content in catalytic oxygen evolving films. *Proceedings of the National Academy of Sciences*, *114*(7), 1486–1491. https://doi.org/10.1073/pnas.1620787114

Li, P., Zhao, X., Duan, X., Li, Y., Kuang, Y., & Sun, X. (2020). A multiphase nickel iron sulfide hybrid electrode for highly active oxygen evolution. *Science China Materials*, *63*(3), 356–363. https://doi.org/10.1007/s40843-019-1215-9

Li, X., & Guan, Y. (2020). Theoretical fundamentals of short pulse laser-metal interaction: A review. *Nami Jishu Yu Jingmi Gongcheng/Nanotechnology and Precision Engineering*, *3*(3), 105–125. https://doi.org/10.1016/j.npe.2020.08.001

Li, X., Walsh, F. C., & Pletcher, D. (2011). Nickel based electrocatalysts for oxygen evolution in high current density, alkaline water electrolysers. *Phys. Chem. Chem. Phys.*, *13*(3), 1162–1167. https://doi.org/10.1039/C0CP00993H

Li, Y., Wu, Z., Lu, P., Wang, X., Liu, W., Liu, Z., Ma, J., Ren, W., Jiang, Z., & Bao, X. (2020). High-Valence Nickel Single-Atom Catalysts Coordinated to Oxygen Sites for Extraordinarily Activating Oxygen Evolution Reaction. *Advanced Science*, *7*(5), 1903089. https://doi.org/10.1002/advs.201903089

Liang, Y., Li, Y., Wang, H., Zhou, J., Wang, J., Regier, T., & Dai, H. (2011). Co3O4 nanocrystals on graphene as a synergistic catalyst for oxygen reduction reaction. *Nature Materials*, *10*(10), 780–786. https://doi.org/10.1038/nmat3087

Lin, J.-F., Heinz, D. L., Campbell, A. J., Devine, J. M., Mao, W. L., & Shen, G. (2002). Iron-Nickel alloy in the Earth's core. *Geophysical Research Letters*, *29*(10), 1471. https://doi.org/10.1029/2002GL015089

Liu, P., Cao, Y. L., Cui, H., Chen, X. Y., & Yang, G. W. (2008). Micro- and nanocubes of silicon with zinc-blende structure. *Chemistry of Materials*, *20*(2), 494–502. https://doi.org/10.1021/cm7027178

Liu, Y., Liang, X., Gu, L., Zhang, Y., Li, G.-D., Zou, X., & Chen, J.-S. (2018). Corrosion engineering towards efficient oxygen evolution electrodes with stable catalytic activity for over 6000 hours. *Nature Communications*, *9*(1), 2609. https://doi.org/10.1038/s41467-018-05019-5

Long, J., Eliceiri, M., Vangelatos, Z., Rho, Y., Wang, L., Su, Z., Xie, X., Zhang, Y., Grigoropoulos, C. P., Ong, J. I. L., Liceiri, M. A. E., Acharias, Z., Angelatos, V., Ho, Y. O. R., Ang, L. E. W., Hengliang, Z., Ie, X. I. X., Hang, Y. O. Z., Ostas, C. P., & Rigoropoulos, G. (2020). Early dynamics of cavitation bubbles generated during ns laser ablation of submerged targets. *Optics Express*, *28*(10), 14300. https://doi.org/10.1364/oe.391584

Long, X., Li, J., Xiao, S., Yan, K., Wang, Z., Chen, H., & Yang, S. (2014). A strongly coupled graphene and FeNi double hydroxide hybrid as an excellent electrocatalyst for the oxygen evolution reaction. *Angewandte Chemie - International Edition*, *53*(29), 7584–7588. https://doi.org/10.1002/anie.201402822

Lu, Z., Xu, W., Zhu, W., Yang, Q., Lei, X., Liu, J., Li, Y., Sun, X., & Duan, X. (2014). Three-dimensional NiFe layered double hydroxide film for high-efficiency oxygen evolution reaction. *Chem. Commun.*, *50*(49), 6479–6482. https://doi.org/10.1039/C4CC01625D

Mafuné, F., Kohno, J. Y., Takeda, Y., Kondow, T., & Sawabe, H. (2001). Formation of gold nanoparticles by laser ablation in aqueous solution of surfactant. *Journal of Physical Chemistry B*, *105*(22), 5114–5120. https://doi.org/10.1021/jp0037091

Malviya, K. D., & Chattopadhyay, K. (2014). Synthesis and mechanism of composition and size dependent morphology selection in nanoparticles of Ag-Cu alloys processed by laser ablation under liquid medium. *Journal of Physical Chemistry C*, *118*(24), 13228–13237. https://doi.org/10.1021/jp502327c

Manshina, A. A., Tumkin, I. I., Khairullina, E. M., Mizoshiri, M., Ostendorf, A., Kulinich, S. A., Makarov, S., Kuchmizhak, A. A., & Gurevich, E. L. (2024). The Second Laser Revolution in Chemistry: Emerging Laser Technologies for Precise Fabrication of Multifunctional Nanomaterials and Nanostructures. *Advanced Functional Materials*, 2405457. https://doi.org/10.1002/adfm.202405457

Marzun, G., Bönnemann, H., Lehmann, C., Spliethoff, B., Weidenthaler, C., & Barcikowski, S. (2017). Role of Dissolved and Molecular Oxygen on Cu and PtCu Alloy Particle Structure during Laser Ablation Synthesis in Liquids. *ChemPhysChem*, *18*(9), 1175–1184. https://doi.org/10.1002/cphc.201601315

Marzun, G., Levish, A., Mackert, V., Kallio, T., Barcikowski, S., & Wagener, P. (2017). Laser synthesis, structure and chemical properties of colloidal nickel-molybdenum nanoparticles for the

substitution of noble metals in heterogeneous catalysis. *Journal of Colloid and Interface Science*, *489*, 57–67. https://doi.org/10.1016/j.jcis.2016.09.014

Marzun, G., Nakamura, J., Zhang, X., Barcikowski, S., & Wagener, P. (2015). Size control and supporting of palladium nanoparticles made by laser ablation in saline solution as a facile route to heterogeneous catalysts. *Applied Surface Science*, *348*, 75–84. https://doi.org/10.1016/j.apsusc.2015.01.108

McCrory, C. C. L., Jung, S., Peters, J. C., & Jaramillo, T. F. (2013). Benchmarking heterogeneous electrocatalysts for the oxygen evolution reaction. *Journal of the American Chemical Society*, *135*(45), 16977–16987. https://doi.org/10.1021/ja407115p

McCrory, C. C. L. L., Jung, S., Ferrer, I. M., Chatman, S. M., Peters, J. C., & Jaramillo, T. F. (2015). Benchmarking Hydrogen Evolving Reaction and Oxygen Evolving Reaction Electrocatalysts for Solar Water Splitting Devices. *Journal of the American Chemical Society*, *137*(13), 4347–4357. https://doi.org/10.1021/ja510442p

Meeker, R. L., Critchfield, F. E., & Bishop, E. T. (1962). Water Determination by Near Infrared Spectrophotometry. *Analytical Chemistry*, *34*(11), 1510–1511. https://doi.org/10.1021/ac60191a048

Mehta, J. S., Faucett, A. C., Sharma, A., & Mativetsky, J. M. (2017). How Reliable Are Raman Spectroscopy Measurements of Graphene Oxide? *Journal of Physical Chemistry C*, *121*(30), 16584–16591. https://doi.org/10.1021/acs.jpcc.7b04517

Menéndez-Manjón, A., Wagener, P., & Barcikowski, S. (2011). Transfer-matrix method for efficient ablation by pulsed laser ablation and nanoparticle generation in liquids. *Journal of Physical Chemistry C*, *115*(12), 5108–5114. https://doi.org/10.1021/jp109370q

Meng, J., Cui, Z., Yang, X., Zhu, S., Li, Z., Qi, K., Zheng, L., & Liang, Y. (2018). Cobalt-iron (oxides) water oxidation catalysts: Tracking catalyst redox states and reaction dynamic mechanism. *Journal of Catalysis*, *365*, 227–237. https://doi.org/10.1016/j.jcat.2018.06.031

Merk, V., Rehbock, C., Becker, F., Hagemann, U., Nienhaus, H., & Barcikowski, S. (2014). *In Situ Non-DLVO Stabilization of Surfactant-Free, Plasmonic Gold Nanoparticles: E ff ect of Hofmeister ' s Anions*.

Ministry of Economy Trade and Industry Japan. (n.d.). *Japan's Roadmap to "Beyond-Zero" Carbon.pdf*. Retrieved January 8, 2024, from https://www.meti.go.jp/english/policy/energy_environment/global_warming/roadmap/

Miranda, R., Carmo, M., Roesch Roland, & Gielen, D. (2021). *Making the breakthrough: Green hydrogen policies and technology costs*.

Nadarajah, R., Tahir, S., Landers, J., Koch, D., Semisalova, A. S., Wiemeler, J., El-Zoka, A., Kim, S. H., Utzat, D., Möller, R., Gault, B., Wende, H., Farle, M., & Gökce, B. (2020). Controlling the oxidation of magnetic and electrically conductive solid-solution iron-rhodium nanoparticles synthesized by laser ablation in liquids. *Nanomaterials*, *10*(12), 1–16. https://doi.org/10.3390/nano10122362

Nag, A., Nguyen, C. M., & Tibbetts, K. M. (2023). Heterogeneous to homogeneous Cu–Ag nanoparticles by laser reduction in liquid. *Applied Surface Science*, *610*(April 2022), 155384. https://doi.org/10.1016/j.apsusc.2022.155384

Nakano, T. (2021). Multi-dimensional Additive Manufacturing. In S. Kirihara & K. Nakata (Eds.), *Multi-dimensional Additive Manufacturing* (Issue February). Springer Singapore. https://doi.org/10.1007/978-981-15-7910-3

Nastulyavichus, A., Kudryashov, S., Ionin, A., & Gonchukov, S. (2022). Optimization of nanoparticle yield for biomedical applications at femto-, pico- and nanosecond laser ablation of thin gold films in water. *Laser Physics Letters*, *19*(4), 045603. https://doi.org/10.1088/1612-202X/ac581a

Nastulyavichus, A., Smirnov, N., & Kudryashov, S. (2022). Quantitative evaluation of LAL productivity of colloidal nanomaterials: Which laser pulse width is more productive, ergonomic, and economic? *Chinese Physics B*, *31*(7), 077803. https://doi.org/10.1088/1674-1056/ac5602

National Grid. (2023). *hydrogen colour spectrum*. National Grid. https://www.nationalgrid.com/stories/energy-explained/hydrogen-colour-spectrum

Neumeister, A., Jakobi, J., Rehbock, C., Moysig, J., & Barcikowski, S. (2014). Monophasic ligand-free alloy nanoparticle synthesis determinants during pulsed laser ablation of bulk alloy and consolidated microparticles in water. *Physical Chemistry Chemical Physics*, *16*(43), 23671–23678. https://doi.org/10.1039/c4cp03316g

Nguyen, T. B., Nguyen, T. D., Tran, T. D., & Thi, T. H. N. (2015). Laser-Induced Synthesis of Au–Ag Alloy Nanoparticles in Polyvinylpyrrolidone (C6H9NO)n Solution. *Journal of Cluster Science*, *26*(5), 1787–1799. https://doi.org/10.1007/s10876-015-0877-7

Office of the Federal Chief Sustainability. (n.d.). *Federal Sustainability*. Https://Www.Whitehouse.Gov/Ceq/News-Updates/2021/12/13/Icymi-President-Biden-Signs-Executive-Order-Catalyzing-Americas-Clean-Energy-Economy-Through-Federal-Sustainability/. https://doi.org/https://www.sustainability.gov/federalsustainabilityplan/index.html

Oseguera-Galindo, D. O., Martínez-Benítez, A., Chávez-Chávez, A., Gómez-Rosas, G., Pérez-Centeno, A., & Santana-Aranda, M. A. (2012). Effects of the confining solvent on the size distribution of silver NPs by laser ablation. *Journal of Nanoparticle Research*, *14*(9). https://doi.org/10.1007/s11051-012-1133-9

Pan, C. J., Tsai, M. C., Su, W. N., Rick, J., Akalework, N. G., Agegnehu, A. K., Cheng, S. Y., & Hwang, B. J. (2017). Tuning/exploiting Strong Metal-Support Interaction (SMSI) in Heterogeneous Catalysis. *Journal of the Taiwan Institute of Chemical Engineers*, *74*(October 2018), 154–186. https://doi.org/10.1016/j.jtice.2017.02.012

Panić, I., Cuculić, A., & Ćelić, J. (2022). Color-Coded Hydrogen: Production and Storage in Maritime Sector. *Journal of Marine Science and Engineering*, *10*(12), 1995. https://doi.org/10.3390/jmse10121995

Park, J., An, K., Hwang, Y., Park, J.-G., Noh, H.-J., Kim, J.-Y., Park, J.-H., Hwang, N.-M., & Hyeon, T. (2004). Ultra-large-scale syntheses of monodisperse nanocrystals. *Nature Materials*, *3*(12), 891–895. https://doi.org/10.1038/nmat1251

Patil, P. P., Phase, D. M., Kulkarni, S. A., Ghaisas, S. V., Kulkarni, S. K., Kanetkar, S. M., Ogale, S. B., & Bhide, V. G. (1987). Pulsed-laser – induced reactive quenching at liquid-solid interface: Aqueous oxidation of iron. *Physical Review Letters*, *58*(3), 238–241. https://doi.org/10.1103/PhysRevLett.58.238

Phenrat, T., Saleh, N., Sirk, K., Tilton, R. D., & Lowry, G. V. (2007). Aggregation and Sedimentation of Aqueous Nanoscale Zerovalent Iron Dispersions. *Environmental Science & Technology*, *41*(1), 284–290. https://doi.org/10.1021/es061349a

Pinilla-Sánchez, A., Chávez-Angel, E., Murcia-López, S., Carretero, N. M., Palardonio, S. M., Xiao, P., Rueda-García, D., Sotomayor Torres, C. M., Gómez-Romero, P., Martorell, J., & Ros, C. (2022). Controlling the electrochemical hydrogen generation and storage in graphene oxide by in-situ Raman spectroscopy. *Carbon*, *200*(May), 227–235. https://doi.org/10.1016/j.carbon.2022.08.055

Qiao, C., Usman, Z., Cao, T., Rafai, S., Wang, Z., Zhu, Y., Cao, C., & Zhang, J. (2021). High-valence Ni and Fe sites on sulfated NiFe-LDH nanosheets to enhance O-O coupling for water oxidation. *Chemical Engineering Journal*, *426*(June), 130873. https://doi.org/10.1016/j.cej.2021.130873

Qiu, C., Jiang, L., Gao, Y., & Sheng, L. (2023). Effects of oxygen-containing functional groups on carbon materials in supercapacitors: A review. *Materials and Design*, *230*, 111952. https://doi.org/10.1016/j.matdes.2023.111952

Rance, G. A., Marsh, D. H., Bourne, S. J., Reade, T. J., & Khlobystov, A. N. (2010). van der Waals Interactions between Nanotubes and Nanoparticles for Controlled Assembly of Composite Nanostructures. *ACS Nano*, *4*(8), 4920–4928. https://doi.org/10.1021/nn101287u

Rasband, W. S. (1997). *ImageJ*. U.S. National Institutes of Health, Bethesda, Maryland. http://imagej.nih.gov/ij/

Rebodos, R. L., & Vikesland, P. J. (2010). Effects of oxidation on the magnetization of nanoparticulate magnetite. *Langmuir*, *26*(22), 16745–16753. https://doi.org/10.1021/la102461z

Rehbock, C., Merk, V., Gamrad, L., Streubel, R., & Barcikowski, S. (2013). Size control of laser-fabricated surfactant-free gold nanoparticles with highly diluted electrolytes and their subsequent bioconjugation. *Physical Chemistry Chemical Physics*, *15*(9), 3057–3067. https://doi.org/10.1039/c2cp42641b

Reich, S., Schönfeld, P., Wagener, P., Letzel, A., Ibrahimkutty, S., Gökce, B., Barcikowski, S., Menzel, A., dos Santos Rolo, T., & Plech, A. (2017). Pulsed laser ablation in liquids: Impact of the bubble dynamics on particle formation. *Journal of Colloid and Interface Science*, *489*, 106–113. https://doi.org/10.1016/j.jcis.2016.08.030

Reichenberger, S., Marzun, G., Muhler, M., & Barcikowski, S. (2019). Perspective of Surfactant-Free Colloidal Nanoparticles in Heterogeneous Catalysis. *ChemCatChem*, *11*(18), 4489–4518. https://doi.org/10.1002/cctc.201900666

Resano-Garcia, A., Champmartin, S., Battie, Y., Koch, A., En Naciri, A., Ambari, A., & Chaoui, N. (2016). Highly-repeatable generation of very small nanoparticles by pulsed-laser ablation in liquids of a high-speed rotating target. *Physical Chemistry Chemical Physics*, *18*(48), 32868–32875. https://doi.org/10.1039/C6CP06511B

Roger, I., Shipman, M. A., & Symes, M. D. (2017). Earth-abundant catalysts for electrochemical and photoelectrochemical water splitting. *Nature Reviews Chemistry*, *1*. https://doi.org/10.1038/s41570-016-0003

Ros, C., Murcia-López, S., Garcia, X., Rosado, M., Arbiol, J., Llorca, J., & Morante, J. R. (2021). Facing Seawater Splitting Challenges by Regeneration with Ni–Mo–Fe Bifunctional Electrocatalyst for Hydrogen and Oxygen Evolution. *ChemSusChem*, *14*(14), 2872–2881. https://doi.org/10.1002/cssc.202100194

Sajti, C. L., Sattari, R., Chichkov, B. N., & Barcikowski, S. (2010). Gram Scale Synthesis of Pure Ceramic Nanoparticles by Laser Ablation in Liquid. *The Journal of Physical Chemistry C*, *114*(6), 2421–2427. https://doi.org/10.1021/jp906960g

Salmanion, M., & Najafpour, M. M. (2023). Oxygen-Evolution Reaction Performance of Nickel (Hydr)Oxide in Alkaline Media: Iron and Nickel Impurities. *The Journal of Physical Chemistry C*, *127*(37), 18340–18349. https://doi.org/10.1021/acs.jpcc.3c05164

Sasaki, K., & Takada, N. (2010). Liquid-phase laser ablation. *Pure and Applied Chemistry*, *82*(6), 1317–1327. https://doi.org/10.1351/PAC-CON-09-10-23

Schille, J., Schneider, L., Streek, A., Kloetzer, S., & Loeschner, U. (2016). High-throughput machining using high average power ultrashort pulse lasers and ultrafast polygon scanner. *Proc.SPIE*, *9736*, 97360R. https://doi.org/10.1117/12.2220112

Schmitz, T., Wiedwald, U., Dubs, C., & Gökce, B. (2017). Ultrasmall Yttrium Iron Garnet Nanoparticles with High Coercivity at Low Temperature Synthesized by Laser Ablation and Fragmentation of Pressed Powders. *ChemPhysChem*, *18*(9), 1125–1132. https://doi.org/10.1002/cphc.201601183

Semaltianos, N. G., Hendry, E., Chang, H., & Wears, M. L. (2014). Laser ablation of a bulk Cr target in liquids for nanoparticle synthesis. *RSC Advances*, *4*(92), 50406–50411. https://doi.org/10.1039/c4ra08393h

Shankar Naik, S., Theerthagiri, J., Nogueira, F. S., Lee, S. J., Min, A., Kim, G. A., Maia, G., Pinto, L. M. C., & Choi, M. Y. (2023). Dual-Cation-Coordinated CoFe-Layered Double-Hydroxide Nanosheets Using the Pulsed Laser Ablation Technique for Efficient Electrochemical Water Splitting: Mechanistic Screening by In Situ/Operando Raman and Density Functional Theory Calculations. *ACS Catalysis*, *13*(2), 1477–1491. https://doi.org/10.1021/acscatal.2c05017

Shen, G., Mao, H., Hemley, R. J., Duffy, T. S., & Rivers, M. L. (1998). Melting and crystal structure of iron at high pressures and temperatures. *Geophysical Research Letters*, *25*(3), 373–376. https://doi.org/10.1029/97GL03776

Shih, C. Y., Shugaev, M. V., Wu, C., & Zhigilei, L. V. (2020). The effect of pulse duration on nanoparticle generation in pulsed laser ablation in liquids: Insights from large-scale atomistic simulations. *Physical Chemistry Chemical Physics*, *22*(13), 7077–7099. https://doi.org/10.1039/d0cp00608d

Shih, C.-Y., Streubel, R., Heberle, J., Letzel, A., Shugaev, M. V., Wu, C., Schmidt, M., Gökce, B., Barcikowski, S., & Zhigilei, L. V. (2018). Two mechanisms of nanoparticle generation in picosecond laser ablation in liquids: the origin of the bimodal size distribution. *Nanoscale*, *10*(15), 6900–6910. https://doi.org/10.1039/C7NR08614H

Shih, C.-Y., Wu, C., Shugaev, M. V, & Zhigilei, L. V. (2017). Atomistic modeling of nanoparticle generation in short pulse laser ablation of thin metal films in water. *Journal of Colloid and Interface Science*, *489*, 3–17. https://doi.org/10.1016/j.jcis.2016.10.029

Shinagawa, T., Garcia-Esparza, A. T., & Takanabe, K. (2015). Insight on Tafel slopes from a microkinetic analysis of aqueous electrocatalysis for energy conversion. *Scientific Reports*, *5*(May), 1–21. https://doi.org/10.1038/srep13801

Singh, R., & Soni, R. K. (2014). Laser synthesis of aluminium nanoparticles in biocompatible polymer solutions. *Applied Physics A: Materials Science and Processing*, *116*(2), 689–701. https://doi.org/10.1007/s00339-014-8487-z

Singh, S. C., Kotnala, R. K., & Gopal, R. (2015). Room temperature ferromagnetism in liquid-phase pulsed laser ablation synthesized nanoparticles of nonmagnetic oxides. *Journal of Applied Physics*, *118*(6), 0–7. https://doi.org/10.1063/1.4928312

Smirnov, N. A., Kudryashov, S. I., Rudenko, A. A., Nastulyavichus, A. A., & Ionin, A. A. (2022). Ablation efficiency of gold at fs/ps laser treatment in water and air. *Laser Physics Letters*, *19*(2), 026001. https://doi.org/10.1088/1612-202X/ac46ab

Smith, R. D. L., Prévot, M. S., Fagan, R. D., Trudel, S., & Berlinguette, C. P. (2013). Water Oxidation Catalysis: Electrocatalytic Response to Metal Stoichiometry in Amorphous Metal Oxide Films Containing Iron, Cobalt, and Nickel. *Journal of the American Chemical Society*, *135*(31), 11580–11586. https://doi.org/10.1021/ja403102j

Soliman, W., Nakano, T., Takada, N., & Sasaki, K. (2010). Modification of Rayleigh-Plesset theory for reproducing dynamics of cavitation bubbles in liquid-phase laser ablation. *Japanese Journal of Applied Physics*, *49*(11). https://doi.org/10.1143/JJAP.49.116202

Song, F., Bai, L., Moysiadou, A., Lee, S., Hu, C., Liardet, L., & Hu, X. (2018). Transition Metal Oxides as Electrocatalysts for the Oxygen Evolution Reaction in Alkaline Solutions: An Application-Inspired Renaissance. *Journal of the American Chemical Society*, *140*(25), 7748–7759. https://doi.org/10.1021/jacs.8b04546

Song, F., & Hu, X. (2014). Exfoliation of layered double hydroxides for enhanced oxygen evolution catalysis. *Nature Communications*, *5*. https://doi.org/10.1038/ncomms5477

Spanos, I., Masa, J., Zeradjanin, A., & Schlögl, R. (2021). The Effect of Iron Impurities on Transition Metal Catalysts for the Oxygen Evolution Reaction in Alkaline Environment: Activity Mediators or Active Sites? *Catalysis Letters*, *151*(7), 1843–1856. https://doi.org/10.1007/s10562-020-03478-4

Stevens, M. B., Trang, C. D. M., Enman, L. J., Deng, J., & Boettcher, S. W. (2017). Reactive Fe-Sites in Ni/Fe (Oxy)hydroxide Are Responsible for Exceptional Oxygen Electrocatalysis Activity. *Journal of the American Chemical Society*, *139*(33), 11361–11364. https://doi.org/10.1021/jacs.7b07117

Streubel, R., Bendt, G., & Gökce, B. (2016). Pilot-scale synthesis of metal nanoparticles by high-speed pulsed laser ablation in liquids. *Nanotechnology*, *27*(20), 205602. https://doi.org/10.1088/0957-4484/27/20/205602

Sylvestre, J. P., Poulin, S., Kabashin, A. V., Sacher, E., Meunier, M., & Luong, J. H. T. (2004). Surface chemistry of gold nanoparticles produced by laser ablation in aqueous media. *Journal of Physical Chemistry B*, *108*(43), 16864–16869. https://doi.org/10.1021/jp047134

Tang, C., Wang, H., Wang, H., Zhang, Q., Tian, G., Nie, J., & Wei, F. (2015). Spatially Confined Hybridization of Nanometer-Sized NiFe Hydroxides into Nitrogen-Doped Graphene Frameworks Leading to Superior Oxygen Evolution Reactivity. *Advanced Materials*, *27*(30), 4516–4522. https://doi.org/10.1002/adma.201501901

Tateno, S., Hirose, K., Komabayashi, T., Ozawa, H., & Ohishi, Y. (2012). The structure of Fe-Ni alloy in Earth's inner core. *Geophysical Research Letters*, *39*(12), n/a-n/a. https://doi.org/10.1029/2012GL052103

Tomko, J., Naddeo, J. J., Jimenez, R., Tan, Y., Steiner, M., Fitz-Gerald, J. M., Bubb, D. M., & O'Malley, S. M. (2015). Size and polydispersity trends found in gold nanoparticles synthesized by laser ablation in liquids. *Physical Chemistry Chemical Physics*, *17*(25), 16327–16333. https://doi.org/10.1039/c5cp01965f

Torchio, R., Boccato, S., Miozzi, F., Rosa, A. D., Ishimatsu, N., Kantor, I., Sévelin-Radiguet, N., Briggs, R., Meneghini, C., Irifune, T., & Morard, G. (2020). Melting Curve and Phase Relations of Fe-Ni Alloys: Implications for the Earth's Core Composition. *Geophysical Research Letters*, *47*(14). https://doi.org/10.1029/2020GL088169

Torres-Mendieta, R., Ventura-Espinosa, D., Sabater, S., Lancis, J., Mínguez-Vega, G., & Mata, J. A. (2016). In situ decoration of graphene sheets with gold nanoparticles synthetized by pulsed laser ablation in liquids. *Scientific Reports*, *6*(1), 30478. https://doi.org/10.1038/srep30478

Trotochaud, L., Young, S. L., Ranney, J. K., & Boettcher, S. W. (2014). Nickel-Iron oxyhydroxide oxygen-evolution electrocatalysts: The role of intentional and incidental iron incorporation. *Journal of the American Chemical Society*, *136*(18), 6744–6753. https://doi.org/10.1021/ja502379c

Tsubonouchi, Y., Zahran, Z. N., Chandra, D., Hoshino, N., & Yagi, M. (2024). Prominent development of Ni-based oxygen-evolving electrocatalysts for water splitting. *Catalysis Science & Technology*, *14*(12), 3287–3319. https://doi.org/10.1039/D4CY00066H

Tsuji, T. (2002). Preparation of silver nanoparticles by laser ablation in solution.pdf. *Applied Surface Science*, *202*, 80.

Tsuji, T., Iryo, K., Nishimura, Y., & Tsuji, M. (2001). Preparation of metal colloids by a laser ablation technique in solution: Influence of laser wavelength on the ablation efficiency (II). *Journal of Photochemistry and Photobiology A: Chemistry*, *145*(3), 201–207. https://doi.org/10.1016/S1010-6030(01)00583-4

Tsuji, T., Thang, D. H., Okazaki, Y., Nakanishi, M., Tsuboi, Y., & Tsuji, M. (2008). Preparation of silver nanoparticles by laser ablation in polyvinylpyrrolidone solutions. *Applied Surface Science*, *254*(16), 5224–5230. https://doi.org/10.1016/j.apsusc.2008.02.048

Twight, L., Tonsberg, A., Samira, S., Velinkar, K., Dumpert, K., Ou, Y., Wang, L., Nikolla, E., & Boettcher, S. W. (2024). Trace Fe activates perovskite nickelate OER catalysts in alkaline media via redox-active surface Ni species formed during electrocatalysis. *Journal of Catalysis*, *432*(October 2023), 115443. https://doi.org/10.1016/j.jcat.2024.115443

Tymoczko, A., Kamp, M., Rehbock, C., Kienle, L., Cattaruzza, E., Barcikowski, S., & Amendola, V. (2019). One-step synthesis of Fe–Au core–shell magnetic-plasmonic nanoparticles driven by interface energy minimization. *Nanoscale Horizons*, *4*(6), 1326–1332. https://doi.org/10.1039/C9NH00332K

United Nations. (2023). *For a livable climate: Net-zero commitments must be backed by credible action*. Net Zero Coalition. https://www.un.org/en/climatechange/net-zero-coalition

van der Heijden, O., Park, S., Vos, R. E., Eggebeen, J. J. J., & Koper, M. T. M. (2024). Tafel Slope Plot as a Tool to Analyze Electrocatalytic Reactions. *ACS Energy Letters*, *9*(4), 1871–1879. https://doi.org/10.1021/acsenergylett.4c00266

Viau, G., Collière, V., Lacroix, L. M., & Shafeev, G. A. (2011). Internal structure of Al hollow nanoparticles generated by laser ablation in liquid ethanol. *Chemical Physics Letters*, *501*(4–6), 419–422. https://doi.org/10.1016/j.cplett.2010.11.032

Vij, V., Sultan, S., Harzandi, A. M., Meena, A., Tiwari, J. N., Lee, W.-G., Yoon, T., & Kim, K. S. (2017). Nickel-Based Electrocatalysts for Energy-Related Applications: Oxygen Reduction, Oxygen Evolution, and Hydrogen Evolution Reactions. *ACS Catalysis*, *7*(10), 7196–7225. https://doi.org/10.1021/acscatal.7b01800

Waag, F., Streubel, R., Gökce, B., & Barcikowski, S. (2021). Synthesis of gold, platinum, and gold-platinum alloy nanoparticle colloids with high-power megahertz-repetition-rate lasers: the importance of the beam guidance method. *Applied Nanoscience (Switzerland)*, *11*(4), 1303–1312. https://doi.org/10.1007/s13204-021-01693-y

Wagener, P., Jakobi, J., Rehbock, C., Chakravadhanula, V. S. K., Thede, C., Wiedwald, U., Bartsch, M., Kienle, L., & Barcikowski, S. (2016). Solvent-surface interactions control the phase structure in laser-generated iron-gold core-shell nanoparticles. *Scientific Reports*, *6*(March), 1–12. https://doi.org/10.1038/srep23352

Wagener, P., Schwenke, A., Chichkov, B. N., & Barcikowski, S. (2010). Pulsed laser ablation of zinc in tetrahydrofuran: Bypassing the cavitation bubble. *Journal of Physical Chemistry C*, *114*(17), 7618–7625. https://doi.org/10.1021/jp911243a

Wang, C., Yang, F., & Feng, L. (2023). Recent advances in iridium-based catalysts with different dimensions for the acidic oxygen evolution reaction. *Nanoscale Horizons*, *8*(9), 1174–1193. https://doi.org/10.1039/D3NH00156C

Wang, C., Yang, H., Zhang, Y., & Wang, Q. (2019). NiFe Alloy Nanoparticles with hcp Crystal Structure Stimulate Superior Oxygen Evolution Reaction Electrocatalytic Activity. *Angewandte Chemie International Edition*, *58*(18), 6099–6103. https://doi.org/10.1002/anie.201902446

Wang, D., Li, Q., Han, C., Lu, Q., Xing, Z., & Yang, X. (2019). Atomic and electronic modulation of self-supported nickel-vanadium layered double hydroxide to accelerate water splitting kinetics. *Nature Communications*, *10*(1), 3899. https://doi.org/10.1038/s41467-019-11765-x

Wang, J., & Lian, Y. (2023). The Self-Supporting NiMn-LDHs/rGO/NF Composite Electrode Showing Much Enhanced Electrocatalytic Performance for Oxygen Evolution Reaction. *Catalysts*, *13*(6). https://doi.org/10.3390/catal13061012

Wang, S., Lu, A., & Zhong, C. J. (2021). Hydrogen production from water electrolysis: role of catalysts. *Nano Convergence*, *8*(1). https://doi.org/10.1186/s40580-021-00254-x

Wang, Y., Wang, X., Min, Y., Li, Q., & Xu, Q. (2023). Investigation of Oxygen Evolution Performance of Highly Efficient Water Electrolysis Catalyst: NiFe LDH/BPene. *Processes*, *11*(7), 2179. https://doi.org/10.3390/pr11072179

Wei, C., & Xu, Z. J. (2018). The Comprehensive Understanding of 10 mA cm −2geo as an Evaluation Parameter for Electrochemical Water Splitting. *Small Methods*, *2*(11), 3–5. https://doi.org/10.1002/SMTD.201800168

Wei, Y., Sun, L., Wang, M., Hong, J., Zou, L., Liu, H., Wang, Y., Zhang, M., Liu, Z., Li, Y., Horike, S., Suenaga, K., & Xu, Q. (2020). Fabricating Dual-Atom Iron Catalysts for Efficient Oxygen Evolution Reaction: A Heteroatom Modulator Approach. *Angewandte Chemie International Edition*, *59*(37), 16013–16022. https://doi.org/10.1002/anie.202007221

Xiao, H., Shin, H., & Goddard, W. A. (2018). Synergy between Fe and Ni in the optimal performance of (Ni,Fe)OOH catalysts for the oxygen evolution reaction. *Proceedings of the National Academy of Sciences of the United States of America*, *115*(23), 5872–5877. https://doi.org/10.1073/pnas.1722034115

Yan, Q., Wei, T., Wu, J., Yang, X., Zhu, M., Cheng, K., Ye, K., Zhu, K., Yan, J., Cao, D., Wang, G., & Pan, Y. (2018). Self-Supported FeNi-P Nanosheets with Thin Amorphous Layers for Efficient Electrocatalytic Water Splitting. *ACS Sustainable Chemistry and Engineering*, *6*(8), 9640–9648. https://doi.org/10.1021/acssuschemeng.7b04743

Yan, Z., Bao, R., & Chrisey, D. B. (2011). Generation of Ag2O micro-/nanostructures by pulsed excimer laser ablation of ag in aqueous solutions of polysorbate 80. *Langmuir*, *27*(2), 851–855. https://doi.org/10.1021/la104331p

Yang, G. W. (2007). Laser ablation in liquids: Applications in the synthesis of nanocrystals. *Progress in Materials Science*, *52*(4), 648–698. https://doi.org/10.1016/j.pmatsci.2006.10.016

Yang, Z., Bao, H., Dai, L., Zhang, H., & Lu, J. (2023). Experimental investigation of nanosecond laser-induced shock waves in water using multiple excitation beams. *Optics Express*, *31*(13), 21845. https://doi.org/10.1364/OE.492613

Yeap, S. P., Lim, J. K., Ooi, B. S., & Ahmad, A. L. (2017). Agglomeration, colloidal stability, and magnetic separation of magnetic nanoparticles: collective influences on environmental engineering applications. *Journal of Nanoparticle Research*, *19*(11), 368. https://doi.org/10.1007/s11051-017-4065-6

Zaharieva, I., Chernev, P., Risch, M., Klingan, K., Kohlhoff, M., Fischer, A., & Dau, H. (2012). Electrosynthesis, functional, and structural characterization of a water-oxidizing manganese oxide. *Energy and Environmental Science*, *5*(5), 7081–7089. https://doi.org/10.1039/c2ee21191b

Zeng, J., Huang, J., Lu, W., Wang, X., Wang, B., Zhang, S., & Hou, J. (2007). Necklace-like Noble-Metal Hollow Nanoparticle Chains: Synthesis and Tunable Optical Properties. *Advanced Materials*, *19*(16), 2172–2176. https://doi.org/10.1002/adma.200602440

Zhang, D., Choi, W., Jakobi, J., Kalus, M. R., Barcikowski, S., Cho, S. H., & Sugioka, K. (2018). Spontaneous shape alteration and size separation of surfactant-free silver particles synthesized by laser ablation in acetone during long-period storage. *Nanomaterials*, *8*(7). https://doi.org/10.3390/nano8070529

Zhang, D., Gökce, B., & Barcikowski, S. (2017). Laser Synthesis and Processing of Colloids: Fundamentals and Applications. *Chemical Reviews*, *117*(5), 3990–4103. https://doi.org/10.1021/acs.chemrev.6b00468

Zhang, D., Li, Z., & Sugioka, K. (2021). Laser ablation in liquids for nanomaterial synthesis: Diversities of targets and liquids. *JPhys Photonics*, *3*(4). https://doi.org/10.1088/2515-7647/ac0bfd

Zhang, D., Liu, J., Li, P., Tian, Z., & Liang, C. (2017). Recent Advances in Surfactant-Free, Surface-Charged, and Defect-Rich Catalysts Developed by Laser Ablation and Processing in Liquids. *ChemNanoMat*, *3*(8), 512–533. https://doi.org/10.1002/cnma.201700079

Zhang, D., & Wada, H. (2021). Laser Ablation in Liquids for Nanomaterial Synthesis and Applications. In *Handbook of Laser Micro- and Nano-Engineering* (Vol. 3, Issue 4, pp. 1–35). Springer International Publishing. https://doi.org/10.1007/978-3-319-69537-2_30-1

Zhang, D., Zhang, C., Liu, J., Chen, Q., Zhu, X., & Liang, C. (2019). Carbon-Encapsulated Metal/Metal Carbide/Metal Oxide Core-Shell Nanostructures Generated by Laser Ablation of Metals in Organic Solvents. *ACS Applied Nano Materials*, *2*(1), 28–39. https://doi.org/10.1021/acsanm.8b01541

Zhang, H., Liu, J., Ye, Y., Tian, Z., & Liang, C. (2013). Synthesis of Mn-doped α-Ni(OH)2 nanosheets assisted by liquid-phase laser ablation and their electrochemical properties. *Physical Chemistry Chemical Physics*, *15*(15), 5684–5690. https://doi.org/10.1039/c3cp50248a

Zhang, J., Su, B.-J., Wu, K.-H., Xia, Q., Knibbe, R., & Gentle, I. (2024). Low-coordinated surface nickel oxide as electrocatalyst for efficient water oxidation. *Journal of Catalysis*, *429*(December 2023), 115278. https://doi.org/10.1016/j.jcat.2023.115278

Zhang, L., Si, R., Liu, H., Chen, N., Wang, Q., Adair, K., Wang, Z., Chen, J., Song, Z., Li, J., Banis, M. N., Li, R., Sham, T.-K., Gu, M., Liu, L.-M., Botton, G. A., & Sun, X. (2019). Atomic layer deposited Pt-Ru dual-metal dimers and identifying their active sites for hydrogen evolution reaction. *Nature Communications*, *10*(1), 4936. https://doi.org/10.1038/s41467-019-12887-y

Zhang, X., Xu, H., Li, X., Li, Y., Yang, T., & Liang, Y. (2016). Facile Synthesis of Nickel-Iron/Nanocarbon Hybrids as Advanced Electrocatalysts for Efficient Water Splitting. *ACS Catalysis*, *6*(2), 580–588. https://doi.org/10.1021/acscatal.5b02291

Zhao, Y., Vargas-Barbosa, N. M., Hernandez-Pagan, E. A., & Mallouk, T. E. (2011). Anodic Deposition of Colloidal Iridium Oxide Thin Films from Hexahydroxyiridate(IV) Solutions. *Small*, *7*(14), 2087–2093. https://doi.org/10.1002/smll.201100485

Zhao, Z., Zhang, B., Fan, D., Wang, Y., Yang, H., Huang, K., Pan, X., Zhang, R., Tang, H., & Lei, M. (2022). Tailoring manganese oxide nanoplates enhances oxygen evolution catalysis in acid. *Journal of Catalysis*, *405*, 265–272. https://doi.org/10.1016/j.jcat.2021.12.009

Zhou, F., Zhou, Y., Liu, G. G., Wang, C. T., & Wang, J. (2021). Recent advances in nanostructured electrocatalysts for hydrogen evolution reaction. *Rare Metals*, *40*(12), 3375–3405. https://doi.org/10.1007/s12598-021-01735-y

Zhu, G., Wang, S., Cheng, W., Wang, G., Liu, W., & Ren, Y. (2019). Investigation on the Surface Properties of 5A12 Aluminum Alloy after Nd: YAG Laser Cleaning. *Coatings*, *9*(9), 578. https://doi.org/10.3390/coatings9090578

7 Appendix

7.1 Study I

Khairani, I. Y.; Lin, Q.; Landers, J.; Salamon, S.; Doñate-Buendía, C.; Karapetrova, E.; Wende, H.; Zangari, G.; Gökce, B. Solvent Influence on the Magnetization and Phase of Fe-Ni Alloy Nanoparticles Generated by Laser Ablation in Liquids. Nanomaterials 2023, 13 (2), 227, doi:10.3390/nano13020227.

CRediT Authorship Contribution of I.Y.K.: Conceptualization, methodology, investigation, visualization, writing – original draft preparation, writing – review and editing.

nanomaterials

MDPI

Article

Solvent Influence on the Magnetization and Phase of Fe-Ni Alloy Nanoparticles Generated by Laser Ablation in Liquids

Inna Y. Khairani [1], Qiyuan Lin [2], Joachim Landers [3], Soma Salamon [3], Carlos Doñate-Buendía [1], Evguenia Karapetrova [4], Heiko Wende [3], Giovanni Zangari [2] and Bilal Gökce [1,*]

[1] Chair of Materials Science and Additive Manufacturing, School of Mechanical Engineering and Safety Engineering, University of Wuppertal, 42119 Wuppertal, Germany
[2] Department of Materials Science and Engineering, University of Virginia, Charlottesville, VA 22903, USA
[3] Faculty of Physics and Center for Nanointegration Duisburg-Essen (CENIDE), University of Duisburg-Essen, 47057 Duisburg, Germany
[4] Advanced Photon Source, Argonne National Laboratory, Argonne, IL 60439, USA
* Correspondence: goekce@uni-wuppertal.de

Abstract: The synthesis of bimetallic iron-nickel nanoparticles with control over the synthesized phases, particle size, surface chemistry, and oxidation level remains a challenge that limits the application of these nanoparticles. Pulsed laser ablation in liquid allows the properties tuning of the generated nanoparticles by changing the ablation solvent. Organic solvents such as acetone can minimize nanoparticle oxidation. Yet, economical laboratory and technical grade solvents that allow cost-effective production of FeNi nanoparticles contain water impurities, which are a potential source of oxidation. Here, we investigated the influence of water impurities in acetone on the properties of FeNi nanoparticles generated by pulsed laser ablation in liquids. To remove water impurities and produce "dried acetone", cost-effective and reusable molecular sieves (3 Å) are employed. The results show that the $Fe_{50}Ni_{50}$ nanoparticles' properties are influenced by the water content of the solvent. The metastable HCP FeNi phase is found in NPs prepared in acetone, while only the FCC phase is observed in NPs formed in water. Mössbauer spectroscopy revealed that the FeNi nanoparticles oxidation in dried acetone is reduced by 8% compared to acetone. The high-field magnetization of $Fe_{50}Ni_{50}$ nanoparticles in water is the highest, 68 Am^2/kg, followed by the nanoparticles obtained after ablation in acetone without water impurities, 59 Am^2/kg, and acetone, 52 Am^2/kg. The core-shell structures formed in these three liquids are also distinctive, demonstrating that a core-shell structure with an outer oxide layer is formed in water, while carbon external layers are obtained in acetone without water impurity. The results confirm that the size, structure, phase, and oxidation of FeNi nanoparticles produced by pulsed laser ablation in liquids can be modified by changing the solvent or just reducing the water impurities in the organic solvent.

Keywords: iron-nickel alloy; core-shell nanoalloys; nickel ferrite; hexagonal closed packed phase; carbon shell; laser synthesis of colloids

Citation: Khairani, I.Y.; Lin, Q.; Landers, J.; Salamon, S.; Doñate-Buendía, C.; Karapetrova, E.; Wende, H.; Zangari, G.; Gökce, B. Solvent Influence on the Magnetization and Phase of Fe-Ni Alloy Nanoparticles Generated by Laser Ablation in Liquids. *Nanomaterials* **2023**, *13*, 227. https://doi.org/10.3390/nano13020227

Academic Editor: Vincenzo Amendola

Received: 6 December 2022
Revised: 28 December 2022
Accepted: 28 December 2022
Published: 4 January 2023

1. Introduction

Iron nickel alloys are one of the most studied magnetic materials due to the abundance of their constituting elements on Earth [1,2] and owing to the interesting properties exhibited depending on their atomic ratio. For example, Invar ($Fe_{64}Ni_{36}$) exhibits very little thermal expansion (almost zero) over a wide temperature variation, while Permalloy ($Fe_{20}Ni_{80}$) offers a notably high magnetic permeability, low coercivity, and small magnetostriction [3–5]. Due to these interesting properties, iron-nickel alloys are employed in various key technologies such as transformers [6], magnetic actuators [7], magnetic sensors [8], electromagnetic shielding [9], spintronics [4,10], and catalysis [11–13]. The equiatomic iron-nickel alloy ($Fe_{50}Ni_{50}$), in particular, gained popularity as an electrocatalyst for the oxygen evolution reaction (OER) [12,14] and as a potential candidate for a

permanent magnet after the discovery of the high-coercive tetrataenite mineral with $L1_0$ structure found in a meteorite [2,15]. In both cases, the high material abundance of the alloy constituent elements on Earth represents a fundamental advantage, envisioned to overcome the price and supply chain problems associated with the current rare-earth-based OER catalysts (RuO_2 and IrO_2) and permanent magnets (NdFeB) in strategic technologies, such as electric mobility and energy storage. Other than the atomic ratio, the iron-nickel alloy particle size is also a crucial parameter defining their properties and performance in certain applications, especially for the catalytic activity of $Fe_{50}Ni_{50}$ alloy in the OER process [13], where nanosized materials are desired. By reducing the size to the nanometer range, especially below 10 nm, the specific surface area of the $Fe_{50}Ni_{50}$ catalyst is significantly increased, thus exposing more of its active sites for the reactions to take place. In addition, the recent report on the non-cubic symmetry in $Fe_{50}Ni_{50}$ nanoparticles [16] sparks the possibility of employing nanosized $Fe_{50}Ni_{50}$ as a rare-earth-free alternative to permanent magnets. These findings highlight the relevance of understanding and controlling the formation of $Fe_{50}Ni_{50}$ nanoparticles and explore novel synthesis techniques that allow $Fe_{50}Ni_{50}$ nanoparticles' phase control.

Conventional fabrication methods of $Fe_{50}Ni_{50}$ nanoparticles (NPs) include chemical reduction and gas condensation routes. The chemical reduction of the iron and nickel salts with hydrazine in the presence of polyvinylpyrrolidone (PVP) resulted in face-centered cubic (FCC) $Fe_{50}Ni_{50}$ with an average diameter of 29 nm [17], and 96 nm without PVP [18]. Gas condensation of iron-nickel alloy in a helium atmosphere was sought, but oxidation took place on the surface of the particle after exposure to oxygen, resulting in the formation of core-shell NPs with FeNi γ-phase and oxides of γ-Fe_2O_3 or Fe_3O_4. These two methods, unfortunately, do not follow the green chemistry principles [19] due to the multi-step processes and the use of hazardous materials and inert gases to reduce oxidation. Meanwhile, pulsed laser ablation in liquid (PLAL) offers a one-step method to produce NPs directly in the desired liquid and avoids the generation of by-products, hence removing purification steps and the generation of extra chemical waste [20]. This technique does not require high vacuum or temperature conditions, making it easily implementable and transferable to industrial environments [21]. PLAL is based on the ablation of the bulk target in the desired liquid providing the versatility to tune the laser parameters and the ablation liquid to influence the temperature, pressure, and surrounding media [22]. By changing the liquid employed for PLAL, properties such as the composition and phase of the produced NPs can be modified [23].

Another NP property that is influenced by the liquid employed in the PLAL is the NP oxidation. Due to their small size and large surface area, NPs are prone to oxidation upon exposure to oxygen or oxidizing agents. In the PLAL, it is reported that the NP oxidation is influenced by the redox activity of the target material [24] and the choice of the ablation liquid [23]. For example, almost 100% of the surface of laser-generated Ti in water is oxidized, while less than 5% of the gold surface is oxidized [24]. For the ablation liquid, complete or partial oxidation of the NPs is observed in the ablation of Ti and Mn in water, which results in the generation of TiO_2 [25] and Mn_3O_4 [26] NPs, respectively. NP oxidation might be purposely performed in some contexts where oxide NPs are desired, such as the generation of TiO_2 by ablating Ti target immersed in water. However, in the cases where oxidation needs to be avoided, organic solvents such as acetone are known to reduce the oxidation of laser-generated NPs [27]. However, the oxidation itself is caused by the exposure of NPs inside the cavitation bubble to the oxygen species generated from the breakdown of liquid or gas in the nearby vicinity of the ablation spot; hence, all species with oxygen atoms might contribute to the oxidation of the NPs, including dissolved oxygen gas. To investigate this matter, Marzun et al. [28] ablated Cu in different ablation liquids, i.e., H_2O (H_2O_{air}), H_2O purged with Ar gas (H_2O_{ar}), and acetone. They reported the formation of Cu oxides in both H_2O_{air} and H_2O_{ar}, with H_2O_{air} having a higher oxidation level and amorphous phase in acetone. This indicates that not only the dissolved oxygen gases in the water contribute to the Cu oxidation, but also the water itself. Meanwhile, acetone

with technical grade or laboratory grade, even with ACS reagent and HPLC grades, still contains water impurity to some extent (≤0.5%) [29,30], which contributes to the oxidation of the produced NPs.

In this study, the influence of water removal in acetone using molecular sieves on the oxidation level of the laser-generated $Fe_{50}Ni_{50}$ NPs is investigated. A molecular sieve is an adsorbent with three-dimensional frameworks of alumina-silicate, which is capable of reducing the water content down to 0.001% [31,32]. The molecular sieves provide an inexpensive and easy way to remove water from acetone, complying with the green chemistry principle due to its reusability. The removal of water in the organic solvents is not only intended to reduce the oxidation but also to directly encapsulate the NPs in a carbon shell during the PLAL synthesis that enhances their catalytic activity [33,34]. In addition to reducing the oxidation level and altering the shell formation, the generation of the non-cubic metastable hexagonal closed packed (HCP) in the organic solvents was investigated. It has been proposed that non-cubic phases might be used as a precursor to generating FeNi with $L1_0$ structure [35], but the suggested methods to fabricate the non-cubic FeNi involve the use of high-pressure and high-temperature conditions such as in the diamond anvil cell (DAC) [36] or high-strain process [35]. Here, we propose PLAL as a method to produce the non-cubic HCP FeNi phase at room conditions, taking advantage of the locally high-pressure and -temperature conditions achieved by the high-intensity laser interaction with the target surface and surrounding liquid.

2. Materials and Methods

2.1. $Fe_{50}Ni_{50}$ Colloidal Nanoparticles Production

A picosecond laser Nd:YAG with a wavelength of 1064 nm, a pulse duration of 10 ps, a power of 8 W, a repetition rate of 100 kHz, a raw beam diameter of 2 mm, and a pulse energy of 80 µJ was employed to produce nanoparticles by PLAL (Figure 1). The laser beam was focused on the immersed (6 mm liquid layer) equiatomic FeNi alloy target by a galvanometric scanner coupled with an f-theta lens (focal length of 100 mm) following an Archimedean spiral pattern (6 mm diameter) with a speed of 2 m/s. The beam radius and peak fluence at the processing plane were 65 µm and 1.2 J/cm^2, respectively. To avoid shielding of the laser beam by the produced nanoparticles, the liquid was pumped by a peristaltic pump at a flow rate of 150 mL/min (calibrated before the experiments of each liquid). The investigated liquids are distilled water, acetone, and "dried" acetone (obtained by immersing molecular sieves type 3 Å for 24 h to capture water molecules in acetone). The FeNi samples ablated in different liquids will be further referred to as FeNi in water, FeNi in acetone, and FeNi in dried acetone, respectively. All colloids have a similar absorbance value at the laser wavelength as shown in Figure S1. To dry the colloids and obtain nanopowders suitable for characterization, we performed magnetic separation using a permanent magnet (NdFeB) followed by liquid evaporation using an exhaust fan.

2.2. Analytical Methods

The generated FeNi NPs colloids were analyzed by transmission electron microscopy (TEM, JEOL JEM-2200FS, 200 kV, ZrO_2/W emitter) and energy dispersive X-ray spectroscopy (EDX) to determine the size distribution, morphology, elemental composition, and oxide formation of the NPs. The sample was drop-casted on a copper grid with lacey carbon coating and was measured within one week after production to ensure minimum particle growth and oxidation due to aging.

Synchrotron X-ray diffraction (SXRD) was used to analyze the phase of the produced NPs qualitatively (using the peak matching technique) and quantitively (using the Rietveld refinement technique). Measurements were carried out at the 33-BM-C beamline of the Advanced Photon Source (APS) at the Argonne National Laboratory, United States with a beam wavelength of 0.77 Å. Since a wavelength of 0.77 Å was employed, the 2θ value is shifted to a lower degree compared to the standard 1.54 Å wavelength. The measurements were performed using the transmission (i.e., Debye-Scherrer) geometry. The colloids were

sealed in Special Glass 10 capillaries (Hampton Research Corp.) by Beeswax (Hampton Research Corp.). The NPs generated in water were transferred to dried acetone to mitigate post-synthesis particle aging (i.e., oxidation and particle growth) before being loaded into capillaries for SXRD measurements.

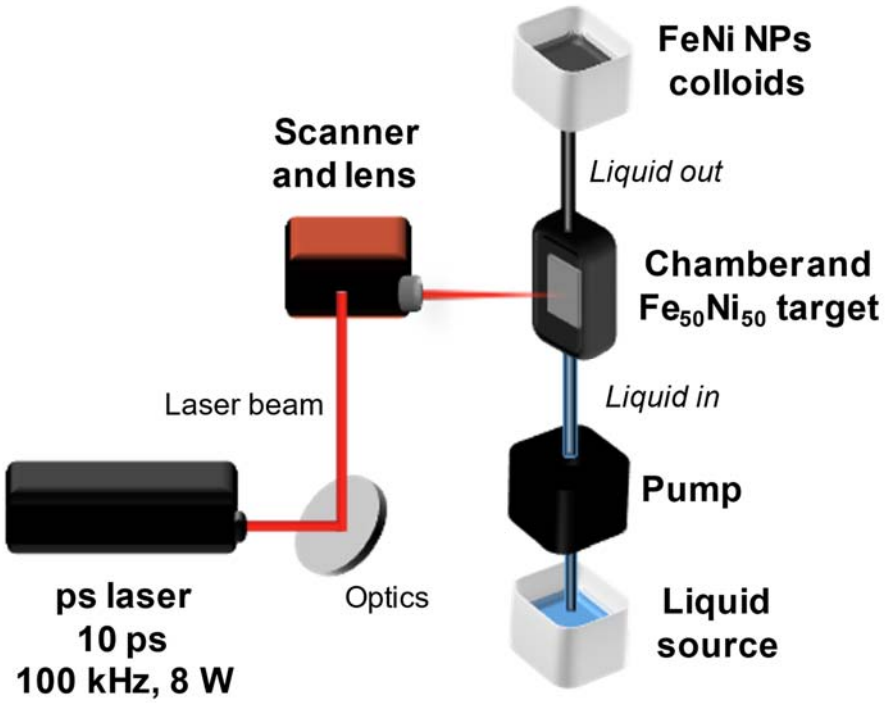

Figure 1. Schematic illustration of pulsed laser ablation in liquid using a flow chamber. The selected liquid flowed through the ablation chamber from the bottom to the top by a pump while the ablation took place. A $Fe_{50}Ni_{50}$ target was placed perpendicular to the incoming laser beam.

Mössbauer spectroscopy was employed to determine the oxidation level and magnetic structure of the FeNi samples in acetone and dried acetone. Spectra of both powder and colloid samples were recorded in transmission geometry, with the latter being placed in an airtight sample container of appropriate geometry. A ^{57}Co(Rh) radiation source was used, mounted on a constant-acceleration driving unit (WissEl GmbH), with low temperatures down to 4.3 K being achieved via a closed-cycle cryostat (Lake Shore Cryotronics). Spectra measured in external magnetic fields up to 8 T were recorded using a magnet cryostat (Oxford Instruments). Subspectra of magnetically ordered phases have been reproduced using hyperfine field distributions; isomer shifts are given relative to α-Fe at room temperature.

Nanoparticle magnetic behavior was studied using vibrating sample magnetometry (PPMS DynaCool, Quantum Design). Field-dependent magnetization loops M(H) were recorded at temperatures between 4.3–300 K and a magnetic field range of ±9 T.

3. Results and Discussion

3.1. Crystallographic Phases

To determine the influence of different liquids on the phase formation of FeNi NPs, XRD phase analysis was performed. The SXRD profiles of FeNi NPs in dried acetone, acetone, and water are presented in Figure 2, and the complete indexing can be found in the supplementary (Figure S2). The FeNi NPs generated in water (Figure 2) show the diffraction peaks of the face-centered cubic (FCC) FeNi and the spinel $NiFe_2O_4$ structure. Meanwhile, the FeNi NPs generated in acetone and dried acetone (Figure 2) consist of the hexagonal closed-packed (HCP) FeNi phase in addition to the FCC FeNi phases and the spinel $NiFe_2O_4$ phases. To quantify the weight fraction (wt%) of the HCP phase, Rietveld refinement was performed (Figure S3) and the results are presented in Table 1.

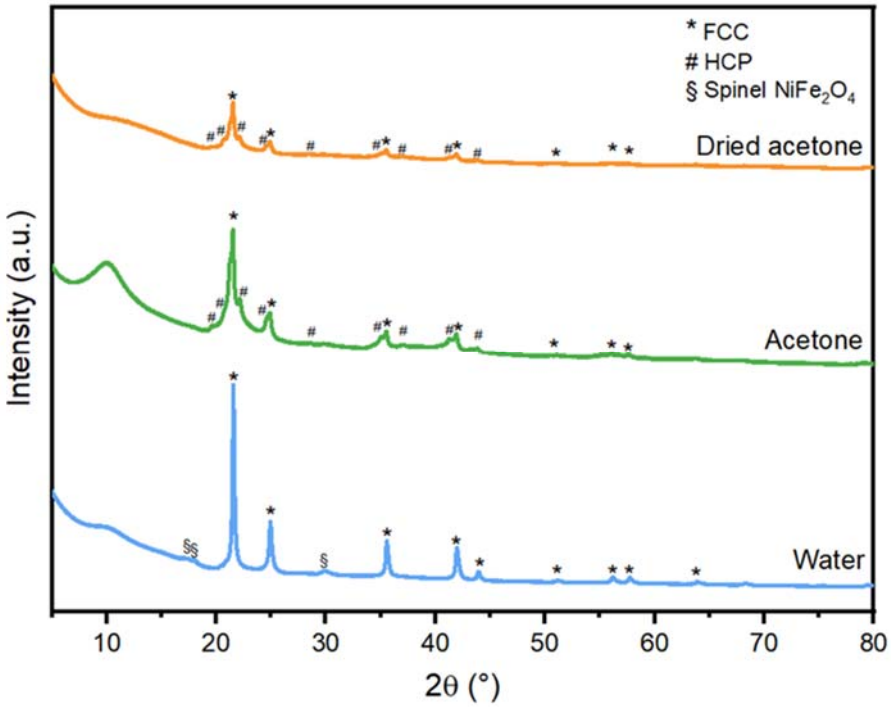

Figure 2. Synchrotron XRD profiles of the FeNi NPs ablated in different liquids. The ablation in acetone or dried acetone produced the FCC phase and the HCP phase, with a small volume of spinel $NiFe_2O_4$ phases (barely visible in this graph). Meanwhile, the ablation in water produced the FCC phase and $NiFe_2O_4$ phase. The complete indexing is presented in the supplementary information (Figure S2).

Table 1. The crystalline phase composition of FeNi NPs synthesized in different ablation liquids. The weight fraction of the HCP FeNi phase was extracted from the SXRD profile by Rietveld refinement.

Ablation liquid	Crystalline Phase Composition	HCP Content (wt%) *
Dried acetone	FCC FeNi, HCP FeNi, $NiFe_2O_4$	35.2 ± 1.0
Acetone	FCC FeNi, HCP FeNi, $NiFe_2O_4$	38.4 ± 0.2
Water	FCC FeNi, $NiFe_2O_4$	0

* The HCP content reported here is the weight fraction of the FeNi HCP phase with respect to the weight of the nanoparticle core. The Rietveld refinement was performed on a structure model of the nanoparticle core that consisted of the FCC FeNi phase(s) and the HCP FeNi phase if existing. The $NiFe_2O_4$ phase in the particle shell was not included in the structure model being refined.

All peaks corresponding to FCC and HCP phases were taken into account, while the $NiFe_2O_4$ peaks are excluded since the contribution of crystalline oxides in the XRD results is significantly low compared to the other phases. The NPs in dried acetone consist of 35.2 ± 1.0 wt% of the HCP phase, while the NPs in acetone account for 38.4 ± 0.2 wt% of the HCP phase, and the NPs in water contain no HCP phase (Table 1). It is interesting to observe that the ablation in acetone and dried acetone produces a mixture of the metastable HCP and stable FCC phases in the NP core, while only the FCC phase was formed in water. Meta- and stable phase mixtures in NPs produced by PLAL of different targets were previously reported. The formation of metastable zinc-blende and the stable diamond structures in silicon NPs [37], metastable hexagonal and stable cubic structures in diamond nanocrystals [38], the metastable γ-Fe and stable cubic FeO and α-Fe phases [39], and Ni NPs with stable FCC and metastable HCP phases [40,41]. Different arguments were postulated regarding the formation of stable and metastable phases during PLAL. (i) The specific heat capacity of the solvent, which influences the cooling rate of the ablation plasma plume generated during PLAL [40]. (ii) Shorter cavitation bubble lifetime compared to the

theoretical lifetime according to the Rayleigh–Plesset theory [41], and (iii) the confinement of the cavitation bubble by the surrounding liquid, which induces the high temperature, high pressure, and high density (HTHPHD) state and shorter quenching time of the plasma plume in the liquid [37]. The above-mentioned hypotheses all pointed to the freezing of the metastable phase during the cooling (quenching), which preserves the metastable phases.

For FeNi alloy, the formation of a metastable FeNi HCP phase is usually associated with high-pressure and high-temperature conditions, such as in the Earth's core [42–46]. It has been produced synthetically using a diamond anvil cell (DAC) from the bulk FeNi with a face-centered cubic (FCC) phase [36,46,47], where the sample is placed in a tiny space (3–4 mm) between two diamonds, which are pressed to each other [48]. Laser ablation in liquid also provides a high-pressure and high-temperature state to the nuclei inside the cavitation bubble (CB) and its collapse [49]. The bubble pressure during laser ablation might provide a suitable environment for the formation of the HCP phase; however, this cannot be the sole reason since the ablation in water does not produce HCP phases. The cavitation bubble dynamic study from the Choi group also showed that the cavitation bubble size was larger for hexane and acetonitrile compared to water [41]. The larger cavitation bubble and longer lifetime indicate lower pressure inside the bubble, as formerly reported from the laser ablation of aluminum oxide in ethanol, water, and isopropanol [50]. Hence, the pressure difference due to the cavitation bubble geometry would favor the HCP formation in water; however, it is only observed in organic solvents. Consequently, the liquid composition seems to be a significant factor influencing the FeNi NP's phase.

Based on the results in Table 1, we have observed that the HCP phase does not scale with the fraction of water content in the organic solvent, consequently, this factor can be ruled out. However, the fact that the ablation in acetone (and dried acetone) produced an HCP phase, while the ablation in water only provided the FCC phase, suggests that the carbon-based solvent plays a significant role in the HCP phase formation. During PLAL, the presence of carbon species in the cavitation bubble generated from the interaction of the high-intensity laser with the organic solvent can influence the nucleation kinetics of the HCP and FCC phases. Hence, not only the FCC phase forms but also the HCP phase. When the cavitation bubble finally collapses, the fast temperature quenching freezes this metastable phase. Nevertheless, many factors related to the liquid and the laser ablation dynamics might form a complex system that contributes to the formation of the HCP phase in the FeNi NPs.

3.2. Oxide Formation

Oxidation of NPs, either partially or completely, changes the NP properties such as catalytic activity [51] and magnetization [52]. Controlling the oxidation level of laser-generated NPs is therefore important to produce NPs with the desired functionality. In this section, the influence of water impurity in acetone on the oxidation of laser-generated FeNi NPs is studied. Based on the XRD results (Figure 2), formations of minor amounts of spinel iron-nickel oxide $NiFe_2O_4$ (ICSD No. 241661) are observed in all studied samples, which shows that oxidation occurs even in dried acetone where most of the water molecules are captured by molecular sieves. Nevertheless, the amount of crystalline oxides in all of the samples is significantly low, approximately 0.7 wt% for FeNi in water, while for FeNi synthesized in acetone and dried acetone, the quantities are lower than the quantification error of the measurement/device, hence, the values are not of significance. Based on the study by Marzun et al., the ablation of a Cu target in water with an inert Ar atmosphere still resulted in oxidized species, due to the splitting of water molecules to reactive OH species. To avoid water impurities in acetone, we used molecular sieves. It was formerly reported that using the molecular sieve with the size of 4 Å for 21 h reduced the water content from 0.45% to 0.001% (*w*/*w*) [31]. Meanwhile, the water molecule has a diameter of 2.8 Å, hence, molecular sieves with a pore size of 3 Å were used to capture the water molecules in acetone and produce the "dried acetone". Nadarajah et al. have investigated the influence of 3 Å molecular sieves to capture water molecules in acetone and reduce the oxidation

level of the laser-ablated FeRh NPs. They reported that the use of molecular sieves resulted in less nanoparticle oxidation compared to NPs produced in untreated acetone [53] and they suggest that the bound oxygen atoms in acetone contribute to NP oxidation. The dissolved oxygen gas in the liquid is also found to partially oxidize NPs due to aging [28], which means that the oxidation occurs also due to the possibly prolonged NPs storage in the liquid before the analysis. Hence, the surface oxidation of FeNi NPs into spinel $NiFe_2O_4$ was likely caused by the NPs' exposure to the oxygen species generated from the pyrolysis of the ablation liquid and later followed by the dissolved gas due to aging.

3.3. Morphology and Particle Size Distribution

The morphologies of the NPs ablated in dried acetone, water, and acetone are presented in Figure 3. Based on the bright field images of NPs in dried acetone (Figure 3a–c), core-shell structures with a core and two layers are formed, independently of the particle size. The thickness of the first layer (inner shell) ranges from 1.5 to 2.9 nm and has an average of 1.9 nm, whereas the average thickness of the second layer (outmost shell) was measured to be 2.4 nm, with a size range of 1.1–4.2 nm (Table 2). The core part shows a darker contrast in comparison to the shell, which can be explained as the change of electron scattering due to the electron density. The high electron density of the core part can be associated with the high material density, and in our case, it is $Fe_{50}Ni_{50}$ with a density of approximately 8.4 g/cm^3. For the inner shell, the formation of a carbide or oxide layer is likely, as the ablation was performed in a solvent with molecularly bound carbon and oxygen atoms. The density of iron and nickel carbide are approximately 4.93 and 7.99 g/cm^3, respectively, while iron, nickel, and iron-nickel oxide densities are between 5–7 g/cm^3, which explains the lower contrast of the inner shell compared to the core. The formation of iron and nickel carbides and oxides after the ablation of $Ni_{50}Fe_{50}$ in acetone was previously reported, but there were still unidentified peaks around 52°, 71°, and between 75–90° despite efforts from the authors [33], which are identified as FCC and HCP peaks of FeNi in this study (Figure 2). XRD results in Figure 2 and the lattice distance observed in Figure 3c confirm that the inner shell of this sample is constituted by spinel iron-nickel oxide ($NiFe_2O_4$). Meanwhile, the outmost layer with the brightest contrast can be attributed to a carbon layer, which was formed due to the pyrolysis of organic solvent by the high-intensity pulses [27]. The laser radiation pyrolyzes the organic solvent and yields carbon species [54], which then become the building block of the outer NP layer. A small part of graphitic carbon is observed in this sample (Figure S4), but most of the observed carbon layers are amorphous.

Table 2. FeNi NPs in dried acetone, acetone, and water shell thicknesses as obtained by TEM.

Ablation Liquid	Average Particle Size (x_c, nm)	Core Phase	Shell Phase	Shell Thickness (nm)	
				Average (Mean)	Range (Min to Max)
Dried acetone	10.2 ± 0.3	HCP/FCC FeNi	$NiFe_2O_4$	2.4	1.1–4.2
			Amorphous carbon	1.9	1.5–2.9
Acetone	12.0 ± 0.2	HCP/FCC FeNi	$NiFe_2O_4$	2.3	1.4–3.5
			Graphitic carbon	1.2	0.7–1.9
Water	17.7 ± 0.6	FCC FeNi	$NiFe_2O_4$	4.9	2.4–9.8

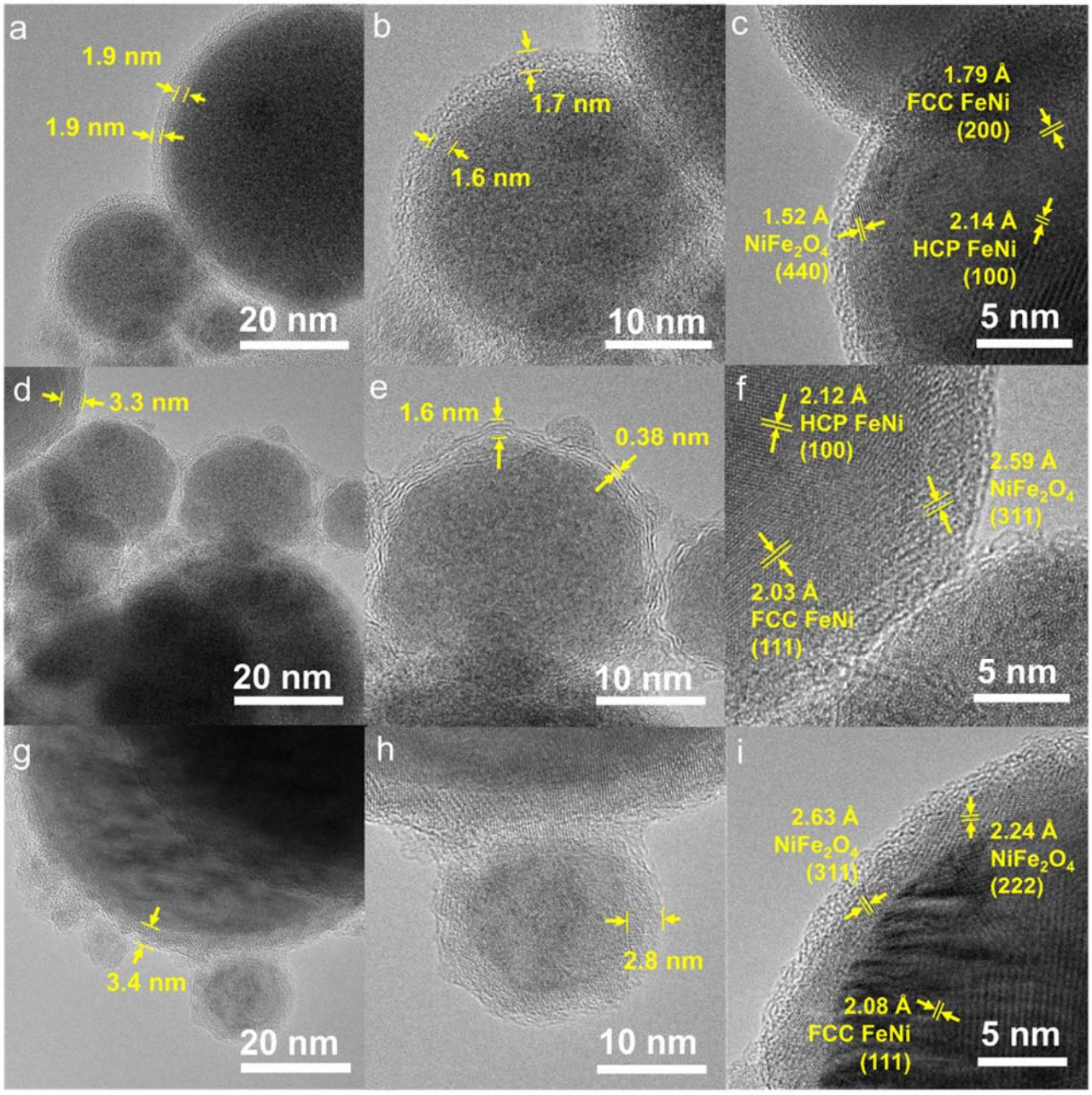

Figure 3. Morphology of FeNi NPs ablated in dried acetone (**a**–**c**), acetone (**d**–**f**), and water (**g**–**i**). (**a**,**d**,**g**) show the core-shell structure and the shell thickness of larger NPs, while (**b**,**e**,**h**) represent the smaller NPs. (**c**,**f**,**i**) confirm the phases observed in the XRD by measuring the lattice distance between the core and the shell.

Contrarily to the FeNi NPs in dried acetone, which exhibit the same core-shell structure for both small and large nanoparticle sizes, the sample in acetone (Figure 3) has two types of core-shell structures. Large NPs (d > 50 nm) form a core-shell structure, and the small NPs (d~20 nm) lean towards the formation of a core with outer graphitic carbon layers. The formation of a graphitic carbon layer was formerly reported after PLAL of metal targets in organic solvents, where the metal acts as a catalyst for the graphitization of the pyrolyzed carbon-based solvent [27,33]. Regarding the ablation of FeNi NPs in water, the formation of a core and a single shell structure for all NPs sizes was found. The formation of a single layer (without the carbon layer) is expected as water decomposes to H_2 and O_2 [54]. Based on the standard reduction potential, O_2 acts as an oxidizing agent in the reaction with Fe

and Ni, hence, the shell is most likely to be composed of oxides as supported by the XRD data (Figure 2).

The particle size distribution of each sample was measured for at least 400 particles (Figure 4). All the histograms of the particle size distribution fit the log-normal distribution, which is common in PLAL-produced NPs. Meanwhile, the NPs produced through chemical synthesis methods, such as coprecipitation, hydrothermal, and sol-gel methods, usually have a Gaussian-type size distribution [18,55–57]. The average particle size of the sample is defined based on the center value of the log-normal fitting curve (x_c) and the polydispersity index (PDI) is calculated from the square of standard deviation divided by the square of the mean value (σ^2/μ^2). The PDI is used to define whether the NPs are monodisperse or polydisperse, where a value of less than 0.3 is considered monodisperse [58]. The NPs size in dried acetone shows the lowest average particle size (x_c) of 10.2 ± 0.3 nm, followed by NPs in acetone (12.0 ± 0.2 nm), and NPs in water (17.7 ± 0.6 nm). The PDI values of NPs in dried acetone, acetone and water are found to be 0.28, 0.28, and 0.91, respectively. Based on these results, the FeNi NPs in dried acetone and acetone can be considered monodisperse, while the FeNi NPs produced in water are polydisperse. The FeNi NPs in dried acetone and acetone are smaller than the FeNi in water due to the carbon coating on the NPs surface, which prevent the growth and coalescence of the NPs [59]. Nevertheless, it should be noted that further growth during storage cannot be completely ruled out even with carbon coating [60].

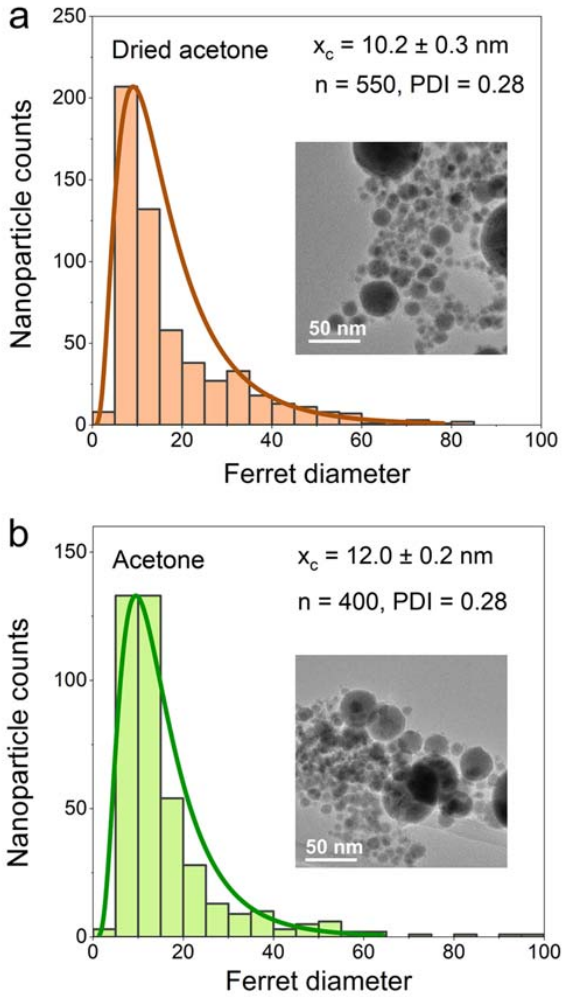

Figure 4. *Cont.*

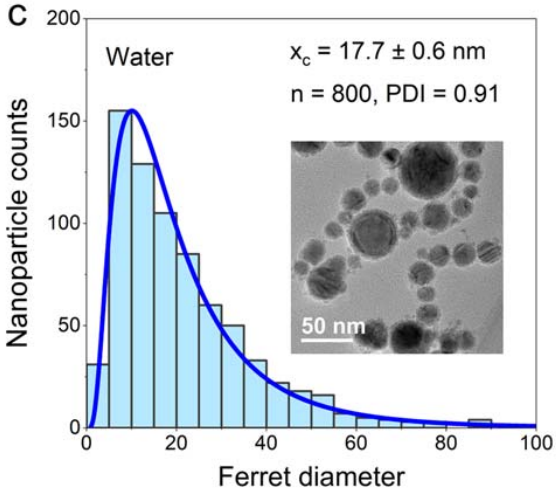

Figure 4. Number-weighted particle size distribution of FeNi NPs in (**a**) dried acetone, (**b**) acetone, and (**c**) water. FeNi NPs produced in dried acetone have the smallest median size and PDI, followed by FeNi produced in acetone, and FeNi produced in water. The number of counted particles (n) is denoted in the figures.

3.4. Elemental Composition

To determine the elemental composition of the NPs' core and shell, elemental scans using EDX-TEM were performed (Figure 5). A particle size of around 50 nm was selected as representative since the NPs generally have a distinct core-shell structure. Smaller NPs (10–20 nm) show distinct core-shell structures as well, but the oxygen signal from the environment sometimes provides a stronger contribution than the actual oxygen level on the NPs, hindering the oxidation analysis of the shell part (Figure S5). Hence, the discussion related to the EDX line scanning is limited to the larger NPs with a diameter of approximately 50 nm.

The EDX line scans (Figure 5) show that the Fe intensity is generally higher than the Ni intensity on the nanoparticle's surface. This signal difference between Ni and Fe represents the composition of the shell, where Fe is present in a higher percentage compared to Ni. The oxygen intensity in all samples increases from the start of the shell where Fe is detected, then the value is constant throughout the particle. This shows that oxidation only occurs on the surface of the particle, but not in the core, where the $Fe_{50}Ni_{50}$ composition of the initial target is preserved. By assuming that all O atomic % (at%) belongs to the shell with a composition of $NiFe_2O_4$, the approximate Fe and Ni at% in the core part were calculated, as shown in Table 3. Note that the drop-casting was not performed in a glovebox; hence, it is likely that some oxygen adsorbs to the grid during the sample preparation prior to the TEM analysis. In addition, the accuracy of the device is around 1 at%, which might influence the estimation of the core composition. The at% of Fe and Ni in the core part of dried acetone, acetone, and water samples show almost similar values with a difference of around 1–3 at%, which means that the bulk composition is maintained. Jakobi et al. argued that similar heat of evaporation and density of Pt and Ir during the ablation of $Pt_{91}Ir_9$ in acetone produced NPs with similar stoichiometry as the target material [61]. The heat of evaporation of Ni and Fe are 370.4 kJ/mol and 349.6 kJ/mol, while the densities are 8.9 g/cm^3 and 7.9 g/cm^3, respectively. These similar values of heat of evaporation and density (1.06 and 1.13-factor difference, respectively) induce the simultaneous evaporation and condensation of the FeNi NPs alloy, which preserves the target's elemental ratio. However, the oxidation level of the sample in dried acetone showed an unexpectedly high O at% value, which is even higher than water and twice the value of the sample in acetone. We have also measured the elemental composition using the EDX map scanning, which represents a larger area covering a larger number of NPs and also different NP sizes. As shown in Figure S6 and Table S1, the O at% of the dried acetone sample is the lowest, with a 15 at% difference

compared to the acetone sample. There is also an anomalous trend where O at% of the water sample is slightly lower by almost 3 at% compared to the acetone sample. Therefore, we believe that the measurement of O at% from EDX-TEM fails to provide a complete representative value for the whole sample and includes the contribution of all the NP sizes, leading to a variation of the O at% values obtained for different NPs or analyzed areas. Thus, we sought another measurement, i.e., Mössbauer spectroscopy, to define the oxidation level of the whole sample with higher statistical confidence.

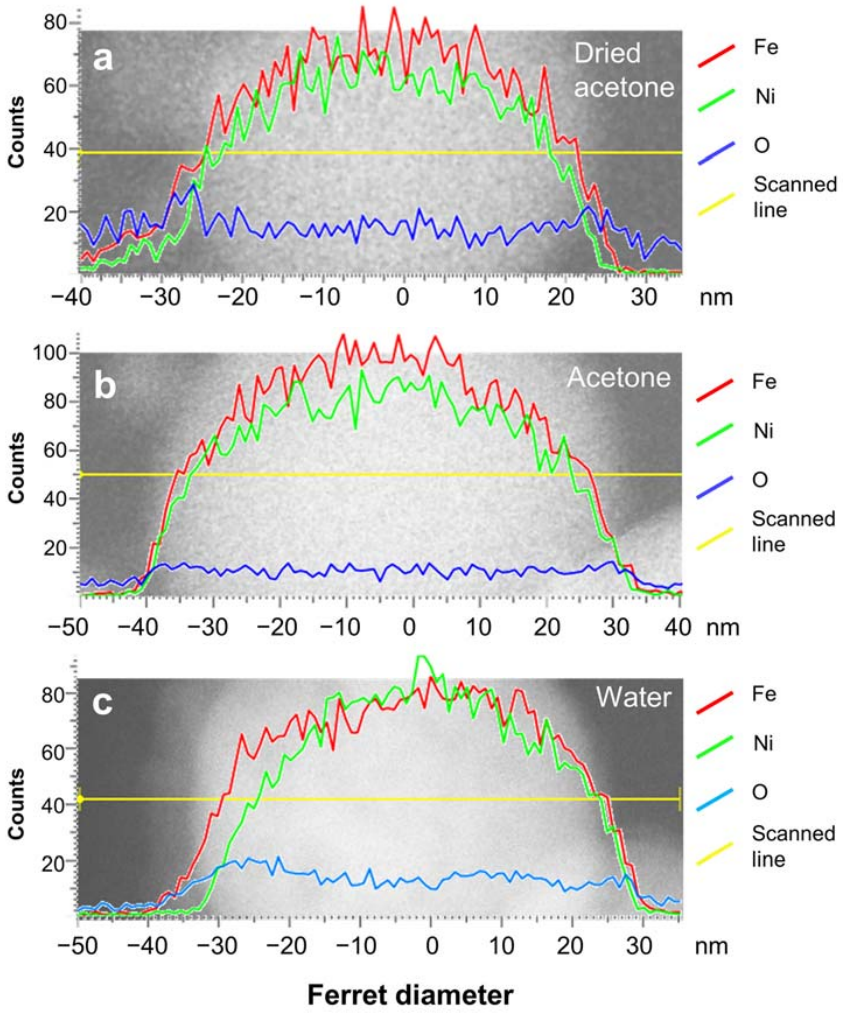

Figure 5. EDX-line scans of FeNi NPs ablated in (**a**) dried acetone, (**b**) acetone, and (**c**) water. The constant oxygen signals, which do not follow the Fe and Ni signals, indicate that oxidation only occurs on the NP surface.

Table 3. Elemental composition (in at%) of the NPs shown in Figure 5 and the estimation of Fe and Ni at% in the core part, assuming that all oxygen at% belongs to the $NiFe_2O_4$ shell.

Ablation Liquid	Whole Particle Composition			Shell Composition *			Core Composition **	
	Fe at%	Ni at%	O at%	Ni at%	Fe_2 at%	O_4 at%	Fe at%	Ni at%
Dried acetone	35.1	29.3	35.6	8.9	17.8	35.6	17.3	20.4
Acetone	43.6	38.1	18.2	4.6	9.1	18.2	34.5	33.6
Water	38.7	33.6	27.7	6.9	13.9	27.7	24.9	26.7

* with the assumption that all O at% of the particle comes from the $NiFe_2O_4$ shell, ** subtracting the whole particle composition with the shell composition.

Mössbauer spectroscopy was employed to quantify the total oxide fraction of the FeNi NPs and their aging behavior for longer oxidation times. The measurements were performed in transmission geometry, providing a measurement signal averaged over the total sample volume, thus, giving a comprehensive overview of the composition of Fe-bearing phases in the nanoparticles as well as their general magnetic structure. Due to different hyperfine interactions of the Fe nuclei with their surroundings, metallic and oxidic Fe-bearing phases result in distinctively different sub-spectra, as visible in Figure 6a. At ca. 4.3 K, two broadened sextet distributions can be identified for the aged, dried acetone sample: a larger one with moderate hyperfine magnetic fields B_{hf} and an average isomer shift of ca. 0.30 mm/s (green) assigned to metallic FeNi, and a second one with a larger B_{hf} and an isomer shift of ca. 0.47 mm/s. The latter is usually indicative of ferric oxides [62,63], whereby this distribution is assigned to iron atoms in the $NiFe_2O_4$ shell. Due to the very broad structure of the metallic FeNi subspectrum, a resolution of HCP- and FCC-components was not feasible.

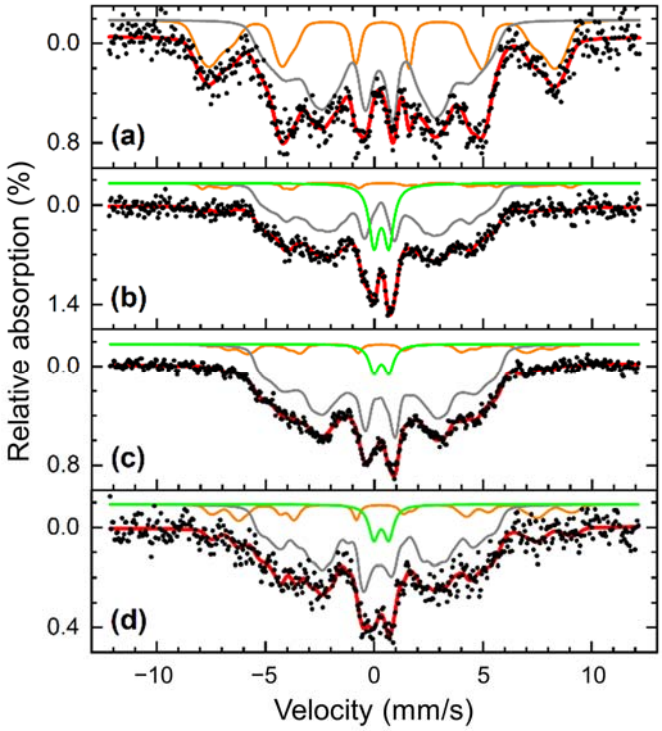

Figure 6. Mössbauer spectra of FeNi NP colloids: Prepared from dried acetone, aged for four months measured at 4.3 K (**a**) and 80 K (**b**), from dried acetone in the initial state at 80 K (**c**) and acetone in the initial state at 80 K (**d**). Spectra consist of an outer sextet distribution (orange) assigned to $NiFe_2O_4$, an inner sextet distribution corresponding to metallic FeNi (grey), and a doublet contribution (green) assigned to oxide material in the para- or superparamagnetic state.

Studying the spectrum at 80 K in Figure 6b in comparison, we observe only minor changes in the metallic FeNi subspectrum, while the oxidic sextet almost vanished, now manifesting mainly in a para- or superparamagnetic doublet state (green), both being mainly identical in spectral intensity and isomer shift. A more detailed analysis can be found in Figure S7, showing the dried acetone FeNi nanopowder spectra between 5 K and room temperature without an external magnetic field. This was done to study whether complete evaporation of the liquid to produce a powdered sample resulted in an oxidation increase due to the exposure to air, and the possibility of storing the colloids as a powder without influencing the oxidation level.

From the spectrum at 5 K, where the sub-spectra can be well resolved, 26% of the spectral area is assigned to the oxide fraction, which would suggest that further oxidation

of this sample takes place following drying and storage before the measurement was completed. This proves our earlier point, that it is important to use freshly produced colloids without extended storage time, either in their original liquid or as dried NP powder. To further reduce the oxidation level, it is also possible to use an organic solvent with no molecularly bound oxygen, such as acetonitrile, or H_2 as a reducing gas. However, the reduced price and the reusability of the molecular sieves employed in this work, which could be re-activated by heat treatment at around 300 °C, offer a beneficial option for the oxidation control of PLAL-generated NPs and the cost-effective upscaling of the production as required for catalysis applications. At higher temperatures, it is found that the sextet to doublet transition of the $NiFe_2O_4$ component mainly takes place between 30 and 60 K. No considerable changes in the spectral structure are visible above ca. 100 K. Corresponding measurements up to room temperature were not attainable for the colloidal samples since Brownian nanoparticle motion leads to severe line broadening, hindering a detailed analysis [64,65].

For the dried acetone colloid 4 months after production shown in Figure 6a,b, the $NiFe_2O_4$ sub-spectra contains roughly 27% of the spectral area. Assuming the oxide shell consists of stoichiometric $NiFe_2O_4$ based on the previous XRD results (Figure 2) and expecting similar Debye-Waller factors for metallic FeNi and $NiFe_2O_4$ at cryogenic temperatures, relative spectral areas represent a simple approximation of the weight percentage (wt%) of the corresponding phase due to very similar atomic Fe fractions per mass. To evaluate the effect of reducing water content on the total oxide fraction as well as the stability of the prepared nanoparticles, the oxide spectral area in aged, and dried acetone colloid is compared to fresh dried acetone (14%) and fresh acetone colloid (22%) shown in Figure 6c,d. The results clearly show a lower oxide fraction after preparation in mole-sieved acetone and minor ongoing oxidation upon a longer aging time. It can be concluded that while the drying process is effective, the reduced oxidation of the sample is lost again after extended storage time, and results in a similar oxide fraction as the fresh colloid made from the commercial, untreated acetone. This also means that the carbon shell and the $NiFe_2O_4$ shell on the NPs did not completely stop further oxidation of the NPs during longer storage time. Oxidation might occur from the presence of molecularly bound O atoms in acetone or the dissolved O_2 gas. Therefore, it is important to use fresh colloids in the posterior intended catalysis or magnetic application to avoid further oxidation that can detriment the produced FeNi NPs performance.

3.5. Magnetic Properties

The magnetic field-dependent magnetization M(H) curves of FeNi NPs formed in different liquids are shown in Figure 7, recorded at 300 K up to a maximum magnetic field of 1 T. A similar saturation alignment for the three samples can be observed, with the overall character of the M(H) curves being comparable, reaching high magnetization values already at ca. 0.4 T and showing a gradual further increase in the high-field region. Based on Mössbauer spectroscopy in-field experiments as shown in Figure S8, this M(H) shape can be explained as follows: A distinctively reduced intensity of lines 2 and 5 of the FeNi subspectrum can be observed already at a magnetic field of 1 T visible in Figure S8b, revealing a state of almost complete magnetic alignment for the metallic core of the nanoparticles [66]. The $NiFe_2O_4$ shell, on the other hand, displays high intensities of lines 2 and 5 even up to 8 T (Figure S8c), proving that magnetic moments here are still relatively random in their orientation, resulting in a limited oxide contribution to magnetization, slowly increasing when going to higher fields. The incomplete magnetic alignment of the oxide shell is also clearly evident by the only partial resolution of the contributions from A- and B-spinel lattice positions at 8 T.

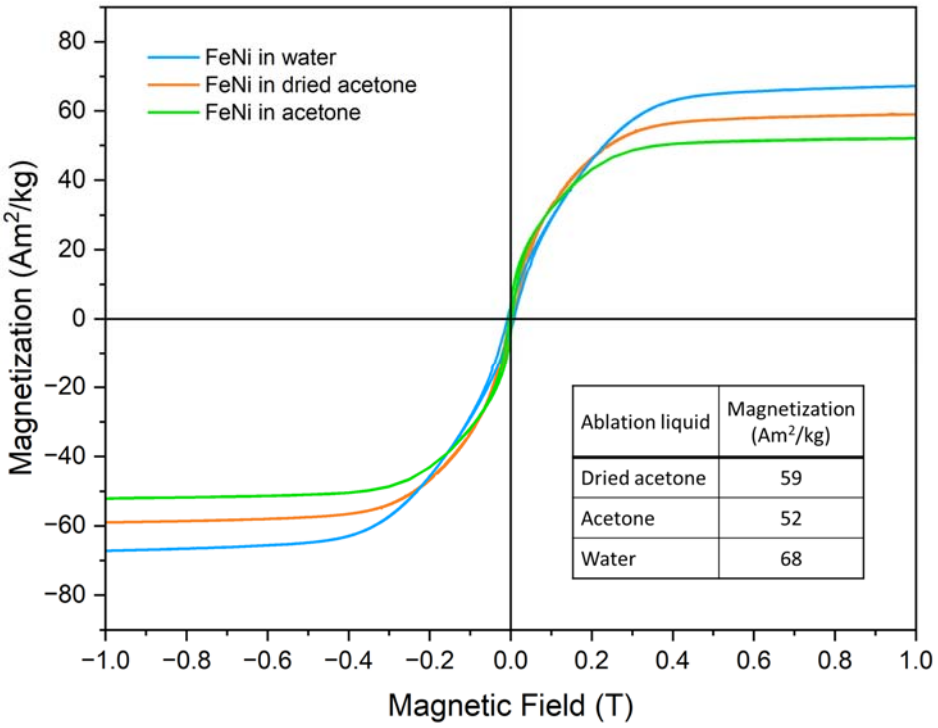

Figure 7. M(H) curves of FeNi nanoparticle powders from colloids prepared in different liquids at room temperature (300 K). FeNi in acetone data reproduced from [67].

Clear differences are apparent when regarding the 1 T magnetization values. When comparing the acetone and dried acetone samples, the effect of the drying process becomes clear, as the mole-sieved sample has a higher magnetization of ca. 59 Am^2/kg compared to the 52 Am^2/kg of the non-sieved sample, which can presumably be attributed to the lower oxidation of the former. However, the sample produced in water shows an even higher magnetization at 68 Am^2/kg. It would be prudent to assume that this difference stems from the fact that the particle size of the water-based sample is significantly higher than that of the two acetone-based ones, which would lead to a lower surface-to-volume ratio and thus a reduced amount of surface spin canting. To discern this difference, additional magnetometry measurements were performed, up to higher fields of 9 T and in a wide range of temperatures from 4.3 K up to 300 K, as shown in Figure S9 for the dried acetone and water-based samples. Here, two aspects can be discussed: on the one hand, the low temperature, and high field measurements show that the water-based sample still retains a slightly higher magnetization value at 9 T of 82 Am^2/kg compared to 76 Am^2/kg for the dried acetone sample. Interestingly, the slightly more pronounced shape of the M(H) curves for the water-based sample indicates that full saturation has not yet been reached at 9 T, which would suggest that the higher magnetization value compared to the acetone-based samples is not solely due to a reduced occurrence of spin canting due to the larger average particle size. An explanation can be provided by the paramagnetic HCP phase being present in the acetone-based samples, but not in the water-based one, leading to a reduction of the overall measured magnetization. Additionally, the previously mentioned carbon shell formation can also contribute to this effect. However, despite this slight decrease relative to the water-based sample, the difference in magnetization visible between the sample formed in dried and regular acetone clearly shows the viability of the method presented here to prevent undesired oxidation of the FeNi NPs.

4. Conclusions

Reducing water impurities in acetone for the generation of $Fe_{50}Ni_{50}$ nanoalloys by PLAL influences the phases, core-shell structure, oxidation, and magnetic property of

the produced NPs. FeNi NPs in dried acetone with reduced water impurity exhibit FCC and HCP phases in the core, an inner $NiFe_2O_4$ shell, and an outer amorphous carbon shell (FCC/HCP FeNi@$NiFe_2O_4$@amorphous carbon). The NPs in commercial, untreated acetone (water impurity of 0.3–0.5%) produced a mixture of FCC and HCP phases in the core with either $NiFe_2O_4$ shell or graphitic carbon (FCC/HCP FeNi@$NiFe_2O_4$ and FCC/HCP FeNi@graphitic carbon). Meanwhile, ablating FeNi alloy in water produced FCC core and $NiFe_2O_4$ shell (FCC FeNi@ $NiFe_2O_4$) NPs without any traces of the HCP phase or carbon shell. Reducing water impurity in acetone was found to lower the oxidation level by 8% (total oxide fraction, as measured by Mössbauer spectroscopy) compared to the NPs in untreated acetone. The magnetization of the dried acetone sample (59 Am^2/kg) was higher than the acetone sample (52 Am^2/kg) due to the lower degree of oxidation. The NPs produced in water exhibit a higher magnetization of 68 Am^2/kg. The higher magnetization in the water sample is due to the larger average NPs size (17 nm), compared to the NPs in dried acetone (10 nm) and acetone (12 nm). The smaller average size of NPs in acetone-based liquid is related to the carbon layer formed in the ablation plume, which constrains the particle growth. The diverse core-shell structure and the modified FeNi NPs properties observed in this study show that FeNi NPs with different phase and shell structures can be generated just by reducing the amount of water impurity in the organic solvent or modifying the solvent employed in PLAL. This opens up a straightforward synthesis approach of different core-shell FeNi NPs that can be adapted to the broad fields where FeNi NPs are applied, such as sensors and actuators development, catalysis, magnetism, or biomedicine.

Supplementary Materials: The following supporting information can be downloaded at: https://www.mdpi.com/article/10.3390/nano13020227/s1, Figure S1: The normalized absorption spectra of Fe50Ni50 nanoparticles generated in dried acetone (black), acetone (red), and water (blue) within the wavelength of 400–1100 nm; Figure S2: Phase identification of FeNi NPs in dried acetone, acetone, and water based on the Synchrotron XRD results; Figure S3: Rietveld refinement of the synchrotron XRD results without the contribution of the oxide phase; Figure S4: HR-TEM image of NP in dried acetone which shows the formation of graphitic carbon; Figure S5: Line scanning EDX-TEM of small NP (d = 16 nm) of FeNi ablated in acetone (top) and in dried acetone (bottom); Figure S6: EDX map scanning of the FeNi NPs in different ablation liquids. Figure S7: Mössbauer spectra of the dried acetone colloid powder sample recorded between 5 K and room temperature. Figure S8: Mössbauer spectra of an aged dried acetone powder sample recorded at ca. 4.3 K in external magnetic fields of (a) 0 T, (b) 1 T, and (c) 8 T parallel to γ-ray incidence direction. Figure S9: Field-dependent magnetization of FeNi nanoparticle powder from the (a) dried acetone and (b) the water-based sample recorded at 4.3 K to 300 K in magnetic fields up to 9 T. Table S1: The elemental composition of the whole area (in at%) obtained by map scanning as shown in Figure S5 and the estimation of Fe and Ni at% in the core part, assuming that all O at% belongs to the $NiFe_2O_4$ shell. Reference [68] is cited in the supplementary materials.

Author Contributions: Conceptualization, I.Y.K., C.D.-B., and B.G.; methodology, I.Y.K., C.D.-B., and B.G.; software, I.Y.K., C.D.-B., Q.L., J.L., S.S., E.K.; validation, C.D.-B., B.G., G.Z..; formal analysis, I.Y.K., C.D.-B., Q.L., J.L., S.S., E.K.; investigation, I.Y.K., C.D.-B., Q.L., J.L., S.S., E.K.; resources, B.G., H.W., G.Z., E.K.; data curation, I.Y.K., Q.L., J.L., S.S.; writing—original draft preparation, I.Y.K.; writing—review and editing, I.Y.K., C.D.-B., B.G., Q.L., J.L., S.S.; visualization, I.Y.K., Q.L., J.L., S.S., C.D.-B.; supervision, C.D.-B., B.G.; project administration, B.G., G.Z., H.W.; funding acquisition, B.G., G.Z., H.W. All authors have read and agreed to the published version of the manuscript.

Funding: Financial funding from the European Union's Horizon 2020 research and innovation program under the grant agreement No 952068 (project LESGO) and funding from the DFG via the CRC/TRR 270 (Project-ID 405553726, projects B08 and B05), the CRC/TRR 247 (Project-ID 388390466, project B02) and GO 2566/10-1-(Project-ID 445127149) are gratefully acknowledged. The synchrotron X-ray diffraction experiments were performed at beamline 33-BM-C at the Advanced Photon Source (APS) at Argonne National Laboratory (ANL). This research used resources of the Advanced Photon Source, a U.S. Department of Energy (DOE) Office of Science user facility operated for the DOE Office of Science by Argonne National Laboratory under Contract No. DE-AC02-06CH11357. Q. Lin and G.

Zangari would like to thank the financial support from the Department of Energy (DOE), Office of Basic Energy Sciences (BES), United States (Grant number: DE-SC0019191).

Data Availability Statement: Besides the data published in this article, no new data were created.

Acknowledgments: The authors acknowledge support from the Open Access Publication Fund of the University of Wuppertal. We would like to thank Markus Heidelmann from ICAN, University of Duisburg-Essen, for the TEM measurements, and Karsten Albe, TU Darmstadt, for the valuable discussion.

Conflicts of Interest: The authors declare no conflict of interest.

References

1. Frey, P.A.; Reed, G.H. The ubiquity of iron. *ACS Chem. Biol.* **2012**, *7*, 1477–1481. [CrossRef]
2. Cui, J.; Kramer, M.; Zhou, L.; Liu, F.; Gabay, A.; Hadjipanayis, G.; Balasubramanian, B.; Sellmyer, D. Current progress and future challenges in rare-earth-free permanent magnets. *Acta Mater.* **2018**, *158*, 118–137. [CrossRef]
3. van Schilfgaarde, M.; Abrikosov, I.A.; Johansson, B. Origin of the Invar effect in iron–nickel alloys. *Nature* **1999**, *400*, 46–49. [CrossRef]
4. Shinjo, T.; Okuno, T.; Hassdorf, R.; Shigeto, K.; Ono, T. Magnetic vortex core observation in circular dots of permalloy. *Science* **2000**, *289*, 930–932. [CrossRef] [PubMed]
5. Clarke, R.S.; Scott, E.R.D. Tetrataenite-ordered FeNi, a new mineral in meteorites. *Am. Mineral.* **1980**, *65*, 624–630.
6. Spooner, T. Current Transformers with Nickel-Iron Cores. *Trans. Am. Inst. Electr. Eng.* **1926**, *45*, 701–707. [CrossRef]
7. Ahn, C.H.; Allen, M.G. Micromachined planar inductors on silicon wafers for MEMS applications. *IEEE Trans. Ind. Electron.* **1998**, *45*, 866–876. [CrossRef]
8. Ahn, C.H.; Kim, Y.J.; Allen, M.G. A fully integrated planar toroidal inductor with a micromachined nickel-iron magnetic bar. *IEEE Trans. Compon. Packag. Manuf. Technol. Part A* **1994**, *17*, 463–469. [CrossRef]
9. Dijith, K.S.; Aiswarya, R.; Praveen, M.; Pillai, S.; Surendran, K.P. Polyol derived Ni and NiFe alloys for effective shielding of electromagnetic interference. *Mater. Chem. Front.* **2018**, *2*, 1829–1841. [CrossRef]
10. Giordano, M.C.; Escobar Steinvall, S.; Watanabe, S.; Fontcuberta i Morral, A.; Grundler, D. Ni 80 Fe 20 nanotubes with optimized spintronic functionalities prepared by atomic layer deposition. *Nanoscale* **2021**, *13*, 13451–13462. [CrossRef]
11. Bokare, A.D.; Chikate, R.C.; Rode, C.V.; Paknikar, K.M. Iron-nickel bimetallic nanoparticles for reductive degradation of azo dye Orange G in aqueous solution. *Appl. Catal. B Environ.* **2008**, *79*, 270–278. [CrossRef]
12. Gong, M.; Dai, H. A mini review of NiFe-based materials as highly active oxygen evolution reaction electrocatalysts. *Nano Res.* **2014**, *8*, 23–39. [CrossRef]
13. Zhang, X.; Xu, H.; Li, X.; Li, Y.; Yang, T.; Liang, Y. Facile Synthesis of Nickel-Iron/Nanocarbon Hybrids as Advanced Electrocatalysts for Efficient Water Splitting. *ACS Catal.* **2016**, *6*, 580–588. [CrossRef]
14. Potvin, E.; Brossard, L. Electrocatalytic activity of Ni-Fe anodes for alkaline water electrolysis. *Mater. Chem. Phys.* **1992**, *31*, 311–318. [CrossRef]
15. Lewis, L.H.; Mubarok, A.; Poirier, E.; Bordeaux, N.; Manchanda, P.; Kashyap, A.; Skomski, R.; Goldstein, J.; Pinkerton, F.E.; Mishra, R.K.; et al. Inspired by nature: Investigating tetrataenite for permanent magnet applications. *J. Phys. Condens. Matter* **2014**, *26*, 10. [CrossRef]
16. Lin, Q.; Nadarajah, R.; Hoglund, E.; Semisalova, A.; Howe, J.M.; Gökce, B.; Zangari, G. Towards synthetic L10-FeNi: Detecting the absence of cubic symmetry in Laser-Ablated Fe-Ni nanoparticles. *Appl. Surf. Sci.* **2021**, *567*, 150664. [CrossRef]
17. Chokprasombat, K.; Pinitsoontorn, S.; Maensiri, S. Effects of Ni content on nanocrystalline Fe–Co–Ni ternary alloys synthesized by a chemical reduction method. *J. Magn. Magn. Mater.* **2016**, *405*, 174–180. [CrossRef]
18. Lima, E.; Drago, V.; Bolsoni, R.; Fichtner, P.F.P. Nanostructured Fe50Ni50 alloy formed by chemical reduction. *Solid State Commun.* **2003**, *125*, 265–270. [CrossRef]
19. Anastas, P.; Eghbali, N. Green Chemistry: Principles and Practice. *Chem. Soc. Rev.* **2010**, *39*, 301–312. [CrossRef]
20. Gökce, B.; Amendola, V.; Barcikowski, S. Opportunities and Challenges for Laser Synthesis of Colloids. *ChemPhysChem* **2017**, *18*, 983–985. [CrossRef]
21. Amendola, V.; Amans, D.; Ishikawa, Y.; Koshizaki, N.; Scirè, S.; Compagnini, G.; Reichenberger, S.; Barcikowski, S. Room-Temperature Laser Synthesis in Liquid of Oxide, Metal-Oxide Core-Shells, and Doped Oxide Nanoparticles. *Chem. Eur. J.* **2020**, *26*, 9206–9242. [CrossRef] [PubMed]
22. Zhang, D.; Gökce, B.; Barcikowski, S. Laser Synthesis and Processing of Colloids: Fundamentals and Applications. *Chem. Rev.* **2017**, *117*, 3990–4103. [CrossRef] [PubMed]
23. Zhang, D.; Li, Z.; Sugioka, K. Laser ablation in liquids for nanomaterial synthesis: Diversities of targets and liquids. *J. Phys. Photonics* **2021**, *3*, 042002. [CrossRef]
24. Kalus, M.R.; Lanyumba, R.; Lorenzo-Parodi, N.; Jochmann, M.A.; Kerpen, K.; Hagemann, U.; Schmidt, T.C.; Barcikowski, S.; Gökce, B. Determining the role of redox-active materials during laser-induced water decomposition. *Phys. Chem. Chem. Phys.* **2019**, *21*, 18636–18651. [CrossRef]

25. Chaturvedi, A.; Joshi, M.P.; Mondal, P.; Sinha, A.K.; Srivastava, A.K. Growth of anatase and rutile phase TiO_2 nanoparticles using pulsed laser ablation in liquid: Influence of surfactant addition and ablation time variation. *Appl. Surf. Sci.* **2017**, *396*, 303–309. [CrossRef]
26. Zhang, D.; Lu, S.; Gökce, B.; Ma, Z.; Spasova, M.; Yelsukova, A.E.; Farle, M.; Wiedwald, U.; Zhang, D.; Ma, Z.; et al. Formation Mechanism of Laser Synthesized Iron-Manganese Alloy Nanoparticles, Manganese Oxide Nanosheets and Nanofibers. *Part. Part. Syst. Charact.* **2017**, *34*, 1600225. [CrossRef]
27. Zhang, D.; Zhang, C.; Liu, J.; Chen, Q.; Zhu, X.; Liang, C. Carbon-Encapsulated Metal/Metal Carbide/Metal Oxide Core-Shell Nanostructures Generated by Laser Ablation of Metals in Organic Solvents. *ACS Appl. Nano Mater.* **2019**, *2*, 28–39. [CrossRef]
28. Marzun, G.; Bönnemann, H.; Lehmann, C.; Spliethoff, B.; Weidenthaler, C.; Barcikowski, S. Role of Dissolved and Molecular Oxygen on Cu and PtCu Alloy Particle Structure during Laser Ablation Synthesis in Liquids. *ChemPhysChem* **2017**, *18*, 1175–1184. [CrossRef]
29. Sigma Aldrich. Acetone, ACS Reagent, ≥99.5%. Available online: https://www.sigmaaldrich.com/DE/de/product/sigald/179124 (accessed on 7 September 2022).
30. Sigma Aldrich. Acetone, Suitable for HPLC, ≥99.9%. Available online: https://www.sigmaaldrich.com/DE/de/product/sigald/270725 (accessed on 7 September 2022).
31. Meeker, R.L.; Critchfield, F.E.; Bishop, E.T. Water Determination by Near Infrared Spectrophotometry. *Anal. Chem.* **1962**, *34*, 1510–1511. [CrossRef]
32. Lin, R.; Ladshaw, A.; Nan, Y.; Liu, J.; Yiacoumi, S.; Tsouris, C.; DePaoli, D.W.; Tavlarides, L.L. Isotherms for Water Adsorption on Molecular Sieve 3A: Influence of Cation Composition. *Ind. Eng. Chem. Res.* **2015**, *54*, 10442–10448. [CrossRef]
33. Davodi, F.; Mühlhausen, E.; Settipani, D.; Rautama, E.L.; Honkanen, A.P.; Huotari, S.; Marzun, G.; Taskinen, P.; Kallio, T. Comprehensive study to design advanced metal-carbide@garaphene and metal-carbide@iron oxide nanoparticles with tunable structure by the laser ablation in liquid. *J. Colloid Interface Sci.* **2019**, *556*, 180–192. [CrossRef] [PubMed]
34. Li, G.; Yang, B.; Xu, X.; Cao, S.; Shi, Y.; Yan, Y.; Song, X.; Hao, C. FeNi Alloy Nanoparticles Encapsulated in Carbon Shells Supported on N-Doped Graphene-Like Carbon as Efficient and Stable Bifunctional Oxygen Electrocatalysts. *Chem. Eur. J.* **2020**, *26*, 2890–2896. [CrossRef] [PubMed]
35. Montes-Arango, A.M.; Marshall, L.G.; Fortes, A.D.; Bordeaux, N.C.; Langridge, S.; Barmak, K.; Lewis, L.H. Discovery of process-induced tetragonality in equiatomic ferromagnetic FeNi. *Acta Mater.* **2016**, *116*, 263–269. [CrossRef]
36. Komabayashi, T.; Hirose, K.; Ohishi, Y. In situ X-ray diffraction measurements of the fcc-hcp phase transition boundary of an Fe-Ni alloy in an internally heated diamond anvil cell. *Phys. Chem. Miner.* **2012**, *39*, 329–338. [CrossRef]
37. Liu, P.; Cao, Y.L.; Cui, H.; Chen, X.Y.; Yang, G.W. Micro- and nanocubes of silicon with zinc-blende structure. *Chem. Mater.* **2008**, *20*, 494–502. [CrossRef]
38. Wang, J.B.; Zhang, C.Y.; Zhong, X.L.; Yang, G.W. Cubic and hexagonal structures of diamond nanocrystals formed upon pulsed laser induced liquid-solid interfacial reaction. *Chem. Phys. Lett.* **2002**, *361*, 86–90. [CrossRef]
39. Patil, P.P.; Phase, D.M.; Kulkarni, S.A.; Ghaisas, S.V.; Kulkarni, S.K.; Kanetkar, S.M.; Ogale, S.B.; Bhide, V.G. Pulsed-laser—Induced reactive quenching at liquid-solid interface: Aqueous oxidation of iron. *Phys. Rev. Lett.* **1987**, *58*, 238–241. [CrossRef] [PubMed]
40. Jung, H.J.; Choi, M.Y. Specific solvent produces specific phase Ni nanoparticles: A pulsed laser ablation in solvents. *J. Phys. Chem. C* **2014**, *118*, 14647–14654. [CrossRef]
41. Lee, S.J.; Theerthagiri, J.; Choi, M.Y. Time-resolved dynamics of laser-induced cavitation bubbles during production of Ni nanoparticles via pulsed laser ablation in different solvents and their electrocatalytic activity for determination of toxic nitroaromatics. *Chem. Eng. J.* **2022**, *427*, 130970. [CrossRef]
42. Tateno, S.; Hirose, K.; Komabayashi, T.; Ozawa, H.; Ohishi, Y. The structure of Fe-Ni alloy in Earth's inner core. *Geophys. Res. Lett.* **2012**, *39*. [CrossRef]
43. Shen, G.; Mao, H.; Hemley, R.J.; Duffy, T.S.; Rivers, M.L. Melting and crystal structure of iron at high pressures and temperatures. *Geophys. Res. Lett.* **1998**, *25*, 373–376. [CrossRef]
44. Torchio, R.; Boccato, S.; Miozzi, F.; Rosa, A.D.; Ishimatsu, N.; Kantor, I.; Sévelin-Radiguet, N.; Briggs, R.; Meneghini, C.; Irifune, T.; et al. Melting Curve and Phase Relations of Fe-Ni Alloys: Implications for the Earth's Core Composition. *Geophys. Res. Lett.* **2020**, *47*, e2020GL088169. [CrossRef]
45. Lin, J.-F.; Heinz, D.L.; Campbell, A.J.; Devine, J.M.; Mao, W.L.; Shen, G. Iron-Nickel alloy in the Earth's core. *Geophys. Res. Lett.* **2002**, *29*, 109-1–109-3. [CrossRef]
46. Huang, E.; Bassett, W.A.; Weathers, M.S. Phase relationships in Fe-Ni alloys at high pressures and temperatures. *J. Geophys. Res.* **1988**, *93*, 7741. [CrossRef]
47. Kuwayama, Y.; Hirose, K.; Sata, N.; Ohishi, Y. Phase relations of iron and iron-nickel alloys up to 300 GPa: Implications for composition and structure of the Earth's inner core. *Earth Planet. Sci. Lett.* **2008**, *273*, 379–385. [CrossRef]
48. Boehler, R. Diamond cells and new materials. *Mater. Today* **2005**, *8*, 34–42. [CrossRef]
49. Soliman, W.; Nakano, T.; Takada, N.; Sasaki, K. Modification of Rayleigh-Plesset theory for reproducing dynamics of cavitation bubbles in liquid-phase laser ablation. *Jpn. J. Appl. Phys.* **2010**, *49*, 116202. [CrossRef]
50. Lam, J.; Lombard, J.; Dujardin, C.; Ledoux, G.; Merabia, S.; Amans, D. Dynamical study of bubble expansion following laser ablation in liquids. *Appl. Phys. Lett.* **2016**, *108*, 074104. [CrossRef]

51. Cuenya, B.R. Synthesis and catalytic properties of metal nanoparticles: Size, shape, support, composition, and oxidation state effects. *Thin Solid Films* **2010**, *518*, 3127–3150. [CrossRef]
52. Rebodos, R.L.; Vikesland, P.J. Effects of oxidation on the magnetization of nanoparticulate magnetite. *Langmuir* **2010**, *26*, 16745–16753. [CrossRef]
53. Nadarajah, R.; Tahir, S.; Landers, J.; Koch, D.; Semisalova, A.S.; Wiemeler, J.; El-Zoka, A.; Kim, S.H.; Utzat, D.; Möller, R.; et al. Controlling the oxidation of magnetic and electrically conductive solid-solution iron-rhodium nanoparticles synthesized by laser ablation in liquids. *Nanomaterials* **2020**, *10*, 2362. [CrossRef] [PubMed]
54. Kalus, M.R.; Bärsch, N.; Streubel, R.; Gökce, E.; Barcikowski, S.; Gökce, B. How persistent microbubbles shield nanoparticle productivity in laser synthesis of colloids—Quantification of their volume, dwell dynamics, and gas composition. *Phys. Chem. Chem. Phys.* **2017**, *19*, 7112–7123. [CrossRef] [PubMed]
55. Khairani, I.Y.; Arifiadi, A.N.; Lee, J.-H.; Bhoi, B.; Patel, S.K.S.; Kim, S. Fabrication, Structure, and Magnetic Properties of Pure-Phase $BiFeO_3$ and $MnFe_2O_4$ Nanoparticles and their Nanocomposites. *J. Magn.* **2020**, *25*, 140–149. [CrossRef]
56. Arifiadi, A.N.; Kim, K.-T.; Khairani, I.Y.; Park, C.B.; Kim, K.H.; Kim, S.-K. Synthesis and multiferroic properties of high-purity CoFe2O4–BiFeO3 nanocomposites. *J. Alloys Compd.* **2021**, *867*, 159008. [CrossRef]
57. Tao, K.; Dou, H.; Sun, K. Interfacial coprecipitation to prepare magnetite nanoparticles: Concentration and temperature dependence. *Colloids Surf. A Physicochem. Eng. Asp.* **2008**, *320*, 115–122. [CrossRef]
58. Barcikowski, S.; Amendola, V.; Lau, M.; Marzun, G.; Rehbock, C.; Reichenberger, S.; Zhang, D.; Gökce, B. *Handbook of Laser Synthesis & Processing of Colloids*, 2nd ed.; Duisburg-Essen Publication Online: Essen, Germany, 2019.
59. Amendola, V.; Riello, P.; Meneghetti, M. Magnetic nanoparticles of iron carbide, iron oxide, iron@iron oxide, and metal iron synthesized by laser ablation in organic solvents. *J. Phys. Chem. C* **2011**, *115*, 5140–5146. [CrossRef]
60. Zhang, D.; Choi, W.; Jakobi, J.; Kalus, M.R.; Barcikowski, S.; Cho, S.H.; Sugioka, K. Spontaneous shape alteration and size separation of surfactant-free silver particles synthesized by laser ablation in acetone during long-period storage. *Nanomaterials* **2018**, *8*, 529. [CrossRef]
61. Jakobi, J.; Menéndez-Manjón, A.; Chakravadhanula, V.S.K.; Kienle, L.; Wagener, P.; Barcikowski, S. Stoichiometry of alloy nanoparticles from laser ablation of PtIr in acetone and their electrophoretic deposition on PtIr electrodes. *Nanotechnology* **2011**, *22*, 145601. [CrossRef]
62. Cornell, R.M.; Schwertmann, U. *The Iron Oxides: Structure, Properties, Reactions, Occurrences and Uses*; Wiley Online Library, Wiley: Weinheim, Germany, 2003; ISBN 9783527302741.
63. Wareppam, B.; Kuzmann, E.; Garg, V.K.; Singh, L.H. Mössbauer spectroscopic investigations on iron oxides and modified nanostructures: A review. *J. Mater. Res.* **2022**. [CrossRef]
64. Keller, H.; Kündig, W. Mössbauer studies of Brownian motion. *Solid State Commun.* **1975**, *16*, 253–256. [CrossRef]
65. Landers, J.; Salamon, S.; Remmer, H.; Ludwig, F.; Wende, H. Simultaneous Study of Brownian and Néel Relaxation Phenomena in Ferrofluids by Mössbauer Spectroscopy. *Nano Lett.* **2016**, *16*, 1150–1155. [CrossRef] [PubMed]
66. Ammar, S.; Jouini, N.; Fiévet, F.; Beji, Z.; Smiri, L.; Moliné, P.; Danot, M.; Grenèche, J.M. Magnetic properties of zinc ferrite nanoparticles synthesized by hydrolysis in a polyol medium. *J. Phys. Condens. Matter* **2006**, *18*, 9055–9069. [CrossRef]
67. Nadarajah, R.; Tasdemir, L.; Thiel, C.; Salamon, S.; Semisalova, A.S.; Wende, H.; Farle, M.; Barcikowski, S.; Erni, D.; Gökce, B. Article formation of fe-ni nanoparticle strands in macroscopic polymer composites: Experiment and simulation. *Nanomaterials* **2021**, *11*, 2095. [CrossRef] [PubMed]
68. Toby, B.H.; Von Dreele, R.B. GSAS-II: The genesis of a modern open-source all purpose crystallography software package. *J. Appl. Crystallogr.* **2013**, *46*, 544–549. [CrossRef]

7.2 Study II

Khairani, I. Y.; Spellauge, M.; Riahi, F.; Huber, H. P.; Gökce, B.; Doñate-Buendía, C. Parallel Diffractive Multi-Beam Pulsed-Laser Ablation in Liquids Toward Cost-Effective Gram Per Hour Nanoparticle Productivity. Adv. Photonics Res. 2024, 5 (5), 2300290, doi:10.1002/adpr.202300290.

CRediT Authorship Contribution of I.Y.K.: Conceptualization, methodology, investigation, visualization, writing – original draft preparation, writing – review and editing.

ADVANCED PHOTONICS RESEARCH
Open Access
www.adpr-journal.com

Parallel Diffractive Multi-Beam Pulsed-Laser Ablation in Liquids Toward Cost-Effective Gram Per Hour Nanoparticle Productivity

Inna Y. Khairani, Maximilian Spellauge, Farbod Riahi, Heinz P. Huber, Bilal Gökce, and Carlos Doñate-Buendía*

Nanoparticles (NPs) generated by pulsed-laser ablation in liquids (PLAL) have benefited many key applications due to their versatility, enlarged surface area, and high purity. However, scaling up NPs production represents one of the main requisites to commercialize this technology. The established upscaling strategy demands high power and repetition rate laser source with fast scanning systems, which are not widely available and costly. Herein, a cost-effective alternative is proposed, the addition of static diffractive optical elements to achieve parallel processing through the multi-beam PLAL (MB-PLAL). In MB-PLAL, the optimum repetition rate is reduced to compensate laser energy splitting, hence achieving a higher interpulse distance, reducing pulse shielding, and increasing NPs productivity. MB-PLAL with 11 beams reached a factor 4 productivity increase for iron–nickel alloy ($Fe_{50}Ni_{50}$) NPs compared to the single-beam setup (0.4–1.6 g h^{-1}), and a factor 3 increase for gold (Au) NPs (0.32–0.94 g h^{-1}). The scalability of the proposed MB-PLAL technique setup is confirmed by Au and $Fe_{50}Ni_{50}$ NPs productivity experiments using 1, 6, and 11 beams, showing a linear increase in productivity.

1. Introduction

Pulsed-laser ablation in liquid (PLAL) is a versatile technique to synthesize a wide variety of colloidal nanoparticles (NPs) by ablation with a high-intensity pulsed laser of a bulk target immersed in the desired liquid.[1] When a high-intensity laser pulse ($>10^9$ W cm^{-2})[2] reaches the target material, the surface of the material is evaporated, forming a hot plasma plume containing ions and atoms of both the target and the liquid. Once the plasma plume collapses and the cavitation bubble is formed from the evaporation of the surrounding liquid, the ions and atoms of the bulk target are released to the liquid media due to the rapid release of vapor,[3] while larger droplets are ejected through the photomechanical spallation.[4] The process is followed by the condensation due to the rapid quenching by the liquid (evaporation–condensation mechanism[5]). Subsequently, primary NPs are formed in the liquid media through condensation nucleation,[6] while coalescence and growth contribute to the formation of larger secondary particle.[7–9] The production of NPs by PLAL offers several advantages, including the synthesis of surfactant-free NPs;[10,11] the versatility of the process[12,13] that allows the generation of metallic;[14] alloyed metal,[15] oxide,[16] ceramic,[17] and organic NPs;[18] and the ability to produce NPs with complex structures and compositions that poses a challenge for standard chemical methods,[19–24] such as metastable bimetallic alloys,[25,26] or high-entropy alloy NPs.[22] Producing NPs with a surfactant-free surface is a highly desirable property in the field of biomedicine and catalysis[27] as the surface composition of the NPs strongly influences the biocompatibility and the cytotoxicity of the NPs,[28] the specific surface area of the nanocatalysts,[2,10,29,30] and generally the active surface sites for light conversion, harvesting, and sensing.[31–33] In addition, PLAL complies with the green chemistry principles[34] compared to chemical synthesis routes as it is performed in an ambient atmosphere, requires less or no hazardous solvents and chemicals, produces less waste, and favors efficient reactant employment (atom economy).[35]

Despite the advantages offered by PLAL, its industrial use is still limited due to the low production rate compared to the chemical synthesis routes.[35] The productivity of PLAL ranges from several milligrams to several grams per hour depending on the experimental parameters, with the highest mass productivity at 8 g h^{-1} achieved for the ablation of Pt in water using a high-power laser and high scanning speed system that requires a huge initial investment.[36,37] Increasing PLAL productivity represents nowadays one of the main challenges of this technique.[2,35] Several approaches to improve and study the deciding factors

I. Y. Khairani, F. Riahi, B. Gökce, C. Doñate-Buendía
Chair of Materials Science and Additive Manufacturing
School of Mechanical Engineering and Safety Engineering
University of Wuppertal
42119 Wuppertal, Germany
E-mail: goekce@uni-wuppertal.de

M. Spellauge, H. P. Huber
Department of Applied Sciences and Mechatronics
Munich University of Applied Sciences HM
Munich 80335, Germany

The ORCID identification number(s) for the author(s) of this article can be found under https://doi.org/10.1002/adpr.202300290.

DOI: 10.1002/adpr.202300290

of PLAL productivity have been discussed,[35] including target-related parameters such as geometry,[38,39] feeding method,[39,40] porosity,[41] and composition;[13,42] liquid-related parameters such as liquid dynamics,[43,44] layer thickness,[40,45] and viscosity;[46–48] as well as laser- and scanner-related parameters such as laser fluence,[49] pulse duration,[50,51] and scanning speed.[52,53] One of the most successful approaches up to date to increase PLAL productivity is employing a high repetition rate (MHz) and high power (hundreds of watts) picosecond laser[35] coupled with a high-speed (hundreds of meter per second) beam steering system to maximize the number of pulses ablating the target (high repetition rate) while keeping the fluence of each pulse above the threshold fluence, ideally at approximately $F = e^2 \cdot F_{\text{thr}}$,[54] where F is the fluence (on the target during the experiment) and F_{thr} is the threshold fluence. This approach allows to maximize the inter-pulse distance on the target to avoid cavitation bubble shielding by utilizing high scanning speed.[53] Furthermore, the use of picosecond pulses effectively avoids nonlinear energy losses in the liquid associated with femtosecond lasers, while also reducing energy losses by thermal diffusion in the target and shielding by the bubble evolving in the early nanosecond time domain,[55,56] which are relevant concerns when using nanosecond laser pulses.[57–59] Further increasing the repetition rate and power of the picosecond laser sources required for high productivity PLAL is limited by the technological advances in the laser manufacturing industry, finding already in the literature PLAL experiments with 3 ps, 500 W, and 10 MHz.[53] The most common laser-steering technology, galvanometer scanner, provides speeds up to $50\,\text{m}\,\text{s}^{-1}$,[60–62] but assuming a cavitation bubble size of 100 μm,[52] this speed can only avoid beam shielding for a repetition rate of 350 kHz.[53] Thus, a scanning speed higher than $100\,\text{m}\,\text{s}^{-1}$ is essential to accommodate a high-power and high-repetition-rate laser in the PLAL process. Barcikowski and coworkers utilized a polygon scanner which can reach a scanning speed of $484\,\text{m}\,\text{s}^{-1}$ to achieve a productivity of $8\,\text{g}\,\text{h}^{-1}$ for the ablation of Pt in water[36] and $3.8\,\text{g}\,\text{h}^{-1}$ for the ablation of Au in water.[52,53] Nevertheless, to avoid uncontrolled beam deflection due to the edges between the rectangular mirrors of the polygon scanner, a duty cycle is required, limiting the effective laser power to 50%.[36,52,53] Furthermore, the high price of the polygon scanner compared to the galvanometer scanner increases the capital investment and so the NP production cost in PLAL,[37] disrupting its prospective use in industrial applications. Consequently, even though a maximum PLAL productivity of $8\,\text{g}\,\text{h}^{-1}$ has been achieved for Pt NPs, the specific laser source and scanning systems require a large initial investment and cannot be acquired extensively in other research labs and industrial facilities to widen the employment of PLAL for large-scale NP production. Hence, alternative approaches that can be implemented with standard commercial laser sources and galvanometric scanners should be explored to deliver pulses with energies above the ablation threshold of the material with megahertz repetition rates while achieving a sufficient interpulse distance to bypass the cavitation bubble and achieve production rates in the gram per hour scale.

In this work, we propose an approach to increase PLAL productivity by adapting the successful strategy of parallel multi-beam processing employed in laser material processing in air to PLAL. Diffractive beam splitting has allowed to increase in the efficiency of laser processing in air, achieving multiple and homogenous surface patterns.[58,63–65] The employed beam-splitting strategies distribute the laser beam into an array of $M \times N$ spots or lines[63] with a pulse energy reduction of a factor $M \times N$, where M and N are natural numbers. If the initial laser pulse has enough energy to maintain the desired fluence in the individual spots, beam splitting allows the production of defined patterns on the target with a single shot instead of requiring $M \times N$ individual laser exposures, hence highly reducing the processing time in the optimum case by a factor of $M \times N$.[66,67] In addition to that, beam splitting enables to operate at the optimal material processing fluence ($\approx e^2 \cdot F_{\text{thr}}$) for high energy and power laser sources.[58] There exist different approaches to split the laser beam,[68] including the employment of static diffractive optical elements (DOEs), spatial light modulators (SLMs), and acousto-optic or electro-optic modulators (AOM/EOM). Each of the methods has a different working principle and advantages: 1) DOEs consist of static optical elements with periodic microstructures that modify the beam's phase and amplitude, 2) SLMs dynamically modulate the beam's phase, amplitude, and/or polarization applying electrical signals to electrically anisotropic liquid-crystal molecules, 3) AOMs use a piezoelectric transducer to generate standing sound waves which modify the refractive index of a crystal, while EOMs employ variable electric voltage signals to modulate the refractive index of an electro-optic crystal. Nevertheless, SLM's diffraction exhibits an efficiency of ≈40%,[69] while AOM/EOM requires a large initial investment and can be limited by the achievable pattern size. In addition, specific SLMs and AOMs/EOMs are required for high power and repetition rate picosecond laser sources due to their damage threshold and cooling requirements, hence significantly increasing the price.[68] In this study, DOEs are chosen due to their high damage threshold;[70] high efficiency (typically in a range of 80–95%);[68,70,71] high pattern homogeneity;[63] robustness against beam parameters modification such as beam size, beam quality, and lateral displacement;[63] and lower price and easy implementation in any optical setup compared to SLMs and AOM/EOMs, allowing to easily adapt and transfer the proposed MB-PLAL system to any PLAL system available worldwide. The MB-PLAL is envisioned to provide the benefits of parallel multi-beam laser processing as higher material removal and efficient employment of high-power laser sources. In addition, an improvement of the essential factor required to increase the productivity of PLAL method is expected: the increase of the interpulse distance by reducing the repetition rate needed to achieve the optimum processing fluence, hence reducing the PLAL demand for faster scanning systems to avoid cavitation bubble pulse shielding and scale up NP production rate. This report highlights the use of MB-PLAL to successfully increase the productivity of iron nickel alloy by factor 4 ($1.6\,\text{g}\,\text{h}^{-1}$) through the integration of 11-beam splitter DOE. Morphology, particle size, and phase of the produced NPs were also analyzed, proving uniform and consistent properties of the generated particles as a function of beam-splitting number, rendering suitable use of MB-PLAL in the upscaling process and industrial outlook.

2. Experimental Section

2.1. Material Selection, Productivity Determination, and NP Characterization

The targets employed to investigate the MB-PLAL production upscale were Au ($1 \times 20 \times 70\,mm^3$, 99.99%, EVOCHEM Advanced Materials GmbH) and $Fe_{50}Ni_{50}$ ($1 \times 20 \times 70\,mm^3$, 99.95%, Sindlhauser Materials GmbH). Au was employed as the reference material in PLAL productivity. On the other side, FeNi was selected as an example of a technologically relevant nanomaterial required in large amounts. One of the primary benefits of FeNi NPs was in the field of electrolyzer technology, where the material was proven as an economic and abundant alternative catalyst to ruthenium oxide (RuO_2) to accelerate oxygen evolution reaction for water splitting.[72–74] As green hydrogen would play a key role in decarbonization,[75] the production of this type of renewable energy through electrolysis represents a major goal to address the UNESCO sustainable development goals.[76] Hence, supplying abundant and efficient FeNi NPs catalysts to meet the demand for electrolyzers is critical. All the obtained productivity values were measured by the gravimetric method after 5 min of PLAL, weighing the target before and after ablation with an analytical balance. The splitting of the beam to generate the multiple beams was done using DOEs and 6-beam DOE and 11-beam DOE were used. The productivity measurements from the PLAL experiments using a single–beam DOE, 6-beam DOE, and 11-beam DOE were repeated three times to ensure reproducibility. The characterizations of the generated FeNi and Au colloidal NPs were performed by a high-resolution transmission electron microscopy (HR-TEM, JEOL JEM-2200FS, 200 kV, ZrO_2/W emitter) and powder X-ray diffraction (XRD) (Bruker D8 Advance Powder Diffractometer, Bragg-Brentano geometry, CuKα radiation 1.5418 Å, 40 kV, and 40 mA). To simplify the naming, standard single-beam PLAL without any DOE will be further addressed as "standard PLAL", while the PLAL process with 1:6- and 1:11-beam-splitter DOE will be referred to as "6-beam MB-PLAL" and "11-beam MB-PLAL", respectively.

2.2. Single-Beam PLAL

A 10 ps neodymium-doped yttrium aluminum garnet (Nd:YAG) laser with a wavelength of 1064 nm, an average power of 120 W, a tunable repetition rate of 400–4000 kHz, a raw beam diameter ($1/e^2$ criteria) of 5 mm, and a beam quality of 1.11 was employed. The laser beam was directed on the $Fe_{50}Ni_{50}$ (FeNi) or Au target by a galvanometer scanner coupled with an f-theta lens (focal length of 167 mm) describing an Archimedean spiral pattern (10 mm diameter) with a marking speed of $20\,m\,s^{-1}$. Several parameters such as repetition rate, working distance, and liquid flow rate were optimized to accommodate the highest productivity achieved in the setup. The laser parameters such as laser power, repetition rate, beam area at plane, and pulse energy are presented in Table S1, Supporting Information. The highest laser power achievable for the employed repetition rate was employed to ensure productivity maximization. Distilled water (18.2 MΩ cm at 25 °C ultrapure Mili-Q water, Synergy Water Purification System) was used as the liquid source and pumped by a peristaltic pump at $500\,mL\,min^{-1}$. A quartz window (2 mm thickness) with an antireflective coating at laser wavelength ($R < 0.25\%$) was employed, and the liquid layer thickness, defined as the distance between the inner side of the glass and the surface of the target, was approximately 6 mm.

2.3. MB-PLAL Process (Multiple Beams)

The splitting of the initial laser beam into 6 and 11 equivalent beams was achieved by the use of beam-splitting DOEs, a 1:6-beam-splitter DOE (HOLOEYE Photonics AG) and a 1:11-beam-splitter DOE (LIMO Lissotschenko Mikrooptik GmbH), respectively. Parameters such as repetition rate and working distance were independently optimized for each material and the number of beams produced by the DOE. The DOE was placed after the *f–θ* lens of the scanner to accommodate the use of a large scanning pattern, **Figure 1**. Placing the DOE before the

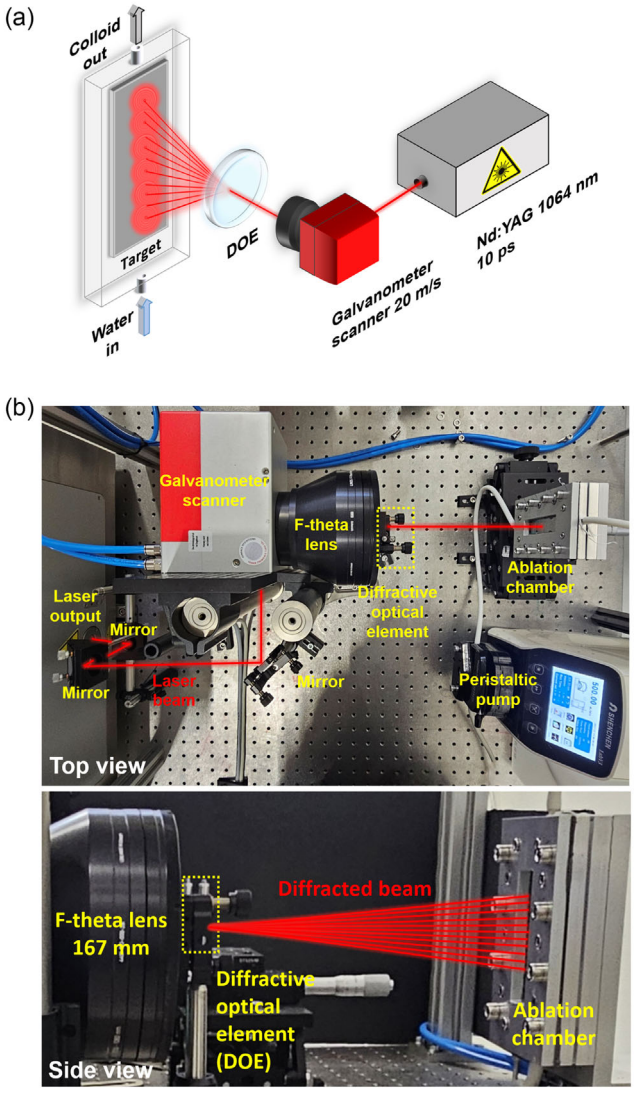

Figure 1. a) Schematic illustrations of the MB-PLAL process in a flow chamber with a 1:11-beam-splitter DOE and b) real setup of the experimental procedure with top and side views. Note that the beam splitter DOE is placed close to the *f–θ* lens to avoid the focused beam damaging the DOE.

scanner limits the length of the array of spots. In addition, separating the beam before the scanner may induce larger positioning uncertainty for the beams at the edge of the f–θ lens.[58] The average power of the laser before adding the DOE was measured to be approx. 100 W at 400 kHz. After implementing 11- and 6-beam DOEs, the power was slightly reduced to ≈98.8 and 99.3 W, respectively, suggesting only minor power losses well below 2%. The beam splitters reduced the pulse energy of each individual beam after the 6-beam and 11-beam DOEs by a factor of 6 and 11, respectively.

To explain the effect of the DOE on the MB-PLAL processing conditions, a schematic representation is shown in **Figure 2**. A standard PLAL without beam splitting is represented in Figure 2a, where the laser beam with a certain power P and repetition rate f_{rep} results in a pulse energy E_{p} as described by Equation (1):

$$E_{\mathrm{p}} = \frac{P}{f_{\mathrm{rep}} \times N} \tag{1}$$

where P is the average laser power (W); f_{rep} is the repetition rate (Hz); and N is the number of beams. The normalized pulse energy in the standard PLAL setup as a function of time and position on the target is depicted in the graphs in Figure 2a. As a representative example, a twofold beam splitting is illustrated, the beam from the laser with a certain repetition rate f_{rep} and pulse energy E_{p} was split into two beam parts, halving the pulse energy for each beam to $(E_{\mathrm{p}}/2)$ (see Figure 2b). Hence, to obtain the same pulse energy E_{p} as in the standard PLAL, see Figure 2a, the laser power had to be doubled $(2P)$ while keeping the same repetition rate f_{rep}; this way, the delivered number of pulses was twice the standard PLAL, while the pulse energy was the same. In the case where power cannot be doubled, the repetition rate needed to be halved $(f_{\mathrm{rep}}/2)$ to obtain, the same pulse energy Figure 2c; this way, the pulse energy for each of the beams generated after the DOE was the same as the initial standard PLAL system as shown in Figure 2a and, as a positive side effect, the spot distance on the target was increased by two times, reducing bubble shielding.

In our case, the goal is to upscale NP productivity, thus, the laser power employed in every experiment was the one that our laser source could deliver. To adjust the fluence employed and maximize productivity, the approach followed was to adjust

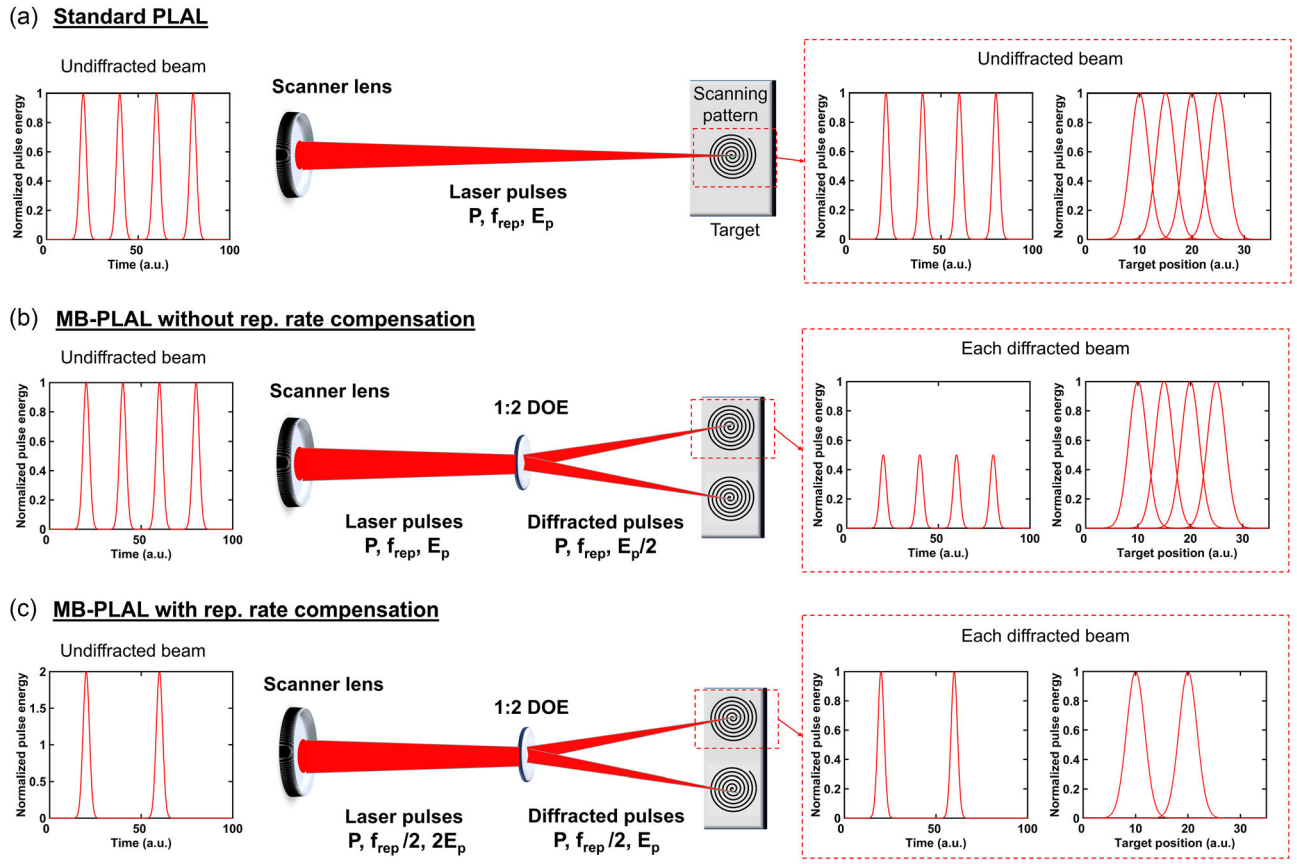

Figure 2. Schematic diagram of the PLAL process to illustrate the relation between pulse energy E_{p} and repetition rate f_{rep} in a) a standard PLAL without beam splitting, b) an MB-PLAL setup generating two beams without repetition rate compensation (using the same repetition rate f_{rep} as the standard PLAL), and c) an MB-PLAL setup generating two beams and with repetition rate compensation (repetition rate value is reduced by a factor of 2 $(f_{\mathrm{rep}}/2)$ according to the number of beams generated, leading to a two times larger spot spacing on the target). Please note that the normalized pulsed energy of the undiffracted beam in (c) is twice $(2E_{\mathrm{p}})$ of the normalized pulsed energy of diffracted beam (E_{p}). The term "a.u." is an abbreviation from "arbitrary unit," indicating a comparative unit for a relative quantification.

the repetition rate. The optimum repetition rate for the standard PLAL of FeNi in water was 3000 kHz (Figure S1, Supporting Information). When the beam was split into 6 and 11 beams, in the case of 6-beam and 11-beam DOE PLAL, the repetition rate was reduced to 500 and 400 kHz, respectively, trying to reach the optimum value that would be dividing the repetition rate of the maximum productivity achieved with the standard PLAL system by 6 and 11. However, 400 kHz was the lowest repetition rate achievable in our laser system.

3. Results and Discussion

3.1. PLAL and MB-PLAL FeNi NPs Productivity

To study the influence of beam splitting on PLAL productivity and investigate the advantages and limitations of the proposed MB-PLAL configuration, we compared the mass productivity values of the standard PLAL and the MB-PLAL setups. As shown in **Figure 3**a, the FeNi NP productivity using the standard PLAL configuration was 0.4 g h^{-1}. After placing the 6-beam DOE, the repetition rate was reduced to 500 kHz (one-sixth of the repetition rate of standard PLAL) to employ a similar pulse energy value, as explained in Section 2.3. With the 6-beam splitter, we obtained a productivity jump from 0.4 to 1.24 g h^{-1}, which represents a factor 3 increase (Figure 3a). The 11-beam MB-PLAL, in contrast, was performed at 400 kHz due to the impossibility of further reducing the repetition rate of our laser source, hence, the pulse energy and fluence in this setup was lower than the standard PLAL and 6-beam MB-PLAL. Nevertheless, the increase in productivity is still observed, obtaining productivity as high as 1.6 g h^{-1} with an increasing factor of 4 compared to the standard PLAL. To the best of our knowledge, this is the first time a productivity value of 1.6 g h^{-1} has been reported for PLAL of $Fe_{50}Ni_{50}$ in water. The power-specific productivity (Figure 3b) was calculated by dividing the mass productivity by the employed laser power. This comparison of power-specific productivities using different beam splitters is important to evaluate the power efficiency of the laser system after the DOE addition. As shown in Figure 3b, the power-specific productivities of 6-beam and 11-beam MB-PLAL were increased 3.5 and 4 times compared to the standard PLAL, respectively. The increasing trend of power-specific productivity is also similar to the trend of mass productivity, which confirms the enhanced laser power delivery to the target for the MB-PLAL configuration.

The underlying reason for this improved delivery of laser power and hence productivity rise lies in the achieved interpulse distance increase from approximately 7 μm (single beam) to 50 μm (11 beams) due to the repetition rate reduction. The larger interpulse distance reduces the laser beam interaction with the cavitation bubble generated by the previous laser pulse (**Table 1**). The advantage of using the beam splitter is the ability to increase the interpulse distance while keeping the same number of pulses delivered to the target. In the standard PLAL system without the beam splitter (and a fixed scanning speed), one might need to reduce the repetition rate value to achieve the desired interpulse distance. However, the reduction of the number of pulses irradiating the target would highly reduce productivity. In addition, the cavitation bubble would be enlarged due to the increase of the pulse energy[77,78] resulting in the subsequent increase of the laser pulse shielding. If the repetition rate and fluence are kept constant, the compromise would be to lower the laser power, which means that the maximum outcome of the laser source is not fully utilized to achieve the highest productivity. Meanwhile, if we want to keep the same pulse energy, fluence, repetition rate, and power while increasing the interpulse distance, the scanning

Table 1. The influence of the proposed repetition rate compensation in MB-PLAL depending on the number of generated beams by the DOE and the effect on the interpulse distances.

Number of beams [N]	Rep. rate [MHz]	Power [W]	Pulse energy [μJ]	Scanning speed [m s^{-1}]	Interpulse distance [μm]
1	3	111.2	37.1	20	7
6	0.5	99.3	33.1	20	40
11	0.4	98.8	22.5	20	50

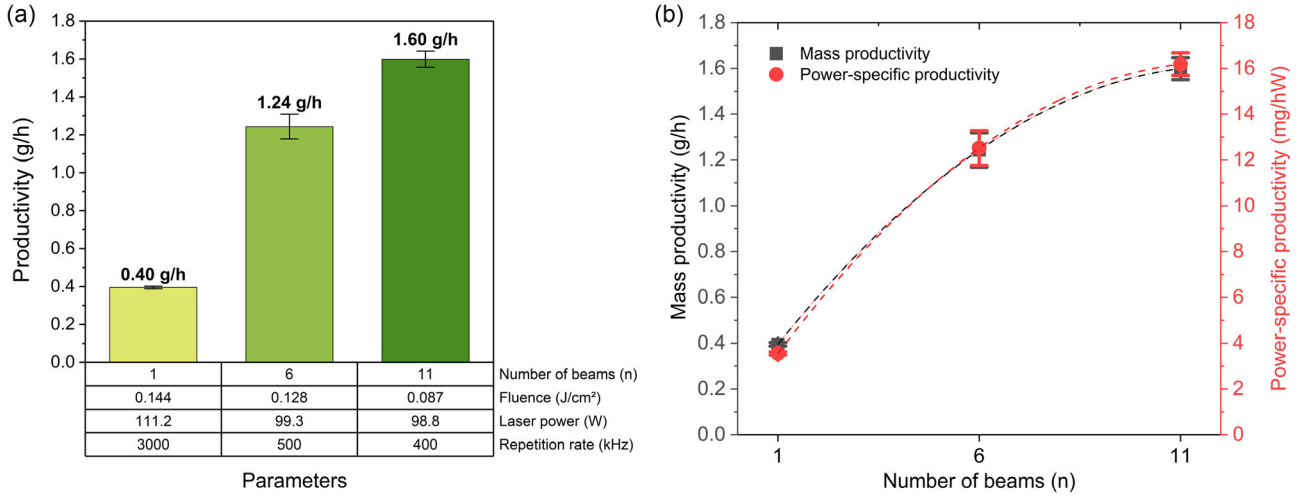

Figure 3. a) FeNi NP productivity in water values at the optimized parameters. b) Productivity and power-specific productivity comparison as a function of the number of beams.

speed has to be increased to at least 150 m s^{-1} to achieve an interpulse distance of 50 µm with 3000 kHz repetition rate (maximum FeNi NP productivity for the standard PLAL system). This high scanning speed can be achieved by a polygon scanner, but the polygon technology requires the laser shutter to be closed when the beam pathway is nearing the corner of the polygon mirrors to avoid uncontrollable beam pathways which can damage the scanner.[36] Depending on the duty cycle, the delivered laser power could be cut by half[53] and the power efficiency is therefore reduced.[36] In addition to that, the capital investment to purchase a polygon scanning system[37] is significantly greater than the price of a galvanometer system combined with the DOE. Based on these considerations, we propose the MB-PLAL system as an economical alternative to boost the productivity of PLAL-generated NPs by increasing the interpulse distance and efficiently delivering pulses at MHz repetition rates without considerable power losses or the necessity to use cutting-edge high-speed scanning systems.

We further measured the productivity of the FeNi target at the same fluence and repetition rate by changing the laser power (Figure S2, Supporting Information). In this measurement, we aim to calculate the productivity increase factor as a function of the number of beam(s) at the same fluence value, as the fluences presented in Figure 3 could not be kept constant due to the laser's technical limitations not allowing to reduce the repetition rate below 400 kHz. The measurement parameters of this study are presented in Table S2, Supporting Information. From the standard PLAL to 6-beam and 11-beam MB-PLAL, the productivity increase factors are 3.6 and 6.4, respectively (Figure S2, Supporting Information). Even though the laser power is increased according to the number of beams, the productivity is not increased 6 and 11 times. The nonlinear scale-up is probably due to the energy lost as shock waves,[79] in addition to turbulences and backflow inside the ablation chamber, promoting laser shielding by the NPs, cavitation bubbles, and persistent microbubbles. Based on the linear fitting, it is possible to infer that increasing the number of beams with other DOEs could result in even higher productivity if a laser with a higher power and higher repetition rate is used. The inset in Figure S2, Supporting Information, shows the ablation area of the FeNi target after the 11-beam MB-PLAL process, confirming an increase of seven times compared to the single-beam ablation. The influence of the ablation area and spatial beam overlapping on productivity have not been evaluated; however, the 11-beam MB-PLAL shows the highest productivity with the largest ablation area, pointing out the possibility of a future further productivity increase by avoiding beam overlap.

Ensuring consistent properties, i.e., morphology, particle size, and crystalline structure, of the produced NPs in the MB-PLAL is a crucial consideration for the scalability of the process and the prospective industrial use. The particle size distribution of the generated FeNi NPs was measured to investigate the influence of MB-PLAL setup to the morphology and size of the resulting NPs, **Figure 4**a. Based on the TEM images in Figure 4a, FeNi NPs are formed as core–shell, which is in agreement with the structure reported in previous FeNi PLAL experiments.[19] The median values (x_c) of the log-normal fitting of all the samples are similar, 14 ± 7 nm for the standard PLAL (1 beam), 11 ± 9 nm for the 6-beam MB-PLAL, and 14 ± 13 nm for the 11-beam MB-PLAL. The x_c is slightly smaller for the 6-beam MB-PLAL, but the difference is not significant and within the standard deviation. The polydispersity index (PDI), obtained from σ^2/μ^2 where σ represents the standard deviation and µ indicates the mean value, shows a value of 0.26 for the single-beam ablation, which is smaller than the samples with beam splitting with respective values of 0.44 and 0.53 for 6- and 11-beam processing. Although there seems to be a trend of increasing PDI and standard deviation values with the increasing number of beams, a more thorough investigation should be performed to confirm this trend. Based on our current observations, as shown in the inset of Figure 4a as well as the HR-TEM images of FeNi and Au NPs generated in different number of beams and repetition rates in Figure S3, Supporting Information, we do not observe any significant changes in the morphology or particle size as a function

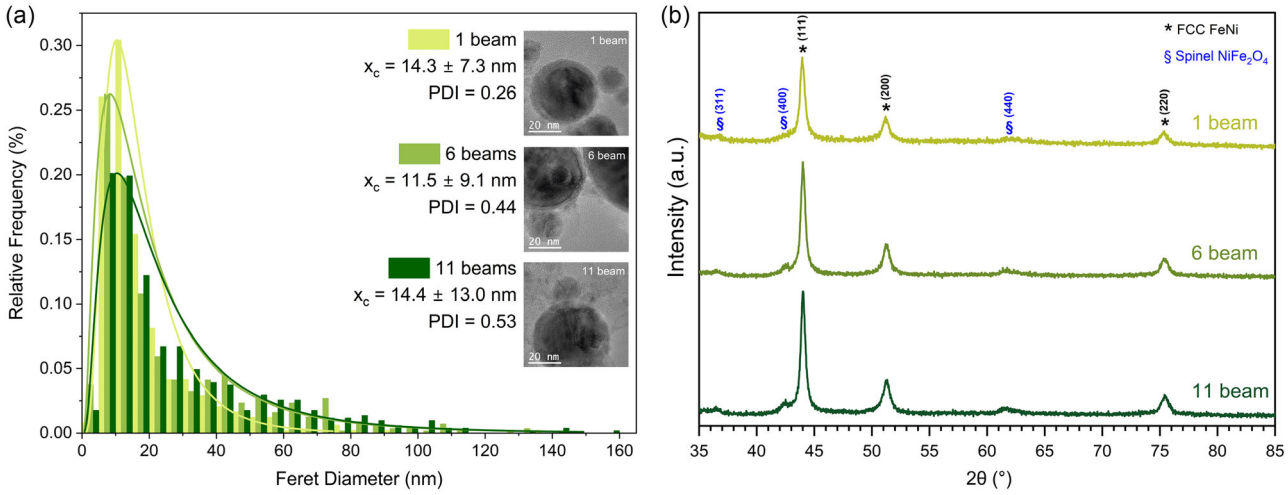

Figure 4. a) Particle size distribution and b) XRD diffractogram of standard PLAL (1 beam) and MB-PLAL (6 beams and 11 beams) of FeNi NPs. The measurements of particle size in (a) were done using ImageJ software of more than 400 particles. The insets in (a) show the HR-TEM images of FeNi NPs generated using different numbers of beams.

of the number of beams. Analysis of the crystalline structure was also sought to ensure consistent phase of the produced NPs, Figure 4b. Two phases are formed in the standard 1-beam PLAL of FeNi in water: face-centered cubic (FCC) FeNi and spinel $NiFe_2O_4$.The FCC FeNi occupies the core part of the NPs, while spinel nickel ferrite ($NiFe_2O_4$) can be found in the shell part as a result of oxidation.[19] Based on the diffractograms of FeNi NPs generated with different number of beams, Figure 4b, there is no formation of new peaks or disappearance of peaks as compared to the single-beam diffractogram, which indicates that the crystalline structure of the FeNi NPs remains constant for MB-PLAL, finding the FCC and spinel nickel ferrite composition. It can be concluded that the MB-PLAL does not influence the properties of the generated FeNi NPs and it is therefore suitable for direct PLAL NP production upscaling without influencing the composition, phase, or size of the produced NPs.

3.2. PLAL and MB-PLAL Au NPs Productivity

The productivity comparison of FeNi with a benchmark material such as Au is essential to help us understand the influence of the material's property on the MB-PLAL productivity value and the possibility of generally extending the results. Colloidal gold NPs are chosen due to their practical versatility in various applications, such as air and water purification, immunotherapy, cancer treatment, sensor, biomarker, and drug delivery,[80–82] and their high-value increase compared to their bulk counterpart.[83] The standard PLAL and MB-PLAL mass productivity of FeNi and Au NPs are compared in **Figure 5**. The results shown were performed at the optimized processing parameters for each material (Table S1, Supporting Information), as each material has a different ablation fluence threshold. The standard PLAL productivity of Au and FeNi is similar, 0.32 and 0.40 g h^{-1}, respectively. The productivity increase factors of Au from the standard PLAL to 6-beam and 11-beam MB-PLAL are found to be 2.1 and 3, which is lower than FeNi increase factors of 3.1 and 4, respectively (Figure 5).

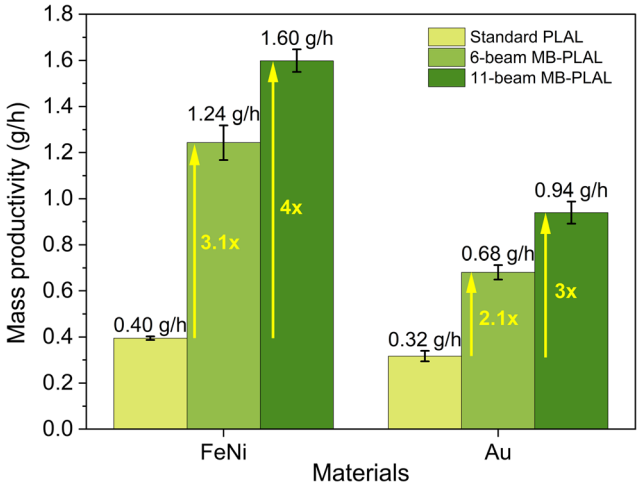

Figure 5. Mass productivity comparison between FeNi and Au ablation in water for PLAL and MB-PLAL NP production experiments.

Although usually material-dependent productivity has been reported to be linked to the trend of material density,[84] other underlying reasons might have influenced the productivity differences observed between FeNi and Au in our case. 1) Larger bubble half-width of Au than FeNi, Figure S5, Supporting Information, which contributes to a larger pulse shielding. The temporal distance between two pulses in the 11-beam MB-PLAL of Au and FeNi is 2.5 µs, as the employed repetition rate was 400 kHz. At this time range, the cavitation bubble half-width of Au is larger than FeNi, Figure S5, Supporting Information, resulting in a larger energy shielding. 2) The steady-state optical absorptance of Au at our laser wavelength (1064 nm) is 3%,[85] lower compared to the FeNi which is 35%. The higher the optical absorptance of the material at the irradiation laser wavelength, the higher the energy absorbed by the target material,[86–88] leading to a higher ablation volume. 3) The intrinsic chemical disorder of alloy materials as FeNi[89] contributes to a stronger electron–phonon coupling and lower thermal conductivity,[89] resulting in a lower threshold fluence than the corresponding elemental materials. The HR-TEM images of FeNi and Au NPs generated by different numbers of beams are presented in Figure S3, Supporting Information, where no change in particle morphology and size could be observed. While the FeNi NPs show mostly spherical morphology, the Au NPs seem to melt forming necks between the NPs.

3.3. Economical Perspective of MB-PLAL for High-Throughput NPs

The definition of productivity in PLAL does not solely revolve around mass productivity, but also power-specific productivity and investment-specific productivity. The power-specific productivity tells us the efficiency of the available laser power used for PLAL. It is important to make this distinction because high productivity values do not always imply high power-specific productivity. The laser power can be partially wasted due to the cavitation bubble pulse shielding, laser–liquid interaction, or the beam steering method such as in the case of polygon scanners.[35] We have discussed in the previous section the power-specific productivity of FeNi and how it follows a similar trend as mass productivity. A similar trend is also observed for Au (**Figure 6**a), although the values are smaller than FeNi due to the aforementioned reasons. As we are aiming to scale up PLAL productivity by proposing the MB-PLAL configuration suitable for any PLAL setup, the value of power-specific productivity can give a hint of how efficiently the MB-PLAL can be implemented in other labs worldwide to upgrade their PLAL system to produce larger amounts of NPs.

However, another definition of productivity is needed to evaluate NP productivity as a function of capital investment, which is related to the price to procure the instruments and units required to start ablation. Capital investment budgeting is a vital part of management policy formulation because it correlates with many business factors such as growth, expansion, budget diversification, modernization, and long-term planning.[90] The value of investment-specific productivity tells us the hourly produced amount of NPs for every 1000 € of capital investment poured into the PLAL system. The higher the value, the more efficient the

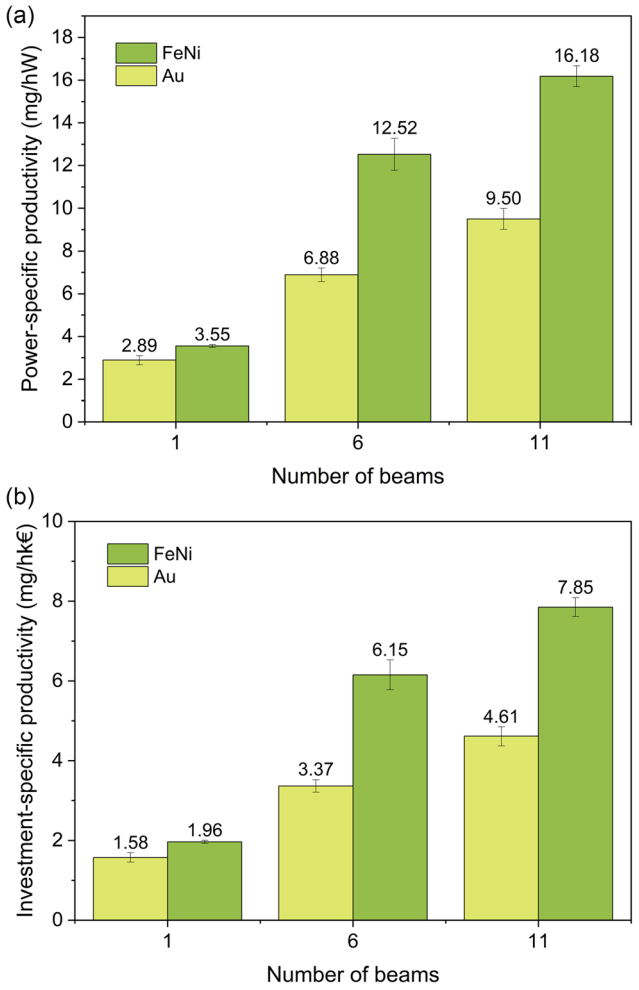

Figure 6. a) Investment-specific productivity and b) power-specific productivity of FeNi and Au NPs for PLAL and MB-PLAL as a function of the number of beams. The shown error bars define the standard deviations calculated from three measurements.

production is in terms of the required investment. Here, we define the PLAL system as the combination of the laser system, the optical table, the scanning system (including the software and the *f–θ* lens), the water pumping system, and the DOE if applicable. From the results presented in Figure 6b, the investment-specific productivity of Au and FeNi with 11-beam MB-PLAL are 4.6 and 7.9 mg $(hk€)^{-1}$, respectively. A linear increasing trend, similar to the mass- and power-specific productivities, is also observed for the investment-specific productivity. This is because the price of the beam-splitter DOE is marginal compared to the laser and scanning systems, thus, the DOE does not significantly increase the total capital investment of the PLAL system. Hence, another advantage of MB-PLAL is the possibility to increase productivity without significantly increasing capital investment.

An intriguing question arises, whether the performance of the MB-PLAL system is more suitable and beneficial for industry compared to the world-record PLAL productivity system proposed by Streubel et al.[52] Here, we present **Table 2**, where we compare our experimental parameters and productivity results of

Table 2. Comparison of experimental parameters and the resulting mass-, power-, and investment-specific productivities from ref.[52] and our experiment for the ablation of Au in water. The initial investment covers the price of purchasing the laser, the scanning system (including the *f–θ* lens), the optical table, the pumping system, and the DOE (if applicable).

Parameters	Streubel et al.[52]	This work	
		With 11 DOE	Without DOE
Laser power [W]	500.0	98.9	109.7
Scanning speed [m s^{-1}]	484	20	
Pulse width [ps]	3	10	
Repetition rate (laser) [MHz]	10.1	0.4	2.0
Delivered pulses (on the target) [pulses s^{-1}]	10.1×10^6	4.4×10^6	2.0×10^6
Pulse energy [μJ]	42.0	22.5	54.9
Interpulse distance [μm]	48	50	10
Mass productivity (Au) [g h^{-1}]	3.80	0.94	0.32
Power-specific productivity (Au) [mg $(hW)^{-1}$]	7.60	9.50	2.92
Initial investment [€]	671,800.00	203,700.00	201,100.00
Investment-specific productivity (Au) [mg $(hk€)^{-1}$]	5.66	4.61	1.59

Au PLAL to ref. [52]. The first and the most striking comparison is the scanning speed. A high-speed polygon scanner with a speed of 484 m s^{-1} is employed in ref.[52] employed to achieve an interpulse distance of 48 μm at a repetition rate of 10.1 MHz. Meanwhile, our beam-splitting system could achieve an interpulse distance of 50 μm using a galvanometer scanner with a scanning speed of 20 m s^{-1}, which is 24 times slower than the polygon scanner.[52] The number of delivered pulses onto the target's surface is also another point worth comparing. In our case, we reduced the repetition rate to the lowest value in our system to compensate for the pulse energy splitting by the DOE and achieved a 50 μm interpulse distance. Nevertheless, we could still deliver 4.4×10^6 pulses s^{-1} due to the splitting by the 11-beam DOE. In addition, as the pulse energy is reduced in the MB-PLAL setup, we can avoid the formation of a large cavitation bubble.[91] Although the number of delivered pulses, 4.4×10^6 pulses s^{-1}, is still lower than in ref. [52] (10^7 pulses s^{-1}), we were able to deliver the equivalent number of pulses to a laser operating in the megahertz regime even using a lower repetition rate of 400 kHz. The number of delivered pulses by the 11-beam MB-PLAL system at 400 kHz also exceeds the maximum number of pulses achievable with our laser in the standard PLAL configuration, operating at 4 MHz. Hence, beam splitting is advantageous for a laser system with high pulse energy but a low repetition rate, as the number of delivered pulses can be adjusted externally by selecting the optimum DOE.

Another point we would like to emphasize is power-specific productivity. The power-specific productivity is trimmed down to 7.6 mg hW^{-1}, which is lower than our value at 9.5 mg hW^{-1} even when we only used an average power of 100 W. Lastly, the investment-specific productivity of our system reached almost a similar value at 4.6 mg $(hk€)^{-1}$ despite requiring only one-third

of the capital investment compared to ref. [52]. The price difference comes mostly from the laser and scanning system, as a custom high-power picosecond laser (500 W) and a high-speed polygon scanner are employed in ref. [52]. A lower initial capital investment, in addition to the commercially available laser and DOE employed in this work, could increase the likelihood for the industry to invest and utilize the MB-PLAL configuration especially for small to medium-sized companies, and also to facilitate access to PLAL to research institutions and universities requiring a versatile NP production technique.

With an aim to upscale and introduce MB-PLAL to the industry, we present the economical perspective of Au NPs production using MB-PLAL. We performed a cost-benefit analysis related to the labor and electricity costs that are needed to produce 1 kg of Au NPs (**Table 3**) and the daily and yearly production rate (**Table 4**). The calculations of labor and electricity costs to produce Au NPs are based on the highest Au productivity achieved in our laser system. Several assumptions are considered, such as the gross salary assumption of the working staff at 21 € h^{-1} and the labor time which considers 2 h daily initial set up and adjustment for every 8 h ablation. The electricity consumption is measured for the whole PLAL system, which is approximately 3 kWh.

Based on the calculation, using the 11-beam MB-PLAL, the total labor working hours are reduced by one-third compared to the standard PLAL, which saves approximately 54 000 € of labor cost for every 1 kg of Au NPs produced. In addition, the electricity consumption could be trimmed down by 66% and it is possible to save around 2500 € per 1 kg of Au NPs when using the 11-beam splitter. As also calculated by Jendrzej et al. in their cost comparison to produce 1 g of Au NPs,[83] the energy cost (electricity) to produce the Au NPs is much smaller compared to the labor cost to operate the laser. Hence, the main advantage of using the MB-PLAL is the labor cost reduction.

Meanwhile, for the time-based production rate, as shown in Table 4, we focus on the daily and annual production as well as the percentage increase of production when using the DOE compared to the standard PLAL. By assuming the 16 h daily ablation time and 350 days of annual working days, the percentage increase of the daily and annual production rate using the 11-beam MB-PLAL compared to the standard PLAL is almost 200%, where the daily production is increased from 3 to 8 g per day, and the annual production is increased from 640 to 1800 g per year. The most important point based on these calculations is that we can achieve this jump in production and cost reduction just by increasing the capital investment by 1.3% to acquire the 11-beam splitting DOE. As for the case of the 6-beam DOE, the price is more affordable and the increase in capital investment is only 0.5%. The minuscule addition of capital investment and the low implementation time of the DOE in the PLAL setup are insignificant compared to the benefits achieved by the proposed MB-PLAL system.

Table 4. Calculation of the annual production rate of Au NPs using different numbers of beam(s). Please note that the electricity and labor costs are the same as the installment of DOE does not change the production costs.

DOE	Productivity [g h^{-1}]	Daily production [g][a)]	Annual production [g][b)]	Annual production increase [%]
1	0.32	5	1792	–
6	0.68	11	3808	113%
11	0.94	15	5264	194%

[a)]Assuming daily ablation time of 16 h. [b)]Assuming 1 year production is equal to 350 days.

Further calculations of the capital expenditure (CAPEX), operational expenditure (OPEX), and production cost per kilogram of the NPs have been done as both are crucial factors in deciding to start a new investment. In the CAPEX calculation, we consider the equipment needed to produce colloidal NPs. For the OPEX calculation, we measured the electricity consumption of the devices and the operational cost, which includes the labor cost to operate and maintain the system. Please note that for these calculations, we do not include the expenditure related to the land acquisition, building and infrastructure establishment, characterization of the produced NPs, and other parameters that are commonly included. Our focus is on the PLAL setup. Hence, the calculated values of CAPEX, OPEX, and production cost per kilogram are still less than the actual expenditure.

The calculated CAPEX of the 11-beam MB-PLAL is 267,000.00 € with 25% of contingency. Meanwhile, the total OPEX is 95,500.00 € consisted of total direct cost of 39,300.00 € (electricity and material cost) and total indirect cost (operational and services) of 56,200.00 €. The calculated production cost per kilogram of Au NPs is approximately 22,400.00 €. As for the standard PLAL and 6-beam MB-PLAL, the CAPEX is only slightly different from the 11-beam MB-PLAL as the DOE is the only changed element and the price is only approximately 1% of the total CAPEX. The CAPEX of standard PLAL is 263,900.00 € while 6-beam MB-PLAL is at 265,200.00 €. The OPEX of the standard PLAL is the lowest as fewer gold targets are required in

Table 3. Calculation of labor and electricity cost to produce 1 kg of Au NPs using different numbers of beam(s).

Number of beam(s)	Productivity [g h^{-1}]	Ablation time [h]	Labor working hours [h][a)]	Labor cost [€][b)]	Labor cost saving [€]	Electricity consumption [kWh][c)]	Electricity price [€][d)]	Electricity cost reduction [%]
1	0.32	3125	3906	82 031	–	9375	3750	–
6	0.68	1471	1838	38 603	43 428	4412	1765	53%
11	0.94	1064	1330	27 926	54 106	3191	1277	66%

[a)]Assuming daily initial setup and manual adjustment of the working distance (+2 h for every 8 h). [b)]Estimation of the average gross salary of a chemical laboratory assistant of 21 € h^{-1}. [c)]Measured value of electricity consumption of the PLAL system of 3 kWh. [d)]Electricity price for medium size industry by February 2023 (source: BDEW 01/2023) 0.40 € (kWh) $^{-1}$.

production. Nevertheless, production cost is the highest at 52,200.00 € kg^{-1}. The OPEX of 6-beam MB-PLAL is approximately 81,400.00 € and the production cost is 26,900.00 € kg^{-1} of Au NPs. Based on this calculation, 11-beam MB-PLAL offers the lowest production cost per kilogram of Au NPs, which is half of the standard PLAL.

Comparison of the PLAL and chemical procedure has been thoroughly investigated by Jendrzej et al.[83] The break-even point of the PLAL method compared to the chemical reduction method to produce Au NPs is at NPs productivity of 550 mg h^{-1}.[83] Hence, 11-beam and 6-beam MB-PLAL already surpassed the cost effectiveness of reduction method and are more economically viable. An interesting discussion of the sustainability footprint of PLAL technique compared to the chemical reduction method can be found in recent publication by Havelka et al.,[92] emphasizing the importance to shift the NPs production method to PLAL as a green chemistry method.

4. Conclusion

MB-PLAL has been shown as a feasible and practical technique to increase NP productivity by only integrating a static DOE into the PLAL system, improving the efficiency and economic viability of colloidal NPs production. The employed 6-beam and 11-beam DOE increased the productivity of FeNi PLAL in water by factors 3 and 4, respectively, with a maximum FeNi NPs productivity of 1.6 g h^{-1}. The energy splitting into multiple beams achieved by the DOEs has been shown to require the reduction of the repetition rate by a factor equal to the number of beams generated to keep the same optimum processing fluence per beam produced by the DOE compared to the single-beam PLAL. This fact allows us to increase the interpulse distance from 7 to 50 µm without the use of expensive high-speed scanners, reducing the beam shielding by the cavitation bubble, while the number of pulses delivered to the target is not affected. In the case of reducing the repetition rate without the use of the DOEs, the high pulse energy promotes nonlinear interactions with the liquid and induces optical breakdown, lowering the productivity due to the extra energy losses. The proposed MB-PLAL system thus enables us to employ the optimal pulse energy and fluence to achieve the highest productivity while increasing the interpulse distance without modifying the scanning parameters. This is further confirmed by the trend observed for increasing power-specific productivity as well as mass productivity, indicating that the MB-PLAL system causes a reduction of the factors affecting the energy delivery to the target as pulse shielding due to the cavitation bubble.

The properties of the produced NPs do not change for MB-PLAL compared to single-beam PLAL, based on the HR-TEM, XRD, and UV–vis results, indicating that the MB-PLAL with repetition rate compensation to keep the same processing fluence as single-beam PLAL does not modify the ablation mechanism or chemical processes during the NPs generation. The only parameter modified from the standard PLAL to the MB-PLAL is the interpulse distance (due to the repetition rate compensation), while the pulse energy, delivered number of pulses to the target's surface, and pulse width are kept approximately the same. The increase of the interpulse distance reduces cavitation bubble shielding, thus increasing NP productivity. Meanwhile, pulse energy and the number of delivered pulses in our setup are kept approximately constant, which is only possible due to the use of the DOE and repetition rate compensation. Hence, the properties of the generated NPs in the MB-PLAL are not modified compared to the single-beam PLAL system.

A comparative study with Au productivity was also performed to investigate the material's influence on the MB-PLAL system and the possibility of extending the MB-PLAL technique to any material processable by PLAL. Productivity increase factors of 2.1 and 3 were observed for the 6-beam and 11-beam MB-PLAL of Au in water, respectively, with a maximum productivity value of 0.94 g h^{-1} for the 11-beam MB-PLAL. The lower productivity increase factor of Au compared to FeNi can be caused by the typically larger cavitation bubble observed for Au. Hence, even for the achieved larger interpulse distance, pulse shielding from the cavitation bubble is expected to further influence Au NP production. In addition, the lower optical absorptance of Au at the 1064 nm employed laser wavelength results in lower energy absorbed by the target material. Further material properties affecting productivity are Au's higher threshold fluence, the weaker electron–phonon coupling, and higher conductivity of Au compared to FeNi, leading to energy thermal dissipation.

With the aim to introduce the MB-PLAL system as a cost-effective NP production system, the MB-PLAL system proposed is compared with the current most productive PLAL system worldwide based on a high-speed polygon scanner configuration proposed by Streubel et al.[52,53] With a laser power five times lower than the polygon–PLAL system, higher power-specific productivity was achieved for the MB-PLAL system, 9.50 mg $(hW)^{-1}$. Meanwhile, the MB-PLAL allowed to reach a similar interpulse distance, 50 µm, using a typical galvanometer scanner with a speed of 20 m s^{-1}, which is 24 times slower than the polygon scanner employed by Streubel et al.[52,53] A further benefit of the MB-PLAL system lies in the lower initial capital investment, which is approximately one-third of the polygon-PLAL configuration, easing the access of PLAL to research institutions and industries that require colloidal NPs.

A comparison of MB-PLAL and PLAL employing the same laser source allows us to conclude that MB-PLAL can achieve an annual production of approximately 1800 g of colloidal Au NPs, which is almost a 200% production increase compared with the PLAL system. A decreased labor cost and electricity consumption of 54 000 € and 20 000 kWh are expected for every 1000 g of Au NPs produced with the 11-beam MB-PLAL compared to the PLAL using the same laser source and scanning system. Prospectively, the proposed MB-PLAL system can be integrated into the current high-productivity PLAL systems available worldwide to further boost achievable productivity with a minimum cost and low experimental effort. Furthermore, the employment of the MB-PLAL system with higher laser power systems with repetition rates in the MHz range or higher would allow to employ beam splitters to generate a larger number of beams. Integration of such systems with a faster scanning speed will increase the interpulse distance, further lowering pulse shielding and reaching even higher production rates, enhancing the efficiency and economic viability of PLAL for industrial applications.

Supporting Information

Supporting Information is available from the Wiley Online Library or from the author.

Acknowledgements

The authors acknowledge funding by the Deutsche Forschungsgemeinschaft (DFG, German Research Foundation), grant numbers GO 2566/10-1, GO 2566/14-1, GO 2566/7-2, HU 1893/6-1, and HU 1893/6-2, and the European Union's Horizon 2020 research and innovation program under the grant agreement no. 952068 (project LESGO).

Conflict of Interest

The authors declare no conflict of interest.

Author Contributions

I.Y.K., C.D.-B., and B.G.: Conceptualization; I.Y.K., M.S., C.D.-B., and B.G.: Methodology; I.Y.K., F.R., and C.D.-B.: Investigation; I.Y.K.: Writing—Original Draft; I.Y.K., M.S., H.H., C.D.-B., and B.G.: Writing—Review & Editing; I.Y.K., F.R., and C.D.-B.: Visualization; C.D.-B. and B.G.: Supervision; C.D.-B. and B.G.: Project administration; C.D.-B. and B.G.: Funding acquisition.

Data Availability Statement

The data that support the findings of this study are available from the corresponding author upon reasonable request.

Keywords

diffractive optical elements, multi-beam laser processings, multi-beam pulsed-laser ablation in liquids (MB-PLAL), nanoparticle production upscales, parallel laser processings, PLAL

Received: October 5, 2023
Revised: December 30, 2023
Published online:

[1] Z. Yan, D. B. Chrisey, *J. Photochem. Photobiol., C* **2012**, *13*, 204.
[2] D. Zhang, B. Gökce, S. Barcikowski, *Chem. Rev.* **2017**, *117*, 3990.
[3] C. Wu, L. V. Zhigilei, *Appl. Phys. A* **2014**, *114*, 11.
[4] C.-Y. Shih, R. Streubel, J. Heberle, A. Letzel, M. V. Shugaev, C. Wu, M. Schmidt, B. Gökce, S. Barcikowski, L. V. Zhigilei, *Nanoscale* **2018**, *10*, 6900.
[5] C. Chen, L. V. Zhigilei, *Appl. Phys. A: Mater. Sci. Process.* **2023**, *129*, 288.
[6] N. T. K. Thanh, N. Maclean, S. Mahiddine, *Chem. Rev.* **2014**, *114*, 7610.
[7] S. Reich, A. Letzel, A. Menzel, N. Kretzschmar, B. Gökce, S. Barcikowski, A. Plech, *Nanoscale* **2019**, *11*, 6962.
[8] V. Amendola, D. Amans, Y. Ishikawa, N. Koshizaki, S. Scirè, G. Compagnini, S. Reichenberger, S. Barcikowski, *Chem. - Eur. J.* **2020**, *26*, 9206.
[9] M. Spellauge, C. Doñate-Buendía, S. Barcikowski, B. Gökce, H. P. Huber, *Light: Sci. Appl.* **2022**, *11*, 68.
[10] D. Zhang, J. Liu, P. Li, Z. Tian, C. Liang, *ChemNanoMat* **2017**, *3*, 512.
[11] S. Kohsakowski, R. Streubel, I. Radev, V. Peinecke, S. Barcikowski, G. Marzun, S. Reichenberger, *Appl. Surf. Sci.* **2019**, *467–468*, 486.
[12] D. Zhang, H. Wada, in *Handbook of Laser Micro- and Nano-Engineering* (Ed: K. Sugioka), Springer International Publishing, Cham **2021**, pp. 1481–1515, ISBN 978-3-030-63647-0, https://doi.org/10.1007/978-3-030-63647-0_30.
[13] D. Zhang, Z. Li, K. Sugioka, *JPhys Photonics* **2021**, *3*, 04200.
[14] M. E. Povarnitsyn, T. E. Itina, P. R. Levashov, K. V. Khishchenko, *Phys. Chem. Chem. Phys.* **2013**, *15*, 3108.
[15] Y. Yu, S. J. Lee, J. Theerthagiri, Y. Lee, M. Y. Choi, *Appl. Catal., B* **2022**, *316*, 121603.
[16] N. E. Jasbi, D. Dorranian, *J. Theor. Appl. Phys.* **2016**, *10*, 157.
[17] C. L. Sajti, R. Sattari, B. N. Chichkov, S. Barcikowski, *J. Phys. Chem. C* **2010**, *114*, 2421.
[18] G. K. Yogesh, S. Shukla, D. Sastikumar, P. Koinkar, *Appl. Phys. A* **2021**, *127*, 810.
[19] I. Y. Khairani, Q. Lin, J. Landers, S. Salamon, C. Doñate-Buendía, E. Karapetrova, H. Wende, G. Zangari, B. Gökce, *Nanomaterials* **2023**, *13*, 227.
[20] D. Zhang, W. Choi, J. Jakobi, M. R. Kalus, S. Barcikowski, S. H. Cho, K. Sugioka, *Nanomaterials* **2018**, *8*, 529.
[21] D. Zhang, C. Zhang, J. Liu, Q. Chen, X. Zhu, C. Liang, *ACS Appl. Nano Mater.* **2019**, *2*, 28.
[22] F. Waag, Y. Li, A. R. Ziefuß, E. Bertin, M. Kamp, V. Duppel, G. Marzun, L. Kienle, S. Barcikowski, B. Gökce, *RSC Adv.* **2019**, *9*, 18547.
[23] Y. Yu, J. Theerthagiri, S. J. Lee, G. Muthusamy, M. Ashokkumar, M. Y. Choi, *Chem. Eng. J.* **2021**, *411*, 128486.
[24] S. Naik Shreyanka, J. Theerthagiri, S. J. Lee, Y. Yu, M. Y. Choi, *Chem. Eng. J.* **2022**, *446*, 137045.
[25] A. Tymoczko, M. Kamp, C. Rehbock, L. Kienle, E. Cattaruzza, S. Barcikowski, V. Amendola, *Nanoscale Horiz.* **2019**, *4*, 1326.
[26] A. Basagni, V. Torresan, P. Marzola, M. B. Fernàndez van Raap, L. Nodari, V. Amendola, *Faraday Discuss.* **2023**, *242*, 286.
[27] J. Theerthagiri, K. Karuppasamy, S. J. Lee, R. Shwetharani, H.-S. Kim, S. K. K. Pasha, M. Ashokkumar, M. Y. Choi, *Light: Sci. Appl.* **2022**, *11*, 250.
[28] G. Sanità, B. Carrese, A. Lamberti, *Front. Mol. Biosci.* **2020**, *7*, https://doi.org/10.3389/fmolb.2020.587012.
[29] Z. Cai, Q. Yao, X. Chen, X. Wang, *Novel Nanomaterials for Biomedical, Environmental and Energy Applications*, Elsevier **2019**, pp. 435–464, ISBN 9780128144985, https://doi.org/10.1016/B978-0-12-814497-8.00014-X.
[30] R. C. Forsythe, C. P. Cox, M. K. Wilsey, A. M. Müller, *Chem. Rev.* **2021**, *121*, 7568.
[31] A. Guglielmelli, F. Pierini, N. Tabiryan, C. Umeton, T. J. Bunning, L. De Sio, *Adv. Photonics Res.* **2021**, *2*, 2000198.
[32] V. Gupta, O. Aftenieva, P. T. Probst, S. Sarkar, A. M. Steiner, N. Vogel, A. Fery, T. A. F. König, *Adv. Photonics Res.* **2022**, *3*, 2200152.
[33] A. Ishii, T. Miyasaka, *Adv. Photonics Res.* **2023**, *4*, 2200222.
[34] P. Anastas, N. Eghbali, *Chem. Soc. Rev.* **2010**, *39*, 301.
[35] I. Y. Khairani, G. Mínguez-Vega, C. Doñate-Buendía, B. Gökce, *Phys. Chem. Chem. Phys.* **2023**, *25*, 19380.
[36] F. Waag, R. Streubel, B. Gökce, S. Barcikowski, *Appl. Nanosci.* **2021**, *11*, 1303.
[37] S. Kohsakowski, *Hochskalierung Der Laserbasierten Nanopartikelsynthese Für Die Heterogene Katalyse*, University of Duisburg Essen **2018**, https://doi.org/10.17185/duepublico/47810.
[38] S. Kohsakowski, B. Gökce, R. Tanabe, P. Wagener, A. Plech, Y. Ito, S. Barcikowski, *Phys. Chem. Chem. Phys.* **2016**, *18*, 16585.
[39] G. C. Messina, P. Wagener, R. Streubel, A. De Giacomo, A. Santagata, G. Compagnini, S. Barcikowski, *Phys. Chem. Chem. Phys.* **2013**, *15*, 3093.
[40] S. Kohsakowski, A. Santagata, M. Dell'Aglio, A. de Giacomo, S. Barcikowski, P. Wagener, B. Gökce, *Appl. Surf. Sci.* **2017**, *403*, 487.

[41] T. Schmitz, U. Wiedwald, C. Dubs, B. Gökce, *ChemPhysChem* **2017**, *18*, 1125.
[42] D. Zhang, Z. Ma, M. Spasova, A. E. Yelsukova, S. Lu, M. Farle, U. Wiedwald, B. Gökce, *Part. Part. Syst. Charact.* **2017**, *34*, 1600225.
[43] A. Resano-Garcia, S. Champmartin, Y. Battie, A. Koch, A. En Naciri, A. Ambari, N. Chaoui, *Phys. Chem. Chem. Phys.* **2016**, *18*, 32868.
[44] S. Dittrich, S. Barcikowski, B. Gökce, *Opto-Electron. Adv.* **2021**, *4*, 200072.
[45] T. T. P. Nguyen, R. Tanabe-Yamagishi, Y. Ito, *Opt. Lasers Eng.* **2020**, *126*, 105937.
[46] M. R. Kalus, R. Lanyumba, S. Barcikowski, B. Gökce, *J. Flow Chem.* **2021**, *11*, 773.
[47] T. Hupfeld, G. Laurens, S. Merabia, S. Barcikowski, B. Gökce, D. Amans, *J. Appl. Phys.* **2020**, *127*, 044306.
[48] J. Long, M. Eliceiri, Z. Vangelatos, Y. Rho, L. Wang, Z. Su, X. Xie, Y. Zhang, C. P. Grigoropoulos, *Opt. Express* **2020**, *28*, 14300.
[49] L. V. Zhigilei, B. J. Garrison, *J. Appl. Phys.* **2000**, *88*, 1281.
[50] A. Nastulyavichus, N. Smirnov, S. Kudryashov, *Chin. Phys. B* **2022**, *31*, 077803.
[51] N. A. Smirnov, S. I. Kudryashov, A. A. Rudenko, D. A. Zayarny, A. A. Ionin, *Appl. Surf. Sci.* **2021**, *562*, 150243.
[52] R. Streubel, S. Barcikowski, B. Gökce, *Opt. Lett.* **2016**, *41*, 1486.
[53] R. Streubel, G. Bendt, B. Gökce, *Nanotechnology* **2016**, *27*, 205602.
[54] B. Neuenschwander, B. Jaeggi, M. Schmid, G. Hennig, *Phys. Procedia* **2014**, *56*, 1047.
[55] S. Dittrich, M. Spellauge, S. Barcikowski, H. P. Huber, B. Gökce, *Opto-Electron. Adv.* **2022**, *5*, 210053.
[56] S. Dittrich, R. Streubel, C. McDonnell, H. P. Huber, S. Barcikowski, B. Gökce, *Appl. Phys. A: Mater. Sci. Process.* **2019**, *125*, 432.
[57] A. Menéndez-Manjón, P. Wagener, S. Barcikowski, *J. Phys. Chem. C* **2011**, *115*, 5108.
[58] A. Gillner, J. Finger, P. Gretzki, M. Niessen, T. Bartels, M. Reininghaus, *J. Laser Micro/Nanoeng.* **2019**, *14*, 129.
[59] C. Doñate-Buendía, M. Fernández-Alonso, J. Lancis, G. Mínguez-Vega, *Photonics Res.* **2019**, *7*, 1249.
[60] R. De Loor, *Phys. Procedia* **2013**, *41*, 544.
[61] P. Bechtold, R. Hohenstein, M. Schmidt, *Opt. Lett.* **2013**, *38*, 2934.
[62] Raylase, SUPERSCAN IV-15 2-Axis Deflection Units, https://www.raylase.de/_Resources/Persistent/9/5/d/a/95da1035b2c564183914aa6c26c6f6e43f20044c/RAYLASE_SUPERSCANIV-15_en.pdf (accessed: February 2023).
[63] S. Rung, C. Bischoff, E. Jäger, U. Umhofer, R. Hellmann, in *Laser Applications in Microelectronic and Optoelectronic Manufacturing (LAMOM) XIX*, Vol. *8967* (Eds: Y. Nakata, X. Xu, S. Roth, B. Neuenschwander), **2014**, p. 89670P, ISBN 9780819498809, https://doi.org/10.1117/12.2038572.
[64] C. Lutz, G. L. Roth, S. Rung, C. Esen, R. Hellmann, *J. Laser Micro/Nanoeng.* **2021**, *16*, 62.
[65] S. Bruening, K. Du, M. Jarczynski, A. Gillner, *J. Laser Appl.* **2020**, *32*, 012003.
[66] S. Torres-Peiró, J. González-Ausejo, O. Mendoza-Yero, G. Mínguez-Vega, P. Andrés, J. Lancis, *Opt. Express* **2013**, *21*, 31830.
[67] S. Hasegawa, H. Ito, H. Toyoda, Y. Hayasaki, *Opt. Express* **2016**, *24*, 18513.
[68] M. Smarra, M. Janitzki, K. Dickmann, *Phys. Procedia* **2016**, *83*, 1145.
[69] A. D. Chandra, A. Banerjee, *J. Mod. Opt.* **2020**, *67*, 628.
[70] J. Finger, M. Hesker, *JPhys Photonics* **2021**, *3*, 02100.
[71] C. Bischoff, E. Jäger, U. Umhofer, *Laser Tech. J.* **2015**, *12*, 53.
[72] C. C. L. McCrory, S. Jung, J. C. Peters, T. F. Jaramillo, *J. Am. Chem. Soc.* **2013**, *135*, 16977.
[73] J. Song, C. Wei, Z. F. Huang, C. Liu, L. Zeng, X. Wang, Z. J. Xu, *Chem. Soc. Rev.* **2020**, *49*, 2196.
[74] N. T. Suen, S. F. Hung, Q. Quan, N. Zhang, Y. J. Xu, H. M. Chen, *Chem. Soc. Rev.* **2017**, *46*, 337.
[75] International Renewable Energy Agency (IRENA), *World Energy Transitions Outlook 2023: 1.5°C Pathway*, IRENA, Abu Dhabi **2022**, ISBN 9789292603342.
[76] United Nations Educational Scientific and Cultural Organization. Unesco and Sustainable Development, https://en.unesco.org/sustainabledevelopmentgoals (accessed: September 2023).
[77] J. Tomko, J. J. Naddeo, R. Jimenez, Y. Tan, M. Steiner, J. M. Fitz-Gerald, D. M. Bubb, S. M. O'Malley, *Phys. Chem. Chem. Phys.* **2015**, *17*, 16327.
[78] S. Reich, P. Schönfeld, P. Wagener, A. Letzel, S. Ibrahimkutty, B. Gökce, S. Barcikowski, A. Menzel, T. dos Santos Rolo, A. Plech, *J. Colloid Interface Sci.* **2017**, *489*, 106.
[79] Z. Yang, H. Bao, L. Dai, H. Zhang, J. Lu, *Opt. Express* **2023**, *31*, 21845.
[80] O. Salata, *J. Nanobiotechnol.* **2004**, *2*, 3.
[81] L. Dykman, N. Khlebtsov, *Chem. Soc. Rev.* **2012**, *41*, 2256.
[82] I. Hammami, N. M. Alabdallah, A. A. Jomaa, M. Kamoun, *J. King Saud Univ., Sci.* **2021**, *33*, 101560.
[83] S. Jendrzej, B. Gökce, M. Epple, S. Barcikowski, *ChemPhysChem* **2017**, *18*, 1012.
[84] M. R. Kalus, R. Lanyumba, N. Lorenzo-Parodi, M. A. Jochmann, K. Kerpen, U. Hagemann, T. C. Schmidt, S. Barcikowski, B. Gökce, *Phys. Chem. Chem. Phys.* **2019**, *21*, 18636.
[85] G. Zhu, S. Wang, W. Cheng, G. Wang, W. Liu, Y. Ren, *Coatings* **2019**, *9*, 578.
[86] I. Bunaziv, O. M. Akselsen, X. Ren, B. Nyhus, M. Eriksson, S. Gulbrandsen-Dahl, *Metals* **2021**, *11*, 1680.
[87] T. Nakano, in *Multi-Dimensional Additive Manufacturing* (Eds: S. Kirihara, K. Nakata), Springer Singapore, Singapore **2021**, ISBN 978-981-15-7909-7, https://doi.org/10.1007/978-981-15-7910-3.
[88] D.-I. J. Berkmanns, D.-I. M. Faerber, *Laser Basics - LASERLINE Technical* **2008**, ISBN 9783642367045.
[89] M. He, C. Wu, M. V. Shugaev, G. D. Samolyuk, L. V. Zhigilei, *J. Phys. Chem. C* **2019**, *123*, 2202.
[90] V. R. Palanivelu, *Financial Management Theory, Problems and Solutions*, 3rd Rev., S. Chand Publishing, New Delhi **2010**, ISBN 9789352833276.
[91] A. Vogel, W. Hentschel, J. Holzfuss, W. Lauterborn, *Ophthalmology* **1986**, *93*, 1259.
[92] O. Havelka, F. Yalcinkaya, S. Wacławek, V. V. T. Padil, V. Amendola, M. Černík, R. Torres-Mendieta, *Environ. Sci. Nano* **2023**, *10*, 2359.

7.3 Study III

Khairani, I. Y.; Jin, B.; Palardonio, S. M.; Hagemann, U.; Alonso, B.; Ortega, A.; Doñate-Buendía, C.; Martorell, J.; Ros, C.; Kallio, T.; Gökce, B. FeNi Nanoparticle-Modified Reduced Graphene Oxide as a Durable Electrocatalyst for Oxygen Evolution. J. Catal. 2024, 439 (September), 115771, DOI: 10.1016/j.jcat.2024.115771.

CRediT Authorship Contribution of I.Y.K.: Conceptualization, methodology, investigation, visualization, writing – original draft preparation, writing – review and editing.

Journal of Catalysis 439 (2024) 115771

Contents lists available at ScienceDirect

Journal of Catalysis

journal homepage: www.elsevier.com/locate/jcat

Research article

FeNi nanoparticle-modified reduced graphene oxide as a durable electrocatalyst for oxygen evolution

Inna Yusnila Khairani [a], Benjin Jin [b], Sidney M. Palardonio [c], Ulrich Hagemann [d,e], Beatriz Alonso [f], Amaya Ortega [f], Carlos Doñate-Buendía [a,g], Jordi Martorell [c,h], Carles Ros [c], Tanja Kallio [b], Bilal Gökce [a,*]

[a] Chair of Materials Science and Additive Manufacturing, School of Mechanical Engineering and Safety Engineering, University of Wuppertal, Wuppertal 42119, Germany
[b] Electrochemical Energy Conversion Group, Department of Chemistry and Materials Science, School of Chemical Engineering, Aalto University, P.O. Box 16100, Aalto FI-00076, Finland
[c] ICFO - Institut de Ciències Fotòniques, The Barcelona Institute of Science and Technology, Castelldefels 08860, Spain
[d] NETZ – NanoEnergieTechnikZentrum, CENIDE – Center for Nanointegration Duisburg-Essen, Carl-Benz-Str. 199, Duisburg 47057, Germany
[e] Interdisciplinary Center for Analytics on the Nanoscale (ICAN), University of Duisburg-Essen, Carl-Benz-Str. 199, Duisburg 47057, Germany
[f] Graphenea S.A., Mikeletegi 83, San Sebastián 20009, Spain
[g] GROC-UJI, Institut de Noves Tecnologies de la Imatge (INIT), Universitat Jaume I, Castellón 12071, Spain
[h] Departament de Física, Universitat Politècnica de Catalunya, Terrassa 08222, Spain

ARTICLE INFO

Keywords:
Iron-nickel catalyst
PLAL
Rare element free
Precious metal free
Electrode fabrication
Green hydrogen

ABSTRACT

Clean energy transition and decarbonization through hydrogen technology hold a crucial role in revitalizing a sustainable world. The development of catalysts free of precious elements to facilitate the water splitting process in an electrolyser represents a key sustainable goal to lower the production cost of green hydrogen fuel, therefore improving its accessibility and affordability. Here we report a hybrid electrocatalyst for oxygen evolution reaction (OER) in alkaline media with high stability and low overpotential, free of precious metals and rare elements. The hybrid catalyst is composed of laser-generated $Fe_{50}Ni_{50}$ nanoparticles (FeNi NPs) dispersed on reduced graphene oxide (rGO) and deposited on FeNi layered double hydroxide (FeNi LDH) grown on Ni foam substrate. The prepared FeNi-rGO/FeNi/Ni foam hybrid catalyst requires an overpotential of only 234 mV at a current density of 10 mA/cm^2, which is 37 mV lower than the tested commercial RuO_2 catalyst on Ni foam substrate. Besides, the hybrid catalyst is extremely robust; it stands 10,000 cycles of accelerated deterioration and runs for more than 1,300 h at a current density of 10 mA/cm^2 without performance decay.

1. Introduction

The urge to decarbonize and achieve net zero carbon emissions represents a goal of the United Nations to avert the worst impacts of climate change and preserve a livable planet [1]. Hydrogen, specifically green hydrogen, is envisioned as one of the green solutions to replace carbon-based fuels. However, the production cost of green hydrogen is approximately 4–6 USD per kg, still 2–3 times higher than the prevailing method of grey hydrogen [2] production [3] via steam methane reformation [4–6] from natural gas (methane). To reduce the production cost of green hydrogen to the ambitioned fossil fuel-based value of 2 USD per kg, the renewable electricity price has to be decreased to 20 USD per MWh, while the electrolyser cost should be reduced to 130 USD per kW at 5 TW installed capacity [2]. Renewable energy prices are decreasing every year due to the global efforts to enhance their production efficiency and the increasing number of installations [7], hence, the focus to produce cost-effective green hydrogen lies in reducing the price of the electrolyser and scaling up its capacity [8,9]. One of the primary costs of an electrolyser comes from its stacks [9]. The electrodes within the cells are coated with catalysts made of precious metals or rare elements such as platinum-group metals (PGM) due to their high catalytic activity for water-splitting. Some of the most studied materials include ruthenium and iridium-based catalysts which exhibit a high catalytic activity for both hydrogen evolution reaction (HER) and oxygen evolution reaction (OER) [10–15]. Platinum itself is a highly active catalyst for HER with exceptionally low overpotential [13,14,16,17]. The required use of

* Corresponding author.
E-mail address: goekce@uni-wuppertal.de (B. Gökce).

https://doi.org/10.1016/j.jcat.2024.115771
Received 9 July 2024; Received in revised form 19 September 2024; Accepted 22 September 2024
Available online 24 September 2024

precious metals or rare elements as catalysts for green H_2 production highly increases the cost of the electrolysers. Hence, abundant and non-precious elements with similar catalytic activity as the PGM elements are desired to facilitate electrolyser serial production at a lower cost [9].

The current efforts to achieve new catalysts for OER, which is kinetically more sluggish than HER, focus on the development of metal oxide and metal alloy catalysts from non-precious and relatively abundant elements, such as cobalt [18–20], manganese [21–23], iron [24–28], and nickel [29–32]. Among these elements, nickel-based catalysts are considered the most promising candidates as PGM-free OER catalysts [33]. Ni-based OER-catalysts gained popularity due to their low overpotentials [32,34,35] along with their high thermal stability, high conductivity, and multivalent nature (−1 to +4), which makes it possible to undergo different electronic transitions [30,36]. Specifically, the addition of iron to nickel-based catalysts has been reported to improve the electrocatalytic activity in alkaline conditions [37–41] due to the additional active sites, change of electronic structure, stabilization of Ni's higher oxidation state, and conductivity increase [39,42–46]. During a test of a Ni oxyhydroxides catalyst, it was reported that the absence of Fe impurities in the KOH electrolyte resulted in poor activity [39] and the addition of Fe increased the catalytic activity [47]. Following this observation, it was confirmed that iron-nickel catalysts in the form of layered double hydroxides (LDH) exhibit high OER activity [48,49] compared to commercial Ir/C catalysts and other bimetal LDH containing Mn^{2+}, Co^{2+}, or Mg^{2+} ions [50]. Its high performance is most likely due to the multivalence states [51] and the incorporation of the Fe atoms into the α-$Ni(OH)_2$/γ-NiOOH lattice [52]. Indeed, Fe-Ni is the most active OER catalyst for alkaline electrolytes among the investigated non-PGM metal and bimetal oxyhydroxide [53] and hydroxide [54] species, indicating that the combination of Fe and Ni has a synergistic effect that outperforms other non-PGM catalysts for OER in alkaline condition.

Catalysts based on nanoparticles (NPs) exhibit superior performance compared to bulk catalysts as they provide a larger surface area and a higher number of active sites [55,56]. The synthesis method of NPs plays a key role in catalytic efficiency since high purity and maximization of the active surface and defects are the main factors that determine the catalyst efficiency. Pulsed laser ablation in liquid (PLAL) produces catalysts that fulfil these requirements and allow the synthesis of a wide library of nanomaterials [57–59], including low dimensional materials [60], and PLAL in different types of solvents [61,62]. Laser-generated NPs excel as catalysts [63–66] and often outperform NPs made by wet chemical methods [63,67], thanks to the surfactant-free and defect-rich [68] properties as a result of a rapid quenching effect, which provides additional active sites [69,70]. In addition, laser ablation of FeNi in water is reported to lead to the formation of the $NiFe_2O_4$ phase [71], which is found to improve OER activity of FeNi-based catalyst [72–75] presumably due to its spinel structures providing higher Fe coordination in both octahedral and tetrahedral sites [72].

Nevertheless, the size distribution of NPs generated by the PLAL method tends to be broad [117], especially for oxidation-prone elements such as iron and nickel. In addition, FeNi NPs tend to agglomerate due to their intrinsic magnetic properties [71], thereby reducing their exposed active sites and adversely influencing their catalytic activity [76]. To achieve bare-surface FeNi NPs with reduced agglomeration and smaller particle size, direct size quenching and support on a layered material have been studied [77]. Reduced graphene oxide (rGO) is a suitable support material for catalytic applications due to its high conductivity and large surface area [78]. The use of rGO as a size quencher and support material in PLAL has been previously reported for the direct synthesis and supporting of Pt-rGO [79], where a slight average size reduction of Pt NPs is observed. Another report on the PLAL of Au NPs in the presence of graphene oxide (GO) in the liquid carrier shows decreased average particle size from 6 nm to 3 nm in addition to NPs immobilization and homogeneous distribution on the GO's surface [77]. This one-step procedure called in situ PLAL offers direct synthesis, size quenching, and supporting of the NPs on the desired support materials.

As catalyst NPs are employed to cover the surface of an electrode in an electrolyser, achieving a larger support surface area for the catalyst NPs on the electrode is important. Hence, the use of 3D porous electrodes such as nickel foam is beneficial to maximize the interacting surface. Nickel foam electrodes not only improve the surface area but also promote electrolyte infiltration and facilitate electron pathways [48,80,81]. Iron nickel LDH can be directly grown on this conductive 3D architecture. The combination of FeNi LDH and Ni foam has been reported to require an overpotential for OER of only 280 mV to reach a current density of 30 mA/cm^2 (η_{30} 280mV), which is significantly lower than commercial Ir/C catalysts with η_{30} 390mV [48]. This hydrothermally grown FeNi LDH provides an even larger surface area, improving it 4 times compared to the pure nickel foam (0.06 m^2/cm^2 to 0.24 m^2/cm^2) [48].

In this study, we synthesized a hybrid FeNi catalyst completely free of precious metals, consisting of laser-generated FeNi NPs deposited on rGO flakes and supported on FeNi-layered double hydroxide (LDH) coated Ni foam. The hybrid catalyst structure was chosen based on the aforementioned advantages of each material to construct an OER catalyst with low overpotential and high stability as required for an alkaline electrolyser. The hybrid catalyst's OER catalytic activity along with the PLAL synthesis mechanism to produce FeNi NPs-rGO composite were investigated.

2. Methods

2.1. Laser-generated $Fe_{50}Ni_{50}$ nanoparticles on reduced graphene oxide

In our study, we chose a Fe:Ni ratio of 50:50 due to several reasons: (1) former reports of its low overpotential [37,74,82,83], (2) PLAL of $Fe_{50}Ni_{50}$ in water forms minor $NiFe_2O_4$ phase [71], which is presumed to improve OER catalytic activity [72,74], and (3) better OER performance at higher current densities (100 and 150 mA/cm^2) [83], which is essentially related to our purpose for industrial application.

A 1064 nm Nd:YAG laser with a pulse width of 10 ps, repetition rate of 400 kHz, and average power of 100 W was employed for the PLAL of a $Fe_{50}Ni_{50}$ target (99.95 % purity, Sindlhauser Materials GmbH). A galvanometer scanner with a scanning speed of 20 m/s was coupled with an f-theta lens (focal length 167 mm) to focus and steer the laser beam into the desired pattern. A static diffractive optical element (DOE) with a 1:11 matrix was placed closely in front of the f-theta lens to split the laser beam into 11 and increase the production rate of the FeNi NPs [84]. PLAL was performed in a flow chamber where the liquid was pumped through with a flow rate of 400 mL/min, Fig. 1.

We investigated two different techniques for the direct synthesis and support of FeNi NPs on rGO, as shown in Fig. 1. The in situ PLAL, Fig. 1 (a), where rGO powder provided by Graphenea (further information can be found in Table S1 and Figure S1) was dispersed in distilled MiliQ water (18.2 MΩ•cm at 25 °C) with a concentration of 15 mg/L and then pumped through the chamber where PLAL happens. In this setup, the supporting of FeNi NPs on the rGO surface took place inside the ablation chamber directly after the NPs formation. The produced sample is further referred to as "in situ FeNi-rGO". Meanwhile, in the second method, downstream PLAL, Fig. 1 (b), distilled MiliQ water was used as NPs carrier and was pumped through the ablation chamber. The rGO dispersion with a concentration of 30 mg/L was placed in the collecting reservoir at the end of the system. In this method, the supporting process was delayed by several seconds until the FeNi NPs colloid reached the collecting reservoir (where rGO was present). The sample is further denoted as "downstream FeNi-rGO". Note that we kept the final concentration of rGO at 15 mg/L and the final colloid volume of 2 L for both samples. A comparative study with graphene oxide (GO), also provided by Graphenea (Spain), as the support material was also performed in the downstream PLAL to investigate the influence of supporting materials on this process. The sample will be further referenced as "downstream

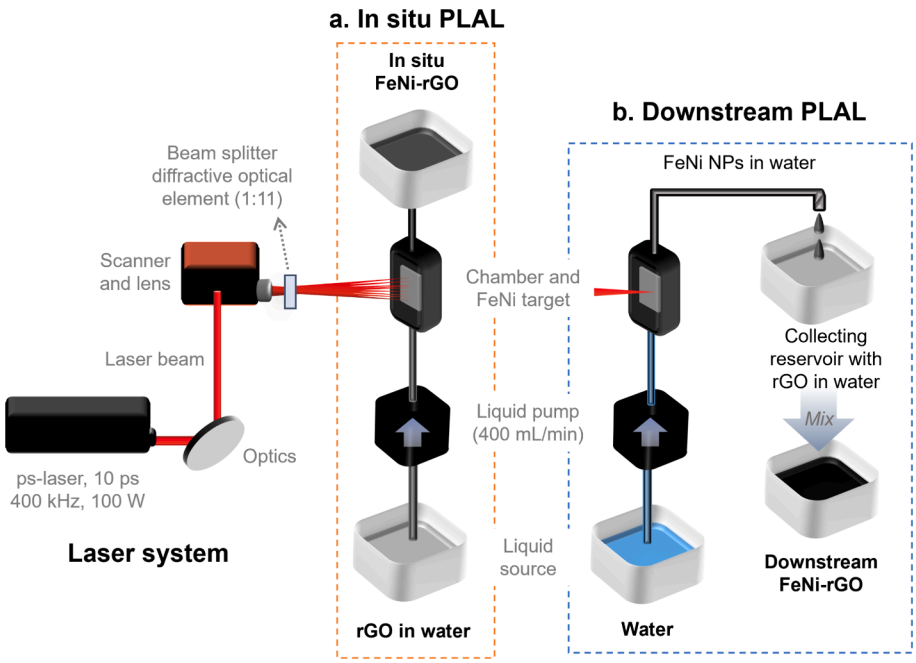

Fig. 1. Schematic illustration of the PLAL flow chamber setup to produce FeNi-rGO in water. Two techniques are compared, (a) in situ PLAL, in which the rGO dispersion in water is used as the NPs carrier for the PLAL and the FeNi NPs supporting directly takes place inside the ablation chamber, and (b) downstream PLAL, where water is used as NPs carrier, thus, the supporting of the FeNi NPs on the rGO surface occurs when FeNi NPs reach the collecting reservoir in which the rGO dispersion in water is present.

FeNi-GO".

2.2. Synthesis of the FeNi-LDH on Ni foam electrode

The preparation of the iron nickel-layered double hydroxide (FeNi-LDH) nanoplates on Ni foam followed the hydrothermal procedure previously reported [48,85]. To successfully form an LDH phase, the ratio of trivalent cations (M^{3+}, in our case Fe^{3+}) and divalent (M^{2+}, in our case Ni^{2+}) should be between 1:1.5 and 1:4.8 [86]. The reactants Ni $(NO_3)_2{\cdot}6H_2O$ (0.67 mmol), $Fe(NO_3)_3{\cdot}9H_2O$ (0.33 mmol), and $CO(NH_2)_2$ (5 mmol) were mixed with 35–38 mL of distilled water and stirred until a clear solution was formed. The Ni foam electrode with a dimension of 3 cm × 4 cm was cleaned in an ultrasound bath for 5 min using HCl solution (32 wt%) to remove the oxidized surface layer. It was later rinsed with deionized water. The Ni foam was then placed in the 40 mL Teflon-lined stainless-steel autoclave and the as-prepared aqueous solution was added. The autoclave was sealed and heated at 120 °C for 12 h and subsequently cooled down naturally. The formation of a thin film on the Ni foam was observed and the substrate was rinsed subsequently with distilled water and absolute ethanol in the ultrasonic bath for 5 min each. The prepared FeNi-LDH/Ni foam was dried naturally and stored in a plastic container.

2.3. Preparation of FeNi-rGO/FeNi/Ni foam and RuO_2/Ni foam electrodes

The FeNi-rGO/FeNi/Ni foam electrode was prepared according to the schematic diagram as shown in Fig. 2. In a typical procedure, 24 µL of FeNi-rGO suspension with a concentration of 68 mg/mL were mixed with 16 µL Nafion (5 wt% Nafion-117 solution, purchased from Aldrich). The mixture was stirred overnight and sprayed on the FeNi LDH/Ni foam electrode with an area of 1 cm^2 using an airbrush. Then, the samples were transferred into a tube furnace and calcinated at 400 °C for 2 h under N_2 flow. The FeNi-rGO/FeNi/Ni foam was obtained after

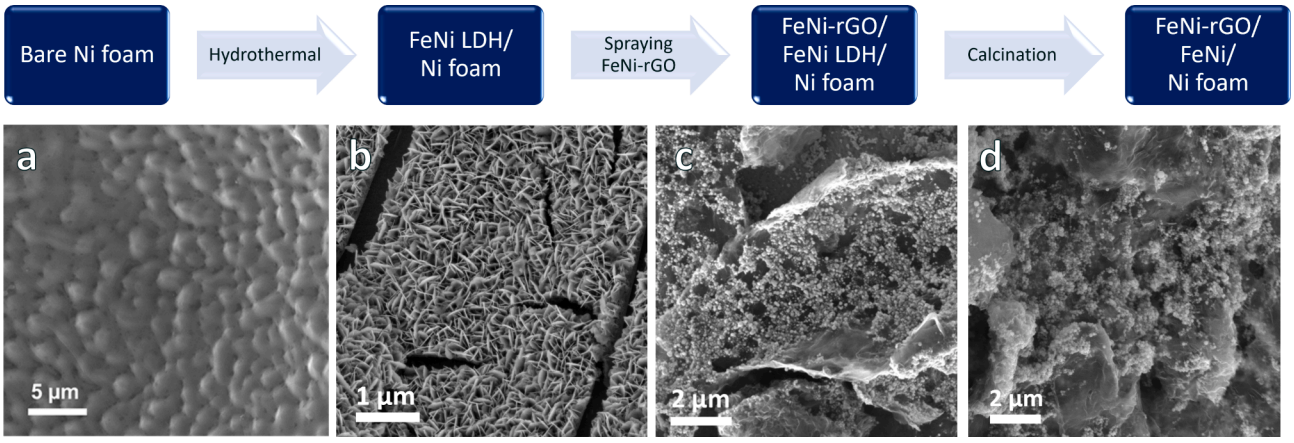

Fig. 2. Schematic procedure of FeNi-rGO/FeNi/Ni foam and each representative SEM image of (a) bare Ni foam, (b) FeNi LDH/Ni foam, (c) FeNi-rGO/FeNi LDH/Ni foam, and (d) FeNi-rGO/FeNi/Ni foam.

cooling down to room temperature and its crystalline structures before and after calcination are shown in Figure S2.

The benchmark OER catalyst, RuO_2, was also spray-coated on Ni foam as a comparative study to our FeNi-based catalyst. In a typical procedure [87], 1.6 mg of commercial RuO_2 (25–30 nm, purchased from Sigma) was dissolved in 24 μL isopropanol with sonication and 16 μL Nafion (5 wt%) was added into the solution. The mixture was sprayed on Ni foam with an area of 1 cm^2 using an airbrush. The RuO_2/Ni foam was obtained after drying in air.

2.4. Characterization

Transmission electron microscopy (TEM) and energy dispersive X-ray (EDX) measurements were performed to analyse the morphology, size distribution, and elemental distribution of the generated FeNi NPs supported on the rGO (HR-TEM, JEOL JEM-2200FS, 200 kV, ZrO_2/W emitter). The nanoparticle size distribution was characterized using ImageJ software [88]. X-ray diffraction (XRD) analysis was done to confirm the crystalline structure of the FeNi-rGO/FeNi/Ni foam hybrid catalyst before and after the 1300 h stability test. XRD patterns were captured by PANalytical X'Pert Powder XRD operating at the voltage of 40 kV and the current of 40 mA with Cu Kα radiation. The scanning electron microscopes (SEM) were obtained by Tescan Mira3.

The electrochemical experiments were conducted at room temperature. A commercial Hg/HgO electrode and a graphite rod were used as a reference and counter electrode, respectively. The Ni foam-based samples were used as work electrodes directly and the electrolyte is 0.1 M KOH. The measured potentials were calibrated to a reversible hydrogen electrode (RHE) by the following equation: $E_{RHE} = E_{Hg/HgO} + 0.098\ V + 0.059 \times pH$ (pH = 13). The accelerated durability tests (ADT) of the catalysts were assessed by cyclic voltammetry (CV) at a scan rate of 100 mVs^{-1} between 1.2 V and 1.65 V vs RHE for 10,000 continuous cycles. The electrochemical experiments were performed in a standard three-electrode cell using an Autolab potentiostat (PGSTAT128N, Metrohm Autolab B.V.). The electrochemical impedance spectroscopy (EIS) was performed at 1.64 V vs RHE with an amplitude of 8 mV from 100 kHz to 0.1 Hz.

The calculation of our Tafel slopes was obtained from a linear potential region. The LSVs exhibit three regions: (1) A low current density region (kinetic control), (2) A linear region (charge transfer control), and (3) A high current density region (mass transport limitations). As bubble formation usually happens in the high current density region, the Tafel slope should be determined from the linear region of the LSV curve [89], where the overpotential (η) increases with the logarithm of the current density (log j), which typically occurs at moderate overpotentials before mass transport limitations start to dominate. Unless specifically indicated, all electrochemical data (CVs and Tafel plots) are *iR* corrected.

Raman spectroscopy was performed on 30 μL of FeNi-rGO suspension dropcast on 4 mm cavity glass slides and then dried at 60 °C vacuum oven to prevent oxidation in air. Raman spectra of the dried samples were obtained by Renishaw inVia spectrometer, using a 532 nm wavelength laser and 50x objective. To avoid laser-induced reduction [90], the laser was limited to 0.5 % power, 1 s exposure time, and 30 acquisitions. The intensities of Raman scattering were corrected by taking the fluorescence as the baseline and then fitted to sums of functions using peak-o-mat 1.2.9 software, using three pseudo-Voigt functions (for D, G and D' bands) and two Gaussian functions (for D* and D'' bands) [91,92].

XPS measurements were performed on a VersaProbe II system (Ulvac Phi, monochromatic Al-Kα at hν = 1486.6 eV, dual charge compensation). The commercial rGO powder and FeNi-rGO/FeNi/Ni foam sample were put on carbon tape, and the colloidal solutions of in situ and downstream FeNi-rGO were dropcast on Si substrates. All samples did not undergo the sputtering step. Secondary x-ray-induced electron imaging (SXI) was used to make sure the X-ray beam was properly focused on the particles. Data evaluation was done using CasaXPS [93].

3. Results and discussion

3.1. Direct synthesis and support of FeNi NPs on rGO

Prior to the assembly of the hybrid catalyst, we explored how different supporting techniques, i.e., in situ and downstream PLAL, Fig. 1, influence the supporting efficiency and properties of the FeNi-rGO composite. In situ PLAL has been proposed to induce the size quenching effect of the laser-generated NPs in liquid [77,79] and avoids NPs growth, resulting in smaller NPs towards improving the catalytic activity. Nevertheless, the dispersion of light-absorbing matter, such as rGO microflakes, between the laser beam and the target reduces PLAL NP productivity [94], which is crucial to bringing this production technique to the industry [57]. Based on our investigation, a reduction of the FeNi NPs productivity from 909 mg/h in the downstream FeNi-rGO to 854.4 mg/h in the in situ PLAL is observed. At larger rGO concentrations, the productivity of in-situ PLAL suffers even more.

To reduce the laser shielding effect observed in the in situ PLAL, we propose another approach which is termed downstream PLAL, Fig. 1 (b), in which the support material is placed in the collecting reservoir after PLAL, thus the NPs will be supported directly after production. Downstream PLAL avoids fragmentation and ablation of the support material, maximizing FeNi NPs productivity as most of the laser energy reaches the target [94]. Despite the above-stated advantages of downstream PLAL, there is still one open question whether the sole advantage of the in situ PLAL, the size quenching effect, is still observed in the downstream PLAL. Thereby, we compared the influence of downstream and in situ PLAL methods on the supporting of FeNi NPs on rGO and studied the properties of the produced composites, including the FeNi NPs dispersion on the rGO surface, the FeNi NPs' size distribution, the OER catalytic activity, the oxidation state of Fe and Ni, and the defect state of the rGO. The aim is to find the most efficient method to directly synthesise and support the produced FeNi NPs on the rGO while achieving high catalytic activity.

3.1.1. Nanoparticle dispersion on rGO

The TEM images of the PLAL-generated FeNi NPs on the rGO sheets through in situ and downstream PLAL are shown in Fig. 3 (a-f). The in situ PLAL shows a more uniform dispersion of small nanoparticles ($d \leq 10$ nm) throughout the surface of the rGO sheet, Fig. 3 (a-c). Meanwhile, more clustered and agglomerated particles can be seen in the downstream PLAL sample, Fig. 3 (d-f). Similar dispersion results were also observed through EDX-mapping, Figure S3, and high-angle annular dark-field imaging (HAADF), Figure S4. Based on these results, it seems that the in situ PLAL offers a benefit, where rGO flakes in the liquid carrier act as a capping agent, thus NPs are more easily anchored within the wrinkles of rGO and their growth and coalescence are avoided [77]. On the other hand, downstream FeNi-rGO shows a less uniform distribution as the wrinkling structure of rGO prevents the NPs from reaching the central area, and the NPs accumulate on the perimeter of rGO microflakes, Fig. 3 (d-f) and Figure S4. A previous study also reported a similar phenomenon where more Au NPs are found at the wrinkles of GO compared to rGO, suggesting that the higher defect density, electrostatic interactions such as van der Waals, and overlapping of GO's π-orbitals with metal NPs' d-orbitals promote the accrued NPs at the wrinkles [77,95]. In our case, however, replacing the rGO with GO in the downstream PLAL resulted in a more uniform distribution of FeNi NPs, Fig. 3 (g-i), probably due to a lower wrinkling structure observed in our pristine GO. It proves the possibility of getting a uniform distribution of NPs via the downstream PLAL by changing the support material. The difference in the NPs dispersion on the rGO surface compared to the GO in the downstream PLAL in our case could be caused by (1) the higher wrinkling morphology of rGO, causing NPs to be accumulated already at the perimeter area during the mixing, and (2) the loss of some oxygen

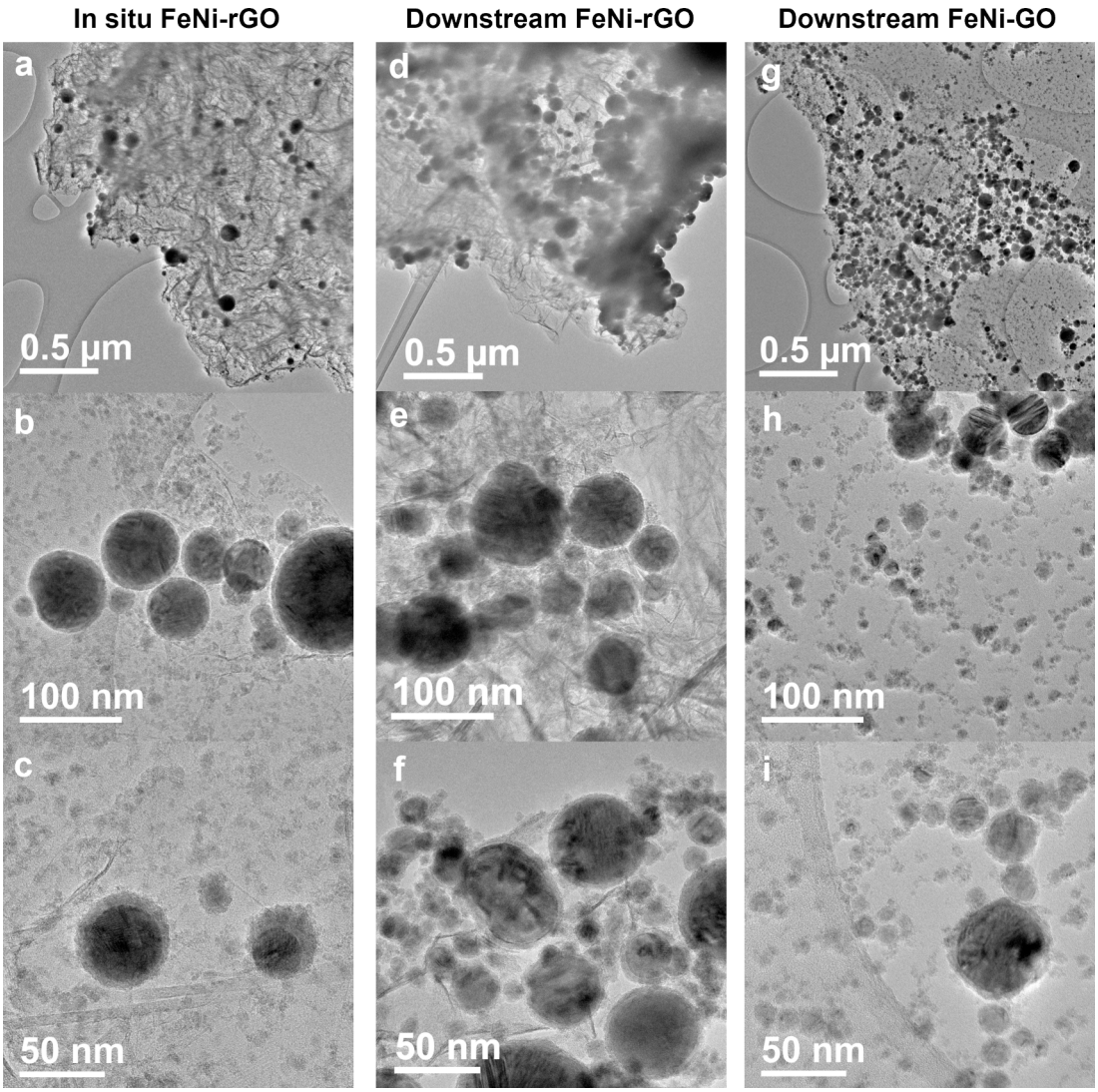

Fig. 3. HR-TEM images of FeNi NPs directly synthesized and supported on support materials. (a-c) In situ FeNi-rGO, (d-f) downstream FeNi-rGO, and (g-i) downstream FeNi-GO.

functional groups in rGO compared to GO, resulting in a more hydrophobic and less dispersible support material. The distribution of the nanoparticles on the rGO or GO microflakes is therefore not only related to the technique but also to the property of the supporting materials, i.e. morphology and electronic structure.

3.1.2. *Particle size distribution*

The particle size distributions (PSD) of the supported NPs are compared in Fig. 4. While in situ PLAL is known to produce smaller nanoparticles due to the size-quenching effect of the support materials [77,79], we observed only a slight difference between in-situ and downstream FeNi-rGO, Fig. 4. The centre value (x_c) of the particle diameter in the log-normal distribution shows that the downstream FeNi-rGO (x_c = 11.3 ± 6.9 nm) exhibits a similar size distribution compared to the in situ FeNi-rGO (x_c = 10.6 ± 9.2 nm). Meanwhile, downstream FeNi-GO has a smaller peak value (x_c = 7.9 ± 5.0 nm) compared to downstream FeNi-rGO (x_c = 11.3 ± 6.9 nm) despite the same supporting technique used. It can be assumed that GO facilitates NP support due to its good dispersibility in water and less wrinkling structure than rGO, making smaller NPs more easily dispersed on the surface of GO.

If no support material is employed, the peak size of unsupported FeNi NPs in water by PLAL is found to be x_c = 14.4 ± 13.0 nm [84].

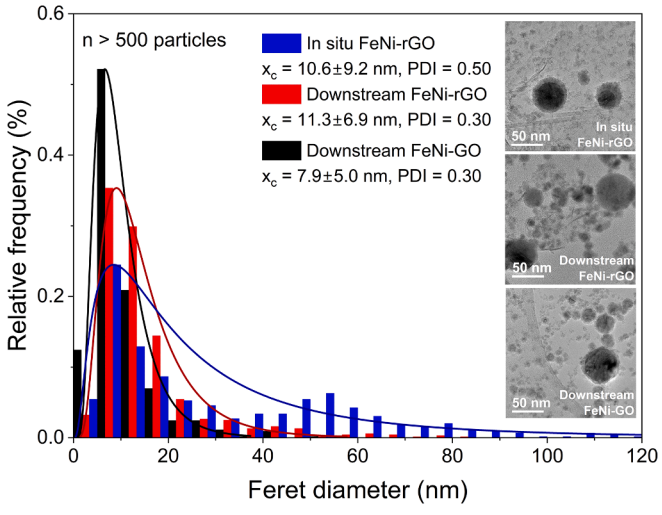

Fig. 4. Histograms of the particle size distribution of in situ FeNi-rGO (blue), downstream FeNi-rGO (red), and downstream FeNi-GO (black). The x_c value corresponds to the median (centre) value of the log-normal distribution, while the polydispersity index (PDI) defines the size dispersity of the NPs.

Compared to this value, we observe a particle size shift towards smaller values by 3.1 nm, 3.8 nm, and 6.5 nm for in situ FeNi-rGO, downstream FeNi-rGO, and downstream FeNi-GO, respectively. Meanwhile, the polydispersity index (PDI) [71] values of each sample, Fig. 4, are 0.50 (in situ FeNi-rGO), 0.30 (downstream FeNi-rGO), and 0.30 (downstream FeNi-GO), which are smaller than the PDI of unsupported FeNi NPs (PDI = 0.53) [84]. Similar average size reductions were also found in the case of in situ PLAL of Pt and Au NPs on rGO and GO, respectively, when compared with the unsupported or ex situ supporting [77,79]. It confirms that both in situ and downstream PLAL could provide a size quenching effect compared to the ex situ and standard PLAL methods.

3.1.3. Electrocatalytic activity

The OER electrocatalytic activities of in situ FeNi-rGO, downstream FeNi-rGO, and downstream FeNi-GO with the same NPs loading were investigated using CV in 0.1 M KOH, Fig. 5 (a). The CVs of in situ FeNi-rGO and downstream FeNi-rGO are almost overlapping, indicating that they have similar OER activity, meanwhile, the activity of downstream FeNi-GO is much lower than the FeNi-rGO samples. Extracting these overpotential data at 10 mA/cm^2 shows that downstream FeNi-rGO has the lowest overpotential at approximately 418 mV, followed closely by in situ FeNi-rGO at 432 mV, and downstream FeNi-GO with the highest overpotential of almost 500 mV, Fig. 5 (b). Despite the more uniform distribution of the FeNi NPs on the surface of GO flakes, GO has more oxygen functional groups which leads to increasing defects and the sp^3 carbon hybridization [96]. This reduces the π electrons conjugation and hinders the electron transfer process, lowering its electrical conductivity [96]. Hence, the performance of FeNi-GO is significantly worse than the FeNi-rGO samples. Meanwhile, the corresponding Tafel slopes of these samples, as shown in Fig. 5 (c), are all lower than 120 mV/dec, indicating that the rate-determining step happens after one-electron transfer reaction [97]. Electrochemical impedance spectroscopy (EIS) was evaluated to assess the charge transfer rate for the three electrodes, Figure S5. The diameter of the semicircle EIS plot represents the resistance of charge transfer (R_{ct}), whereas the smaller diameter shows a higher charge diffusion rate. The in situ FeNi-rGO and downstream FeNi-rGO have similar R_{ct} values, which are smaller than that of downstream FeNi-GO. Based on these electrochemical performances, FeNi-rGO prepared by in situ and downstream PLAL have higher OER catalytic activities and charge transfer rates than the downstream FeNi-GO. In addition, similar performance between in situ and downstream FeNi-rGO shows that the supporting mechanism of FeNi on the rGO does not significantly influence its electrochemical performance. Consequently, due to the higher FeNi NPs productivity achievable by downstream PLAL, the downstream FeNi-rGO sample is selected for further testing.

3.1.4. Surface elemental analysis

The influence of different supporting mechanisms, in situ and downstream PLAL, on the FeNi NPs' surface oxidation and rGO microflakes' carbon structures are further investigated. The presence of carbon and residual oxygen functional groups in rGO may contribute to the formation of oxide, hydroxide, or carbon layer in the FeNi NPs due to pyrolysis of rGO. Furthermore, FeNi NPs produced during in situ PLAL might be attached and anchored in the intercalation of the carbon layers, possibly increasing the interlayer distance of rGO sheets. Hereby, we performed XPS and Raman spectroscopy measurements of in situ and downstream FeNi-rGO to confirm the elements and phases of dispersed FeNi NPs and the carbon network structures of the rGO.

Surface elemental analysis of as-prepared FeNi-rGO is important to unveil their catalytic response and to elucidate the influence of supporting techniques. The XPS results of pristine commercial rGO, Figure S6, show the carbon and oxygen 1 s spectra, which are the only detectable elements (90 at% C, 10 at% O). The carbon was fitted using the oxygen intensities as loose constraints on the intensity of the oxidized carbon species (C–O, C=O and COOH) [98]. The carbon signal is then best described by an asymmetric graphitic C–C peak (asymmetry parameters in CasaXPS LA(0.95,1.9,50)) and a minor contribution of non-graphitic carbon (about 10 % of the carbon signal), which possibly can be attributed to carbon contaminations on the surface of the rGO. Meanwhile, the XPS results of the dropcast in situ FeNi-rGO and downstream FeNi-rGO samples are shown in Fig. 6. The determined atomic concentrations of the elements are given in Table 1. The atomic ratio of Fe to Ni is roughly 2:1 for both in situ and downstream FeNi-rGO, which might verify the formation of the $NiFe_2O_4$ layer on the surface of FeNi NPs [71]. Nevertheless, in situ FeNi-rGO shows a higher oxygen content than the downstream FeNi-rGO (35 at% to 29 at%), presumably due to the presence of rGO during the PLAL process leading to further oxidation and higher O content, or due to surface contamination.

The best fitting results for Ni $2p_3$ spectra, Fig. 6 (b), were achieved by assuming the existence of three Ni species: $NiFe_2O_4$, metallic Ni, and Ni oxide/hydroxide [99]. The intensity of the $NiFe_2O_4$ was constrained to the corresponding metal oxide signal in the respective O 1 s spectrum. The same was done for the Fe $2p_3$ signal, Fig. 6 (a). Due to the small signal intensity and low signal/noise ratio, the results of the fitting procedure have a large uncertainty. However, the amount of metallic Ni is significantly smaller for the in situ FeNi-rGO (9 % of the total Ni signal) than for the downstream FeNi-rGO (16 % of the total Ni signal). Meanwhile, the ratio of the Ni oxide/hydroxide to the $NiFe_2O_4$ contribution is, within the error, the same for both FeNi-rGO samples. The Fe $2p_3$ spectrum for the downstream FeNi-rGO shows the typical Fe_2O_3 satellite at around 720 eV binding energy, Fig. 6 (a). Pure $NiFe_2O_4$ does not seem to show this satellite [99] and this satellite is not visible for the in situ FeNi-rGO. It can be deduced, that the Fe_2O_3-like configuration of the Fe is smaller for in situ FeNi-rGO than downstream FeNi-rGO. Nevertheless, the signal intensity of this Fe_2O_3 satellite is low and no influence on the electrocatalytic performance is observed. As for the

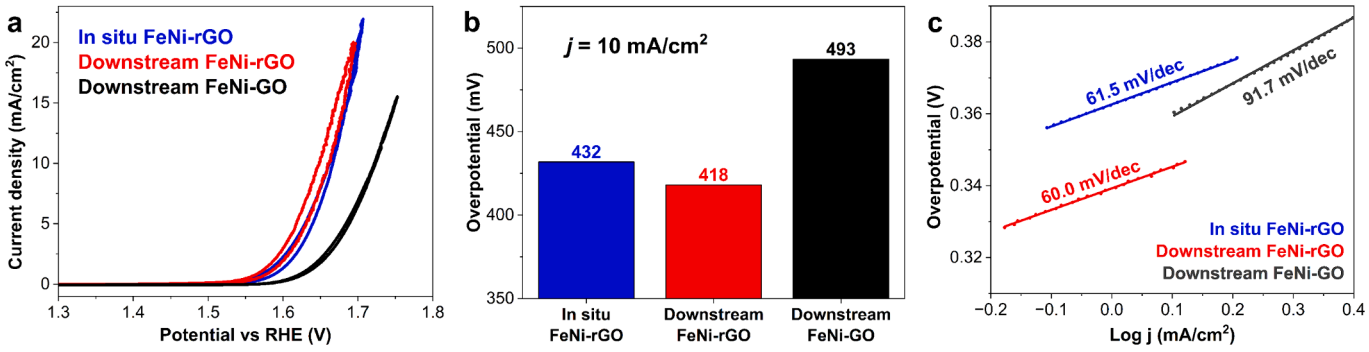

Fig. 5. (a) cyclic voltammetry curves in O_2 saturated 0.1 M KOH at a scan rate of 5 mV/s, (b) its respective overpotential at a current density of 10 mA/cm^2, and (c) the corresponding Tafel slope.

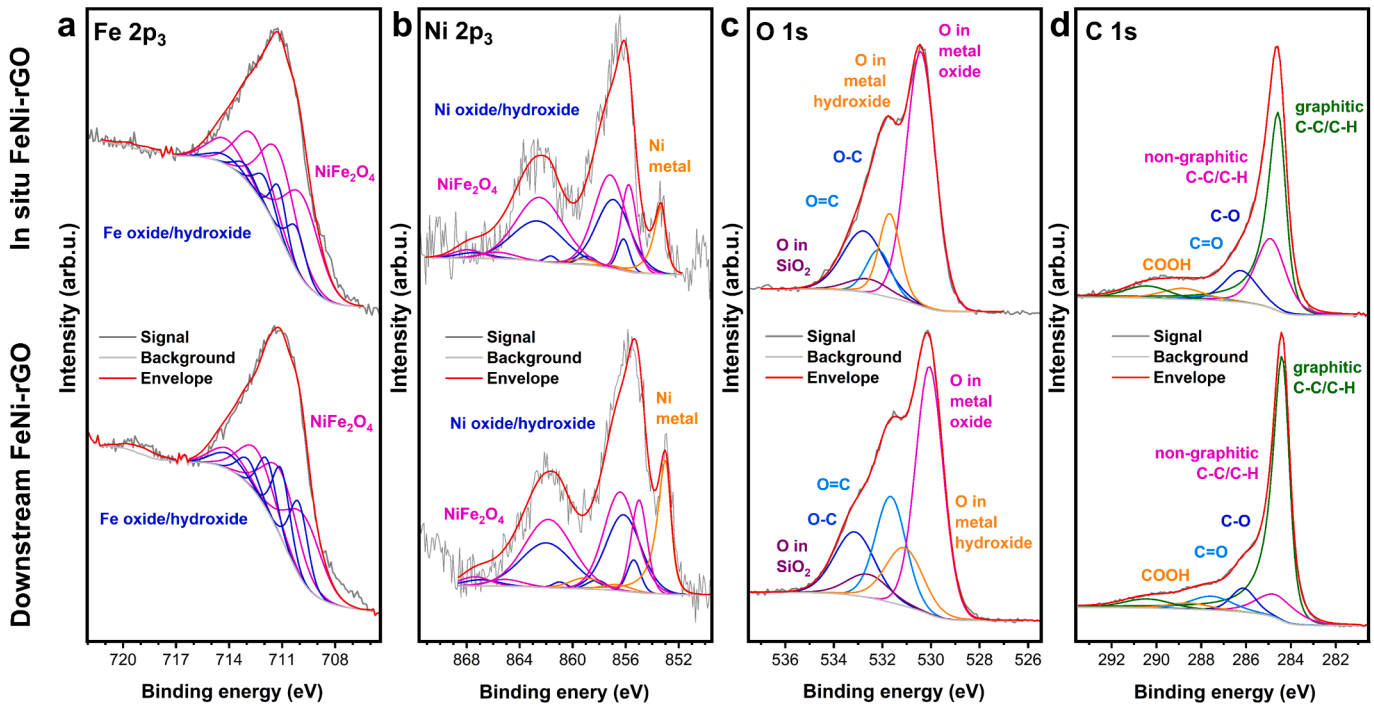

Fig. 6. High-resolution XPS spectra of (a) Fe $2p_3$, (b) Ni $2p_3$, (c) O 1 s, and (d) C1s for in situ FeNi-rGO (top) and downstream FeNi-rGO (bottom).

Table 1
Determined elemental concentrations in the sample surface using the XPS data.

Sample	Fe	Ni	O	C	Si
Pristine rGO	–	–	10 at%	90 at%	–
In situ FeNi-rGO	8 at%	3 at%	35 at%	54 at%	< 1 at%
Downstream FeNi-rGO	6 at%	3 at%	29 at%	62 at%	< 1 at%

contribution of metallic Fe, it is less pronounced and thus omitted from the fitting. Yet, the 707 eV binding energy can be attributed to metallic Fe and it is slightly larger for the downstream FeNi-rGO than in situ FeNi-rGO. A more detailed deconvolution of the metal oxide/hydroxide species for Ni and Fe is not possible due to the small signal intensities.

The O 1 s peaks for both in situ FeNi-rGO and downstream FeNi-rGO, Fig. 6 (c), show the strongest signal at slightly below 530 eV binding energy, which can be attributed to the existence of metal oxides [99]. Aside from the expected organic oxygen species from the rGO, some contributions of metal hydroxide at around 531.5 eV and a minor contribution of oxygen from the SiO_2 substrate are detected.

Comparing the C 1 s signals of in situ FeNi-rGO and downstream FeNi-rGO, Fig. 6 (d), to that of pristine rGO, Figure S6, the main difference is that both samples, especially the in situ FeNi-rGO, show a slightly higher non-graphitic C–C and also C–O content compared to that of pristine rGO. The contribution to the total C 1 s spectrum increases from 25 % in pristine rGO to about 45 % for the in situ FeNi-rGO. This could be an effect of the laser interaction with the rGO during the synthesis in the in situ setup, inducing pyrolysis and the formation of non-graphitic carbon, or carbon contamination during the PLAL process.

3.1.5. *Structural analysis of reduced graphene oxide*

Raman spectroscopy is employed as an effective tool to quantify the structural changes in the carbon network of the rGO. Raman spectra of all samples, Fig. 7 (a), show a similar peak profile, the presence of the rGO. After baseline correction and performing peak-fitting, the signature D and G bands were deconvoluted into five interbands [92,100,101], Fig. 7 (b) and Table 2. The D peak (~1350 cm^{-1}) is correlated to the breathing mode of the hexagonal sp^2 carbon lattice of the rGO. The broad and faint D* (~1200 cm^{-1}) is related to the breathing

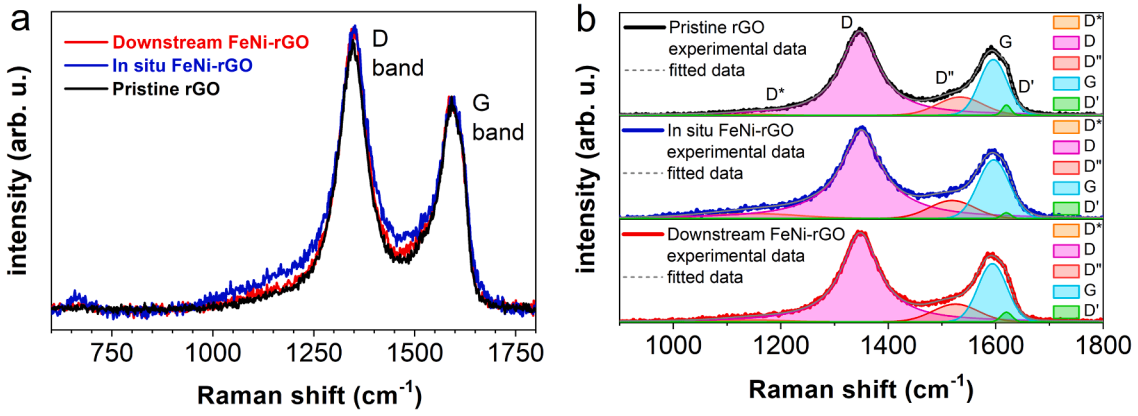

Fig. 7. (a) Raman scattering of pristine rGO, in situ FeNi-rGO, and downstream FeNi-rGO with the same D and G band profile. (b) Representative deconvolution of Raman spectra of pristine rGO, in situ FeNi-rGO, and downstream FeNi-rGO highlighting the D*, D', and D" interbands at the shoulders of D and G peaks.

Table 2
Relevant peak parameters were calculated for pristine rGO and FeNi-rGOs.

Sample	I_D/I_G	I_{D*}/I_G	$I_{D"}/I_G$	D position, cm^{-1}	D" position, cm^{-1}
Pristine rGO	1.49 ± 0.02	0.014 ± 0.008	0.306 ± 0.008	1347.7 ± 0.2	1531 ± 1
In situ FeNi-rGO	1.41 ± 0.05	0.102 ± 0.018	0.324 ± 0.020	1350.1 ± 0.5	1506 ± 5
Downstream FeNi-rGO	1.49 ± 0.02	0.038 ± 0.008	0.303 ± 0.008	1348.9 ± 0.5	1526 ± 1

of the lattice disorder by sp^2-sp^3 bonds and, consequently, interlayer distance. The G peak signature (~1600 cm^{-1}), associated with the vibration of graphitic sp^2 domains, shows a D' peak shoulder (~1625 cm^{-1}) originating from structurally defective graphene, and another D" peak shoulder (~1550 cm^{-1}) attributed to the amorphization of the rGO. These peaks can shift in intensity and position depending on the structure and functionalization [91].

The intensity ratios, sensitive to the formation of defects and material functionalization, depict the interaction of rGO with the FeNi NPs. In Table 2, the I_D/I_G values are consistent for pristine rGO and downstream FeNi-rGO, which rule out the possibilities of (1) further growth of sp^2 clusters and (2) any structurally damaging effect of laser and/or FeNi NP to the rGO hexagonal sp^2 lattice. Only in situ FeNi-rGO registered a slight decrease in I_D/I_G value. In addition, in situ FeNi-rGO shows a higher $I_{D"}/I_G$ and I_{D*}/I_G which correlates to the loss of crystallinity and increase in interlayer distance between rGO sheets. As evidenced by TEM, Fig. 3, and HAADF images, Figure S4, in situ FeNi-rGO achieved better FeNi NPs dispersion on rGO sheets compared to downstream FeNi-rGO. This homogenous distribution of FeNi NPs may explain the expanded interlayer distance of rGO sheets, increasing the I_{D*}/I_G tenfold, Table 2, while the intercalation of polydisperse FeNi NPs between rGO sheets can prevent intimate and regular stacking of layers (i.e., amorphization), generating a higher $I_{D"}/I_G$.

As the rGO sheets wrap around FeNi NPs, structures in the curvature suffer from a biaxial strain that shifts the phonon dispersion to higher frequencies [102,103]. The position of the D peak, sensitive to structural stress and doping [104–106], registers a blueshift (~3 cm^{-1}) in the in situ FeNi-rGO sample. The oxygen content of the rGO sheets can be estimated using the peak position of the D" peak [91]. The D" peak of in situ FeNi-rGO shifts to a much lower frequency suggesting laser-induced removal of oxygen functional groups, Table 2, further reducing rGO.

3.2. Electrocatalytic activity of a Ni foam-based electrode

The produced downstream FeNi-rGO was chosen as the constituent of the Ni foam-based electrode. As discussed in Section 3.1, no significant difference can be observed in the influence of supporting techniques on the FeNi particle size, Fig. 4. Although in situ FeNi-rGO has a more uniform dispersion, Fig. 3, and a larger expansion of rGO sheets' interlayer spacings, Table 2, there is no evidence that it improves the OER catalytic activity, Fig. 5. Since the in situ FeNi-rGO does not offer higher electrocatalytic performance, we further tested the downstream FeNi-rGO for the larger electrode (with FeNi LDH/Ni-foam substrate) as the productivity of the downstream PLAL is higher, facilitating a prospective transfer to industrial fabrication of electrodes.

The produced downstream FeNi-rGO was spray-coated on a FeNi LDH/Ni foam substrate, Fig. 2. Ni foam was used instead of planar electrodes since the porous 3D structures promote electron transport and provide a larger active surface area for the water and electrolytes to be exposed to the catalyst [48]. The FeNi layered double hydroxides (LDH) were grown on the surface of the Ni foam Fig. 2 to further increase the surface area and help the attachment of the FeNi-rGO to the Ni foam [107]. LDH could enhance the attachment of FeNi-rGO composites on the Ni foam due to the electrostatic attraction [107], and its extremely high stability [50] makes it suitable as a component of the hybrid catalyst. Nevertheless, the FeNi LDH grown on Ni-foam was found to lose its LDH structure after undergoing calcination at 400 °C, Figure S7. For the downstream FeNi-rGO spray-coated on FeNi LDH/Ni foam substrate, we could not confirm whether the LDH is ruptured or sustained after the calcination as the LDH is not visible behind the FeNi NPs-rGO, Fig. 8. Hence, we conducted XRD measurements of FeNi LDH/Ni foam and FeNi-rGO/FeNi LDH/Ni foam before and after calcination, Figure S8. FeNi LDH peaks [39,108] in our XRD data are located at $2\theta =$ 34.86° (012), 39.17° (015), 46.05° (018), 60.07° (110), and 61.31° (113), which are visible in both FeNi LDH/Ni foam and FeNi-rGO/FeNi LDH/Ni foam before the calcination step, confirming the presence of FeNi LDH. After the calcination, however, we found those peaks diminishing from the XRD data and there was the formation of new peaks at $2\theta =$ 29.24°, 44.13°, 47.31°, and 63.20° which might correspond to oxides of iron and nickel, such as $NiFe_2O_4$, NiO, and Fe_3O_4. Thereby we suppress the descriptor of "LDH" in the FeNi LDH/Ni-foam and FeNi-rGO/FeNi LDH/Ni foam and will further refer to them as FeNi/Ni foam and FeNi-rGO/FeNi/Ni foam, respectively.

The XPS data of FeNi-rGO/FeNi/Ni foam, Figure S9, is very similar to that of the downstream FeNi-rGO, except for two visible features. The electrode shows a higher non-graphitic C–C/C–H contribution without an increase in the relative C–O content. Secondly, more Ni oxide/hydroxide is found, which is represented by the higher Ni/Fe ratio, which is close to 1. Both findings can be explained by a non-complete coverage of the foam by the particles. Hence, the foam surface might contain higher carbon contamination than the FeNi-rGO.

Meanwhile, the Raman spectroscopy result of FeNi-rGO/FeNi/Ni foam shows higher graphitic C content and lower oxygen functional group (OFG) content as seen in lower I_D/I_G and I_{D*}/I_G values, respectively, Figure S10. These two observations are synergistic since during calcination unstable OFGs are released [109] and the graphitic lattice is restored, thus lowering the I_D/I_G. Furthermore, the elimination of OFGs produces CO and CO_2 gases which may have reacted with the nickel foam and produced more nickel oxide, as observed in XPS.

In this part onward, we are focusing on the electrocatalytic activity results of 3 samples: (1) calcinated downstream FeNi-rGO spray-coated on the FeNi LDH grown on Ni foam, referred to as FeNi-rGO/FeNi/Ni foam, (2) calcinated FeNi LDH/Ni-foam electrode substrate, referred to as FeNi/Ni-foam, and (3) commercial ruthenium oxide spray-coated on Ni-foam as the benchmark electrocatalyst, referred to as RuO_2/Ni-foam.

The resulting linear sweep voltammetry (LSV) polarization curves performed in O_2-saturated 0.1 M KOH of the aforementioned samples are shown in Fig. 9 (a). The OER polarization curves of the FeNi-rGO/FeNi/Ni foam exhibit smaller onset potentials and higher current densities at a fixed potential compared to RuO_2/Ni foam and FeNi/Ni foam, suggesting a better OER activity. The required overpotentials at a current density of 10 mA/cm^2 are shown in Fig. 9 (b). FeNi/Ni foam requires the highest overpotential of 330 mV, presumably due to the rupture of the FeNi LDH structure by calcination, Figure S7, thus less active surface area is available for the OER. Meanwhile, an overpotential of only 234 mV was required for FeNi-rGO/FeNi/Ni foam, which is lower than the benchmark material RuO_2/Ni foam at 271 mV. The Tafel slopes of FeNi-rGO/FeNi/Ni foam (76.0 mV/dec), RuO_2/Ni foam (237.7 mV/dec), and FeNi/Ni foam (377.5 mV/dec) are presented in Fig. 9 (c). FeNi/Ni foam and RuO_2/Ni foam with Tafel slope values higher than 120 mV/dec indicate that surface species are formed just before the rate-determining step (RDS) is predominant [97], which is similar to a single electron transfer reaction. Meanwhile, FeNi NPs-rGO/FeNi/Ni foam results in a Tafel slope lower than 120 mV/dec, at approximately 70–80 mV/dec, indicating that the adsorbed surface species are produced in the earlier stage of the predominant OER step [97], hence the rate-determining step happens after one-electron transfer reaction.

The high catalytic activity of the hybrid catalyst may be attributed to the formation of a thin oxidized layer of $NiFe_2O_4$ on the surface of laser-

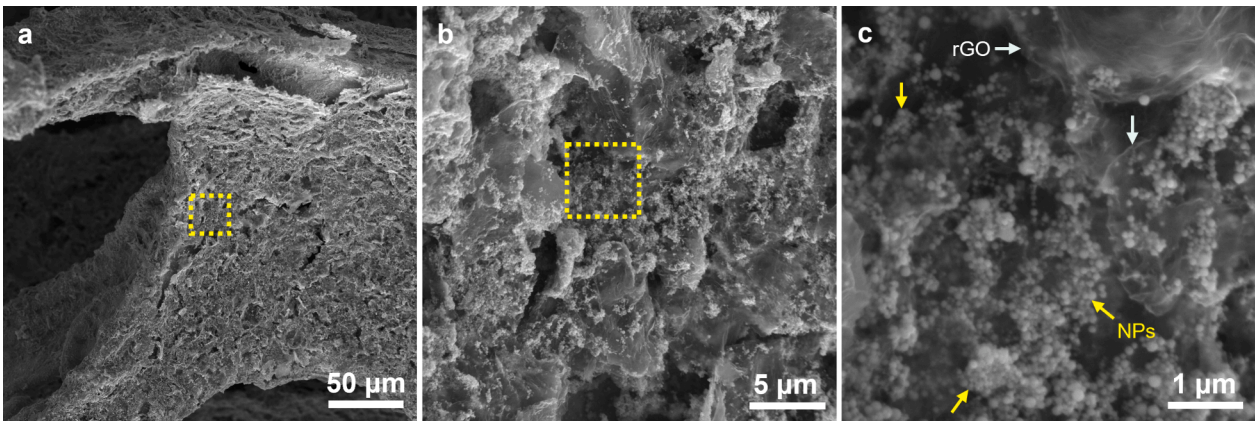

Fig. 8. SEM images of FeNi-rGO/FeNi/Ni foam after calcination at 400 °C, taken in different magnifications (magnified areas are indicated by the yellow rectangles). Figure (c) shows FeNi NPs (yellow arrow) which are dispersed on the surface of rGO sheets (white arrow).

generated FeNi NPs [71], which was found to enhance the OER activity [72–75]. In addition, the dispersion of these FeNi NPs on FeNi/Ni foam may form a synergistic effect between the $NiFe_2O_4$ layer, FeNi core, and FeNi/Ni foam, as the metal-oxide surface could host reaction intermediates, which then may migrate to the more active area for the reaction to complete [110,111]. Besides the aforementioned hypothesis, the high catalytic activity of FeNi-rGO/FeNi/Ni foam may also be attributed to the following factors, (1) the high conductivity of rGO as support material, Table S1, (2) dispersion of FeNi NPs on rGO surface, Fig. 3, reducing NPs overlapping and obstruction or shielding of the active sites, (3) synergistic interaction between FeNi and rGO which induces charge redistribution and electron transfer between the metal-support at the interface [111], and (4) hybrid catalyst providing more cations' valence state suitable for wide range bonding with intermediate species [110]. In addition, while we cannot completely rule out the contribution of the ruptured FeNi LDH to the increased surface area and overall current, and it complicates direct comparisons of intrinsic catalytic activity between FeNi-rGO alone and RuO_2, our primary goal was to develop a catalyst using only abundant elements—specifically Fe and Ni—without relying on rare elements. We achieved this by combining FeNi-rGO with FeNi LDH (which is ruptured after calcination) and utilizing Ni foam. This hybrid catalyst system, referred to as FeNi-rGO/FeNi/Ni foam, demonstrates promising performance with low overpotential for the OER.

The stability of the OER catalyst is critical from a practical viewpoint. The electrochemical durability was investigated by ADT and chronopotentiometry in N_2-saturated 0.1 M KOH. As shown in Fig. 9 (d), the degradation of OER activity is negligible after running 10,000 cycles, indicating its superior durability. Fig. 9 (e) also shows the chronopotentiometry result where the potential required to achieve a current density of 10 mA/cm^2 remains relatively constant even after 1300 h of testing. The hybrid FeNi NPs, rGO, and FeNi/Ni foam catalysts are confirmed to have outstanding stability. XRD results before and after 1300 h of testing, Fig. 9 (f), show no considerable structural changes in the hybrid catalyst. Based on the electrocatalytic performance presented in Fig. 9, the FeNi-rGO/FeNi/Ni foam hybrid catalyst is proven as a high-performance catalyst in both activity and stability.

Economic analysis is performed to compare the production cost of FeNi-rGO/FeNi/Ni foam to the benchmark catalyst, RuO_2/Ni foam (calculation constraints can be found in the Supporting Materials). Based on our calculation, the production cost of FeNi-rGO/FeNi/Ni foam is approximately 2,393 €/kg, with Ni foam as the highest mass and cost contributor. Meanwhile, the production cost of RuO_2/Ni foam is approximately 4,763 €/kg, with RuO_2 being the highest cost contributor despite the small quantity used. The production cost of RuO_2/Ni foam is twice as high as that of FeNi-rGO/FeNi/Ni foam due to the significantly higher price of RuO_2 NPs at 400 €/g [112]. Comparing the prices of bulk material, Ru is sold at 13,000 €/kg (purity 99.90 %) [113] and is priced at 11,700 €/kg (purity 99.95 %) according to Shanghai Metals Market [114]. Meanwhile, Ni with a purity of 99.90 % is priced at 17 €/kg [115]. As for iron, a direct comparison is difficult as it is usually traded as ores, steel, or other alloy forms, hence, we could only consider the price of bulk steel (iron content > 97 %), which is 0.8 €/kg [116]. The estimated cost difference between RuO_2/Ni foam to FeNi-rGO/FeNi/Ni foam is extremely large, with RuO_2/Ni requiring an additional 2,370 €/kg. It is therefore important to use abundant elements such as Fe and Ni for large-scale applications.

4. Conclusion

A hybrid catalyst free of precious metals or rare elements has been synthesized and investigated as an OER catalyst in the alkaline water splitting process. The hybrid catalyst consisting of laser-generated FeNi NPs dispersed on rGO microflakes and spray-coated on a FeNi/Ni foam substrate, FeNi-rGO/FeNi/Ni foam, shows an outstanding performance in terms of catalytic activity and stability. To produce FeNi-rGO/FeNi/Ni foam catalyst, FeNi-rGO composites were first generated and supported on rGO sheets through the PLAL method. Two techniques to directly synthesise and support the FeNi NPs to rGO were compared, namely in situ and downstream PLAL. In situ PLAL is known to quench produced NPs, resulting in smaller size and theoretically higher catalytic activity, but the presence of light-absorbing or light-scattering matters in the liquid carrier during PLAL results in lower production rate, which was 50 mg/h productivity reduction in this study at rGO concentration of only 15 mg/L. At a higher concentration of rGO, FeNi NPs productivity will be reduced even further due to laser shielding by rGO microflakes. Hence, downstream PLAL was investigated as a more productive approach to synthesizing and supporting FeNi NPs on rGO without the optical shielding effect.

Based on our investigation, both in situ and downstream PLAL show a size-quenching effect on the generated FeNi NPs, resulting in size reductions of approximately 3–4 nm compared to unsupported FeNi NPs. Although NPs dispersion is more uniform in the case of in situ FeNi-rGO than in downstream FeNi-rGO, both samples show similar results in terms of particle size and overpotential (at 10 mA/cm^2) of approximately 10 nm and 400 mV, respectively. In addition, Raman spectroscopy reveals ten-fold increases of $I_{D''}/I_G$ and I_{D*}/I_G of in situ FeNi-rGO compared to downstream FeNi-rGO, implying to loss of crystallinity and an increase in rGO sheets' interlayer spacing in the case of in situ FeNi-rGO. As we aim to produce a catalyst free of precious metals or rare elements with high activity and production rate, downstream PLAL has clear advantages over in situ PLAL to produce FeNi-rGO composites. Combining the downstream FeNi-rGO composite with FeNi/Ni foam substrate, the hybrid FeNi-rGO/FeNi/Ni foam catalyst achieved high

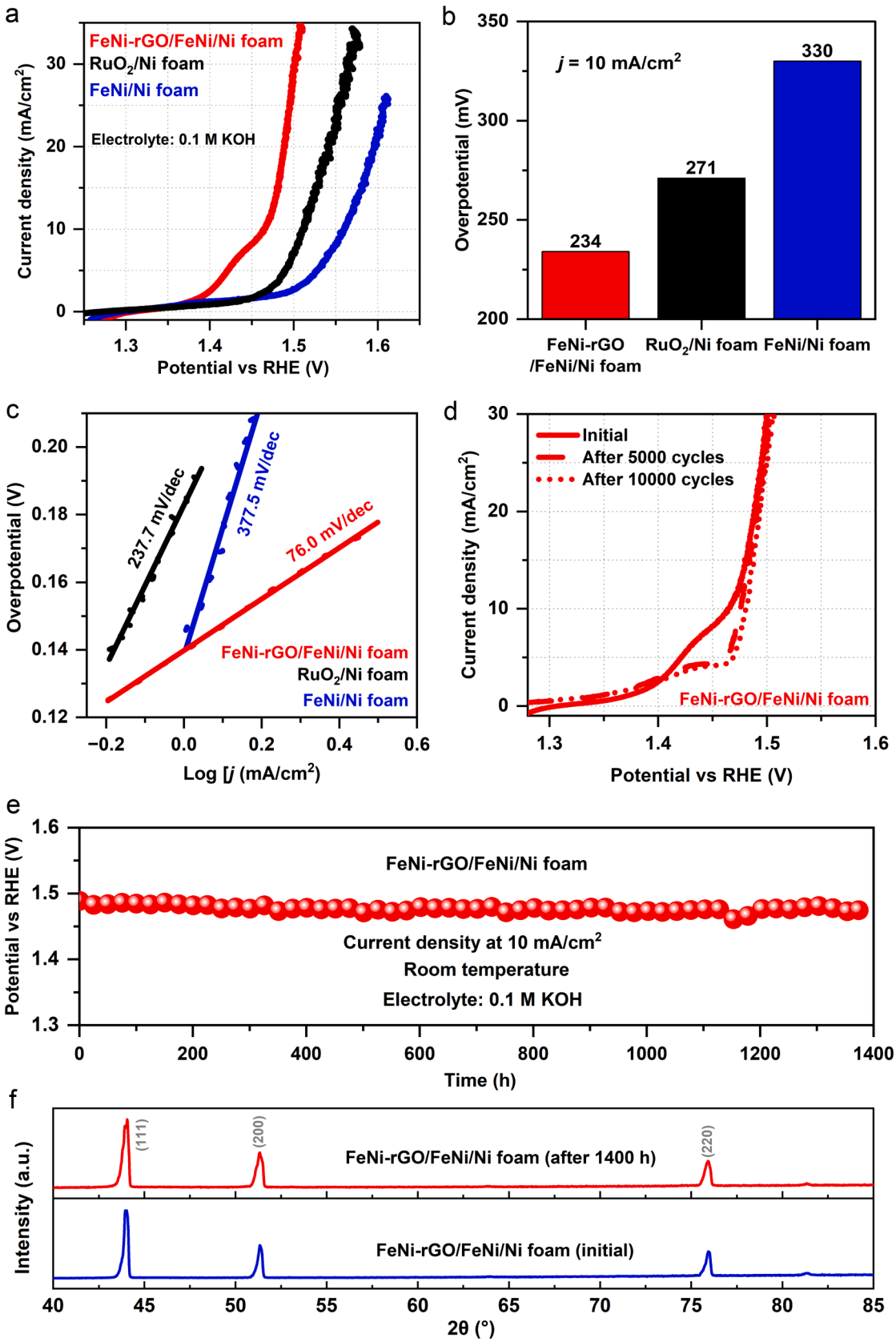

Fig. 9. Electrocatalytic performance of FeNi-rGO/FeNi/Ni foam, FeNi/Ni foam (substrate), and RuO_2/Ni foam. (a) The LSV results in 0.1 M KOH, (b) the overpotential at a current density of 10 mA/cm^2, and (c) the corresponding Tafel slope. Stability test of our hybrid FeNi-rGO/FeNi/Ni foam catalyst: (d) ADT test of FeNi-rGO/FeNi/Ni foam, (e) chronopotentiometry results at a current density of 10 mA/cm^2 for more than 1300 h, and (f) XRD diffractogram of the hybrid catalyst after more than 1300 h durability test compared to the initial state.

OER catalytic activity which requires an overpotential of only 234 mV at a current density of 10 mA/cm^2, in addition to exceptional durability and stability, depicted from the stable chronopotentiometry results for over 1300 h at a current density of 10 mA/cm^2.

Author Contributions

Conceptualization: I.Y.K., B.J., T.K., C.D-B., B.G.; Methodology: I.Y.K., B.J., S.P., U.H., C.R., T.K., C.D-B., B.G.; Investigation: I.Y.K., B.J., S.P., U.H.; Writing – Original Draft: I.Y.K., B.J., S.P., U.H.; Writing – Review & Editing: I.Y.K., B.J., S.P., C.R., C.D-B., B.A., T.K., B.G.; Visualization: I.Y.K., B.J., S.P., U.H., C.D-B.; Supervision: J.M., C.R., T.K., C.D-B., B.G.; Project administration: I.Y.K., C.D-B., B.A., A.O., J.M., C.R., T.K., B.G.; Funding acquisition: B.A., A.O., J.M., C.R., T.K., B.G. All authors have read and agreed to the published version of the manuscript.

Funding

The authors acknowledge funding by the European Union's Horizon 2020 research and innovation program under the grant agreement No 952,068 (project LESGO) and the Deutsche Forschungsgemeinschaft (DFG, German Research Foundation), grant numbers GO 2566/14–1 and GO 2566/7–2. The authors further thank the DFG and NRW for funding in the frame of the major equipment program (INST 218/87–1, 503865051). The Interdisciplinary Center for Analytics on the Nanoscale (ICAN) of the University of Duisburg-Essen (DFG RIsources reference: RI_00313), is a DFG-funded core facility (Project Nos. 233,512,597 and 324659309). ICFO additionally acknowledges financial support from CEX2019-000910-S (MCIN/AEI/https://doi.org/10.13039/501100011033), BIST, Fundació Cellex, Fundació Mir-Puig, and Generalitat de Catalunya through CERCA. Bilal Gökce further thanks DFG for funding of the project GO 2566/10–1. Carlos Doñate Buendia thanks Generalitat Valenciana for funding of the project CIDEIG/2023/08 within Gen-T program. Sidney M. Palardonio acknowledges the support from Secretaria d'Universitats i Recerca del Departament de Recerca i Universitats de la Generalitat de Catalunya under grant 2024 FI-3 00390, as well as the European Social Fund Plus. Carles Ros acknowledges support from the MCIN/AEI (FJC2020-043223-I) and the Severo Ochoa Excellence Post-doctoral Fellowship (CEX2019-000910-S).

CRediT authorship contribution statement

Inna Yusnila Khairani: Writing – review & editing, Writing – original draft, Visualization, Validation, Project administration, Methodology, Investigation, Formal analysis, Data curation, Conceptualization. **Benjin Jin:** Writing – review & editing, Writing – original draft, Visualization, Validation, Methodology, Investigation, Formal analysis, Data curation, Conceptualization. **Sidney M. Palardonio:** Writing – review & editing, Writing – original draft, Visualization, Methodology, Investigation, Formal analysis, Data curation. **Ulrich Hagemann:** Writing – original draft, Visualization, Methodology, Investigation, Formal analysis, Data curation. **Beatriz Alonso:** Writing – review & editing, Resources, Funding acquisition, Formal analysis, Data curation. **Amaya Ortega:** Resources, Funding acquisition. **Carlos Doñate-Buendía:** Writing – review & editing, Supervision, Project administration, Methodology, Conceptualization. **Jordi Martorell:** Supervision, Resources, Funding acquisition. **Carles Ros:** Writing – review & editing, Supervision, Resources, Project administration, Methodology, Funding acquisition, Formal analysis. **Tanja Kallio:** Writing – review & editing, Supervision, Resources, Project administration, Methodology, Funding acquisition. **Bilal Gökce:** Writing – review & editing, Supervision, Resources, Project administration, Methodology, Funding acquisition, Conceptualization.

Declaration of competing interest

The authors declare that they have no known competing financial interests or personal relationships that could have appeared to influence the work reported in this paper.

Data availability

Data will be made available on request.

Acknowledgements

The authors would like to thank Markus Heidelmann (ICAN, University of Duisburg Essen) for the TEM measurements.

Appendix A. Supplementary data

Supplementary data to this article can be found online at https://doi.org/10.1016/j.jcat.2024.115771.

References

[1] United Nations, For a livable climate: Net-zero commitments must be backed by credible action, Net Zero Coalit. (2023). https://www.un.org/en/climatechange/net-zero-coalition (accessed April 19, 2024).
[2] R. Miranda, M. Carmo, Roesch Roland, D. Gielen, Making the breakthrough: Green hydrogen policies and technology costs, 2021. www.irena.org.
[3] National Grid, hydrogen colour spectrum, Natl. Grid. (2023). https://www.nationalgrid.com/stories/energy-explained/hydrogen-colour-spectrum (accessed April 19, 2024).
[4] J.M.M. Arcos, D.M.F. Santos, The Hydrogen Color Spectrum: Techno-Economic Analysis of the Available Technologies for Hydrogen Production, Gases. 3 (2023) 25–46, https://doi.org/10.3390/gases3010002.
[5] I. Panić, A. Cuculić, J. Ćelić, Color-Coded Hydrogen: Production and Storage in Maritime Sector, J. Mar. Sci. Eng. 10 (2022) 1995, https://doi.org/10.3390/jmse10121995.
[6] J. Incer-Valverde, A. Korayem, G. Tsatsaronis, T. Morosuk, "Colors" of hydrogen: Definitions and carbon intensity, Energy Convers. Manag. 291 (2023) 117294, https://doi.org/10.1016/j.enconman.2023.117294.
[7] Irena, Renewable Generation Costs in 2022, Abu Dhabi (2022).
[8] IRENA, Electrolyser costs, Int. Renew. Energy Agency. (2022). https://www.irena.org/Energy-Transition/Technology/Hydrogen/Electrolyser-costs (accessed February 27, 2024).
[9] IRENA, Green,, Hydrogen Cost Reduction: Scaling up Electrolysers to Meet the 1.50C Climate Goal, International Renewable Energy Agency, International Renewable Energy Agency, Abu Dhabi (2020) www.irena.org/publications.
[10] C. Wang, F. Yang, L. Feng, Recent advances in iridium-based catalysts with different dimensions for the acidic oxygen evolution reaction, Nanoscale Horizons. 8 (2023) 1174–1193, https://doi.org/10.1039/D3NH00156C.
[11] Y. Zhao, N.M. Vargas-Barbosa, E.A. Hernandez-Pagan, T.E. Mallouk, Anodic Deposition of Colloidal Iridium Oxide Thin Films from Hexahydroxyiridate(IV) Solutions, Small. 7 (2011) 2087–2093, https://doi.org/10.1002/smll.201100485.
[12] Y. Lee, J. Suntivich, K.J. May, E.E. Perry, Y. Shao-Horn, Synthesis and Activities of Rutile IrO_2 and RuO_2 Nanoparticles for Oxygen Evolution in Acid and Alkaline Solutions, J. Phys. Chem. Lett. 3 (2012) 399–404, https://doi.org/10.1021/jz2016507.
[13] C. Li, J.-B. Baek, Recent Advances in Noble Metal (Pt, Ru, and Ir)-Based Electrocatalysts for Efficient Hydrogen Evolution Reaction, ACS Omega. 5 (2020) 31–40, https://doi.org/10.1021/acsomega.9b03550.
[14] C.C.L.L. McCrory, S. Jung, I.M. Ferrer, S.M. Chatman, J.C. Peters, T.F. Jaramillo, Benchmarking Hydrogen Evolving Reaction and Oxygen Evolving Reaction Electrocatalysts for Solar Water Splitting Devices, J. Am. Chem. Soc. 137 (2015) 4347–4357, https://doi.org/10.1021/ja510442p.
[15] S. Wang, A. Lu, C.J. Zhong, Hydrogen production from water electrolysis: role of catalysts, Nano Converg. 8 (2021), https://doi.org/10.1186/s40580-021-00254-x.
[16] F. Zhou, Y. Zhou, G.G. Liu, C.T. Wang, J. Wang, Recent advances in nanostructured electrocatalysts for hydrogen evolution reaction, Rare Met. 40 (2021) 3375–3405, https://doi.org/10.1007/s12598-021-01735-y.
[17] L. Zhang, R. Si, H. Liu, N. Chen, Q. Wang, K. Adair, Z. Wang, J. Chen, Z. Song, J. Li, M.N. Banis, R. Li, T.-K. Sham, M. Gu, L.-M. Liu, G.A. Botton, X. Sun, Atomic layer deposited Pt-Ru dual-metal dimers and identifying their active sites for hydrogen evolution reaction, Nat. Commun. 10 (2019) 4936, https://doi.org/10.1038/s41467-019-12887-y.
[18] Y. Liang, Y. Li, H. Wang, J. Zhou, J. Wang, T. Regier, H. Dai, Co3O4 nanocrystals on graphene as a synergistic catalyst for oxygen reduction reaction, Nat. Mater. 10 (2011) 780–786, https://doi.org/10.1038/nmat3087.

[19] M.W. Kanan, D.G. Nocera, In Situ Formation of an Oxygen-Evolving Catalyst in Neutral Water Containing Phosphate and Co 2+, Science (80-,) 321 (2008) 1072–1075, https://doi.org/10.1126/science.1162018.

[20] J. Meng, Z. Cui, X. Yang, S. Zhu, Z. Li, K. Qi, L. Zheng, Y. Liang, Cobalt-iron (oxides) water oxidation catalysts: Tracking catalyst redox states and reaction dynamic mechanism, J. Catal. 365 (2018) 227–237, https://doi.org/10.1016/j.jcat.2018.06.031.

[21] Z. Zhao, B. Zhang, D. Fan, Y. Wang, H. Yang, K. Huang, X. Pan, R. Zhang, H. Tang, M. Lei, Tailoring manganese oxide nanoplates enhances oxygen evolution catalysis in acid, J. Catal. 405 (2022) 265–272, https://doi.org/10.1016/j.jcat.2021.12.009.

[22] I. Zaharieva, P. Chernev, M. Risch, K. Klingan, M. Kohlhoff, A. Fischer, H. Dau, Electrosynthesis, functional, and structural characterization of a water-oxidizing manganese oxide, Energy Environ. Sci. 5 (2012) 7081–7089, https://doi.org/10.1039/c2ee21191b.

[23] C. Hu, L. Zhang, Z. Huang, W. Zhu, Z.-J. Zhao, J. Gong, Facet-evolution growth of Mn3O4@CoxMn3-xO4 electrocatalysts on Ni foam towards efficient oxygen evolution reaction, J. Catal. 369 (2019) 105–110, https://doi.org/10.1016/j.jcat.2018.10.034.

[24] H. Bandal, K.K. Reddy, A. Chaugule, H. Kim, Iron-based heterogeneous catalysts for oxygen evolution reaction; change in perspective from activity promoter to active catalyst, J. Power Sources. 395 (2018) 106–127, https://doi.org/10.1016/j.jpowsour.2018.05.047.

[25] Y. Wei, L. Sun, M. Wang, J. Hong, L. Zou, H. Liu, Y. Wang, M. Zhang, Z. Liu, Y. Li, S. Horike, K. Suenaga, Q. Xu, Fabricating Dual-Atom Iron Catalysts for Efficient Oxygen Evolution Reaction: A Heteroatom Modulator Approach, Angew. Chemie Int. Ed. 59 (2020) 16013–16022, https://doi.org/10.1002/anie.202007221.

[26] B. Han, A. Grimaud, L. Giordano, W.T. Hong, O. Diaz-Morales, L. Yueh-Lin, J. Hwang, N. Charles, K.A. Stoerzinger, W. Yang, M.T.M. Koper, Y. Shao-Horn, Iron-Based Perovskites for Catalyzing Oxygen Evolution Reaction, J. Phys. Chem. c. 122 (2018) 8445–8454, https://doi.org/10.1021/acs.jpcc.8b01397.

[27] C. Feng, M.B. Faheem, J. Fu, Y. Xiao, C. Li, Y. Li, Fe-Based Electrocatalysts for Oxygen Evolution Reaction: Progress and Perspectives, ACS Catal. 10 (2020) 4019–4047, https://doi.org/10.1021/acscatal.9b05445.

[28] L. Bai, Z. Duan, X. Wen, J. Guan, Bifunctional atomic iron-based catalyst for oxygen electrode reactions, J. Catal. 378 (2019) 353–362, https://doi.org/10.1016/j.jcat.2019.09.009.

[29] Y. Li, Z. Wu, P. Lu, X. Wang, W. Liu, Z. Liu, J. Ma, W. Ren, Z. Jiang, X. Bao, High-Valence Nickel Single-Atom Catalysts Coordinated to Oxygen Sites for Extraordinarily Activating Oxygen Evolution Reaction, Adv. Sci. 7 (2020) 1903089, https://doi.org/10.1002/advs.201903089.

[30] V. Vij, S. Sultan, A.M. Harzandi, A. Meena, J.N. Tiwari, W.-G. Lee, T. Yoon, K. S. Kim, Nickel-Based Electrocatalysts for Energy-Related Applications: Oxygen Reduction, Oxygen Evolution, and Hydrogen Evolution Reactions, ACS Catal. 7 (2017) 7196–7225, https://doi.org/10.1021/acscatal.7b01800.

[31] D.R. Kauffman, D. Alfonso, D.N. Tafen, J. Lekse, C. Wang, X. Deng, J. Lee, H. Jang, J.S. Lee, S. Kumar, C. Matranga, Electrocatalytic Oxygen Evolution with an Atomically Precise Nickel Catalyst, ACS Catal. 6 (2016) 1225–1234, https://doi.org/10.1021/acscatal.5b02633.

[32] Y. Chen, K. Rui, J. Zhu, S.X. Dou, W. Sun, Recent Progress on Nickel-Based Oxide/(Oxy)Hydroxide Electrocatalysts for the Oxygen Evolution Reaction, Chem. – A Eur. J. 25 (2019) 703–713, https://doi.org/10.1002/chem.201802068.

[33] Y. Tsubonouchi, Z.N. Zahran, D. Chandra, N. Hoshino, M. Yagi, Prominent development of Ni-based oxygen-evolving electrocatalysts for water splitting, Catal Sci. Technol. 14 (2024) 3287–3319, https://doi.org/10.1039/D4CY00066H.

[34] I. Roger, M.A. Shipman, M.D. Symes, Earth-abundant catalysts for electrochemical and photoelectrochemical water splitting, Nat. Rev. Chem. 1 (2017), https://doi.org/10.1038/s41570-016-0003.

[35] C.C.L. McCrory, S. Jung, J.C. Peters, T.F. Jaramillo, Benchmarking heterogeneous electrocatalysts for the oxygen evolution reaction, J. Am. Chem. Soc. 135 (2013) 16977–16987, https://doi.org/10.1021/ja407115p.

[36] J. Zhang, B.-J. Su, K.-H. Wu, Q. Xia, R. Knibbe, I. Gentle, Low-coordinated surface nickel oxide as electrocatalyst for efficient water oxidation, J. Catal. 429 (2024) 115278, https://doi.org/10.1016/j.jcat.2023.115278.

[37] D.A. Corrigan, The Catalysis of the Oxygen Evolution Reaction by Iron Impurities in Thin Film Nickel Oxide Electrodes, J. Electrochem. Soc. 134 (1987) 377–384, https://doi.org/10.1149/1.2100463.

[38] S. Klaus, Y. Cai, M.W. Louie, L. Trotochaud, A.T. Bell, Effects of Fe Electrolyte Impurities on Ni(OH) 2 /NiOOH Structure and Oxygen Evolution Activity, J. Phys. Chem. c. 119 (2015) 7243–7254, https://doi.org/10.1021/acs.jpcc.5b00105.

[39] L. Trotochaud, S.L. Young, J.K. Ranney, S.W. Boettcher, Nickel-Iron oxyhydroxide oxygen-evolution electrocatalysts: The role of intentional and incidental iron incorporation, J. Am. Chem. Soc. 136 (2014) 6744–6753, https://doi.org/10.1021/ja502379c.

[40] C. Ros, S. Murcia-López, X. Garcia, M. Rosado, J. Arbiol, J. Llorca, J.R. Morante, Facing Seawater Splitting Challenges by Regeneration with Ni−Mo−Fe Bifunctional Electrocatalyst for Hydrogen and Oxygen Evolution, ChemSusChem. 14 (2021) 2872–2881, https://doi.org/10.1002/cssc.202100194.

[41] L. Twight, A. Tonsberg, S. Samira, K. Velinkar, K. Dumpert, Y. Ou, L. Wang, E. Nikolla, S.W. Boettcher, Trace Fe activates perovskite nickelate OER catalysts in alkaline media via redox-active surface Ni species formed during electrocatalysis, J. Catal. 432 (2024) 115443, https://doi.org/10.1016/j.jcat.2024.115443.

[42] I. Spanos, J. Masa, A. Zeradjanin, R. Schlögl, The Effect of Iron Impurities on Transition Metal Catalysts for the Oxygen Evolution Reaction in Alkaline Environment: Activity Mediators or Active Sites? Catal. Letters. 151 (2021) 1843–1856, https://doi.org/10.1007/s10562-020-03478-4.

[43] M. Salmanion, M.M. Najafpour, Oxygen-Evolution Reaction Performance of Nickel (Hydr)Oxide in Alkaline Media: Iron and Nickel Impurities, J. Phys. Chem. c. 127 (2023) 18340–18349, https://doi.org/10.1021/acs.jpcc.3c05164.

[44] N. Li, D.K. Bediako, R.G. Hadt, D. Hayes, T.J. Kempa, F. von Cube, D.C. Bell, L. X. Chen, D.G. Nocera, Influence of iron doping on tetravalent nickel content in catalytic oxygen evolving films, Proc. Natl. Acad. Sci. 114 (2017) 1486–1491, https://doi.org/10.1073/pnas.1620787114.

[45] R.D.L. Smith, M.S. Prévot, R.D. Fagan, S. Trudel, C.P. Berlinguette, Water Oxidation Catalysis: Electrocatalytic Response to Metal Stoichiometry in Amorphous Metal Oxide Films Containing Iron, Cobalt, and Nickel, J. Am. Chem. Soc. 135 (2013) 11580–11586, https://doi.org/10.1021/ja403102j.

[46] J.S. Kim, B. Kim, H. Kim, K. Kang, Recent Progress on Multimetal Oxide Catalysts for the Oxygen Evolution Reaction, Adv. Energy Mater. 8 (2018) 1702774, https://doi.org/10.1002/aenm.201702774.

[47] M.B. Stevens, C.D.M. Trang, L.J. Enman, J. Deng, S.W. Boettcher, Reactive Fe-Sites in Ni/Fe (Oxy)hydroxide Are Responsible for Exceptional Oxygen Electrocatalysis Activity, J. Am. Chem. Soc. 139 (2017) 11361–11364, https://doi.org/10.1021/jacs.7b07117.

[48] Z. Lu, W. Xu, W. Zhu, Q. Yang, X. Lei, J. Liu, Y. Li, X. Sun, X. Duan, Three-dimensional NiFe layered double hydroxide film for high-efficiency oxygen evolution reaction, Chem. Commun. 50 (2014) 6479–6482, https://doi.org/10.1039/C4CC01625D.

[49] M. Gong, Y. Li, H. Wang, Y. Liang, J.Z. Wu, J. Zhou, J. Wang, T. Regier, F. Wei, H. Dai, An Advanced Ni–Fe Layered Double Hydroxide Electrocatalyst for Water Oxidation, J. Am. Chem. Soc. 135 (2013) 8452–8455, https://doi.org/10.1021/ja4027715.

[50] Y. Liu, X. Liang, L. Gu, Y. Zhang, G.-D. Li, X. Zou, J.-S. Chen, Corrosion engineering towards efficient oxygen evolution electrodes with stable catalytic activity for over 6000 hours, Nat. Commun. 9 (2018) 2609, https://doi.org/10.1038/s41467-018-05019-5.

[51] S. Jiang, M. Zhang, C. Xu, G. Liu, K. Zhang, Z. Zhang, H.Q. Peng, B. Liu, W. Zhang, Recent Developments in Nickel-Based Layered Double Hydroxides for Photo(-/)electrocatalytic Water Oxidation, ACS Nano. 18 (2024) 16413–16449, https://doi.org/10.1021/acsnano.4c03153.

[52] C. Tang, H. Wang, H. Wang, Q. Zhang, G. Tian, J. Nie, F. Wei, Spatially Confined Hybridization of Nanometer-Sized NiFe Hydroxides into Nitrogen-Doped Graphene Frameworks Leading to Superior Oxygen Evolution Reactivity, Adv. Mater. 27 (2015) 4516–4522, https://doi.org/10.1002/adma.201501901.

[53] M.S. Burke, S. Zou, L.J. Enman, J.E. Kellon, C.A. Gabor, E. Pledger, S. W. Boettcher, Revised Oxygen Evolution Reaction Activity Trends for First-Row Transition-Metal (Oxy)hydroxides in Alkaline Media, J. Phys. Chem. Lett. 6 (2015) 3737–3742, https://doi.org/10.1021/acs.jpclett.5b01650.

[54] X. Li, F.C. Walsh, D. Pletcher, Nickel based electrocatalysts for oxygen evolution in high current density, alkaline water electrolysers, Phys. Chem. Chem. Phys. 13 (2011) 1162–1167, https://doi.org/10.1039/C0CP00993H.

[55] H.M. Lu, X.K. Meng, Theoretical Model to Calculate Catalytic Activation Energies of Platinum Nanoparticles of Different Sizes and Shapes, J. Phys. Chem. c. 114 (2010) 1534–1538, https://doi.org/10.1021/jp9106475.

[56] S. Cao, F.F. Tao, Y. Tang, Y. Li, J. Yu, Size- and shape-dependent catalytic performances of oxidation and reduction reactions on nanocatalysts, Chem. Soc. Rev. 45 (2016) 4747–4765, https://doi.org/10.1039/C6CS00094K.

[57] I.Y. Khairani, G. Mínguez-Vega, C. Doñate-Buendía, B. Gökce, Green nanoparticle synthesis at scale: a perspective on overcoming the limits of pulsed laser ablation in liquids for high-throughput production, Phys. Chem. Chem. Phys. 25 (2023) 19380–19408, https://doi.org/10.1039/D3CP01214J.

[58] A. Nag, C.M. Nguyen, K.M. Tibbetts, Heterogeneous to homogeneous Cu–Ag nanoparticles by laser reduction in liquid, Appl. Surf. Sci. 610 (2023) 155384, https://doi.org/10.1016/j.apsusc.2022.155384.

[59] L.M. Frias Batista, A. Nag, V.K. Meader, K.M. Tibbetts, Generation of nanomaterials by reactive laser-synthesis in liquid, Sci. China Physics, Mech. Astron. 65 (2022) 274202, https://doi.org/10.1007/s11433-021-1835-x.

[60] F. Ye, K.P. Musselman, Synthesis of low dimensional nanomaterials by pulsed laser ablation in liquid, APL Mater. 12 (2024) 050602, https://doi.org/10.1063/5.0199104.

[61] T. Fromme, S. Reichenberger, K.M. Tibbetts, S. Barcikowski, Laser synthesis of nanoparticles in organic solvents – products, reactions, and perspectives, Beilstein J. Nanotechnol. 15 (2024) 638–663, https://doi.org/10.3762/bjnano.15.54.

[62] L.M. Frias Batista, E. Kaplan, C. Weththasingha, B. Cook, S. Harris, A. Nag, K. M. Tibbetts, How Pulse Width Affects Laser Ablation of Organic Liquids, J. Phys. Chem. b. 127 (2023) 6551–6561, https://doi.org/10.1021/acs.jpcb.3c03708.

[63] B.M. Hunter, J.D. Blakemore, M. Deimund, H.B. Gray, J.R. Winkler, A.M. Müller, Highly Active Mixed-Metal Nanosheet Water Oxidation Catalysts Made by Pulsed-Laser Ablation in Liquids, J. Am. Chem. Soc. 136 (2014) 13118–13121, https://doi.org/10.1021/ja506087h.

[64] R.C. Forsythe, C.P. Cox, M.K. Wilsey, A.M. Müller, Pulsed Laser in Liquids Made Nanomaterials for Catalysis, Chem. Rev. 121 (2021) 7568–7637, https://doi.org/10.1021/acs.chemrev.0c01069.

[65] D. Zhang, J. Liu, P. Li, Z. Tian, C. Liang, Recent Advances in Surfactant-Free, Surface-Charged, and Defect-Rich Catalysts Developed by Laser Ablation and Processing in Liquids, ChemNanoMat. 3 (2017) 512–533, https://doi.org/10.1002/cnma.201700079.

[66] S. Reichenberger, G. Marzun, M. Muhler, S. Barcikowski, Perspective of Surfactant-Free Colloidal Nanoparticles in Heterogeneous Catalysis, ChemCatChem. 11 (2019) 4489–4518, https://doi.org/10.1002/cctc.201900666.
[67] J.D. Blakemore, H.B. Gray, J.R. Winkler, A.M. Müller, Co3O4 Nanoparticle Water-Oxidation Catalysts Made by Pulsed-Laser Ablation in Liquids, ACS Catal. 3 (2013) 2497–2500, https://doi.org/10.1021/cs400639b.
[68] A.A. Manshina, I.I. Tumkin, E.M. Khairullina, M. Mizoshiri, A. Ostendorf, S. A. Kulinich, S. Makarov, A.A. Kuchmizhak, E.L. Gurevich, The Second Laser Revolution in Chemistry: Emerging Laser Technologies for Precise Fabrication of Multifunctional Nanomaterials and Nanostructures, Adv. Funct. Mater. (2024) 2405457, https://doi.org/10.1002/adfm.202405457.
[69] S. Shankar Naik, J. Theerthagiri, F.S. Nogueira, S.J. Lee, A. Min, G.A. Kim, G. Maia, L.M.C. Pinto, M.Y. Choi, Dual-Cation-Coordinated CoFe-Layered Double-Hydroxide Nanosheets Using the Pulsed Laser Ablation Technique for Efficient Electrochemical Water Splitting: Mechanistic Screening by In Situ/Operando Raman and Density Functional Theory Calculations, ACS Catal. 13 (2023) 1477–1491, https://doi.org/10.1021/acscatal.2c05017.
[70] G.W. Yang, Laser ablation in liquids: Applications in the synthesis of nanocrystals, Prog. Mater. Sci. 52 (2007) 648–698, https://doi.org/10.1016/j.pmatsci.2006.10.016.
[71] I.Y. Khairani, Q. Lin, J. Landers, S. Salamon, C. Doñate-Buendía, E. Karapetrova, H. Wende, G. Zangari, B. Gökce, Solvent Influence on the Magnetization and Phase of Fe-Ni Alloy Nanoparticles Generated by Laser Ablation in Liquids, Nanomaterials. 13 (2023) 227, https://doi.org/10.3390/nano13020227.
[72] J. Landon, E. Demeter, N. İnoğlu, C. Keturakis, I.E. Wachs, R. Vasić, A.I. Frenkel, J.R. Kitchin, Spectroscopic Characterization of Mixed Fe–Ni Oxide Electrocatalysts for the Oxygen Evolution Reaction in Alkaline Electrolytes, ACS Catal. 2 (2012) 1793–1801, https://doi.org/10.1021/cs3002644.
[73] N. Dalai, B. Mohanty, A. Mitra, B. Jena, Highly Active Ternary Nickel-Iron oxide as Bifunctional Catalyst for Electrochemical Water Splitting, ChemistrySelect. 4 (2019) 7791–7796, https://doi.org/10.1002/slct.201901465.
[74] J. Jiang, C. Zhang, L. Ai, Hierarchical iron nickel oxide architectures derived from metal-organic frameworks as efficient electrocatalysts for oxygen evolution reaction, Electrochim. Acta. 208 (2016) 17–24, https://doi.org/10.1016/j.electacta.2016.05.008.
[75] M. Gong, H. Dai, A mini review of NiFe-based materials as highly active oxygen evolution reaction electrocatalysts, Nano Res. 8 (2014) 23–39, https://doi.org/10.1007/s12274-014-0591-z.
[76] F. Maillard, S. Schreier, M. Hanzlik, E.R. Savinova, S. Weinkauf, U. Stimming, Influence of particle agglomeration on the catalytic activity of carbon-supported Pt nanoparticles in CO monolayer oxidation, Phys. Chem. Chem. Phys. 7 (2005) 385–393, https://doi.org/10.1039/B411377B.
[77] R. Torres-Mendieta, D. Ventura-Espinosa, S. Sabater, J. Lancis, G. Mínguez-Vega, J.A. Mata, In situ decoration of graphene sheets with gold nanoparticles synthetized by pulsed laser ablation in liquids, Sci. Rep. 6 (2016) 30478, https://doi.org/10.1038/srep30478.
[78] T.M. Magne, T. de Oliveira Vieira, L.M.R. Alencar, F.F.M. Junior, S. Gemini-Piperni, S.V. Carneiro, L.M.U.D. Fechine, R.M. Freire, K. Golokhvast, P. Metrangolo, P.B.A. Fechine, R. Santos-Oliveira, Graphene and its derivatives: understanding the main chemical and medicinal chemistry roles for biomedical applications, J. Nanostructure Chem. 12 (2022) 693–727, https://doi.org/10.1007/s40097-021-00444-3.
[79] I. Haxhiaj, S. Tigges, D. Firla, X. Zhang, U. Hagemann, T. Kondo, J. Nakamura, G. Marzun, S. Barcikowski, Platinum nanoparticles supported on reduced graphene oxide prepared in situ by a continuous one-step laser process, Appl. Surf. Sci. 469 (2019) 811–820, https://doi.org/10.1016/j.apsusc.2018.10.257.
[80] X. Lang, A. Hirata, T. Fujita, M. Chen, Nanoporous metal/oxide hybrid electrodes for electrochemical supercapacitors, Nat. Nanotechnol. 6 (2011) 232–236, https://doi.org/10.1038/nnano.2011.13.
[81] Z. Lu, Q. Yang, W. Zhu, Z. Chang, J. Liu, X. Sun, D.G. Evans, X. Duan, Hierarchical Co3O4@Ni-Co-O supercapacitor electrodes with ultrahigh specific capacitance per area, Nano Res. 5 (2012) 369–378, https://doi.org/10.1007/s12274-012-0217-2.
[82] D. Friebel, M.W. Louie, M. Bajdich, K.E. Sanwald, Y. Cai, A.M. Wise, M.-J. Cheng, D. Sokaras, T.-C. Weng, R. Alonso-Mori, R.C. Davis, J.R. Bargar, J.K. Nørskov, A. Nilsson, A.T. Bell, Identification of Highly Active Fe Sites in (Ni, Fe)OOH for Electrocatalytic Water Splitting, J. Am. Chem. Soc. 137 (2015) 1305–1313, https://doi.org/10.1021/ja511559d.
[83] P. Acharya, Z.J. Nelson, M. Benamara, R.H. Manso, S.I.P. Bakovic, M. Abolhassani, S. Lee, B. Reinhart, J. Chen, L.F. Greenlee, Chemical Structure of Fe–Ni Nanoparticles for Efficient Oxygen Evolution Reaction Electrocatalysis, ACS Omega. 4 (2019) 17209–17222, https://doi.org/10.1021/acsomega.9b01692.
[84] I.Y. Khairani, M. Spellauge, F. Riahi, H.P. Huber, B. Gökce, C. Doñate-Buendía, Parallel Diffractive Multi-Beam Pulsed-Laser Ablation in Liquids Toward Cost-Effective Gram Per Hour Nanoparticle Productivity, Adv. Photonics Res. 5 (2024) 2300290, https://doi.org/10.1002/adpr.202300290.
[85] P. Li, X. Zhao, X. Duan, Y. Li, Y. Kuang, X. Sun, A multiphase nickel iron sulfide hybrid electrode for highly active oxygen evolution, Sci. China Mater. 63 (2020) 356–363, https://doi.org/10.1007/s40843-019-1215-9.
[86] L.-J. Zhou, X. Huang, H. Chen, P. Jin, G.-D. Li, X. Zou, A high surface area flower-like Ni–Fe layered double hydroxide for electrocatalytic water oxidation reaction, Dalt. Trans. 44 (2015) 11592–11600, https://doi.org/10.1039/C5DT01474C.
[87] D. Wang, Q. Li, C. Han, Q. Lu, Z. Xing, X. Yang, Atomic and electronic modulation of self-supported nickel-vanadium layered double hydroxide to accelerate water splitting kinetics, Nat. Commun. 10 (2019) 3899, https://doi.org/10.1038/s41467-019-11765-x.
[88] W.S. Rasband, ImageJ, U.S. Natl. Institutes Heal, Bethesda, Maryl, 1997 http://imagej.nih.gov/ij/ (accessed November 28, 2023.
[89] Y. Wang, H. Arandiyan, K. Dastafkan, Y. Li, C. Zhao, Common Pitfalls of Reporting Electrocatalysts for Water Splitting, Chem. Res. Chinese Univ. 36 (2020) 360–365, https://doi.org/10.1007/s40242-020-0107-1.
[90] J.S. Mehta, A.C. Faucett, A. Sharma, J.M. Mativetsky, How Reliable Are Raman Spectroscopy Measurements of Graphene Oxide? J. Phys. Chem. c. 121 (2017) 16584–16591, https://doi.org/10.1021/acs.jpcc.7b04517.
[91] S. Claramunt, A. Varea, D. López-Díaz, M.M. Velázquez, A. Cornet, A. Cirera, The importance of interbands on the interpretation of the raman spectrum of graphene oxide, J. Phys. Chem. c. 119 (2015) 10123–10129, https://doi.org/10.1021/acs.jpcc.5b01590.
[92] A. Pinilla-Sánchez, E. Chávez-Angel, S. Murcia-López, N.M. Carretero, S. M. Palardonio, P. Xiao, D. Rueda-García, C.M. Sotomayor Torres, P. Gómez-Romero, J. Martorell, C. Ros, Controlling the electrochemical hydrogen generation and storage in graphene oxide by in-situ Raman spectroscopy, Carbon n. y. 200 (2022) 227–235, https://doi.org/10.1016/j.carbon.2022.08.055.
[93] N. Fairley, V. Fernandez, M. Richard-Plouet, C. Guillot-Deudon, J. Walton, E. Smith, D. Flahaut, M. Greiner, M. Biesinger, S. Tougaard, D. Morgan, J. Baltrusaitis, Systematic and collaborative approach to problem solving using X-ray photoelectron spectroscopy, Appl. Surf. Sci. Adv. 5 (2021) 100112, https://doi.org/10.1016/j.apsadv.2021.100112.
[94] D. Zhang, H. Wada, in: Laser Ablation in Liquids for Nanomaterial Synthesis and Applications BT - Handbook of Laser Micro- and Nano-Engineering, Springer International Publishing, Cham, 2021, pp. 1481–1515, https://doi.org/10.1007/978-3-030-63647-0_30.
[95] G.A. Rance, D.H. Marsh, S.J. Bourne, T.J. Reade, A.N. Khlobystov, van der Waals Interactions between Nanotubes and Nanoparticles for Controlled Assembly of Composite Nanostructures, ACS Nano. 4 (2010) 4920–4928, https://doi.org/10.1021/nn101287u.
[96] C. Qiu, L. Jiang, Y. Gao, L. Sheng, Effects of oxygen-containing functional groups on carbon materials in supercapacitors: A review, Mater. Des. 230 (2023) 111952, https://doi.org/10.1016/j.matdes.2023.111952.
[97] T. Shinagawa, A.T. Garcia-Esparza, K. Takanabe, Insight on Tafel slopes from a microkinetic analysis of aqueous electrocatalysis for energy conversion, Sci. Rep. 5 (2015) 1–21, https://doi.org/10.1038/srep13801.
[98] D.J. Morgan, Comments on the XPS Analysis of Carbon Materials, C. 7 (2021) 51, https://doi.org/10.3390/c7030051.
[99] M.C. Biesinger, B.P. Payne, A.P. Grosvenor, L.W.M. Lau, A.R. Gerson, R.S. C. Smart, Resolving surface chemical states in XPS analysis of first row transition metals, oxides and hydroxides: Cr, Mn, Fe, Co and Ni, Appl. Surf. Sci. 257 (2011) 2717–2730, https://doi.org/10.1016/j.apsusc.2010.10.051.
[100] L. Ciammaruchi, L. Bellucci, G.C. Castillo, G.M.D. Sánchez, Q. Liu, V. Tozzini, J. Martorell, Water splitting for hydrogen chemisorption in graphene oxide dynamically evolving to a graphane character lattice, Carbon n. y. 153 (2019) 234–241, https://doi.org/10.1016/j.carbon.2019.06.087.
[101] F. Delfino, C. Ros, S.M. Palardonio, N.M. Carretero, S. Murcia-López, J. R. Morante, J. Martorell, Z.G. Fthenakis, M.F. Sgroi, V. Tozzini, L. Bellucci, Multi-methodological analysis of hydrogen desorption from graphene, Carbon n. y. 227 (2024) 119211, https://doi.org/10.1016/j.carbon.2024.119211.
[102] T.M.G. Mohiuddin, A. Lombardo, R.R. Nair, A. Bonetti, G. Savini, R. Jalil, N. Bonini, D.M. Basko, C. Galiotis, N. Marzari, K.S. Novoselov, A.K. Geim, A. C. Ferrari, Uniaxial strain in graphene by Raman spectroscopy: G peak splitting, Grüneisen parameters, and sample orientation, Phys. Rev. B - Condens. Matter Mater. Phys. 79 (2009) 1–8, https://doi.org/10.1103/PhysRevB.79.205433.
[103] Z.H. Ni, W. Chen, X.F. Fan, J.L. Kuo, T. Yu, A.T.S. Wee, Z.X. Shen, Raman spectroscopy of epitaxial graphene on a SiC substrate, Phys. Rev. B - Condens. Matter Mater. Phys. 77 (2008) 1–6, https://doi.org/10.1103/PhysRevB.77.115416.
[104] M.W. Iqbal, M.Z. Iqbal, M.F. Khan, X. Jin, C. Hwang, J. Eom, Modification of the structural and electrical properties of graphene layers by Pt adsorbates, Sci. Technol. Adv. Mater. 15 (2014) 055002, https://doi.org/10.1088/1468-6996/15/5/055002.
[105] R. Yang, Q.S. Huang, X.L. Chen, G.Y. Zhang, H.J. Gao, Substrate doping effects on Raman spectrum of epitaxial graphene on SiC, J. Appl. Phys. 107 (2010) 034305, https://doi.org/10.1063/1.3283922.
[106] Z.H. Ni, H.M. Wang, Y. Ma, J. Kasim, Y.H. Wu, Z.X. Shen, Tunable stress and controlled thickness modification in graphene by annealing, ACS Nano. 2 (2008) 1033–1039, https://doi.org/10.1021/nn800031m.
[107] X. Long, J. Li, S. Xiao, K. Yan, Z. Wang, H. Chen, S. Yang, A Strongly Coupled Graphene and FeNi Double Hydroxide Hybrid as an Excellent Electrocatalyst for the Oxygen Evolution Reaction, Angew. Chemie Int. Ed. 53 (2014) 7584–7588, https://doi.org/10.1002/anie.201402822.
[108] Y. Wang, X. Wang, Y. Min, Q. Li, Q. Xu, Investigation of Oxygen Evolution Performance of Highly Efficient Water Electrolysis Catalyst: NiFe LDH/BPene, Processes. 11 (2023) 2179, https://doi.org/10.3390/pr11072179.
[109] R. Sadek, M.S. Sharawi, C. Dubois, H. Tantawy, J. Chaouki, Superior quality chemically reduced graphene oxide for high performance EMI shielding materials, RSC Adv. 12 (2022) 22608–22622, https://doi.org/10.1039/D2RA02678C.
[110] C. Chang, L. Zhang, C.W. Hsu, X.F. Chuah, S.Y. Lu, Mixed NiO/NiCo2O4 Nanocrystals Grown from the Skeleton of a 3D Porous Nickel Network as Efficient Electrocatalysts for Oxygen Evolution Reactions, ACS Appl. Mater. Interfaces. 10 (2018) 417–426, https://doi.org/10.1021/acsami.7b13127.

[111] C.J. Pan, M.C. Tsai, W.N. Su, J. Rick, N.G. Akalework, A.K. Agegnehu, S.Y. Cheng, B.J. Hwang, Tuning/exploiting Strong Metal-Support Interaction (SMSI) in Heterogeneous Catalysis, J. Taiwan Inst. Chem. Eng. 74 (2017) 154–186, https://doi.org/10.1016/j.jtice.2017.02.012.
[112] fuelcellstore.com, Ruthenium Oxide Nanoparticles (FC Catalyst), (2002). https://www.fuelcellstore.com/ruthenium-oxide-catalyst-powder (accessed August 19, 2024).
[113] Umicore, Ruthenium Bulk Price, Umicore. (n.d.). https://pmm.umicore.com/en/prices/ruthenium/ (accessed August 19, 2024).
[114] SMM Metal Market, Ruthenium 99.95% Bulk Price, Metal.Com. (2024). https://www.metal.com/Other-Precious-Metals/201102250083 (accessed August 20, 2024).
[115] SMM Metal Market, Nickel 99.90% Bulk Price, Metal.Com. (2024). https://www.metal.com/Nickel/201102250239 (accessed August 20, 2024).
[116] SMM Metal Market, Steel Bulk Price, Metal, Com, 2024 https://www.metal.com/Finished-Steel/202112200002 (accessed August 20, 2024).
[117] B. Gökce, V. Amendola, S. Barcikowski, Opportunities and Challenges for Laser Synthesis of Colloids, ChemPhysChem 18 (2017) 983, https://doi.org/10.1002/cphc.201700310.

7.4 Perspective Paper

Khairani, I. Y., Mínguez-Vega, G., Doñate-Buendía, C., & Gökce, B. (2023). Green nanoparticle synthesis at scale: a perspective on overcoming the limits of pulsed laser ablation in liquids for high-throughput production. Physical Chemistry Chemical Physics, 25(29), 19380–19408. https://doi.org/10.1039/D3CP01214J

CRediT Authorship Contribution of I.Y.K.: Conceptualization, literature research, visualization, writing – original draft preparation, writing – review and editing.

PCCP

PERSPECTIVE

View Article Online
View Journal

Cite this: DOI: 10.1039/d3cp01214j

Green nanoparticle synthesis at scale: a perspective on overcoming the limits of pulsed laser ablation in liquids for high-throughput production

Inna Y. Khairani,[a] Gladys Mínguez-Vega,[b] Carlos Doñate-Buendía[a] and Bilal Gökce *[a]

Nanoparticles have become increasingly important for a variety of applications, including medical diagnosis and treatment, energy harvesting and storage, catalysis, and additive manufacturing. The development of nanoparticles with different compositions, sizes, and surface properties is essential to optimize their performance for specific applications. Pulsed laser ablation in liquid is a green chemistry approach that allows for the production of ligand-free nanoparticles with diverse shapes and phases. Despite these numerous advantages, the current production rate of this method remains limited, with typical rates in the milligram per hour range. To unlock the full potential of this technique for various applications, researchers have dedicated efforts to scaling up production rates to the gram-per-hour range. Achieving this goal necessitates a thorough understanding of the factors that limit pulsed laser ablation in liquid (PLAL) productivity, including laser, target, liquid, chamber, and scanner parameters. This perspective article explores these factors and provides a roadmap for increasing PLAL productivity that can be adapted to specific applications. By carefully controlling these parameters and developing new strategies for scaling up production, researchers can unlock the full potential of pulsed laser ablation in liquids.

Received 17th March 2023,
Accepted 19th May 2023

DOI: 10.1039/d3cp01214j

rsc.li/pccp

[a] Chair of Materials Science and Additive Manufacturing, School of Mechanical Engineering and Safety Engineering, University of Wuppertal, 42119 Wuppertal, Germany. E-mail: goekce@uni-wuppertal.de
[b] GROC-UJI, Institut de Noves Tecnologies de la Imatge (INIT), Universitat Jaume I, 12071, Castellón, Spain

Inna Y. Khairani

Inna Yusnila Khairani, MSc obtained her BSc summa cum laude from the Chemistry Department, Universitas Gadjah Mada, Indonesia. She was later awarded the Korean Government Scholarship Program (KGSP) at the Department of Materials Science and Engineering, Seoul National University (SNU) in South Korea, and graduated summa cum laude. During her master's degree, she won an award in a writing competition held by the SNU Foundation. She is currently a PhD candidate under the supervision of Prof. Bilal Gökce, and her task is to scale up the productivity of nickel–iron alloy nanoparticles produced by the pulsed laser ablation in liquid (PLAL).

Gladys Mínguez-Vega

Professor Gladys Mínguez Vega obtained her BSc and PhD degrees in Physics from the University of Valencia in 1997 and 2002, respectively. In 2002, she joined the Universitat Jaume I of Castellón (Spain). She has developed several research stays in the Centro de Investigaciones en Óptica (Mexico, 1998), the Applied Optics Institute (Poland, 2002), the Fernuniversität in Hagen (Germany, 2003), and the Purdue University (USA, 2004 and 2009). Her research interest includes ultrafast optics and the synthesis of nanomaterials with laser. Since 2017, she has co-led the Photonics research group "GROC·UJI," and in 2022, she became a Full Professor.

1. Introduction

Nanoparticles have been utilized by humans for centuries, with early examples dating back to the Roman Empire. The Lycurgus cup, a piece of Roman glassware from the 4th century AD, contains gold nanoparticles that provide a striking optical dichroism effect. The cup appears green when lit from the front but red when illuminated from the back, due to the interaction of light with the gold nanoparticles. This ancient artifact provides a remarkable testament to the unique properties of nanoparticles and their potential applications.[1,2] Since then, the field of nanotechnology has undergone tremendous growth. Nanoparticles, with sizes typically ranging from 1 to 100 nanometers, exhibit unique electronic, optical, and mechanical properties that differ from their bulk counterparts. Applications of NPs stretch from drug delivery and contrast agents for magnetic resonance in the biomedical field,[3–6] catalysts for the development of renewable energy systems and environment remediation,[7–10] for the photo- and electrocatalytic application,[11] such as the water-splitting process,[12] fabrication of solar nanofluids,[13] properties enhancement and smart materials printing by additive manufacturing,[14,15] to the development of food packaging with antibacterial effects in the food industry.[16–18] The broad application spectrum that nanotechnology has reached during the last decades has been possible due to the unique physicochemical properties of the NP compared to bulk materials. The increased surface area-to-volume ratio, which exposes more active sites, is key to enhancing catalysts' response. The possibility of tuning the optical, thermal, and conductivity properties depending on the particle size, surface functionalization, and doping has given rise to the sensors' development,[19–21] advanced materials,[22] and optoelectronic devices.[20,23,24]

The dependence of the NPs' properties on their physicochemical parameters represents a key advantage in many applications. However, in the previous century, the synthesis of NPs with controlled characteristics represented a major challenge, limiting application development. Even nowadays, with the appearance of novel materials and the continuous innovation of the current nanomaterials' functionalities, synthesis techniques represent a central pillar of nanotechnology development, requiring green methods that offer material versatility, size control, NP purity, controlled surface doping, and in many cases, high productivity to address the industrial demands.[25]

Nanoparticle synthesis techniques can be divided into two groups, top-down and bottom-up approaches. The top-down methods are based on the breaking of bulk material to achieve nanometer-sized particles, including methods such as ball-milling, sputtering, and thermal evaporation. Meanwhile, the bottom-up approaches involve building NPs through the joint of their atomic constituents, usually performed by chemical synthesis methods, such as co-precipitation, sol–gel, hydrothermal, and chemical vapor deposition methods. Laser ablation is typically considered a top-down approach to the synthesis of nanoparticles since it involves the use of laser energy to ablate bulk materials and create nanoparticles. Nevertheless, this method can also be considered a bottom-up approach due to the subsequent NPs formation through nucleation and growth processes of the material constituents generated by the high-intensity pulsed laser interaction.

Laser ablation can be performed within a vacuum, gas, or liquid medium.[11] The production of nanomaterials by laser ablation in a vacuum is mostly known as pulsed laser deposition (PLD), where the ablated nanomaterials are deposited onto a substrate after ablation.[26] This technique offers the versatility to produce thin films with controlled elemental composition by combining the ablation of different targets.[26] Besides, the film thickness can be controlled within the nano- to micrometer range.[27] Laser ablation can also be performed in a gas environment, either with a certain gas flow or in the air. In this case, the method is usually aimed to modify the target material to

Carlos Doñate-Buendía

Dr Carlos Doñate Buendía obtained his PhD in 2019 distinguished with the international mention and summa cum laude from the University Jaume I after being awarded a FPI-UJI contract to develop nanomaterials by high throughput pulsed-laser based systems and their application in biomedicine and material processing. In 2020, he became postdoctoral researcher at the University of Duisburg-Essen working in the development of nanofunctionalized materials for additive manufacturing. In 2021, he joined the Chair of Materials Science and Additive Manufacturing at University of Wuppertal, where he is currently the group leader of the Particles and Additive Manufacturing of Polymers group.

Bilal Gökce

Professor Bilal Gökce completed his physics diploma at RWTH Aachen University in 2008 and his PhD in physics at North Carolina State University in 2012. After post-doctoral work on non-linear optics and a year at T-systems international, he joined the University of Duisburg-Essen in 2014 as a group leader for Laser Material Processing & Nanoparticle Generation. He achieved habilitation in 2018 and won the Fojtik-Henglein Prize. In 2020, he became a full professor at the University of Wuppertal, creating the Chair of Materials Science and Additive Manufacturing, after receiving the DFG Heisenberg Programme fellowship and being awarded with the Berthold-Leibinger-Innovation-Prize.

achieve the desired structure and properties, since the NPs will be re-deposited onto the surface of the target at a very fast rate.[28]

The production of nanomaterials using a laser in liquid is usually named laser ablation in liquid (LAL). It is based on the irradiation with a high-intensity laser beam ($>10^9$ W cm^{-2}) of a bulk target immersed in a liquid.[29] In LAL, two situations are generally differentiated depending on the laser source employed. When a continuous laser is employed, the technique is known as continuous wave laser ablation in liquid (CLAL), while the methodology is known as pulsed laser ablation in liquids (PLAL) if the source is a pulsed laser. Generally, the research field has evolved towards the standard employment of pulsed lasers, as the constant emission of light from the continuous wave laser heats the target and induces the boiling of the surrounding liquid. The boiling liquid scatters the incoming laser beam to the target, making CLAL unfeasible for continuous or large-scale NP production.

PLAL was first introduced in 1987 by Patil *et al.*[30] through the ablation of iron foils in water using a nanosecond laser and in 1993 by Fojtik and Henglein[31,32] for their work on laser synthesized-colloidal nanoparticles dispersed in a liquid. The operational steps of PLAL are relatively straightforward; the laser is directly shot onto a target fixed inside a liquid medium (Fig. 1). The ablated material is collected in the surrounding liquid media, avoiding user inhalation and safety risks, and directly producing colloidal nanoparticles of the desired material in the selected solvent. This technique gained popularity due to the possibility of producing bare-surface – ligand-free NPs, which offer improved catalytic activity, efficient conjugation, and higher affinity to biomolecules.[33–35] Furthermore, it is also possible to produce complex structures through PLAL, such as hollow NPs[36,37] and core–shell NPs,[38,39] which might require multiple steps in other synthesis methods.[40,41] Moreover, PLAL complies with green chemistry principles.[42] Most synthesis techniques require surfactants, certain solvents, gas atmospheres, and pre-and post-processing, such as stirring, heating, centrifugation, filtration, and annealing, to produce NPs.[43–45] Meanwhile, PLAL is usually performed in an ambient atmosphere, pressure, and temperature conditions, without the use of surfactants and hazardous substances, and with no or limited side products or waste generation.[46] Nevertheless, one critical drawback of this method is the low nanoparticle production rate. With the increase in the global population and its demands, the need for a more efficient way to synthesize PLAL nanomaterials will grow. Production rates achievable for oxide nanoparticles through the standard PLAL processes using an oxide target, typically on the order of milligrams per hour,[47–49] may be adequate for certain nanoparticle applications in bioimaging, biomedicine, and sensing, where only small amounts of nanoparticles are needed. However, increasing productivity to the grams per hour scale for the variety of nanomaterials produced by PLAL will reduce the synthesis cost, and possibly lower the market price and increase the interest of the NPs produced by this method.[50] As an example of PLAL productivity compared to high-yield chemical methods, the thermolysis of a metal oleate precursor has achieved a yield value of 40 grams of iron oxide NPs per batch.[51] Meanwhile, PLAL produces NPs in a scale of tens to hundreds of milligrams, which has been extended achieving g h^{-1} productivities for other metallic[52] and ceramic NPs,[53] and with a record of 8 grams per hour for Pt NPs produced by Waag *et al.*[54] in 2021.

The aim of this perspective article is to critically review the current status of PLAL productivity and provide strategies to continue upscaling the process. To understand the factors that limit PLAL productivity and provide a clear roadmap to overcome them, first, the PLAL technique principles will be described. Besides, to avoid ambiguities, the production rate

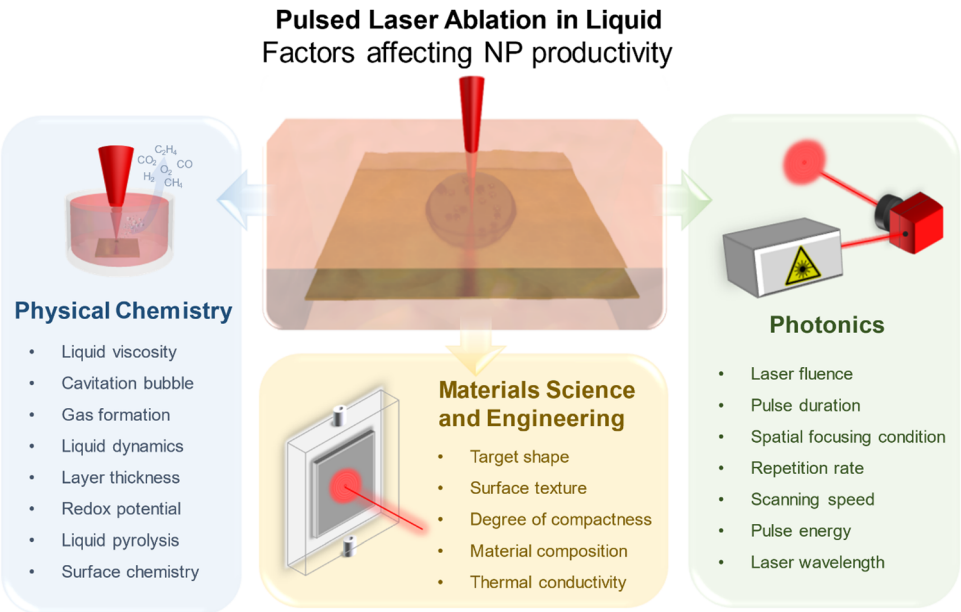

Fig. 1 A schematic illustration of PLAL depicting the laser-irradiated target immersed in a liquid and the factors affecting nanoparticle productivity categorized by its respective scientific field.

or productivity will be defined. Afterward, the perspective aim will be to enlighten the reader by providing responses to the following fundamental questions defining PLAL productivity. How does the employed laser source influence the productivity in LAL? What physicochemical factors of the target and the solvent are influencing PLAL productivity? How do those factors correlate? What are the current and upcoming strategies to increase PLAL productivity to the demanded g h^{-1} scale?

2. The fundamentals of PLAL

The main tool of PLAL is a pulsed laser, that sends its laser energy in packages (pulses) with a certain pulse duration or pulse width (τ_{pulse}). The average power and peak power of a pulsed laser can be calculated with eqn (1) and (2), respectively.

$$\bar{P}(\mathrm{W}) = E_p(\mathrm{J}) x f(\mathrm{Hz}) \quad (1)$$

$$P_{peak}(\mathrm{W}) = \frac{\bar{P}(\mathrm{W})}{f(\mathrm{Hz}) \times \tau_{pulse}(\mathrm{s})} = \frac{E_p(\mathrm{J})}{\tau_{pulse}(\mathrm{s})} \quad (2)$$

where $\bar{P}$ is the average power of the laser, P_{peak} is the peak power, f is the repetition rate or number of pulses in one second, τ_{pulse} is the pulse width or pulse duration, and E_p is the pulse energy. The peak power is inversely proportional to the pulse width, hence, the shorter the laser pulse duration the larger the peak power. In comparison to continuous wave lasers, pulsed lasers with the same average power can reach a significantly higher peak power, making laser ablation more efficient by reducing material heating.

The process of material removal and nanoparticle formation in PLAL involves a series of complex physical and chemical interactions between the material, the laser, and the liquid.[55–59] The interaction between the laser beam and the target induces a fast phase transition between the target-liquid boundary, leading to the formation of high pressure, temperature, and density plasma containing ionized and atomized species.[33,60,61] As the plasma decays at a fast-cooling rate, the surrounding liquid absorbs the energy and it is transformed into a layer of supercritical vapor containing the evaporated and dissociated species from the liquid, namely the cavitation bubble.[62] The cavitation bubble is presumed to be the reservoir of solid crystallization, *i.e.*, the formation of the atomic cluster, and primary and secondary particles.[63–65] The cavitation bubble might undergo expansion and shrinkage[65] before its final collapse, which releases the NPs to the surrounding liquid.[58]

Depending on the operating laser pulse duration τ_{pulse}, the ablation mechanism differs as shown in Fig. 2.[61] When a nanosecond laser is employed, the bulk target absorbs the energy and transfers it to the lattice, inducing energy release by heating the target, which causes melting, vaporization, bond-breaking, or defects formation that leads to material removal. All these processes take place while the laser is still irradiating the target. Meanwhile, when ultrashort pulses are employed (in pico- or femtosecond regime), the heating, melting, and material removal occur at a different time frame due to the electron–phonon coupling time being longer than the laser pulse duration. These differences due to the pulse duration

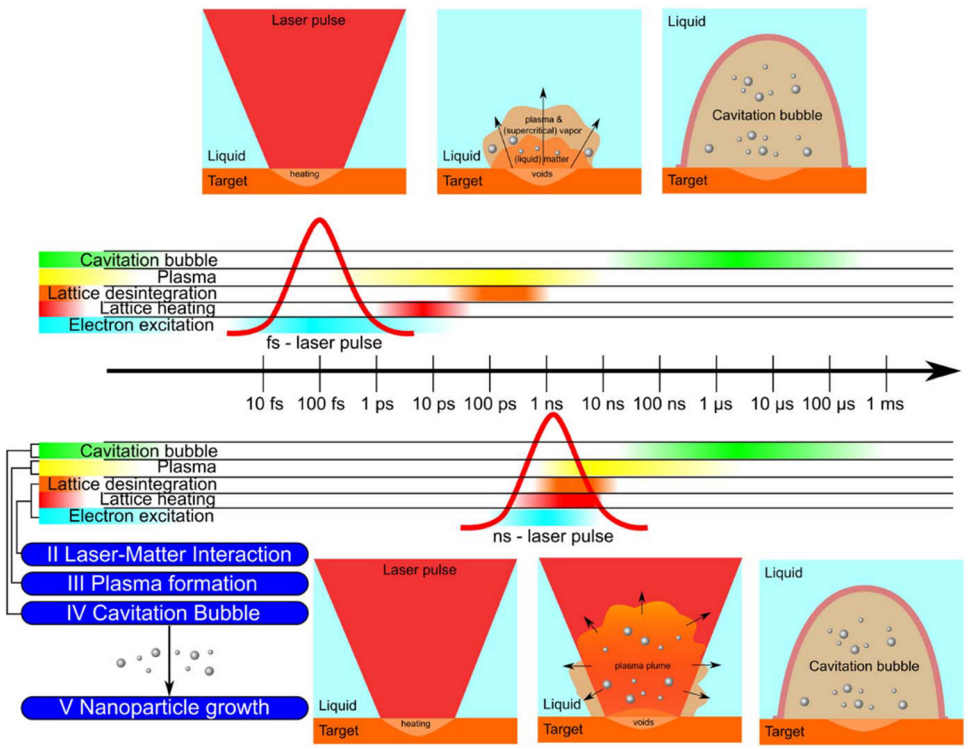

Fig. 2 Schematic illustration of the laser ablation occurring after pulse irradiation of the bulk target immersed in a liquid for femtosecond (top) and nanosecond (bottom) PLAL. Reproduced from ref. 61 with permission from IOP Publishing Ltd, copyright 2019.

influence the lifetime and cooling rate of the plasma, which leads to a unique plasma–liquid interaction, and thus, nanoparticle phase, size, and composition.[61]

A deeper understanding of the processes occurring at the time scale that goes from the pulse interaction with the material until NP ejection would help to select the optimum experimental parameters for every material and liquid.[66–68] This fact could lead to the desired nanoparticle's size, shape, composition, and surface coating, for example, the formation of CoFe layered double hydroxide from the sequential ablation of Co and Fe target in low concentration of $(NH_4)_2CO_3$,[69] which unlocks potential applications of laser-generated NPs in catalysis,[70] medicine,[71] additive manufacturing,[72] and energy generation and storage.[73] Nonetheless, productivity has been always one of the main limitations of the application of laser-synthesized NPs. Their outstanding properties have been mainly directed to applications demanding reduced NPs quantities due to the low yield. Consequently, the search for novel configurations and laser sources that permit an improved efficiency of the process, as well as productivity increase, has been one of the main research lines in the past years.[53,54,74–76] Nowadays, it still represents a major goal of the field.

3. Definition and measurement of nanoparticle productivity

The amount of NPs produced within a certain period of time is defined as the production rate or productivity. Its value commonly lies within the milligrams per hour range, meanwhile, it is important to achieve NPs productivity in gram per hour scale to popularize this technology, reduce cost and move toward industrial applications.

There are several strategies that can be employed to measure the ablated mass: (1) gravimetric, (2) optical extinction, and (3) analytical chemistry approaches.[77] In the gravimetric approach, the mass difference of a target before and after PLAL is measured to be the total mass of NPs produced. A high precision balance is usually employed, and the target should be dried from the liquid beforehand to reduce artifacts in the measurement due to the extra weight from the remaining liquid. The advantage of this approach is the easy and undemanding labor, but is not suitable for low productivities below the balance detection range, and the target mass difference can differ from the amount of colloidal nanoparticles produced if larger fractions of the target are ablated. This is especially relevant for powder-pressed targets where the compactness and porosity facilitate the detachment of larger particles by the laser action. The second approach, optical extinction, employs a spectrophotometer at the wavelength range between 200–1000 nm to measure the intensity difference of light passed through the liquid used as a reference compared to the colloidal NPs. Based on the Lamber-Beer law, the absorbance of a dissolved substance is correlated with the colloid concentration.[78] Hence, the absorbance of the dispersed NPs in the liquid can be linearly correlated to its concentration after a calibration of the spectrophotometer for the given material and solvent. It should be noted, however, that the concentration determination could only be applied if extinction (which consists of absorbance and scattering) is dominated by absorbance and the scattering effect is insignificant. If the scattering effect is significant, for example, in the case of big NPs sizes, the absorbance and scattering elements should be separated before one can determine the concentration through the extinction method. In addition, size-dependent effects due to plasmonic absorption cause a wavelength shift depending on the particle size which may affect the calibration.[79] Therefore, it is suggested to build two types of calibration curves: (1) at the peak wavelength of the surface plasmon resonance as a function of nanoparticle size[80] to estimate the size and simulate by Mie theory if the scattering should be considered or can be avoided, and (2) at a wavelength outside of the plasmon of resonance where we have a linear dependence of the absorbance with the concentration. Once the calibration curves are obtained, this approach is more efficient than the gravimetric method since the target does not need to be removed and placed for each measurement. The drawback of this approach is the unreliability for colloids at extreme concentrations (too high or too low) and materials which easily agglomerate and sediment, such as magnetic NPs.[81–83] In the case of highly concentrated colloids where the high absorption obscures the characterization, dilution of the colloid can be employed to reduce agglomeration effects. Furthermore dilution increases colloidal stability while bringing the absorption value to the linear regime of the concentration calibration curve without reducing the resolution of the concentration determination. Meanwhile, the approach to use analytical chemistry techniques usually requires a dilution of the sample, for instance, the inductively coupled plasma mass spectrometry (ICP-MS), as the system is well suited for very low concentrations. These techniques can be used to provide the calibration curve required for optical extinction spectroscopy. The drawback of this approach comes from the high price of the equipment and the possible inaccuracies in the dilution process.

To obtain a reliable value of the gram per hour productivity in an experimental procedure, long irradiation times of 1 hour could be required to showcase the robustness and reliability. Nevertheless, the productivity is commonly obtained by extrapolating the ablated mass in minutes to one hour. Please note that in this situation some factors that may affect the productivity, *i.e.*, nanoparticle shielding, permanent bubbles, and successive irradiation of the same area of the target, maybe neglected in the extrapolation. For this reason, the minimum ablation duration of 5 minutes is required to obtain a reliable gram per-hour value while also accounting for the effect of nanoparticle shielding,[76] target depth variation, persistent microbubbles,[84] and scanning and repetition rate effects.[54] It has been shown that there is no major discrepancy in the productivity between 5, 10, 15, and 30 minute ablation time when using a flow chamber.[53] Please note that depending on the ablation chamber, an extrapolation from 5 minutes of ablation to 1 hour ablation might not be accurate. For example, colloidal concentration saturation (indicated by low transparency) will be reached faster if the ablation is done in a batch chamber with a

smaller liquid volume, leading to an ineffective ablation and lower productivity overtime, thus, inaccurate results when extrapolating from shorter ablation time to long term ablation. Therefore, it is recommended to use a flow chamber with an optimum flow rate and a constant feed of fresh liquid to avoid colloidal concentration variation over time.

Other than the aforementioned mass per time unit (mass productivity), we can also define productivity by the laser parameters or material properties, such as laser power and material density. Dividing the value of mass productivity by the laser power results in "power-specific productivity" with a unit of mg h^{-1} W^{-1}, which defines the efficiency independent of the laser power used to produce the NPs. Since the laser sources employed in PLAL differ from one lab to another, it represents a comparable value to facilitate the repeatability of the process, however, other key laser parameters such as the pulse duration, repetition rate, and scanning speed have to be considered when transferring results to a new setup.[85] The density-dependent productivity is obtained by dividing the mass productivity by the material density. Therefore, it is also called "volume productivity" (usually provided as mm^3 h^{-1}). This approach is useful to compare the productivity of different materials with different densities since high-density materials usually show higher mass productivity compared to low-density materials.[86] Another way to define productivity is the "molar productivity", obtained by dividing the ablated mass by the molar mass of the material, which gives out the final units of mmol h^{-1}. Since the unit is in mole (defining a number of 6.022×10^{23} ions, atoms, molecules, *etc.*) instead of molar (mole per liter), the terminology of "mole productivity" would be more appropriate. This terminology describes the number of atoms ablated from a target within a period of time, which might be useful in the field of reactive laser ablation in liquid to determine the stoichiometric reactant amount and study its influence on the generated phase of the NPs or the gas composition.

Despite many terminologies used to evaluate and define the productivity of a PLAL system, there are too many factors influencing this complex system. It is therefore implausible to define only one measurement technique and one unit as a standard in PLAL. The chosen measurement technique and the unit will then depend on the feasibility of the experimental procedure in the laboratory and the focus of the research itself, whether it is to compare the productivity of different materials or to compare a common material irradiated with different laser systems. For the goal to scale-up PLAL and reach an industry-relevant production, the simplest way to define the productivity is the gravimetric approach combined with well-calibrated optical spectrophotometry characterization of the colloids to confirm the absence of large fractions of the target. This way, it is possible to achieve good repeatability and accuracy of the method, especially for large production of NPs.

Once the PLAL principles have been introduced, and the productivity has been defined, the influence of the laser and material parameters on productivity and strategies to increase productivity will be discussed. In order to achieve the gram per hour productivity, approaches such as developing new types of chambers,[74,87–89] bypassing the cavitation bubble,[52,90] and reducing the liquid layer thickness,[88,91] have been sought. In the following chapter, we will discuss the parameters related to the NPs productivity starting from the laser fundamentals, *i.e.*, laser fluence, pulse width, and laser wavelength, to the practical point of view including the chamber design and target geometry.

4. Strategies to increase nanoparticle production

The benefits from employing laser-synthesized nanomaterials for catalysis,[10–12,69,70] biocidal elements,[92,93] bioimaging,[94] and modification of material properties such as the absorption for additive manufacturing[95] has already been proven. Nevertheless, these processes demand not only large amounts of nanoparticles but also cost-effective production processes. As lasers are easily integrated into the production chain and their industrial use is widely extended, the incorporation of PLAL is straightforward.[96] The development of higher production and cost-effective processes to boost the employment of laser-generated nanomaterials at a large scale represents one major challenge that researchers working in this field are facing nowadays.[97]

A first thought on the possibilities for increasing productivity in PLAL immediately leads to the study of laser-matter interaction. The first approach that can come to mind is to optimize laser parameters by increasing laser power and repetition rate, and find the optimum irradiation wavelength for the employed material. Nowadays, there exist commercial laser systems operating at wavelengths from the UV to the IR able to achieve mean power values of hundreds of Watts that allow obtaining huge fluence values at the focal spot even operating at repetition rates in the order of the MHz. However, above a fluence threshold, limitations that depend on the scanning velocity,[52] repetition rate,[53] pulse width,[68] focusing conditions,[98] interaction with the liquid media,[99] and target geometry appear.[100] Consequently, several parameters are involved, and their optimization turns into a difficult task that even varies depending on the material, liquid, and pulse duration.

4.1. Finding the optimal laser fluence and pulse duration

A fundamental parameter for nanoparticle production is laser fluence. Its influence can be explained starting from the well-established model for material processing in air.[101,102] Depending on the pulse duration, the ablation mechanism differs. In the case where pulse duration is shorter than the electron cooling time, typically pulses shorter than 1 ps, the strong evaporation regime is produced and material removal is associated with the direct solid–vapor or solid–plasma transition, avoiding melting of the material. If the pulse duration exceeds the electron cooling time, the released heat causes first the melting of the material surface and its posterior vaporization or solidification. Following the results obtained by this model,[101–103] the ablation depth (L) can be described in terms of the fluence:

$$L = \delta \cdot \ln\left(\frac{\phi_{inc}}{\phi_{th}}\right) \quad (3)$$

$$\phi_{inc} = \frac{2E_p}{\pi w_0^2} \quad (4)$$

Here, δ is the effective penetration depth, ϕ_{inc} is the incident fluence on the target (which can be calculated by eqn (4)), ϕ_{th} is the threshold fluence, E_p is the pulse energy, and w_0 is the beam half-waist (spot radius). This model of laser ablation in air can be used to explain the relationship between ablated volume per pulse and fluence by assuming a Gaussian-shaped laser intensity profile. Integrating eqn (3), then substituting beam waist w_0 with incidence fluence ϕ_{inc} based on eqn (4), to get eqn (5). The derivation of this equation can be found in the ref. 104 and 105. Please note that this equation cannot be directly implemented for PLAL, as the presence of the liquid causes non-linear interactions, absorption, as well as scattering, and shielding due to the cavitation bubble and generated NPs. Nevertheless, this equation will help to understand the relationship between ablated volume and incident fluence, which is an important parameter in PLAL.

$$V = \frac{E_p}{2\phi_{inc}} \cdot \delta \cdot \ln\left(\frac{\phi_{inc}}{\phi_{th}}\right)^2 \quad (5)$$

From eqn (5), the ablated volume per pulse exhibits a logarithmic relationship with the incident fluence; the higher the fluence, the larger the ablated volume per pulse. The incident fluence can be increased by focusing the laser beam, increasing the laser power, and reducing the repetition rate (to increase the pulse energy). The fundamental parameter defining the ablation process regime is the threshold fluence (Fig. 3). When the incident fluence is below the ablation threshold, the NP yield is negligible. When the incidence fluence reaches the ablation threshold, the ejection of matter increases significantly by more than one order of magnitude.[106] After overcoming the ablation threshold, increasing the incident fluence has a lower effect on the ablation yield, and the ablation volume is determined by the effective penetration depth.[105]

Above the ablation threshold, the effective penetration depth is a key parameter to increasing the ablation volume. The penetration depth of a material is influenced by the pulse width and the materials' properties, such as reflectivity, absorbed wavelength, and surface structure. An increasing pulse width results in a decrease in the penetration depth.[107,108] The penetration depth can be classified into optical penetration depth and thermal penetration depth. The optical penetration depth dominates in the low fluence, ultrashort pulsed lasers (<1 ps) regime because the pulse duration is shorter than the electron cooling time, avoiding energy dissipation through heat transfer to the target materials. Reduction of target heating results in a more efficient ablation. Meanwhile, the thermal penetration depth is the dominating factor for longer pulses (≥ 20 ps). When the pulse duration is longer than the electron–phonon relaxation time, usually a few picoseconds for metals,[55] the energy received by the material will be dissipated to the atom lattice of the material as heat and subsequent melting, leading to a lower process yield.

In addition to the penetration depth, the ablation threshold is also affected by the pulse width. A simulation for a 150 ps laser *versus* a 15 ps laser (Fig. 3),[106] found that the ablation threshold is $\sim$20% higher for the longer pulse width (35 J m^{-2} at 150 ps) than the shorter pulse width (29 J m^{-2} at 15 ps). It is also reported that the ablation yield of the 15 ps laser pulse is constantly higher at all fluences above the ablation threshold compared to the 150 ps laser. Meanwhile, if the ablation is performed at a fluence lower than the ablation threshold, the pulse duration does not change the yield of the ejected species.[106] Experimental results confirm the ablation threshold variation with the pulse width (100–4500 fs) for copper, aluminum, and steel.[109]

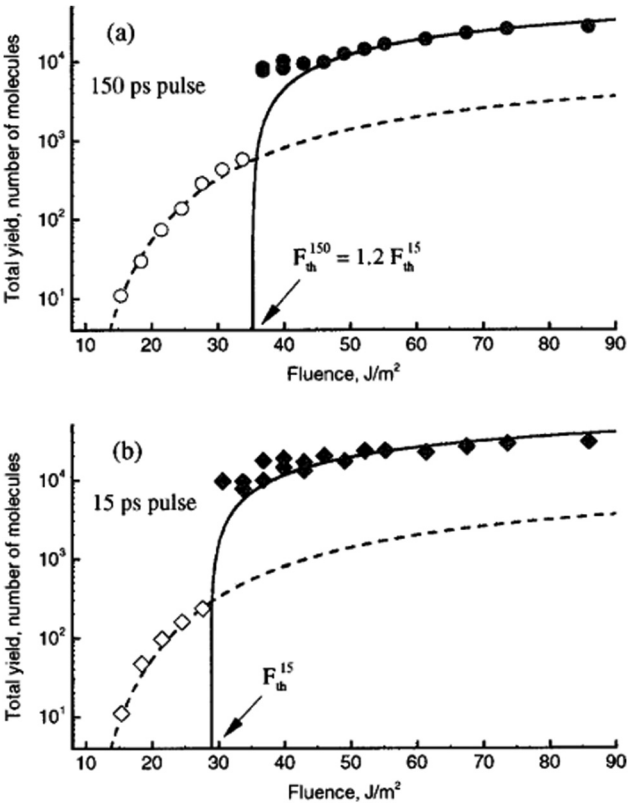

Fig. 3 Simulation of laser ablation of organic solids at different fluences using two different pulse widths. Hollow data points represent the ablation regime below the ablation threshold and the filled data points denote the ablation at or above the ablation threshold. The graphs show that the ablation using a shorter pulse width resulted in a lower ablation threshold fluence. Reproduced from ref. 106 with the permission from AIP Publishing, copyright 2000.

Based on the above discussion, we might consider using ultrashort pulse lasers (femtosecond lasers) over picosecond and nanosecond lasers for a higher production rate. Nevertheless, the influence of pulse width on NP productivity by PLAL is not only the ablation threshold reduction as in air, but also peak power and intensity-dependent interaction of the pulses with the liquid.[110–113] Picosecond lasers are found to provide a suitable subcritical peak pulse power for the ablation process in the liquid medium, thus, generating the highest NPs yield per pulse and per unit energy.[112] The ultrashort femtosecond lasers, on the other hand, trigger non-linear optical absorption, self-focusing, and filamentation effects in the liquid medium as it reaches supercritical peak pulse power, which affects the beam spatial profile and generates energy losses, decreasing the overall

productivity.[112,114] The same trend is also observed for longer pulse duration in the nanosecond regime, in which plasma screening is attributed to be the main cause of productivity reduction, besides the energy loss from thermal processes such as localized heating and melting.[112] It has been suggested that the use of picosecond lasers is advantageous compared to femtosecond lasers if the generated thermal energy can be redistributed, *i.e.*, by using a liquid flow ablation chamber.[114]

Regarding the efficiency of ns and ps PLAL, a study by Kohsakowski *et al.* (2018)[115] compared the mass-, power-, and investment-specific productivities of three different laser systems for the ablation of gold, platinum, silver, and nickel in water. In terms of absolute productivity depicted as mass per unit time, (Fig. 4a), the picosecond laser system supported by the 500 m s^{-1} scanning speed polygon scanner[52] achieved the highest value compared to the nanosecond laser system. Nevertheless, as the use of a polygon scanner reduced the laser power reaching the target by half, thus the power-specific productivity is also reduced by half, making clear that the scanning technology is one of the main limits to overcome the barrier of PLAL productivity. For gold and silver, the power-specific productivity is lower for the picosecond laser compared to the 10 ns-laser, while it is almost similar for platinum and nickel (Fig. 4b). In addition, the investment-specific productivity, which defines the mass of generated NPs divided by time and investment cost (Fig. 4c), showed that the 10 ns-laser performed better than the 3 ps-laser for gold and silver NP production by 11% and 15% in every 1000 € investment, respectively. The absolute power and investment-specific productivities confirm that longer pulses, 40 ns laser source, lead to lower productivity due to thermal interactions and plasma shielding. Although the investment-specific productivity depends on the target material, from the economic point of view, the consideration of laser power and investment cost is crucial as even a small difference can turn into a significant profit in the long run. In addition, the lower initial investment cost of the 10 ns-laser at around 100 000 €, compared to the approx. 500 000 € for the 3 ps-laser, enables small-scale industries to begin investing in this green method to produce NPs. Furthermore, both ns and ps lasers can be complementary in terms of producing different material phases, core–shell structures, or composites, making productivity upscaling relevant in both cases.

The fluence defines the ablation regime, and the pulse duration has been proved to play a key role by influencing the threshold fluence of the material and the intensity that determines the interactions with the liquid. However, the pulse duration is not the only important factor to define the intensity and fluence of the laser beam interacting with the liquid and the target. The spatial focusing conditions define the incident fluence and laser intensity during propagation, influencing PLAL productivity. Placing the focal spot in front of the target, *i.e.*, in the liquid, leads to the laser mainly interacting with the liquid in front of the target, inducing liquid breakdown and scattering of the incoming laser beam. Depending on the laser wavelength, focusing the laser beam in the liquid may also induce fragmentation of the generated NPs that shield the laser beam energy from reaching the target.[76] Placing the focal spot

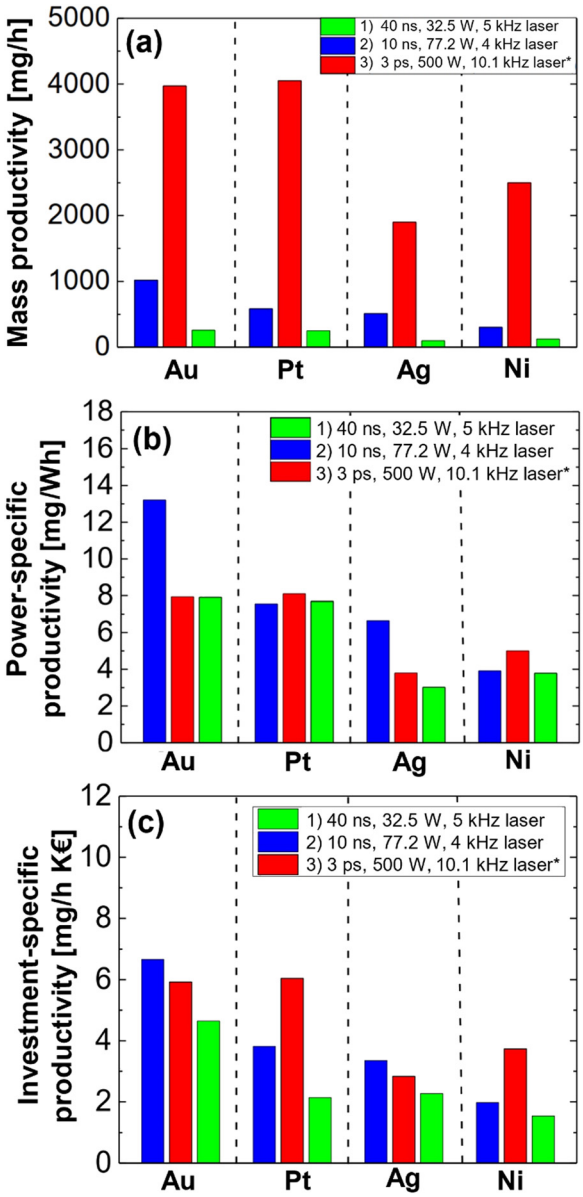

Fig. 4 Productivity comparison of three different laser systems for the ablation of Au, Pt, Ag, and Ni in water, adapted from ref. 115 with permission from author, licensed under CC BY 4.0, copyright 2018. Each figure indicates a different productivity calculation approach: (a) mass productivity, (b) power-specific productivity, and (c) investment-specific productivity. The asterisk (*) indicates that the data is reproduced from ref. 52 with permission from IOP Publishing Ltd, copyright 2016.

on the target surface is usually preferred to maximize the laser fluence and get the maximum ablated volume. Nevertheless, Waag *et al.*[75] suggested that placing the focal spot slightly behind the target (0.7–4.7 mm) increases NP productivity compared to placing the focal spot on the surface of the target (0 mm) (Fig. 5). The authors argue that the highest productivity does not occur at the focal spot due to the minimized spot area of the laser, which would be equivalent to performing the process with a longer focal length or smaller diameter of the laser beam before the lens. Thermal analysis of the liquid and the target revealed that the target reached the minimum heating

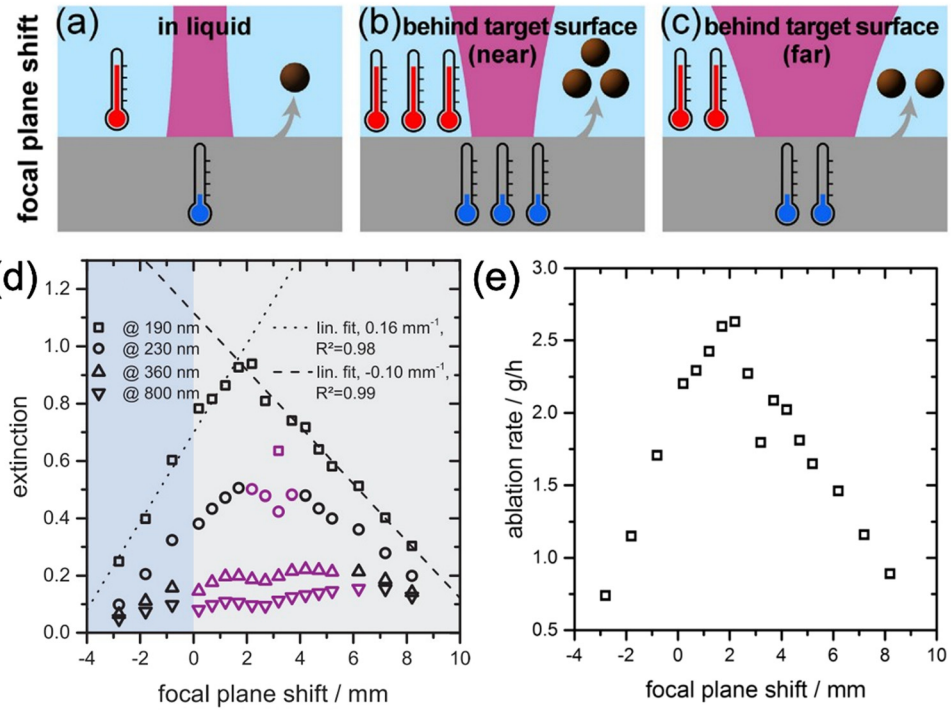

Fig. 5 Schematic illustration of how different focusing conditions affect the productivity: (a) focal spot on the liquid resulted in the lowest productivity, (b) focal spot behind the target (near, 2 mm) resulted in the highest productivity, and (c) focal spot behind the target (far) resulted in the moderate productivity. Ablation rate results are based on (d) extinction approach and € gravimetrical approach. Adapted from ref. 75 with permission from Elsevier, copyright 2019.

while the colloid reached the highest temperature under the experimental conditions proposed. The temperature distribution in the liquid and target is explained by the reduction of heating effects by the proposed laser defocusing. The high temperature of the liquid is caused by the heat released from the larger number of generated NPs.[75] Later results confirmed that the material removal rate can be maximized by changing the focusing conditions and varying the size of the beam waist.[104]

Overall, the spatial focusing conditions influence PLAL productivity by affecting the fluence and intensity profile of the beam at the focal spot and propagation through the liquid. The focal length and beam diameter, directly affect the numerical aperture and focal spot size, which completely modifies the laser intensity during propagation as well as the fluence. The optimum focal length and beam diameter depend on the target due to the differences in the threshold fluence between materials, the liquid due to the nonlinear threshold fluence and intensity, and the pulse duration. The modification of the focal length within a PLAL system is many times unfeasible since fast galvanometric scanners are employed, and the f-theta lens exchange requires an economical investment and sometimes difficult modification of the chamber positioning. Consequently, for PLAL systems with fixed optics, defocusing the beam appears as a straightforward solution to achieve the optimum processing fluence.

4.2. Taking into account the nonlinear effects

The impact of pulse duration on the primary mechanism of laser material removal has been previously discussed. Furthermore, the width of the laser pulse, which affects peak power and intensity, has been shown to have an impact on PLAL through its influence on parameters such as cavitation bubble properties, absorption, scattering, and target temperature. For example, experiments on the laser ablation of metal targets in air showed that material removal efficiency is increased as the employed laser pulse width is shorter,[116,117] due to the reduced thermal interaction and more efficient use of the energy for material removal process.[114,118,119] This evidence points towards femtosecond lasers as an ideal tool for efficient material removal.

However, the nonlinear interactions that dominate the ablation process at the femtosecond time scale also represent a source of energy losses due to the generation of these phenomena in the liquid prior to the interaction with the target.[120] Besides, nonlinear effects like filamentation and self-focusing not only produce energy losses but also modify the divergence of the beam and so the focal spot position.[98] This variation alters the ablation fluence if the target is not conveniently realigned and complicates the reproducibility of the experiment.[98] This fact is even more critical considering that the modification of the focal spot position is power dependent, and so a variation of the laser energy turns into a shift in the focal spot location.[121] It should be noted that the appearance of this phenomenon is not only related to the laser pulse width but also to the laser peak power and intensity.[112] The frontier between linear and nonlinear effects predominance is generally assumed to be in the limit between ps and fs timescales.[113,122] Nevertheless, parameters related to the material and laser properties should be considered for every specific situation to obtain the threshold value and evaluate the optimum experimental conditions.[99]

The limitations related to the presence of a liquid medium and energy losses due to the generation of nonlinear effects restrict the application of fs lasers for nanoparticle production upscaling.[123] Then, as an intermediate solution to decrease thermal interaction while avoiding strong nonlinear interactions, ps lasers are commonly employed when production upscaling is desired.[74] Nevertheless, effective control of nonlinear effects produced in the liquid media is a promising path towards PLAL production increase by the employment of high power and high repetition rate femtosecond lasers. Recently, the Simultaneous Spatial and Temporal Focusing (SSTF) technique has been proposed in PLAL as an alternative to conventional single-lens focusing to address the problem of energy losses due to the nonlinear effects interaction of femtosecond pulses propagation through the liquid layer. The key idea of the SSTF system is that a diffractive grating provides a spatial chirp to the femtosecond beam, so the different spectral components are separated and only recombine at the spatial focus of the objective lens (Fig. 6a). This produces a significant increase in the pulse width during its propagation in the liquid and, consequently, the reduction of the nonlinear losses. However, thanks that the grating is imaged into the sample by means of an optical setup, the original femtosecond pulse width is recovered over the target so keeping the desired high-efficiency ablation of femtosecond pulses. This strategy for beam delivery allows a reduction of a 70% factor of the nonlinear energy losses compared to the standard fs PLAL system, resulting in a productivity increase of 2.4[99] (Fig. 6b).

4.3. Reducing liquid and nanoparticles absorption and scattering *via* laser wavelength selection

Nonlinear effects are not the only interaction with the liquid that influences productivity, linear interactions such as absorption, reflection, and scattering occurring both in the liquid and the target need to be accounted for to maximize PLAL NPs yield. The laser wavelength defines these processes, as each material's absorption, reflectance, and scattering depend on the wavelength of the incident light.[124–126] Higher absorption of the target at the laser wavelength leads to a higher energy density delivered to the sample and so the ablated volume increases. For example, for laser ablation in air, if a material has a low absorptivity at 1064 nm, the amount of ablated material with an Nd:YAG 1064 nm laser will be lower.[126]

The optimum processing wavelength of the material can be determined by spectrophotometry, hence defining the most suitable wavelength for laser ablation in air. Nevertheless, the absorption of the liquid and generated nanoparticles in the laser ablation in liquid produce energy losses, requiring a laser wavelength with low liquid absorption and high material absorption.[127,128] This key difference with ablation in air is shown in materials such as Au and Ag where the maximum ablation efficiency laser wavelength differs from ablation in air.[129,130] Scattering and inter- and intra-pulse absorption are commonly found as the main hurdles to increasing PLAL productivity. Intra-pulse absorption is related to the laser pulse width, which is found for longer pulses in the ns regime and above, as the pulse tail can be absorbed by the generated NPs and plasma plume from the pulse front.[127] The scattering and inter-pulse absorption, on the other hand, are associated with the extinction coefficient of the liquid and the generated colloidal NPs, which affect the laser energy delivered to the target.

As reported by Intartaglia *et al.* (2014),[131] the ablation of Si in water using a UV laser (355 nm) resulted in lower productivity compared to the ablation using a NIR laser (1064 nm) as shown in Fig. 7. They observed two different regimes in the UV laser ablation, termed transient and steady-state regimes, where the productivity is higher during the transient regime (smaller number of pulses, shorter ablation time) compared to the steady-state regime (larger number of pulses, longer ablation time) (Fig. 7b). TEM analysis shows that the smaller Si NPs size is obtained with increasing ablation time, proving the photofragmentation phenomenon.[131] Meanwhile, the ablation using a NIR laser (Fig. 7a) shows a steady ablation yield and the particle size is also bigger than the UV-ablated Si NPs. These effects are especially prominent if a batch chamber is used in PLAL, where the generated NPs stay in the chamber after the

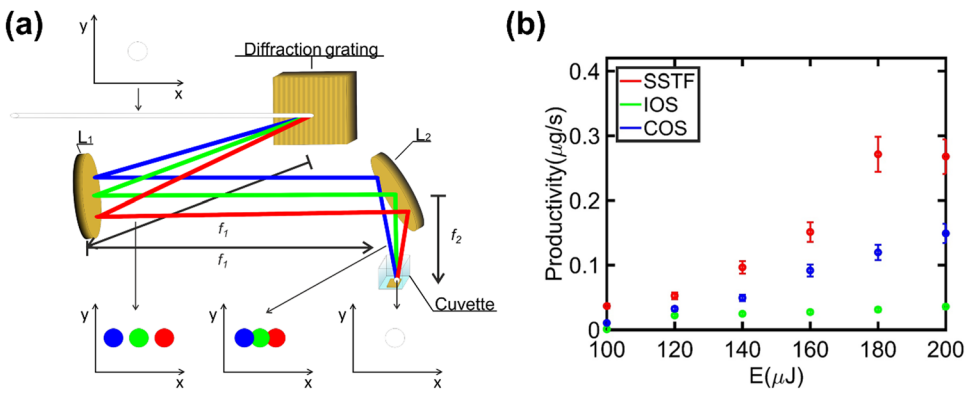

Fig. 6 (a) Experimental setup of the fs SSTF-PLAL system based on the spatial separation of the spectral components of an fs pulse that is only recombined at the focal spot, returning to the initial fs pulse duration. (b) NP productivity as a function of the pulse energy for the fs SSTF-PLAL, standard fs PLAL (COS), and analogous system to fs SSTF-PLAL without spatial separation of the spectral components (IOS). Reproduced from ref. 99 with permission from Chinese Laser Press, copyright 2019.

generation and shield the laser beam. The employment of a flow chamber is thus recommended to reduce scattering and absorption related to the generated NPs and to improve the productivity. Selecting the laser wavelength with minimum absorption and scattering by the generated NPs is crucial to maximizing the laser energy delivered to the target. While UV laser is more beneficial to produce smaller NPs due to the fragmentation effect, the NIR laser is the most ideal choice to obtain high ablation yield due to the low absorption by generated NPs.

4.4. Bypassing the cavitation bubble

The optical phenomena occurring in the liquid are not the only difference between laser ablation in air and PLAL. The presence of the liquid and the laser interaction promotes the formation of a cavitation bubble for each pulse interacting with the target. This vapor bubble is formed when the local pressure drops below the liquid's vapor pressure; hence, the inside of the bubble is filled with vapor. The cavitation bubble in PLAL is formed due to the instant vaporization of the liquid exposed to the heat of the plasma plume. The temperature of the plasma plume was measured experimentally by capturing the optical emission intensity of the plasma during the ablation of a target using an ICCD camera with a resolution of 50 ns.[60,132–135] The obtained continuum spectra are fitted to the Planck equation to obtain the plasma plume temperature.[136,137] The ablation of materials in water is reported to generate plasma plumes with a temperature in the range of 4000–8000 K.[132,133,135,137] Meanwhile, another study of graphite ablation in water with a 5 ns resolution shows a maximum plasma temperature of 25 000 K, which reached 20 ns after the laser pulse interaction.[138] After the cavitation bubble formation and expansion up to the maximum height, the cavitation bubble undergoes a shrinkage process and finally collapses, releasing a shockwave to the surrounding liquid. The lifetime and maximum height of a cavitation bubble depend on many factors, including laser fluence,[76] pulse width,[76,139,140] number of irradiated pulses at the same spot,[141,142] liquid density,[143] the thickness of liquid layer,[144] liquid viscosity,[145] target geometry,[100] and liquid compressibility.[146] Its maximum height varies strongly with the pulse width, ranging from tens of μm as in femtosecond tissue ablation,[139] to several mm in nanosecond ablation of alumina.[140]

The cavitation bubble's lifetime and size strongly constrain PLAL productivity. In continuous ablation PLAL, the first bubble generated by the first laser pulse can shield the subsequent pulses, hindering the laser energy that reaches the target material. Two strategies have been proposed to bypass the cavitation bubble (Fig. 8a). The first one is to temporally bypass the cavitation bubble, which means that the subsequent pulse is sent when the previous cavitation bubble already collapsed.[90] This approach is only suitable for low repetition rate laser sources, for example, if the lifetime of the cavitation bubble is 100 μs, the maximum repetition rate that can be employed is 10 kHz to temporally bypass the cavitation bubble.[147] Nevertheless, high repetition rate lasers with high pulse energy are desired to increase PLAL productivity. Hence, the second proposed mechanism, *i.e.*, spatially bypassing the cavitation bubble, represents a more feasible way to achieve industrial-scale PLAL production. Spatial bypassing of the cavitation bubble can be achieved by a high scanning speed of the processing pattern. The distance

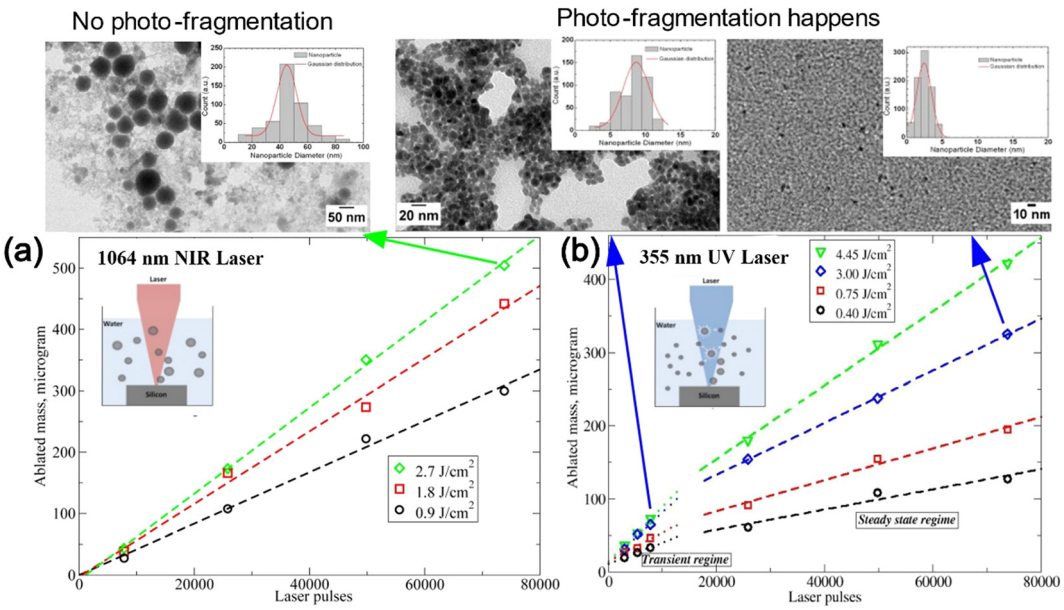

Fig. 7 Laser wavelength influence on the productivity and particle size of Si ablation in water. (a) Ablation using a 1064 nm NIR laser shows steady ablated mass as a function of a number of pulses (ablation time) in different fluences. The inset, indicated by the green arrow, shows the TEM image and particle size distribution of Si ablated using a 1064 nm NIR laser. (b) Ablation using a 355 nm UV laser produces smaller Si NPs with increasing ablation time due to photo-fragmentation. Insets, indicated by the blue arrows of the respective data point, show the TEM image and particle size distribution of Si ablated using a 355 nm UV laser. Adapted from ref. 131 with permission from The Optical Society, copyright 2014.

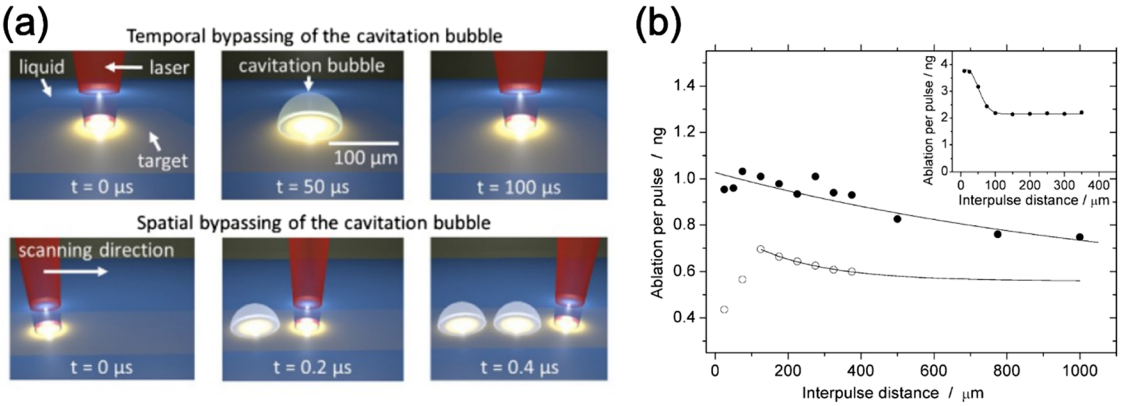

Fig. 8 Bypassing the cavitation bubbles. (a) Schematic representation of temporal and spatial bypassing of the cavitation bubble (reproduced from ref. 74 with permission from The Optical Society, copyright 2016) and (b) ablation per-pulse of Zn in tetrahydrofuran as a function of the interpulse distance, depending on the bypassing mechanism. Filled data points are temporal bypassing by using a low repetition rate (1 kHz), while hollow data points represent spatial bypassing (repetition rate of 10 kHz). The inset shows the ablation per pulse of the Zn target in air. Adapted from ref. 90 with permission from American Chemical Society, copyright 2010.

between pulses has to be at least equal to the cavitation bubble radius so the subsequent pulse does not interact with the bubble formed by the previous pulse. The suitability of this approach for PLAL production upscale was confirmed by Wagener *et al.* (2010),[90] comparing the productivity of Zn ablation in tetrahydrofuran (THF) varying the inter-pulse distance and repetition rate to study the influence of temporal and spatial bypassing of the cavitation bubble in picosecond PLAL.[90] In their setup, the inter-pulse distance was kept constant for different repetition rates, maintaining the number of pulses irradiation of the sample (10^6 pulses) to obtain comparable productivity values. At 10 kHz, increasing the inter-pulse distance up to 125 µm enhanced the ablation efficiency. Then, a gradual decay of the ablation rate is observed (Fig. 8b, hollow data points). The initial productivity increase is related to the spatial bypassing of the cavitation bubble combined with the incomplete thermal relaxation of the material irradiated by the previous pulse, leading to trapped heat and a phase explosion as the dominant ablation mechanism. Contrarily, for inter-pulse distance larger than 125 microns, the irradiated area has not experienced heat accumulation due to the previous pulse, being thermal ablation as the main mechanism instead of phase explosion, and gradually lowering the ablation rate.[90] Temporal bypassing is achieved at 1 kHz, with a low productivity variation for lower repetition rates (Fig. 8b, filled data points). It is important to critically note that when evaluating the size and lifetime of cavitation bubbles with respect to productivity, the dimensions of a bubble induced by a single pulse are being considered. Nevertheless, it is known that these dimensions vary when multiple pulses hit a target.[142]

In a real NP production scenario, the laser power and repetition rates are maximized while keeping the optimum fluence in order to deliver the larger amount of pulses and maximize the ablated volume. In this scenario, a fast-scanning system is required to increase the inter-pulse distance and increase the ablated area to ensure that the target has enough time between successive scanning patterns to cool down. The scanning speed becomes a fundamental parameter together with the repetition rate and the cavitation bubble size for each specific system to ensure cavitation bubble bypass. As an example, for a cavitation bubble with an average radius of 100 µm produced with a laser source operating at a 100 kHz repetition rate, the minimum scanning speed required to completely bypass the cavitation bubble is 10 m s^{-1}. The galvanometer scanner technology can reach 10 m s^{-1}. Nevertheless, if the repetition rate is further increased to the MHz range, scanning speeds of at least 100 m s^{-1} are required. As the number of delivered pulses per second is critical for PLAL productivity, the required scanning speeds reach the current technological limitations.

The galvanometer scanners are based on the mirror(s) revolved with rotary motor(s) that deflect the input beam into a designed pattern with micrometric precision.[148] This working principle limits the maximum speed that can be achieved by this technology due to the inertia from the mass of the mirror(s) and other moving parts.[149] The fastest reachable speed of a galvanometer scanner is less than 200 rad s^{-1}.[150,151] If the scanner is paired with an f-theta lens with a focal length of 167 mm, the maximum scanning speed at the working field is approximately 35 m s^{-1}.[152] In 2013, De Loor introduced a new scanning technology based on the rotation of mirrors fixed on a polygon wheel.[150] The wheel rotates at a constant speed and the incoming beam is deflected on the flat facet of the mirrors (Fig. 9a). This polygon scanning technology offers a beam deflection speed of up to ~1000 m s^{-1}.[150,153] However, since the corner of the polygon wheel will deflect the beam at uncontrolled angles, the laser beam is shut off during this time and the laser beam only irradiates the target within a certain percentage of the duty cycle. This effect is more pronounced for small processing patterns, requiring large patterns with lower spatial resolution than the galvanometric scanners.[148] Streubel *et al.* (2016)[74] proposed for the first time the employment of a unidimensional polygon scanner (500 m s^{-1}) together with a galvanometric scanner to achieve a 2D scanning of the target sample (Fig. 9a). The fast scanning system was employed with a 500 W, 10 MHz, 3 ps laser source to maximize the number of

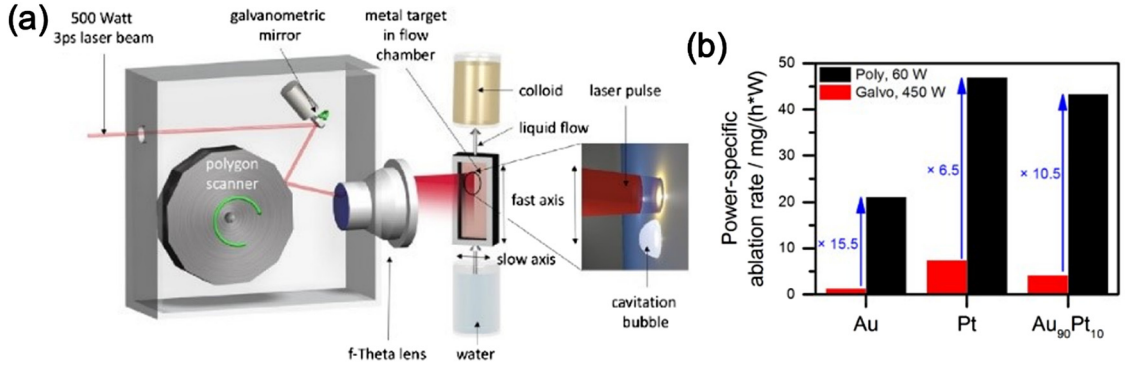

Fig. 9 (a) Schematic illustration of the ablation set-up using a polygon scanner (reproduced from ref. 74 with permission from The Optical Society, copyright 2016) and (b) power-specific ablation rate comparison of a galvanometer scanner (red) to the polygon scanner (black) for different materials (reproduced from ref. 54 licensed under CC BY 4.0, copyright 2021).

pulses per second by processing the target at 10 MHz achieving fluences above the threshold fluence thanks to the high power delivered.[74] The fast scanning speed allows the bypass of the cavitation bubble, reaching productivities as high as 4 g h^{-1} for PLAL of Pt. A direct comparison of PLAL with a galvanometric scanner (5 m s^{-1}) compared to the polygon scanner (484 m s^{-1}) resulted in a difference up to 16, 7, and 11 times for the ablation of Au, Pt, and $Au_{90}Pt_{10}$ targets, respectively (Fig. 9b).

In conclusion, PLAL upscaling requires faster scanning technologies. Using high-speed polygon scanners is one of the easiest ways to enhance NPs production.[154] However, their high prices, low precision demanding large scanning patterns, and their duty cycle that reduces the initial laser power employed in the target processing by a 50% factor, make it difficult the implementation of this technology in every PLAL system. Consequently, galvanometric scanners generally still represent more economical and repost alternative for PLAL, especially when fast galvanometric scanners reaching 30 m s^{-1} are employed.

4.5. Avoiding persistent microbubbles

The productivity of PLAL can be adversely affected not only by cavitation bubbles and NPs in the laser path but also by the formation of so-called persistent microbubbles during the ablation process. Persistent microbubbles are spherical and stable gas bubbles, generated from the collapse of the cavitation bubbles. While a cavitation bubble lifetime is approximately 0.1–1 ms,[145] persistent microbubbles can stay even as long as seconds.[135] Consequently, it is critical to understand the liquid, target, and laser processing parameters related to the lifetime of the persistent microbubbles in order to avoid their presence that shields the laser beam and can even become a safety issue when they stick to the chamber window, increasing reflectivity and even leading to glass breakage by the high-intensity laser source. Kalus *et al.* (2017)[145] investigated the formation of persistent microbubbles during the ablation of gold in 11 different liquids with various viscosity, as shown in Fig. 10a and b. The influence of the liquid viscosity over the amount, cross-sectional area, size, dwell time, and ascending speed of the persistent bubbles was evaluated. It was found that higher liquid viscosities increased the size and dwell time of the generated persistent microbubbles.[145] As shown in Fig. 10b, the ablation yield difference based on the liquid viscosity shows a factor 3 reduction when the ablation is done in liquids with a viscosity higher than 20 mPa s compared to liquids with a viscosity lower than 1 mPa s. A different study[86] revealed the influence of the target material over persistent bubbles generation. Different targets were irradiated in water and the gas formation (H_2 and O_2) was measured. The results show that less-noble metal such as Al produces the largest gas volume, followed by titanium, iron, and copper, respectively, while less oxidation-sensitive metals such as Au, Pt, and Ag produce the lowest gas formation (Fig. 10c). The authors suggest that the standard reduction potential (E^0) of these elements influences the volume of gas formed. In the PLAL system, the elements with negative E^0 values readily react with water vapor to form oxides and molecular hydrogen as a side product.[86] The formation of more gas bubbles for these types of elements results in a lower ablation yield due to the shielding of the incoming laser beam (Fig. 10d).[86] Meanwhile, noble metals such as Au and Pt are less prone to oxidation, thus, the gasses formed during the PLAL of these elements are associated with the laser-induced breakdown of the liquid molecules.[86,155,156]

Unlike cavitation bubbles, which can be spatially and temporally located, thus allowing the implementation of bypassing strategies, persistent microbubbles exhibit an unpredictable evolution that limits their bypass. Consequently, liquid flow strategies such as a high flow rate and good laminar flow represent the best approach to remove the detached persistent bubbles. Controlling the liquid flow by the chamber design becomes a fundamental factor for PLAL upscaling since turbulences would extend the retention time of these shielding bubbles inside the chamber, resulting in a reduction of the process efficiency.

4.6. Knowing the effect of target morphology

The morphology of the target influences PLAL productivity due to the different shapes, lifetimes, and dynamics of the produced bubbles. These bubble dynamics influence NP formation. Kohsakowski *et al.* (2016)[100] studied 3 different target geometries: wire tip, clamped wire, and bulk target, in relation

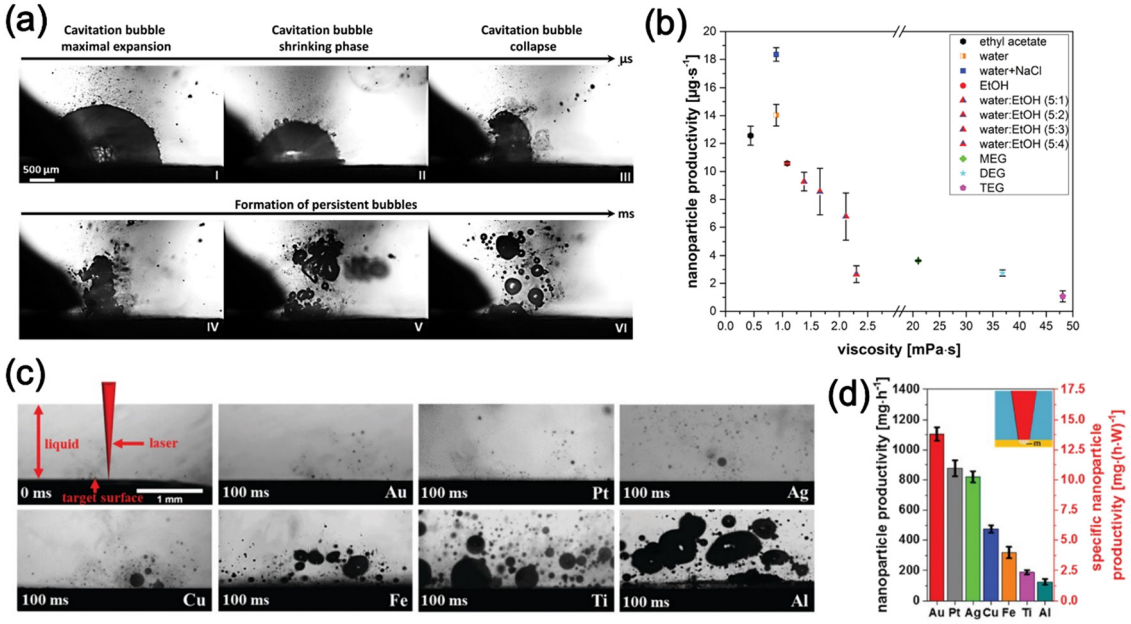

Fig. 10 The influence of persistent microbubbles on the productivity. (a) The formation of persistent microbubbles and (b) the influence of liquid viscosity on the productivity of Au ablation in the respective liquids. Adapted from ref. 145 with permission from the PCCP Owner Societies, copyright 2017. (c) The formation of persistent microbubbles in the ablation of different elements and (d) NPs productivity and power specific productivity for different elements. Adapted from ref. 86 with permission from the PCCP Owner Societies, copyright 2019.

to their bubble formation and dynamics for a single pulse experiment (Fig. 11). Ablation at the tip of the wire results in a 23% shorter bubble lifetime compared to the ablation in a bulk target, due to the springboard movement, which allows a larger displacement of the bubble, as shown in Fig. 11b. This springboard movement also provides a larger displacement of the bubble rebound from the target, compared to the clamped wire and the bulk target (Fig. 11a and c, respectively), which showed a longer duration of the bubble rebound attachment to the target. Multi-pulse experiments were also performed to evaluate PLAL productivity for these three geometries. Wire-type targets (clamped wire and wire tip) showed a productivity increase of up to 2.5 times higher compared to the bulk target. The productivity increase is associated with the elasticity of the wires, which can provide better bubble movement. Nevertheless, the spring-like movement of the wire tip target does not increase the productivity compared to the clamped wire target, due to the limitation in the ablation set-up where the incident laser is shielded by the bubbles rising upward. The authors suggest that the productivity could be improved if the liquid flow is perpendicular to the target which helps to transport the bubbles away from the ablation area.

In a different study, the influence of the wire diameter on PLAL productivity was evaluated for a silver wire target ablated by a 10 ns laser. The highest ablation efficiency is found for a wire diameter of 750 µm, resulting in a 2 times higher ablation rate than the wire diameter of 1500 µm.[89] Based on these two reports, a wire target is an interesting target geometry to increase PLAL productivity due to the changes in bubble dynamics. The modification of the silver target geometry (wire or bulk) does not influence the NP size distribution.[89] Nevertheless, a wire target requires precise laser beam positioning to get the correct focalization of the beam on the wire surface, and not all materials are available as wire shapes. Hence, conventional targets in a form of a bulk plate or a compressed powder pellet are still chosen over the wire shape for easier beam positioning and availability.

Not only the shape but also the texture[157] of the target's surface affect how the laser beam interacts with the target. Nadarajah *et al.* (2020)[158] studied the correlation between the change of surface microstructure during picosecond PLAL with the productivity of some metals and alloys, such as Fe, Au, Ag, and their binary alloys. In the study, the formation of laser-induced periodic surface structures (LIPSS) was observed on the ablated surface of Au and Fe targets and their binary alloys, while Ag does not show the formation of LIPSS (Fig. 12a). Regarding the productivity, it is suggested that the formation of LIPSS on the surface of some alloys affects the reflectivity, as measured for the reflectivity of $Ag_{50}Au_{50}$ without LIPSS formation that is 20% lower compared to the surface with LIPSS.[158] Since LIPSS stem from the linear polarization of the laser, using a quarter wave plate to convert the linear polarization to circular polarization was found to reduce LIPSS formation and increase the productivity of the metal alloys tested (Fig. 12b). Nevertheless, LIPSS is a material specific and fluence-specific phenomenon, and the correlation of LIPSS to the PLAL productivity is still newly explored, hence, further studies are required.

The compactness (degree of porosity) of the target should also be considered to avoid biased results of the productivity due to the removal of large parts of the target not contributing to NP formation. Schmitz *et al.* (2016)[48] compared the gravimetrical and optical (extinction) techniques to measure the

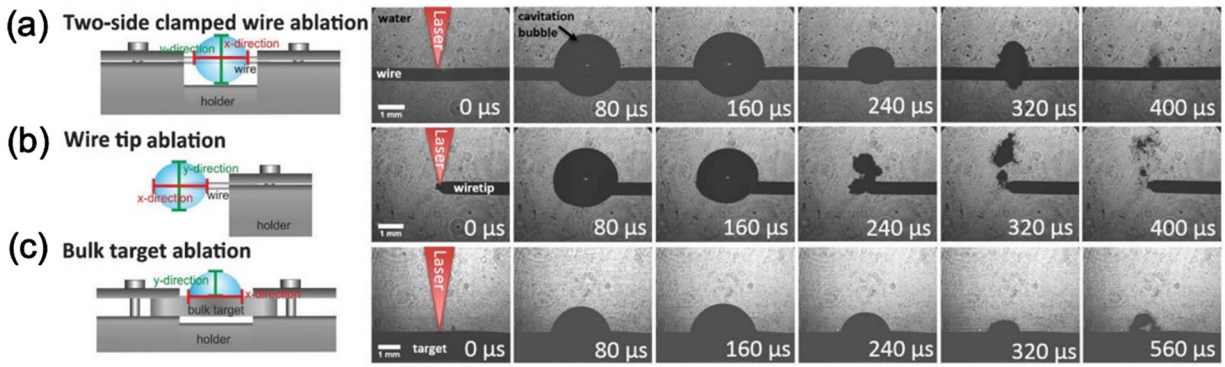

Fig. 11 Bubble morphology depending on the target geometry of (a) wire target clamped on both ends, (b) wire target clamped on one end, and (c) bulk target. Adapted from ref. 100 with permission from the PCCP Owner Societies, copyright 2016.

productivity of targets with different porosity, namely micro-powder-pressed targets (69, 76, and 87% density), a nano-powder-pressed target (99% density), and a bulk target (100% density).[48] The micro-powder-pressed targets showed the highest productivity in the gravimetrical approach compared to the nanopowder-pressed and bulk targets. The absorption measurements indicated that the absorbance values remained fairly consistent across the three samples. However, the apparent contradiction can be attributed to the formation of larger particles in the micro- and millimeter range from the low-density targets, which led to higher productivity values in gravimetric measurements. The absorbance values, on the other hand, only represent smaller particles, which were stable in the colloid during the measurement. The bigger particles already settled at the bottom in less than one minute, thus, did not increase the concentration of the colloid. Hence, it is important to use densely packed pressed powder or bulk targets to avoid biased result especially when PLAL productivity is characterized by the gravimetrical approach.

There is a significant correlation between the target morphology and the productivity of the PLAL system due to its influence on the bubble formation and the laser interaction with the target and liquid. Cylindrical target such as wire is shown to improve the productivity due to the spring-like movement which reduces the bubble lifetime, but the small area makes it difficult to align the beam. Moreover, the curved shape changes the focusing condition within the ablated area, thus resulting in uneven fluences. The plate and sheet types are the most commonly used targets for ablation due to their flat surface and accessibility from the manufacturing company. Employing the flat target is thus recommended. Compact targets such as pressed powder with high density and low porosity, or bulk metal and alloy targets should be used in order to avoid the removal of larger particles.

4.7. Optimizing the ablation chamber design

The simplest ablation chamber design in PLAL is a glass beaker or a cuvette where the target is placed either laying or standing depending on the direction of the incoming beam (Fig. 13a). This setup is sufficient for the production of NPs in a small batch, but for larger production, the employment of these chambers is no longer feasible. Due to the limited volume of the chamber, the colloid becomes concentrated rapidly, which hinders the incoming laser beam to reach the target. In addition, the NPs and persistent bubbles that are formed scatter the incoming laser beam since there is no liquid flow to remove them.[159] Hence, different chamber designs have been proposed to improve the

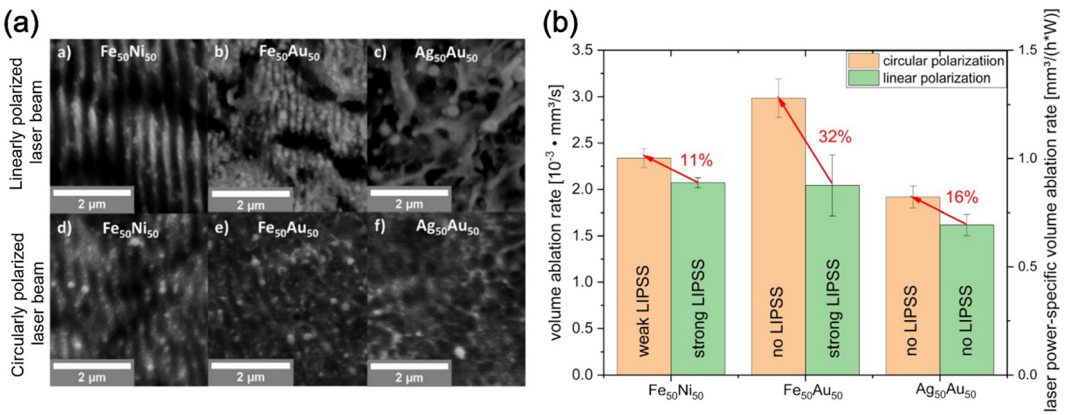

Fig. 12 The influence of laser polarization on the laser-induced periodic surface structures (LIPSS) formation for picosecond PLAL of different targets. (a) SEM images and (b) productivity increase with different laser polarization. Adapted from ref. 158 with permission from The Optical Society, copyright 2020.

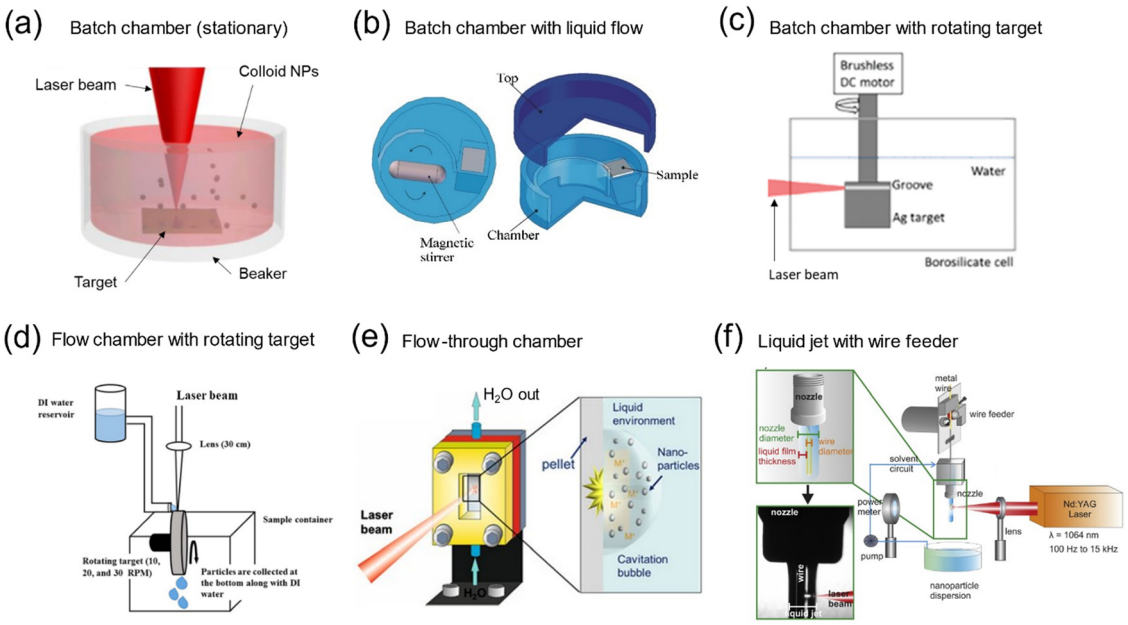

Fig. 13 Type of ablation chambers in the LAL: (a) stationary batch chamber, (b) batch chamber with the liquid flow (reproduced from ref. 114 with permission of AIP Publishing, copyright 2007), (c) batch chamber with rotating target (adapted from ref. 87 with permission from the PCCP Owner Societies, copyright 2016), (d) flow chamber with a rotating target (adapted from ref. 160 with permission from SNCSC, copyright 2017), (e) flow-through chamber (adapted from ref. 161 with permission from Elsevier, copyright 2017), (f) liquid jet with wire feeder (reproduced from ref. 88 with permission from Elsevier, copyright 2017).

PLAL production rate. Barcikowski *et al.* (2007)[114] presented a type of batch chamber with a magnetic stirrer to make the liquid flow inside the chamber (Fig. 13b). The liquid flow inside the chamber is aimed to induce target cooling during ablation and displace the generated NPs away from the target to reduce laser shielding. With this setup, the productivity of femtosecond laser ablation is increased from 0.79 ± 0.36 mg h^{-1} (stationary) to 3.0 ± 0.4 mg h^{-1} (liquid flow). The authors also compared ablation using a picosecond laser with higher pulse energy and repetition rate, resulting in an NP production rate of 31.0 ± 0.4 mg h^{-1} (liquid flow).

A different approach includes the liquid flow within the chamber produced by the rotation of the cylindrical target attached to a brushless motor, as shown in Fig. 13c.[87] At the same time, the rotating target drives away the generated NPs from the vicinity of the target and increases the inter-pulse distance reducing cavitation bubble shielding.[87] The influence of the rotation speed on the ablation rate was evaluated by the colloidal optical extinction approach. The highest PLAL productivity was found at the lowest rotation speed (300 rpm), decreasing with the increasing rotation speed. Based on the flow simulation results as shown in Fig. 14, increasing the rotation speed leads to the formation of unsteady flows and vortices in front of the target's surface, which traps the bubbles produced during PLAL increasing laser shielding.[87] A similar result, reporting lower ablation efficiency with the increasing speed of the rotating target was reported for the ablation of NiTi in water.[160] In this case, the target rotated while the liquid was poured on the ablation spot instead of rotating the target immersed in the liquid, as shown in Fig. 13d. The authors suggest that the high ablation rate with lower rotation speeds is due to close pulse proximity and overlapping effects, which might improve laser absorption of the next pulse.[160]

The next evolution in chamber design is a flow-through chamber that allows PLAL with a continuous feed of fresh liquid and collection of the generated colloid[161] (Fig. 13e). The liquid is pumped through the chamber where ablation takes place, and the generated NPs are carried out of the ablation chamber so that laser shielding is avoided. An optimum liquid flow rate is achieved when the generated NPs are completely removed from the ablation area, confirmed by monitoring the productivity with increasing flow rates.[53] An advantage of this chamber is the capacity to extend PLAL without a colloid concentration saturation and is only limited by the target drilling which allows processing times of several hours even for thin (1 mm) targets.[52]

Alternative flow chamber designs include a nozzle and a wire feeder (Fig. 13f) to reduce the liquid layer thickness and achieve long-term ablation by continuously feeding the target material into the system.[88] This novel system avoids the batch chamber's main limitation for PLAL large productivity, which is the need to replace the liquid frequentlz as NPs concentration reaches a saturation value that does not allow the laser beam to reach the target. The flow chamber is more efficient than the batch chamber, but focus readjustment is still needed due to the depletion of the target's thickness. Meanwhile, a wire target feeder in a liquid jet setup provides the option to feed continuously the target material while keeping the advantages of a continuous liquid flow (Fig. 13f). Prospectively, this setup is proposed to be more efficient, as there is no need to stop the ablation to change

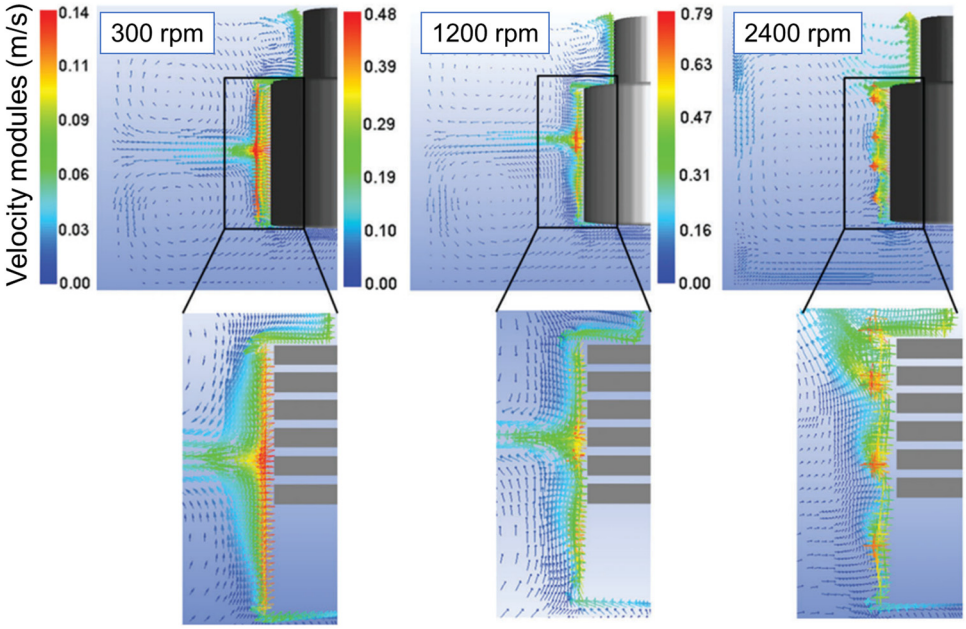

Fig. 14 Numerical simulation of the liquid dynamics inside the rotating target chamber at different rotating speeds. The bottom panels show the magnification of the region on the target surface and the grey rectangles represent the groves produced by the laser. Adapted from ref. 87 with permission from the PCCP Owner Societies, copyright 2016.

the target and/or the liquid. Nevertheless, due to the small wire size, the beam alignment takes longer and represents a major challenge compared to the flow chamber bulk targets. In addition, the stability of the wire feed system represents a challenge for long-term ablation, as well as control of the incident laser fluence. The advantages described and the easier handling and alignment turn the flow through chamber design into the current standard for PLAL upscaling.

Even though the wire feed setup presents some challenges, it highlights another approach to increase PLAL production: liquid layer reduction. It has been reported that decreasing the liquid layer thickness from 8 to 2.5 mm improves the PLAL productivity of an α-Al_2O_3 pressed target from 172 to 592 mg h^{-1}.[53] The authors suggest that absorption and scattering of the laser energy by the generated NPs reduce the laser energy deposition on the target's surface. In a different work, it was reported an optimum liquid layer thickness of 1.2 mm to get the highest yield of Ge NPs in water, based on absorbance characterization.[162] The liquid layer thickness effect was also evaluated in a flow chamber with a silver wire target. Different nozzles were employed to create various liquid layer thicknesses. The optimum productivity was obtained for a liquid layer thickness of 0.5 mm (243 mg h^{-1}). For a liquid layer thickness below 0.3 mm, the ablation showed low reproducibility, which is suggested to stem from partial ablation in air and liquid ejection.

Following this idea, Monsa *et al.* (2020)[91] proposed a strategy to increase NP productivity by focusing the beam at the meniscus interface of a tilted target, as shown in Fig. 15a. An order of magnitude larger concentration of the Pd, Cu, and Ag colloids in ethanol was reported.[91] The comparison of the colloids generated after 5 minute ablation at the meniscus interface and 4 mm liquid layer thickness is shown in Fig. 15b. It should be noted, however, that the optimum liquid layer thickness depends on the material and the experimental set-up (laser parameters, ablation chamber, target and liquid properties, and focusing method) since higher intensities can lead to vaporization of a thicker liquid layer and strong scattering of the beam.

The flow chamber reduced the liquid layer by a closed chamber design and irradiation of the target through a glass window. In this case, extra precautions must be taken to avoid damage to the window glass. The high-temperature plasma plume, shockwave, cavitation bubble, and nanoparticle ejection can cause damage to the window glass if the distance between the target and the window glass is too narrow. It is usually recommended to have a distance of at least 3 mm to avoid damaging the window; naturally, this value depends on other parameters, such as pulse energy, pulse width, and focusing condition. For the ablation without a window (open chamber), the liquid layer thickness could be much lower, but keeping the linear flow represents a major challenge if a large liquid flow rate is employed. These turbulences in the liquid surface affect the laser focusing on the target. Removing the liquid flow allows a stable and thinner liquid layer, however, the effect of the NP shielding due to the rapidly growing colloid concentration represents a larger limitation for PLAL upscaling.

Many ablation chamber designs are proposed to increase the productivity and improve the efficiency of the PLAL process, nevertheless, the discussion related to the fluid dynamics inside the chamber is limited. As the design of the chamber strongly influences the liquid flow, an ineffective chamber produces fluid turbulences which increases the retention time of the NPs inside the chamber, giving rise to the NPs shielding effect of the incoming laser beam. Producing ablation

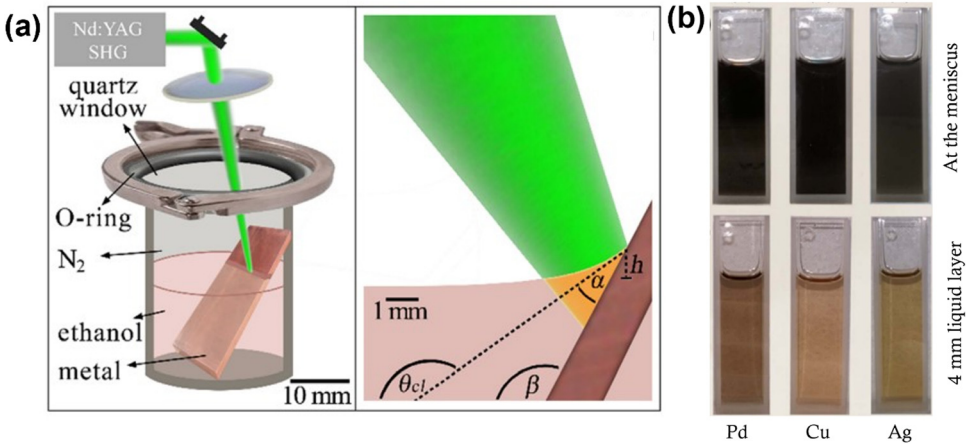

Fig. 15 Proposed strategy to increase productivity by ablating at the meniscus interface of the liquid layer and tilted target. (a) Schematic illustration of the experimental set-up and the enlarged view of the beam at the interface of liquid-target, (b) the colloidal dispersions of Pd, Cu, and Ag NPs produced at the meniscus interface (top) and liquid thickness of 4 mm (bottom). The production of NPs at the meniscus resulted in an order of magnitude higher concentrations compared to the ablation at 4 mm liquid layer thickness. Adapted from ref. 91 with permission from IOP Publishing Ltd, copyright 2020.

chambers with a laminar flow is needed to increase ablation efficiency and the productivity. To produce a laminar flow, a fluid dynamic simulation of the newly designed chamber should be done prior to the production step, to analyze the formation of turbulences and vortices. Studying different liquid viscosities and the influence of species and effects generated by the PLAL process, including the persistent gas, nanoparticles, heat transfer, and the collapse of the cavitation bubbles, are some further stages that can be done in this regard. In summary, the design of an ablation chamber should be accompanied by an engineering approach of fluid mechanical design, which addresses the shortcomings of the inefficient chamber in order to produce laminar flow with minimum turbulence and vortices.

4.8. Continuous production, automatization, remote monitoring, and control of the ablation process

One of the advantages of the PLAL process to produce NPs is the option to perform continuous production. Unlike the wet chemical synthesis methods where the NPs production is commonly done in batches using a certain recipe with tight control over reactants amount and synthesis conditions, continuous production in PLAL can be performed simply by using a flow chamber, either with or without the recirculation of liquid (loop) as shown in ref. 163 for the ablation of a gold target using a nanosecond laser. The continuous production of NPs in the industry is critical to reducing the cost, yet scaling up the batches of chemical synthesis procedure is not as easy as multiplying the amount of the reagents and increasing the reactor's volume. Various parameters such as the reactants concentration, amount of catalyst and stabilizer, heating temperature, stirring speed, and the duration of each process should be optimized accordingly.[164] Moreover, the properties of NPs could possibly change during the scaling up, as the nanoscale control is difficult at larger reactants quantity.[164]

To ensure both safety and economic efficiency, it would be ideal for the implementation of PLAL in the industry to include an automated system for controlling and remotely monitoring the ablation process.[165,166] As the PLAL process only requires the operator for the first setup and periodical monitoring of the status,[166] the required automatization and remote controlling include maintaining the optimum working distance,[165,167] regulating the liquid flow,[166,168] and controlling the laser.[166]

In terms of the automatic control of the working distance, the utilization of acoustic emission as the input data to control the working distance has been proposed. The acoustic emission is considered more practical than the gravimetric approach where the target has to be periodically removed, and it is also applicable in a wide range of material composition, colloid concentration, particle size, and shape,[165] which prove its advantage compared to the extinction approach discussed in Section 3. Definition and measurement of nanoparticle productivity. A prior study by Zhu *et al.* (2001)[169] proved the correlation between material productivity in PLAL and the produced intensity of the audible acoustic waves (sounds) measured by a wideband microphone. Afterward, the following studies to use acoustic emission not only to monitor the production rate of a PLAL process but also to control the system were performed by another group.[165,167] The system uses a piezoelectric sensor to record the acoustic emission waveforms during the PLAL process and the data is forwarded to a Field Programmable Gate Array (FPGA)-based system coupled by Discrete Wavelet Transform (DWT), which is able to perform an online, real-time processing of the acoustic emission while reducing the noise and accelerating the processing time (Fig. 16a). To find and maintain the ideal working distance, an iterative search algorithm is employed by finding the maximum acoustic wave energy (amplitude) at various working distances. The system is thus connected to a stepper motor, which can automatically position the ablation chamber based on the received acoustic emission data.[165,167] Based on the comparative study with the UV-Vis spectra, this system shows similar results as shown in Fig. 16b,[165,167] offering a reliable option for the automatic adjustment of the working distance.

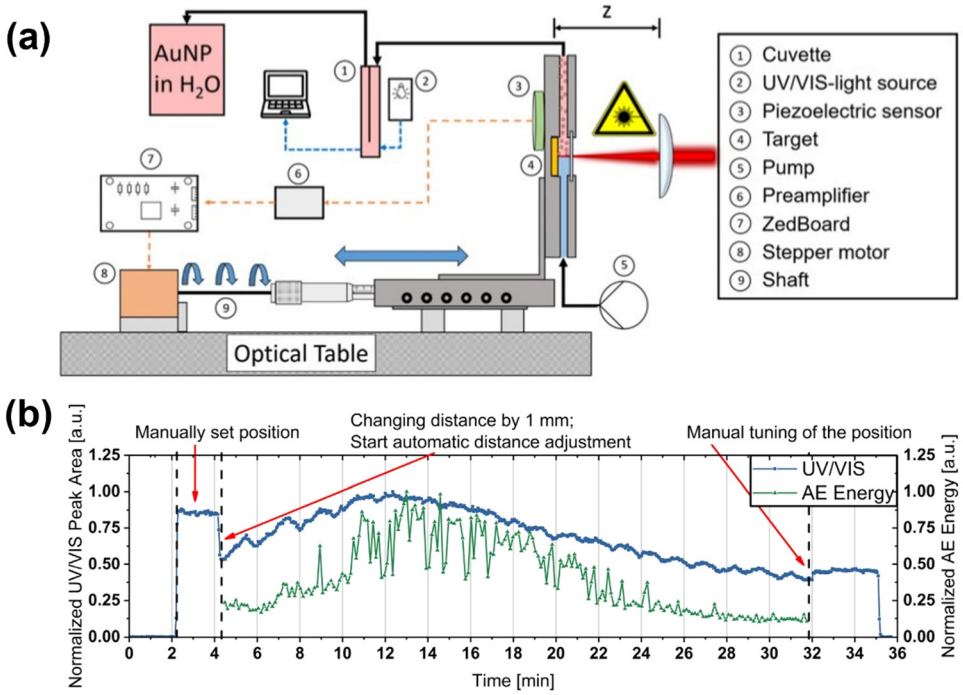

Fig. 16 Real-time monitoring and automatic control of the working distance in the PLAL system, where (a) shows the experimental set-up and (b) shows the comparison between the acoustic emission (AE) signal and UV-Vis spectra over time. Adapted from ref. 167 with permission from Elsevier, copyright 2019.

The automatization of the liquid flow is proposed by Freeland *et al.* (2020)[168] in order to produce NP colloids with a high concentration using a semi-batch recirculatory flow system. The common production step of NP colloids with high concentration requires a separate post-processing step, such as magnetic decantation, centrifugation, destabilization, or vaporization of the liquid, which is time-consuming. By recirculating the liquid flow, the concentration of NP colloid can be increased until the desired value. The liquid flow control is operated through a LabVIEW program which is connected to an automatic valve and peristaltic pump.[168] Unfortunately, there is no discussion on how the automatization of liquid flow using the automatic valve is done.

Complete remote monitoring and controlling of a PLAL system were built using the combination of a LabVIEW program and a TeamViewer program (Fig. 17a).[166] The LabVIEW program is used to control the instruments by connecting them to the on-site PC using a serial connector and several devices are controlled by the PC, namely the laser, the pump, the interlock webcam, the camera, and the XY-stage (Fig. 17b). Meanwhile, the TeamViewer program is used to remotely access the on-site PC, either from a smartphone or an off-site PC (Fig. 17b). With this online, remotely controlled setup, the PLAL system can be accessed from any place with an internet connection having bandwidth larger than 1–0.1 Mbytes s^{-1},[166] and the response time for shutting off the laser

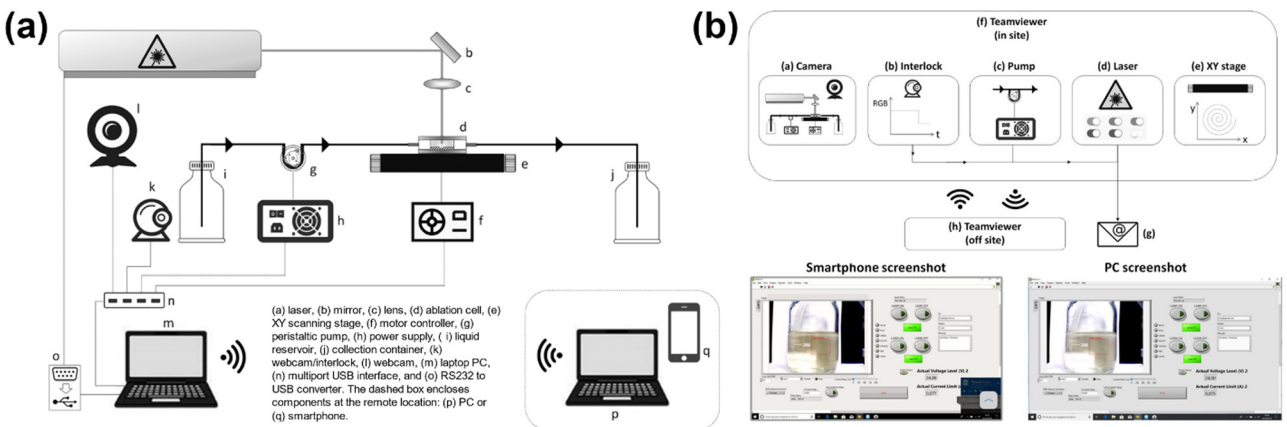

Fig. 17 Remote monitoring and controlling system. (a) Schematic representation of the system configuration, (b) controlled devices with in-site PC and the screenshot of off-site controlling devices. Adapted from ref. 166 with permission from AIP Publishing, copyright 2019.

is of 10^{-3} s.[166] In case of the automatization, the system offers an automatic shutdown when the colloid concentration, measured by the interlock webcam coupled with color analysis software, reaches the desired threshold value. The interlock webcam is also used to gauge the liquid amount in the bottle, thus preventing liquid spillover and running out of liquid.[166] The set-up presents a solution to the industrial needs where off-site controlling is required, for example in the ablation process of dangerous substances, such as radioactive materials. In addition to that, it provides a more efficient and practical way to control the PLAL process from anywhere, while the automatization allows us to produce colloidal NPs with certain concentrations and prevent undesired lab accidents, even without constant human supervision.

The development of automatization, remote monitoring, and off-site controlling of the PLAL process is necessary to open the pathway of PLAL usage in the industry. Automatization offers a faster task execution based on feedback systems, which results in a more efficient and economical way compared to the manual adjustment by labor workers. It also reduces the chance of human error during the process, thus avoiding the chance of laboratory and industrial accidents. The automatization to produce certain colloid concentrations and automatically stop the laser system means that the expenses for labor workers could be minimized. The remote monitoring and off-site controlling provide us with the ability to control on-site experiments from anywhere, which means that the operator does not need to be continuously present nearby the PLAL system. The shown configuration in this subchapter is still limited to a laboratory experiment with a small production batch, but the system is potentially applicable for the production of large batches of NP colloids such as in tens or hundreds of liters. Coupled with an injectable manufacturing process, the use of a high-power laser, a fast scanner, a large and efficient ablation chamber, a continuous liquid flow, automatization, and a remotely controlled system, the production of colloidal nanoparticles for industrial application could surely be achieved.

5. Conclusion and outlook

We have conducted a thorough re-examination of the factors that influence the productivity of PLAL. Based on the discussion of the laser and target properties, it should be noted that several parameters such as laser fluence and wavelength, the target properties, and the focal length, among others, should be taken into account in each experiment to comprehensively evaluate the productivity of PLAL. Although it appears that productivity is strongly linked to the material and architecture of the ablation system, the PLAL method still holds high potential to be used widely in industry. The advantages offered by PLAL over the chemical synthesis method lies in the possibility to produce various type of nanoparticles from bulk materials in a straightforward manner as it only requires a laser, a scanner, a chamber, a liquid, and a target. To produce a different type of nanoparticle composition, one can simply change the target, which varies from metal, ceramics, and alloy to organic compounds. Meanwhile, in the conventional synthesis method, each type of desired nanoparticles requires new ingredients, reagents, catalysts, and optimization of each physical treatment step (stirring, heating, exposure to certain gas). The challenge with the low production rate can be overcome by other means which are not directly related to the material properties or laser parameters, such as using a high scanning speed, a chamber with laminar flow and small liquid layer thickness, and the use of additional optical elements to change the beam profile. Besides, the gram-per-hour production rate of NPs has been achieved for different materials by increasing the interpulse distance and bypassing the cavitation bubble.[52–54,74,170]

As a general guideline, higher productivities of PLAL can be obtained by the utilization of high power and repetition rate picosecond laser sources, which can mitigate nonlinear interactions, in conjunction with a fast-scanning strategy to circumvent the cavitation bubble spatially. In addition to the laminar liquid flow with a reduced layer, when feasible, it is advised to use low-viscosity liquid to prevent the shielding of nanoparticles and eliminate persistent bubbles.

As we have shown, considerable efforts have been devoted to enhancing productivity over the course of this century, resulting in remarkable advancements of up to three orders of magnitude, leading to outputs in the range of grams per hour. Nevertheless, certain unresolved issues remain that require attention to facilitate further improvements.

- The automatization of the PLAL process. Automated processes perform tasks much faster than humans and the use of feedback systems allows for adjustments to be made on the fly of the fabrication. By removing human intervention from certain tasks, such as the focalization of the beam over the target, the refill of the liquid, and the cleaning of the components, variations due to human error can be minimized. Furthermore, this decrease in the labor-intensive nature of PLAL can save time in situations where production would otherwise need to be halted and, as a result, potentially reduced. Although some preliminary studies have been conducted on monitoring and managing off-site fabrication,[166] greater levels of automation will be necessary to enable the broader commercialization of this technology.
- Enhance productivity across various pulse duration regimes. Laser pulse width impacts the mechanism of synthesis of the nanomaterial at multiple stages, as evidenced by large-scale atomistic simulation,[68] thereby influencing the nanomaterials properties such as the morphology,[171] the composition,[38] the atomic redistribution of metal domains,[172] the oxidation and aging effects,[173] the shape,[174] and the crystalline size domains[175] among others. Using pulse widths in the femtosecond and nanosecond range represents an approach to synthesizing different nanomaterial properties without additional post-production steps, which is interesting for industrial setup. As an example, lattice heating and prolonged plasma exposure from the nanosecond pulses can stimulate the phase transition of the NPs, such as the reversible transformation between nanodiamond and carbon-onion structure,[176] the restructuring

and surface decoration of RuO_2 nanoparticles to RuO_2@Ru/RuO_2,[177] and the formation of carbon-based quantum dots with either graphene or amorphous structure.[178,179] The use of a thermosetting polymer solution as the ablation liquid for nanosecond PLAL can promote different core–shell structures.[38,180,181] In addition, femtosecond lasers allow to obtain the atomic redistribution in bimetallic Au–Pd nanorods[172] and reshape gold nanorods with ultranarrow surface plasmon resonances.[174] Consequently, to achieve precise control of PLAL nanomaterials, it is essential to improve productivity across different pulse width regimes and not settle for high production solely with picosecond pulses. Furthermore, it should be noted that extreme pulse durations in the attosecond range have yet to be utilized for generating nanoparticles in PLAL.

• The utilization of temporal pulse tailoring strategies. The ability to manipulate the temporal profile of the laser pulse enables the energy rate to be tailored to the specific material reaction. Although various techniques have been used for temporal beam manipulation, such as double-pulse laser irradiation,[147,182,183] or irradiation with a burst of pulses,[184] there is still room for improvement to maximize productivity. Some of these techniques require further study, while others can be introduced for the first time in PLAL, such as the conformation of the temporal pulse envelope of ultrashort pulses.

• To use fluid mechanics simulations (CFD) to optimize the nanomaterial ablation. Although different strategies related to fluid dynamics have been developed to increase production rate, as explained in the variations of the ablation chamber (4.7. Optimizing the ablation chamber design), there is still room for improvement. In this direction, CFD simulations can help to optimize not only the chamber geometry but also the control of turbulence, bubble removal, reduction of areas of nanoparticle accumulation, and selection of suitable liquids based on viscosity, density, and refractive index, among others.

• The implementation of smart beam delivery optical systems for controlling pulse the spatial distribution of the energy over a target. Galvanometric scanners and polygonal wheels are commonly used for beam delivery in PLAL. However, the focal length of these setups is typically fixed, and this determines key parameters, such as the numerical aperture, the fluence, and the spot size that constrains the flexibility of the ablation processes. Therefore, some flexibility in the beam delivery must be considered for further improvements in productivity. Our recommendation is to integrate advanced smart beam delivery devices, such as the SSTF system that mitigates non-linearities, into high-speed scanners. Additionally, dynamic (spatial light modulators) or static (diffractive optical elements or freeform optics) beam-shaping elements can be utilized. Given that the current high-power laser used in PLAL exceeds the required optimum energy for laser ablation by several orders of magnitude, parallel processing presents an efficient alternative to reduce processing time.[185] Furthermore, different spatial profiles at the focus can be designed[186] to study how they affect the laser-matter interaction and influence the ablated mass. Finally, it is crucial for the PLAL scientific community to keep abreast of the research that emerged in the last few years regarding the use of smart beam delivery systems for focusing through turbid media,[187] as some of the devices developed for other disciplines may be adapted for its use in PLAL.

• Artificial intelligence (AI) has the potential to enhance productivity by optimizing the various parameters involved in the PLAL process. Through the analysis of vast amounts of data on target material properties, laser parameters, and liquid media, AI algorithms can identify optimal conditions for nanoparticle synthesis, resulting in a more efficient, reproducible, and productive PLAL process. Moreover, this advanced knowledge of the optimal PLAL conditions can facilitate the rapid scaling-up of production by minimizing trial-and-error experimentation and will help to generate large-scale production to meet the market demands.

• Although laser power and repetition rates have been increasing, scanner technology remains a bottleneck in achieving high ablation rates. Therefore, there is a need for improvements in the current laser and scanning technology. All the improvements in the laser technology or the high-speed scanning systems will have a direct impact on PLAL productivity.

To conclude, as the global population continues to increase alongside its corresponding demands, the imperative for more efficient methods to synthesize nanomaterials will undoubtedly intensify. In this regard, PLAL has emerged as a promising approach with a myriad of applications, supported by a large community of researchers who are actively pursuing the development of eco-friendly technology. Continuously striving to enhance PLAL productivity represents a crucial endeavor, as it has the potential to make the green fabrication of nanomaterials more affordable and accessible to a wider range of consumers, researchers, and industries. Moreover, such advancements will undoubtedly broaden the horizons of its potential applications.

Author contributions

Writing – original draft I. Y. K., C. D.-B., G. M.-V; writing – review & editing I. Y. K, C. D.-B., G. M.-V, B. G; visualization I. Y. K, C. D.-B; supervision C. D.-B, B. G.; project administration C. D.-B, B. G.; funding acquisition C. D.-B, B. G.

Conflicts of interest

There are no conflicts to declare.

Acknowledgements

The authors acknowledge funding by the Deutsche Forschungsgemeinschaft (DFG, German Research Foundation), grant numbers GO 2566/10-1 and GO 2566/14-1, and the European Union's Horizon 2020 research and innovation program under the grant agreement No. 952068 (project LESGO).

References

1 L. Kool, F. Dekker, A. Bunschoten, G. J. Smales, B. R. Pauw, A. H. Velders and V. Saggiomo, Gold and silver dichroic nanocomposite in the quest for 3D printing the Lycurgus cup, *Beilstein J. Nanotechnol.*, 2020, **11**, 16–23, DOI: 10.3762/bjnano.11.2.

2 I. Freestone, N. Meeks, M. Sax and C. Higgitt, The Lycurgus Cup—A Roman nanotechnology, *Gold Bull.*, 2007, **40**(4), 270–277, DOI: 10.1007/BF03215599.

3 A. K. Gupta and M. Gupta, Synthesis and surface engineering of iron oxide nanoparticles for biomedical applications, *Biomaterials*, 2005, **26**(18), 3995–4021, DOI: 10.1016/j.biomaterials.2004.10.012.

4 Q. A. Pankhurst, J. Connolly, S. K. Jones and J. Dobson, Applications of magnetic nanoparticles in biomedicine, *J. Phys. D: Appl. Phys.*, 2003, **36**(13), R167–R181, DOI: 10.1088/0022-3727/36/13/201.

5 D. A. Giljohann, D. S. Seferos, W. L. Daniel, M. D. Massich, P. C. Patel and C. A. Mirkin, Gold nanoparticles for biology and medicine, *Angew. Chem., Int. Ed.*, 2010, **49**(19), 3280–3294, DOI: 10.1002/anie.200904359.

6 R. Pérez-Tanoira, M. Fernández-Arias, C. Potel, R. Carballo-Fernández, S. Pérez-Castro, M. Boutinguiza, M. Górgolas, F. Lusquiños and J. Pou, Silver Nanoparticles Produced by Laser Ablation and Re-Irradiation Are Effective Preventing Peri-Implantitis Multispecies Biofilm Formation, *Int. J. Mol. Sci.*, 2022, **23**(19), 12027, DOI: 10.3390/ijms231912027.

7 Y. Liang, Y. Li, H. Wang, J. Zhou, J. Wang, T. Regier and H. Dai, Co_3O_4 nanocrystals on graphene as a synergistic catalyst for oxygen reduction reaction, *Nat. Mater.*, 2011, **10**(10), 780–786, DOI: 10.1038/nmat3087.

8 Y. Li, H. Wang, L. Xie, Y. Liang, G. Hong and H. Dai, MoS 2 Nanoparticles Grown on Graphene: An Advanced Catalyst for the Hydrogen Evolution Reaction, *J. Am. Chem. Soc.*, 2011, **133**(19), 7296–7299, DOI: 10.1021/ja201269b.

9 Q. Xiang, J. Yu and M. Jaroniec, Synergetic Effect of MoS_2 and Graphene as Cocatalysts for Enhanced Photocatalytic H_2 Production Activity of TiO_2 Nanoparticles, *J. Am. Chem. Soc.*, 2012, **134**(15), 6575–6578, DOI: 10.1021/ja302846n.

10 J. Theerthagiri, K. Karuppasamy, A. Min, D. Govindarajan, M. L. A. Kumari, G. Muthusamy, S. Kheawhom, H. S. Kim and M. Y. Choi, Unraveling the fundamentals of pulsed laser-assisted synthesis of nanomaterials in liquids: applications in energy and the environment, *Appl. Phys. Rev.*, 2022, **9**(4), 041314, DOI: 10.1063/5.0104740.

11 J. Theerthagiri, K. Karuppasamy, S. J. Lee, R. Shwetharani, H. S. Kim, S. K. K. Pasha, M. Ashokkumar and M. Y. Choi, Fundamentals and comprehensive insights on pulsed laser synthesis of advanced materials for diverse photo- and electrocatalytic applications, *Light: Sci. Appl.*, 2022, **11**(1), 250, DOI: 10.1038/s41377-022-00904-7.

12 S. Naik Shreyanka, J. Theerthagiri, S. J. Lee, Y. Yu and M. Y. Choi, Multiscale design of 3D metal–organic frameworks (M−BTC, M: Cu, Co, Ni) via PLAL enabling bifunctional electrocatalysts for robust overall water splitting, *Chem. Eng. J.*, 2022, **446**, 137045, DOI: 10.1016/j.cej.2022.137045.

13 R. Torres-Mendieta, R. Mondragón, V. Puerto-Belda, O. Mendoza-Yero, J. Lancis, J. E. Juliá and G. Mínguez-Vega, Characterization of Tin/Ethylene Glycol Solar Nanofluids Synthesized by Femtosecond Laser Radiation, *ChemPhysChem*, 2017, **18**(9), 1055–1060, DOI: 10.1002/cphc.201601083.

14 M. B. Wilms, N. Pirch and B. Gökce, Manufacturing oxide-dispersion-strengthened steels using the advanced directed energy deposition process of high-speed laser cladding, *Prog. Addit. Manuf.*, 2022, 0123456789, DOI: 10.1007/s40964-022-00319-1.

15 C. Doñate-Buendía, D. Gu, M. Schmidt, S. Barcikowski, A. M. Korsunsky and B. Gökce, On the selection and design of powder materials for laser additive manufacturing, *Mater. Des.*, 2021, **204**, 109653, DOI: 10.1016/j.matdes.2021.109653.

16 M. J. Hajipour, K. M. Fromm, A. Akbar Ashkarran, D. Jimenez de Aberasturi, I. R. Larramendi, T. Rojo, V. Serpooshan, W. J. Parak and M. Mahmoudi, Antibacterial properties of nanoparticles, *Trends Biotechnol.*, 2012, **30**(10), 499–511, DOI: 10.1016/j.tibtech.2012.06.004.

17 A. Sirelkhatim, S. Mahmud, A. Seeni, N. H. A. Kaus, L. C. Ann, S. K. H. Bakhori, H. Hasan and D. Mohamad, Review on zinc oxide nanoparticles: antibacterial activity and toxicity mechanism, *Nano-Micro Lett.*, 2015, **7**(3), 219–242, DOI: 10.1007/s40820-015-0040-x.

18 A. Jain, L. S. Duvvuri, S. Farah, N. Beyth, A. J. Domb and W. Khan, Antimicrobial Polymers, *Adv. Healthcare Mater.*, 2014, **3**(12), 1969–1985, DOI: 10.1002/adhm.201400418.

19 G. A. Lopez, M. C. Estevez, M. Soler and L. M. Lechuga, Recent advances in nanoplasmonic biosensors: applications and lab-on-a-chip integration, *Nanophotonics*, 2017, **6**(1), 123–136, DOI: 10.1515/nanoph-2016-0101.

20 K. Ai, B. Zhang and L. Lu, Europium-Based Fluorescence Nanoparticle Sensor for Rapid and Ultrasensitive Detection of an Anthrax Biomarker, *Angew. Chemie*, 2009, **121**(2), 310–314, DOI: 10.1002/ange.200804231.

21 Y. Wang, H. Zhang, Y. Zhu, Z. Dai, H. Bao, Y. Wei and W. Cai, Au-NP-Decorated Crystalline FeOCl Nanosheet: Facile Synthesis by Laser Ablation in Liquid and its Exclusive Gas Sensing Response to HCl at Room Temperature, *Adv. Mater. Interfaces*, 2016, **3**(9), 1500801, DOI: 10.1002/admi.201500801.

22 R. Torres-Mendieta, D. Ventura-Espinosa, S. Sabater, J. Lancis, G. Mínguez-Vega and J. A. Mata, In situ decoration of graphene sheets with gold nanoparticles synthetized by pulsed laser ablation in liquids, *Sci. Rep.*, 2016, **6**, 1–9, DOI: 10.1038/srep30478.

23 T. Kim, S. Kang, J. Heo, S. Cho, J. W. Kim, A. Choe, B. Walker, R. Shanker, H. Ko and J. Y. Kim, Nanoparticle-Enhanced Silver-Nanowire Plasmonic Electrodes for High-Performance Organic Optoelectronic Devices, *Adv. Mater.*, 2018, **30**(28), 1800659, DOI: 10.1002/adma.201800659.

24 H. Choi, S. -J. Ko, Y. Choi, P. Joo, T. Kim, B. R. Lee, J. -W. Jung, H. J. Choi, M. Cha, J. -R. Jeong, I. -W. Hwang,

M. H. Song, B. -S. Kim and J. Y. Kim, Versatile surface plasmon resonance of carbon-dot-supported silver nanoparticles in polymer optoelectronic devices, *Nat. Photonics*, 2013, **7**(9), 732–738, DOI: **10.1038/nphoton.2013.181**.

25 N. Baig, I. Kammakakam, W. Falath and I. Kammakakam, Nanomaterials: a review of synthesis methods, properties, recent progress, and challenges, *Mater. Adv.*, 2021, **2**(6), 1821–1871, DOI: **10.1039/D0MA00807A**.

26 M. N. R. Ashfold, F. Claeyssens, G. M. Fuge and S. J. Henley, Pulsed laser ablation and deposition of thin films, *Chem. Soc. Rev.*, 2004, **33**(1), 23, DOI: **10.1039/b207644f**.

27 S. V. Starinskiy, Y. G. Shukhov and A. V. Bulgakov, Dynamics of pulsed laser ablation of gold in vacuum in the regime of nanostructured film synthesis, *Tech. Phys. Lett.*, 2016, **42**(4), 411–414, DOI: **10.1134/S1063785016040258**.

28 Z. Lin, S. Shen, Z. Wang and W. Zhong, Laser ablation in air and its application in catalytic water splitting and Li-ion battery, *iScience*, 2021, **24**(5), 102469, DOI: **10.1016/j.isci.2021.102469**.

29 D. Zhang, Z. Li and K. Sugioka, Laser ablation in liquids for nanomaterial synthesis: diversities of targets and liquids, *JPhys Photonics*, 2021, **3**(4), 1–35, DOI: **10.1088/2515-7647/ac0bfd**.

30 P. P. Patil, D. M. Phase, S. A. Kulkarni, S. V. Ghaisas, S. K. Kulkarni, S. M. Kanetkar, S. B. Ogale and V. G. Bhide, Pulsed-laser – induced reactive quenching at liquid–solid interface: aqueous oxidation of iron, *Phys. Rev. Lett.*, 1987, **58**(3), 238–241, DOI: **10.1103/PhysRevLett.58.238**.

31 A. Fojtik and A. Henglein, Laser ablation of films and suspended particles in a solvent: formation of cluster and colloid solutions, *Berichte der Bunsen-Gesellschaft*, 1993, **97**(2), 252–254.

32 A. Henglein, Physicochemical properties of small metal particles in solution: 'microelectrode' reactions, chemisorption, composite metal particles, and the atom-to-metal transition, *J. Phys. Chem.*, 1993, **97**(21), 5457–5471, DOI: **10.1021/j100123a004**.

33 D. Zhang, B. Gökce and S. Barcikowski, Laser Synthesis and Processing of Colloids: Fundamentals and Applications, *Chem. Rev.*, 2017, **117**(5), 3990–4103, DOI: **10.1021/acs.chemrev.6b00468**.

34 B. Gökce, V. Amendola and S. Barcikowski, Opportunities and Challenges for Laser Synthesis of Colloids, *ChemPhysChem*, 2017, **18**(9), 983–985, DOI: **10.1002/cphc.201700310**.

35 E. Fazio, B. Gökce, A. De Giacomo, M. Meneghetti, G. Compagnini, M. Tommasini, F. Waag, A. Lucotti, C. G. Zanchi, P. M. Ossi, M. Dell'Aglio, L. D'Urso, M. Condorelli, V. Scardaci, F. Biscaglia, L. Litti, M. Gobbo, G. Gallo, M. Santoro, S. Trusso and F. Neri, Nanoparticles Engineering by Pulsed Laser Ablation in Liquids: Concepts and Applications, *Nanomaterials*, 2020, **10**(11), 2317, DOI: **10.3390/nano10112317**.

36 M. Alheshibri, S. Akhtar, A. Al Baroot, K. A. Elsayed, H. S. Al Qahtani and Q. A. A. Drmosh, Template-free single-step preparation of hollow CoO nanospheres using pulsed laser ablation in liquid enviroment, *Arab. J. Chem.*, 2021, **14**(9), 103317, DOI: **10.1016/j.arabjc.2021.103317**.

37 H. S. Desarkar, P. Kumbhakar and A. K. Mitra, One-step synthesis of Zn/ZnO hollow nanoparticles by the laser ablation in liquid technique, *Laser Phys. Lett.*, 2013, **10**(5), 055903, DOI: **10.1088/1612-2011/10/5/055903**.

38 A. Tymoczko, M. Kamp, C. Rehbock, L. Kienle, E. Cattaruzza, S. Barcikowski and V. Amendola, One-step synthesis of Fe–Au core–shell magnetic-plasmonic nanoparticles driven by interface energy minimization, *Nanoscale Horiz.*, 2019, **4**(6), 1326–1332, DOI: **10.1039/c9nh00332k**.

39 I. Y. Khairani, Q. Lin, J. Landers, S. Salamon, C. Doñate-Buendía, E. Karapetrova, H. Wende, G. Zangari and B. Gökce, Solvent Influence on the Magnetization and Phase of Fe–Ni Alloy Nanoparticles Generated by Laser Ablation in Liquids, *Nanomaterials*, 2023, **13**(2), 227, DOI: **10.3390/nano13020227**.

40 Y. Jia, T. -Y. Sun, J. -H. Wang, H. Huang, P. Li, X. -F. Yu and P. K. Chu, Synthesis of hollow rare-earth compound nanoparticles by a universal sacrificial template method, *CrystEngComm*, 2014, **16**(27), 6141–6148, DOI: **10.1039/C4CE00440J**.

41 J. Zeng, J. Huang, W. Lu, X. Wang, B. Wang, S. Zhang and J. Hou, Necklace-like Noble-Metal Hollow Nanoparticle Chains: Synthesis and Tunable Optical Properties, *Adv. Mater.*, 2007, **19**(16), 2172–2176, DOI: **10.1002/adma.200602440**.

42 P. Anastas and N. Eghbali, Green Chemistry: Principles and Practice, *Chem. Soc. Rev.*, 2010, **39**(1), 301–312, DOI: **10.1039/b918763b**.

43 A. N. Arifiadi, K.-T. Kim, I. Y. Khairani, C. B. Park, K. H. Kim and S.-K. Kim, Synthesis and multiferroic properties of high-purity $CoFe_2O_4$–$BiFeO_3$ nanocomposites, *J. Alloys Compd.*, 2021, **867**, 159008, DOI: **10.1016/j.jallcom.2021.159008**.

44 I. Y. Khairani, A. N. Arifiadi, J.-H. Lee, B. Bhoi, S. K. S. Patel and S. Kim, Fabrication, Structure, and Magnetic Properties of Pure-Phase $BiFeO_3$ and $MnFe_2O_4$ Nanoparticles and their Nanocomposites, *J. Magn.*, 2020, **25**(2), 140–149, DOI: **10.4283/JMAG.2020.25.2.140**.

45 I. Kartini, I. Y. Khairani, C. Chotimah, S. Mustofa, S. J. Santosa and L. Z. Wang, The effect of alkaline ratios of NaOH to NH_3 on the formation of nanostructured titania, *Mater. Sci. Forum*, 2017, **886**, 42–47, DOI: **10.4028/www.scientific.net/MSF.886.42**.

46 A. V. Shabalina, V. A. Svetlichnyi and S. A. Kulinich, Green laser ablation-based synthesis of functional nanomaterials for generation, storage, and detection of hydrogen, *Curr. Opin. Green Sustainable Chem.*, 2022, **33**, 100566, DOI: **10.1016/j.cogsc.2021.100566**.

47 V. Amendola, D. Amans, Y. Ishikawa, N. Koshizaki, S. Scirè, G. Compagnini, S. Reichenberger and S. Barcikowski, Room-Temperature Laser Synthesis in Liquid of Oxide, Metal-Oxide Core–Shells, and Doped Oxide Nanoparticles, *Chem. – Eur. J.*, 2020, **26**(42), 9206–9242, DOI: **10.1002/chem.202000686**.

48 T. Schmitz, U. Wiedwald, C. Dubs and B. Gökce, Ultrasmall Yttrium Iron Garnet Nanoparticles with High Coercivity at Low Temperature Synthesized by Laser Ablation and Fragmentation of Pressed Powders, *ChemPhysChem*, 2017, **18**(9), 1125–1132, DOI: 10.1002/cphc.201601183.

49 A. Chemin, J. Lam, G. Laurens, F. Trichard, V. Motto-Ros, G. Ledoux, V. Jarý, V. Laguta, M. Nikl, C. Dujardin and D. Amans, Doping nanoparticles using pulsed laser ablation in a liquid containing the doping agent, *Nanoscale Adv.*, 2019, **1**(10), 3963–3972, DOI: 10.1039/c9na00223e.

50 S. Jendrzej, B. Gökce, M. Epple and S. Barcikowski, How Size Determines the Value of Gold: Economic Aspects of Wet Chemical and Laser-Based Metal Colloid Synthesis, *ChemPhysChem*, 2017, **18**(9), 1012–1019, DOI: 10.1002/cphc.201601139.

51 J. Park, K. An, Y. Hwang, J. Park, H Noh, J Kim, J Park, N Hwang and T Hyeon, Ultra-large-scale syntheses of monodisperse nanocrystals, *Nat. Mater*, 2004, **3**, 891–895, DOI: 10.1038/nmat1251.

52 R. Streubel, G. Bendt and B. Gökce, Pilot-scale synthesis of metal nanoparticles by high-speed pulsed laser ablation in liquids, *Nanotechnology*, 2016, **27**(20), 205602, DOI: 10.1088/0957-4484/27/20/205602.

53 C. L. Sajti, R. Sattari, B. N. Chichkov and S. Barcikowski, Gram Scale Synthesis of Pure Ceramic Nanoparticles by Laser Ablation in Liquid, *J. Phys. Chem. C*, 2010, **114**(6), 2421–2427, DOI: 10.1021/jp906960g.

54 F. Waag, R. Streubel, B. Gökce and S. Barcikowski, Synthesis of gold, platinum, and gold-platinum alloy nanoparticle colloids with high-power megahertz-repetition-rate lasers: the importance of the beam guidance method, *Appl. Nanosci.*, 2021, **11**(4), 1303–1312, DOI: 10.1007/s13204-021-01693-y.

55 B. Barcikowski, S. Amendola, V. Lau, M. Marzun, G. Rehbock, C. Reichenberger, S. Zhang and D. Gökce, *Handbook of Laser Synthesis & Processing of Colloids*, Duisburg-Essen Publication Online, Second edn, 2019.

56 N. L. Lahaye, S. S. Harilal, P. K. Diwakar and A. Hassanein, The effect of laser pulse duration on ICP-MS signal intensity, elemental fractionation, and detection limits in fs-LA-ICP-MS, *J. Anal. At. Spectrom.*, 2013, **28**(11), 1781–1787, DOI: 10.1039/c3ja50200g.

57 K. Chaudhary, S. Z. H. Rizvi and J. Ali, Laser-Induced Plasma and its Applications, *Plasma Science and Technology - Progress in Physical States and Chemical Reactions*, InTech, 2016.

58 C. Y. Shih, R. Streubel, J. Heberle, A. Letzel, M. V. Shugaev, C. Wu, M. Schmidt, B. Gökce, S. Barcikowski and L. V. Zhigilei, Two mechanisms of nanoparticle generation in picosecond laser ablation in liquids: the origin of the bimodal size distribution, *Nanoscale*, 2018, **10**(15), 6900–6910, DOI: 10.1039/c7nr08614h.

59 X. Li and Y. Guan, Theoretical fundamentals of short pulse laser-metal interaction: a review, *Nami Jishu Yu Jingmi Gongcheng*, 2020, **3**(3), 105–125, DOI: 10.1016/j.npe.2020.08.001.

60 M. Dell'Aglio, R. Gaudiuso, O. De Pascale and A. De Giacomo, Mechanisms and processes of pulsed laser ablation in liquids during nanoparticle production, *Appl. Surf. Sci.*, 2015, **348**, 4–9, DOI: 10.1016/j.apsusc.2015.01.082.

61 A. Kanitz, M. R. Kalus, E. L. Gurevich, A. Ostendorf, S. Barcikowski and D. Amans, Review on experimental and theoretical investigations of the early stage, femtoseconds to microseconds processes during laser ablation in liquid-phase for the synthesis of colloidal nanoparticles, *Plasma Sources Sci. Technol.*, 2019, **28**(10), 103001, DOI: 10.1088/1361-6595/ab3dbe.

62 J. Long, M. Eliceiri, Z. Vangelatos, Y. Rho, L. Wang, Z. Shu, X. Xie, Y. Zhang and C. P. Grigoropoulos, Early dynamics of cavitation bubbles generated during ns laser ablation of submerged targets, *Opt. Express*, 2020, **28**(10), 14300, DOI: 10.1364/oe.391584.

63 C.-Y. Shih, C. Wu, M. V. Shugaev and L. V. Zhigilei, Atomistic modeling of nanoparticle generation in short pulse laser ablation of thin metal films in water, *J. Colloid Interface Sci.*, 2017, **489**, 3–17, DOI: 10.1016/j.jcis.2016.10.029.

64 S. Jendrzej, B. Gökce, V. Amendola and S. Barcikowski, Barrierless growth of precursor-free, ultrafast laser-fragmented noble metal nanoparticles by colloidal atom clusters – A kinetic in situ study, *J. Colloid Interface Sci.*, 2016, **463**, 299–307, DOI: 10.1016/j.jcis.2015.10.032.

65 S. Ibrahimkutty, P. Wagener, T. D. S. Rolo, D. Karpov, A. Menzel, T. Baumbach, S. Barcikowski and A. Plech, A hierarchical view on material formation during pulsed-laser synthesis of nanoparticles in liquid, *Sci. Rep.*, 2015, **5**(1), 16313, DOI: 10.1038/srep16313.

66 A. Hamad, L. Li and Z. Liu, A comparison of the characteristics of nanosecond, picosecond and femtosecond lasers generated Ag, TiO_2 and Au nanoparticles in deionised water, *Appl. Phys. A: Mater. Sci. Process.*, 2015, **120**(4), 1247–1260, DOI: 10.1007/s00339-015-9326-6.

67 V. Amendola, D. Amans, Y. Ishikawa, N. Koshizaki, S. Scirè, G. Compagnini, S. Reichenberger and S. Barcikowski, Room-Temperature Laser Synthesis in Liquid of Oxide, Metal-Oxide Core–Shells, and Doped Oxide Nanoparticles, *Chem. – Eur. J.*, 2020, **26**(42), 9206–9242, DOI: 10.1002/chem.202000686.

68 C. Y. Shih, M. V. Shugaev, C. Wu and L. V. Zhigilei, The effect of pulse duration on nanoparticle generation in pulsed laser ablation in liquids: insights from large-scale atomistic simulations, *Phys. Chem. Chem. Phys.*, 2020, **22**(13), 7077–7099, DOI: 10.1039/d0cp00608d.

69 S. Shankar Naik, J. Theerthagiri, F. S. Nogueira, S. J. Lee, A. Min, G. A. Kim, G. Maia, L. M. C. Pinto and M. Y. Choi, Dual-Cation-Coordinated CoFe-Layered Double-Hydroxide Nanosheets Using the Pulsed Laser Ablation Technique for Efficient Electrochemical Water Splitting: Mechanistic Screening by In Situ/Operando Raman and Density Functional Theory Calculations, *ACS Catal.*, 2023, **13**(2), 1477–1491, DOI: 10.1021/acscatal.2c05017.

70 R. C. Forsythe, C. P. Cox, M. K. Wilsey and A. M. Müller, Pulsed Laser in Liquids Made Nanomaterials for Catalysis, *Chem. Rev.*, 2021, **121**(13), 7568–7637, DOI: 10.1021/acs.chemrev.0c01069.

71 S. A. Yehia, L.G. Carpen, F. Stokker-Cheregi, C. Poronicu, V. Sătulu, C. Staicu, B. Butoi, I. Lungu, F. Virot, C. Grisolia and G. Dinescu, Laser ablation of a solid target in liquid medium for beryllium nanoparticles synthesis, *Nucl. Mater. Energy*, 2022, **31**, 101160, DOI: 10.1016/j.nme.2022.101160.

72 S. N. Sanders, T. H. Schloemer, M. K. Gangishetty, D. Anderson, M. Seitz, A. O. Gallegos, R. C. Stokes and D. N. Congreve, Triplet fusion upconversion nanocapsules for volumetric 3D printing, *Nature*, 2022, **604**(7906), 474–478, DOI: 10.1038/s41586-022-04485-8.

73 H. Zeng, X. -W. Du, S. C. Singh, S. A. Kulinich, S. Yang, J. He and W. Cai, Nanomaterials via laser ablation/irradiation in liquid: a review, *Adv. Funct. Mater.*, 2012, **22**(7), 1333–1353, DOI: 10.1002/adfm.201102295.

74 R. Streubel, S. Barcikowski and B. Gökce, Continuous multigram nanoparticle synthesis by high-power, high-repetition-rate ultrafast laser ablation in liquids, *Opt. Lett.*, 2016, **41**(7), 1486, DOI: 10.1364/OL.41.001486.

75 F. Waag, B. Gökce and S. Barcikowski, Ablation target cooling by maximizing the nanoparticle productivity in laser synthesis of colloids, *Appl. Surf. Sci.*, 2019, **466**, 647–656, DOI: 10.1016/j.apsusc.2018.10.030.

76 S. Dittrich, S. Barcikowski and B. Gökce, Plasma and nanoparticle shielding during pulsed laser ablation in liquids cause ablation efficiency decrease, *Opto-Electron. Adv.*, 2021, **4**(1), 1–13, DOI: 10.29026/oea.2021.200072.

77 W. Haiss, N. T. K. Thanh, J. Aveyard and D. G. Fernig, Determination of Size and Concentration of Gold Nanoparticles from UV-Vis Spectra, *Anal. Chem.*, 2007, **79**(11), 4215–4221, DOI: 10.1021/ac0702084.

78 T. Hendel, M. Wuithschick, F. Kettemann, A. Birnbaum, K. Rademann and J. Polte, In situ determination of colloidal gold concentrations with UV-vis spectroscopy: limitations and perspectives, *Anal. Chem.*, 2014, **86**(22), 11115–11124, DOI: 10.1021/ac502053s.

79 J. Katyal and R. K. Soni, Size- and shape-dependent plasmonic properties of aluminum nanoparticles for nanosensing applications, *J. Mod. Opt.*, 2013, **60**(20), 1717–1728, DOI: 10.1080/09500340.2013.856483.

80 X. Liu, M. Atwater, J. Wang and Q. Huo, Extinction coefficient of gold nanoparticles with different sizes and different capping ligands, *Colloids Surf., B*, 2007, **58**(1), 3–7, DOI: 10.1016/j.colsurfb.2006.08.005.

81 S. P. Yeap, J. K. Lim, B. S. Ooi and A. L. Ahmad, Agglomeration, colloidal stability, and magnetic separation of magnetic nanoparticles: collective influences on environmental engineering applications, *J. Nanopart. Res.*, 2017, **19**(11), 368, DOI: 10.1007/s11051-017-4065-6.

82 P. L. Golas, S. Louie, G. V. Lowry, K. Matyjaszewski and R. D. Tilton, Comparative Study of Polymeric Stabilizers for Magnetite Nanoparticles Using ATRP, *Langmuir*, 2010, **26**(22), 16890–16900, DOI: 10.1021/la103098q.

83 T. Phenrat, N. Saleh, K. Sirk, R. D. Tilton and G. V. Lowry, Aggregation and Sedimentation of Aqueous Nanoscale Zerovalent Iron Dispersions, *Environ. Sci. Technol.*, 2007, **41**(1), 284–290, DOI: 10.1021/es061349a.

84 S. Reich, Patrick Schönfeld, P. Wagener, A. Letzel, S. Ibrahimkutty, B. Gökce, S. Barcikowski, A. Menzel, T. D. S. Rolo and A. Plech, Pulsed laser ablation in liquids: impact of the bubble dynamics on particle formation, *J. Colloid Interface Sci.*, 2017, **489**, 106–113, DOI: 10.1016/j.jcis.2016.08.030.

85 S. Dittrich, R. Streubel, C. McDonnell, H. P. Huber, S. Barcikowski and B. Gökce, Comparison of the productivity and ablation efficiency of different laser classes for laser ablation of gold in water and air, *Appl. Phys. A: Mater. Sci. Process.*, 2019, **125**(6), 1–10, DOI: 10.1007/s00339-019-2704-8.

86 M. R. Kalus, R. Lanyumba, N. Lorenzo-Parodi, M. A. Jochmann, K. Kerpen, U. Hagemann, T. C. Schmidt, S. Barcikowski and B. Gökce, Determining the role of redox-active materials during laser-induced water decomposition, *Phys. Chem. Chem. Phys.*, 2019, **21**(34), 18636–18651, DOI: 10.1039/c9cp02663k.

87 A. Resano-Garcia, S. Champmartin, Y. Battie, A. Koch, A. En Naciri, A. Ambari and N. Chaoui, Highly-repeatable generation of very small nanoparticles by pulsed-laser ablation in liquids of a high-speed rotating target, *Phys. Chem. Chem. Phys.*, 2016, **18**(48), 32868–32875, DOI: 10.1039/c6cp06511b.

88 S. Kohsakowski, A. Santagata, A. Dell'Aglio, A. de Giacomo, S. Barcikowski, P. Wagener and B. Gökce, High productive and continuous nanoparticle fabrication by laser ablation of a wire-target in a liquid jet, *Appl. Surf. Sci.*, 2017, **403**, 487–499, DOI: 10.1016/j.apsusc.2017.01.077.

89 G. C. Messina, P. Wagener, R. Streubel, A. De Giacomo, A. Santagata, G. Compagnini and S. Barcikowski, Pulsed laser ablation of a continuously-fed wire in liquid flow for high-yield production of silver nanoparticles, *Phys. Chem. Chem. Phys.*, 2013, **15**(9), 3093–3098, DOI: 10.1039/c2cp42626a.

90 P. Wagener, A. Schwenke, B. N. Chichkov and S. Barcikowski, Pulsed laser ablation of zinc in tetrahydrofuran: bypassing the cavitation bubble, *J. Phys. Chem. C*, 2010, **114**(17), 7618–7625, DOI: 10.1021/jp911243a.

91 Y. Monsa, G. Gal, N. Lerner and I. Bar, A simple strategy for enhanced production of nanoparticles by laser ablation in liquids, *Nanotechnology*, 2020, **31**(23), 235601, DOI: 10.1088/1361-6528/ab78ac.

92 P. F. S. Pereira, A. C. A. de Paula e Silva, B. N. A. da Silva Pimentel, I. M. Pinatti, A. Z. Simões, C. E. Vergani, D. F. Barreto-Vieira, M. A. N. da Silva, M. D. Miranda, M. E. S. Monteiro, A. Tucci, C. Doñate-Buendía, G. Mínguez-Vega, J. Andrés and E. Longo, Inactivation of SARS-CoV-2 by a chitosan/α-Ag_2WO_4 composite generated by femtosecond laser irradiation, *Sci. Rep.*, 2022, **12**(1), 8118, DOI: 10.1038/s41598-022-11902-5.

93 J. G. Cuadra, S. Molina-Prados, G. Mínguez-Vega, Ana. C. Estrada, T. Trindade, C. Oliveira, M. P. Seabra, J. Labrincha, S. Porcar, R. Cadena, D. Fraga and J. B. Carda, Multifunctional Silver-Coated Transparent TiO_2 Thin Films for Photocatalytic and Antimicrobial Applications, *Appl. Surf. Sci.*, 2023, **617**, 156519, DOI: 10.1016/j.apsusc.2023.156519.

94 C. Doñate-Buendia, R. Torres-Mendieta, A. Pyatenko, E. Falomir, M. Fernández-Alonso and G. Mínguez-Vega, Fabrication by Laser Irradiation in a Continuous Flow Jet of Carbon Quantum Dots for Fluorescence Imaging, *ACS Omega*, 2018, **3**(3), 2735–2742, DOI: 10.1021/acsomega.7b02082.

95 T. Hupfeld, A. Wegner, M. Blanke, C. Doñate-Buendía, V. Sharov, S. Nieskens, M. Piechotta, M. Giese, S. Barcikowski and B. Gökce, Plasmonic Seasoning: Giving Color to Desktop Laser 3D Printed Polymers by Highly Dispersed Nanoparticles, *Adv. Opt. Mater.*, 2020, **8**(15), 2000473, DOI: 10.1002/adom.202000473.

96 K. Sugioka and Y. Cheng, Ultrafast lasers-reliable tools for advanced materials processing, *Light: Sci. Appl.*, 2014, **3**(390), 1–12, DOI: 10.1038/lsa.2014.30.

97 S. I. Kudryashov, A. A. Nastulyavichus, A. K. Ivanova, N. A. Smirnov, R. A. Khmelnitskiy, A. A. Rudenko, I. N. Saraeva, E. R. Tolordava, A. Yu. Kharin, I. N. Zavestovskaya, Y. M. Romanova, D. A. Zayarny and A. A. Ionin, High-throughput laser generation of Si-nanoparticle based surface coatings for antibacterial applications, *Appl. Surf. Sci.*, 2019, **470**, 825–831, DOI: 10.1016/j.apsusc.2018.11.201.

98 A. Menéndez-Manjón, P. Wagener and S. Barcikowski, Transfer-matrix method for efficient ablation by pulsed laser ablation and nanoparticle generation in liquids, *J. Phys. Chem. C*, 2011, **115**(12), 5108–5114, DOI: 10.1021/jp109370q.

99 C. Doñate-Buendía, M. Fernández-Alonso, J. Lancis and G. Mínguez-Vega, Overcoming the barrier of nanoparticle production by femtosecond laser ablation in liquids using simultaneous spatial and temporal focusing, *Photonics Res.*, 2019, **7**(11), 1249, DOI: 10.1364/PRJ.7.001249.

100 S. Kohsakowski, B. Gökce, R. Tanabe, P. Wagener, A. Plech, Y. Ito and S. Barcikowski, Target geometry and rigidity determines laser-induced cavitation bubble transport and nanoparticle productivity-a high-speed videography study, *Phys. Chem. Chem. Phys.*, 2016, **18**(24), 16585–16593, DOI: 10.1039/c6cp01232a.

101 B. N. Chichkov, C. Momma, S. Nolte, F. Alvensleben and A. Tünnermann, Femtosecond, picosecond and nanosecond laser ablation of solids, *Appl. Phys. A: Mater. Sci. Process.*, 1996, **63**(2), 109–115, DOI: 10.1007/BF01567637.

102 S. Nolte, C. Momma, H. Jacobs, A. Tünnermann, B. N. Chichkov, B. Wellegehausen and H. Welling, Ablation of metals by ultrashort laser pulses, *J. Opt. Soc. Am. B*, 1997, **14**(10), 2716–2722, DOI: 10.1364/JOSAB.14.002716.

103 S. Preuss, A. Demchuk and M. Stuke, Sub-picosecond UV laser ablation of metals, *Appl. Phys. A: Mater. Sci. Process.*, 1995, **61**(1), 33–37, DOI: 10.1007/BF01538207.

104 G. Račiukaitis, M. Brikas, P. Gečys, B. Voisiat and M. Gedvilas, Use of high repetition rate and high power lasers in microfabrication: How to keep the efficiency high?, *J. Laser Micro Nanoeng.*, 2009, **4**(3), 186–191, DOI: 10.2961/jlmn.2009.03.0008.

105 B. Neuenschwander, B. Jaeggi, M. Schmid, V. Rouffiange and P.-E. Martin, Optimization of the volume ablation rate for metals at different laser pulse-durations from ps to fs, *Laser Appl. Microelectron. Optoelectron. Manuf. XVII*, 2012, **8243**, 824307, DOI: 10.1117/12.908583.

106 L. V. Zhigilei and B. J. Garrison, Microscopic mechanisms of laser ablation of organic solids in the thermal and stress confinement irradiation regimes, *J. Appl. Phys.*, 2000, **88**(3), 1281–1298, DOI: 10.1063/1.373816.

107 B. Le Drogoff, F. Vidal, S. Laville, M. Chaker, T. Johnston, O. Barthélemy, J. Margot and M. Sabsabi, Laser-ablated volume and depth as a function of pulse duration in aluminum targets, *Appl. Opt.*, 2005, **44**(2), 278–281, DOI: 10.1364/AO.44.000278.

108 A. Ostendorf, G. Kamlage, U. Klug, F. Korte and B. N. Chichkov, Femtosecond versus picosecond laser ablation (Keynote Address), *Phot. Process. Microelectron. Photonics IV*, 2005, **5713**, 1, DOI: 10.1117/12.597975.

109 R. Le Harzic, D. Breitling, M. Weikert, S. Sommer, C. Föhl, S. Valette, C. Donnet, E. Audouard and F. Dausinger, Pulse width and energy influence on laser micromachining of metals in a range of 100 fs to 5 ps, *Appl. Surf. Sci.*, 2005, **249**(1–4), 322–331, DOI: 10.1016/j.apsusc.2004.12.027.

110 A. Nastulyavichus, S. Kudryashov, A. Ionin and S. Gonchukov, Optimization of nanoparticle yield for biomedical applications at femto-, pico- and nanosecond laser ablation of thin gold films in water, *Laser Phys. Lett.*, 2022, **19**(4), 045603, DOI: 10.1088/1612-202X/ac581a.

111 S. Kudryashov, A. Samokhvalov, A. Nastulyavichus, I. Saraeva, V. Mikhailovskii, A. Ionin and V. Veiko, Nanosecond-Laser Generation of Nanoparticles in Liquids: From Ablation through Bubble Dynamics to Nanoparticle Yield, *Materials*, 2019, **12**(4), 562, DOI: 10.3390/ma12040562.

112 A. Nastulyavichus, N. Smirnov and S. Kudryashov, Quantitative evaluation of LAL productivity of colloidal nanomaterials: Which laser pulse width is more productive, ergonomic, and economic?, *Chin. Phys. B*, 2022, **31**(7), 077803, DOI: 10.1088/1674-1056/ac5602.

113 N. A. Smirnov, S. I. Kudryashov, A. A. Rudenko, A. A. Nastulyavichus and A. A. Ionin, Ablation efficiency of gold at fs/ps laser treatment in water and air, *Laser Phys. Lett.*, 2022, **19**(2), 026001, DOI: 10.1088/1612-202X/ac46ab.

114 S. Barcikowski, A. Meńndez-Manjón, B. Chichkov, M. Brikas and G. Račiukaitis, Generation of nanoparticle colloids by picosecond and femtosecond laser ablations in liquid flow, *Appl. Phys. Lett.*, 2007, **91**(8), 083113, DOI: 10.1063/1.2773937.

115 S. Kohsakowski, *Hochskalierung der laserbasierten Nanopartikelsynthese für die heterogene Katalyse*, University of Duisburg Essen, 2018.

116 A. Ancona, S. Döring, C. Jauregui, F. Röser, J. Limpert, S. Nolte and A. Tünnermann, Femtosecond and picosecond laser drilling of metals at high repetition rates and average powers, *Opt. Lett.*, 2009, **34**(21), 3304–3306, DOI: 10.1364/OL.34.003304.

117 A. Tunnermann and S. Nolte, Femtosecond vs. Picosecond Laser Material Processing Challenges in ultrafast precision laser Micro-machining of Metals at high repetition rates, *Pulse*, 2010, **49**(1), 34–38.

118 M. E. Povarnitsyn, T. E. Itina, P. R. Levashov and K. V. Khishchenko, Mechanisms of nanoparticle formation by ultra-short laser ablation of metals in liquid environment, *Phys. Chem. Chem. Phys.*, 2013, **15**(9), 3108–3114, DOI: 10.1039/c2cp42650a.

119 T. E. Itina, On nanoparticle formation by laser ablation in liquids, *J. Phys. Chem. C*, 2011, **115**(12), 5044–5048, DOI: 10.1021/jp1090944.

120 I. N. Saraeva, S. I. Kudryashov, A. A. Rudenko, M. I. Zhilnikova, D. S. Ivanov, D. A. Zayarny, A. V. Simakin, A. A. Ionin and M. E. Garcia, Effect of fs/ps laser pulsewidth on ablation of metals and silicon in air and liquids, and on their nanoparticle yields, *Appl. Surf. Sci.*, 2019, **470**, 1018–1034, DOI: 10.1016/j.apsusc.2018.11.199.

121 C. Ma and W. Lin, Normal dispersion effects on the nonlinear focus, *J. Opt. Soc. Am. B*, 2016, **33**(6), 1055–1059, DOI: 10.1364/JOSAB.33.001055.

122 D. Riabinina, M. Chaker and J. Margot, Dependence of gold nanoparticle production on pulse duration by laser ablation in liquid media, *Nanotechnology*, 2012, **23**(13), 135603, DOI: 10.1088/0957-4484/23/13/135603.

123 N. A. Smirnov, S. I. Kudryashov, A. A. Rudenko, D. A. Zayarny and A. A. Ionin, Pulsewidth and ambient medium effects during ultrashort-pulse laser ablation of silicon in air and water, *Appl. Surf. Sci.*, 2021, **562**, 150243, DOI: 10.1016/j.apsusc.2021.150243.

124 I. Bunaziv, O. M. Akselsen, X. Ren, B. Nyhus, M. Eriksson and S. Gulbrandsen-Dahl, A review on laser-assisted joining of aluminium alloys to other metals, *Metals*, 2021, **11**(11), 1680, DOI: 10.3390/met11111680.

125 T. Nakano, *Multi-dimensional Additive Manufacturing*, 2021.

126 D.-I. J. Berkmanns and D.-I. M. Faerber, *Laser basics - LASERLINE Technical.*, 2008.

127 T. Tsuji, K. Iryo, Y. Nishimura and M. Tsuji, Preparation of metal colloids by a laser ablation technique in solution: influence of laser wavelength on the ablation efficiency (II), *J. Photochem. Photobiol., A*, 2001, **145**(3), 201–207, DOI: 10.1016/S1010-6030(01)00583-4.

128 T. Tsuji, K. Iryo, N. Watanabe and M. Tsuji, Preparation of silver nanoparticles by laser ablation in solution: influence of laser wavelength on particle size, *Appl. Surf. Sci.*, 2002, **202**(1–2), 80–85, DOI: 10.1016/S0169-4332(02)00936-4.

129 T. Tsuji, D. H. Thang, Y. Okazaki, M. Nakanishi, Y. Tsuboi and M. Tsuji, Preparation of silver nanoparticles by laser ablation in polyvinylpyrrolidone solutions, *Appl. Surf. Sci.*, 2008, **254**(16), 5224–5230, DOI: 10.1016/j.apsusc.2008.02.048.

130 F. Mafuné, J. Y. Kohno, Y. Takeda, T. Kondow and H. Sawabe, Formation of gold nanoparticles by laser ablation in aqueous solution of surfactant, *J. Phys. Chem. B*, 2001, **105**(22), 5114–5120, DOI: 10.1021/jp0037091.

131 R. Intartaglia, K. Bagga and F. Brandi, Study on the productivity of silicon nanoparticles by picosecond laser ablation in water: towards gram per hour yield, *Opt. Express*, 2014, **22**(3), 3117, DOI: 10.1364/OE.22.003117.

132 B. Kumar and R. K. Thareja, Laser ablated copper plasmas in liquid and gas ambient, *Phys. Plasmas*, 2013, **20**(5), 053503, DOI: 10.1063/1.4807041.

133 A. De Giacomo, M. Dell'Aglio, A. Santagata, R. Gaudiuso, O. De Pascale, P. Wagener, G. C. Messina, G. Compagnini and S. Barcikowski, Cavitation dynamics of laser ablation of bulk and wire-shaped metals in water during nanoparticles production, *Phys. Chem. Chem. Phys.*, 2013, **15**(9), 3083–3092, DOI: 10.1039/c2cp42649h.

134 B. Kumar and R. K. Thareja, Synthesis of nanoparticles in laser ablation of aluminum in liquid, *J. Appl. Phys.*, 2010, **108**(6), 064906, DOI: 10.1063/1.3486517.

135 K. Sasaki and N. Takada, Liquid-phase laser ablation, *Pure Appl. Chem.*, 2010, **82**(6), 1317–1327, DOI: 10.1351/PAC-CON-09-10-23.

136 A. De Giacomo, R. Gaudiuso, M. Dell'Aglio and A. Santagata, The role of continuum radiation in laser induced plasma spectroscopy, *Spectrochim. Acta, Part B*, 2010, **65**(5), 385–394, DOI: 10.1016/j.sab.2010.03.016.

137 H. Ushida, N. Takada and K. Sasaki, Diagnostics of liquid-phase laser ablation plasmas by spectroscopic methods, *J. Phys.: Conf. Ser.*, 2007, **59**(1), 563–566, DOI: 10.1088/1742-6596/59/1/120.

138 J. Hoffman, J. Chrzanowska, T. Moscicki, J. Radziejewska, L. Stobinski and Z. Szymanski, Plasma generated during underwater pulsed laser processing, *Appl. Surf. Sci.*, 2017, **417**, 130–135, DOI: 10.1016/j.apsusc.2017.01.185.

139 A. Vogel, N. Linz, S. Freidank and G. Paltauf, Femtosecond-laser-induced nanocavitation in water: implications for optical breakdown threshold and cell surgery, *Phys. Rev. Lett.*, 2008, **100**(3), 1–4, DOI: 10.1103/PhysRevLett.100.038102.

140 J. Lam, J. Lombard, C. Dujardin, G. Ledoux, S. Merabia and D. Amans, Dynamical study of bubble expansion following laser ablation in liquids, *Appl. Phys. Lett.*, 2016, **108**(7), 1–6, DOI: 10.1063/1.4942389.

141 R. Tanabe, T. T. P. Nguyen, T. Sugiura and Y. Ito, Bubble dynamics in metal nanoparticle formation by laser ablation in liquid studied through high-speed laser stroboscopic videography, *Appl. Surf. Sci.*, 2015, **351**, 327–331, DOI: 10.1016/j.apsusc.2015.05.030.

142 A. Letzel, M. Santoro, J. Frohleiks, A. R. Ziefuß, S. Reich, A. Plech, E. Fazio, F. Neri, S. Barcikowski and B. Gökce, How the re-irradiation of a single ablation spot affects cavitation bubble dynamics and nanoparticles properties in laser ablation in liquids, *Appl. Surf. Sci.*, 2019, **473**, 828–837, DOI: 10.1016/j.apsusc.2018.12.025.

143 J. Long, M. H. Eliceiri, L. Wang, Z. Vangelatos, Y. Ouyang, X. Xie, Y. Zhang and C. P. Grigoropoulos, Capturing the final stage of the collapse of cavitation bubbles generated during nanosecond laser ablation of submerged targets, *Opt. Laser Technol.*, 2021, **134**, 106647, DOI: 10.1016/j.optlastec.2020.106647.

144 T. T. P. Nguyen, R. Tanabe-Yamagishi and Y. Ito, Effects of liquid depth on the expansion and collapse of a hemispherical cavitation bubble induced in nanosecond pulsed laser ablation of a solid in liquid, *Opt. Lasers Eng.*, 2020, **126**, 105937, DOI: 10.1016/j.optlaseng.2019.105937.

145 M. R. Kalus, N. Bärsch, R. Streubel, E. Gökce, S. Barcikowski and B. Gökce, How persistent microbubbles

shield nanoparticle productivity in laser synthesis of colloids – Quantification of their volume, dwell dynamics, and gas composition, *Phys. Chem. Chem. Phys.*, 2017, **19**(10), 7112–7123, DOI: **10.1039/c6cp07011f**.

146 M. Dell'Aglio, A. Santagata, G. Valenza, A. De Stradis and A. De Giacomo, Study of the Effect of Water Pressure on Plasma and Cavitation Bubble Induced by Pulsed Laser Ablation in Liquid of Silver and Missed Variations of Observable Nanoparticle Features, *ChemPhysChem*, 2017, **18**(9), 1165–1174, DOI: **10.1002/cphc.201601231**.

147 C. Doñate-Buendia, M. Spellauge, E. Streubel, F. Riahi, S. Barcikowski, H. P. Huber and B. Gökce, Double-pulse laser ablation in liquids: nanoparticle bimodality reduction by sub-nanosecond interpulse delay optimization, *J. Phys. D: Appl. Phys.*, 2023, **56**(10), 104001, DOI: **10.1088/1361-6463/acbaaa**.

148 D. Franz, T. Häfner, T. Kunz, G-L. Roth, S. Rung, C. Esen and R. Hellmann, Characterization of a hybrid scanning system comprising acousto-optical deflectors and galvanometer scanners, *Appl. Phys. B: Lasers Opt.*, 2022, **128**(3), 55, DOI: **10.1007/s00340-022-07782-2**.

149 G. R. B. E. Römer and P. Bechtold, Electro-optic and acousto-optic laser beam scanners, *Phys. Proc.*, 2014, **56**(C), 29–39, DOI: **10.1016/j.phpro.2014.08.092**.

150 R. De Loor, Polygon Scanner System for Ultra Short Pulsed Laser Micro-Machining Applications, *Phys. Proc.*, 2013, **41**, 544–551, DOI: **10.1016/j.phpro.2013.03.114**.

151 P. Bechtold, R. Hohenstein and M. Schmidt, Evaluation of disparate laser beam deflection technologies by means of number and rate of resolvable spots, *Opt. Lett.*, 2013, **38**(16), 2934–2937, DOI: **10.1364/OL.38.002934**.

152 Raylase, SUPERSCAN IV-15 2-Axis Deflection Units, **www.raylase.com**, 2020. **https://www.raylase.de/_Resources/Persistent/9/5/d/a/95da1035b2c564183914aa6c26c6f6e43f20044c/RAYLASE_SUPERSCANIV-15_en.pdf** (accessed Feb. 26, 2023).

153 J. Schille, L. Schneider, A. Streek, S. Kloetzer and U. Loeschner, High-throughput machining using high average power ultrashort pulse lasers and ultrafast polygon scanner, *Proc. SPIE*, 2016, **9736**, 97360R, DOI: **10.1117/12.2220112**.

154 S. Kudryashov, P. Danilov, L. Schneider, J. Schille, U. Loeschner, A. Nastulyavichus, N. Smirnov, A. Kuchmizhak and O. Vitrik, Polygon-facilitated generation of colloidal gold nanoparticles by multi-MHz ultrashort-pulse laser trains: key optical factors, *Laser Phys. Lett.*, 2021, **18**(1), 016101, DOI: **10.1088/1612-202X/abd171**.

155 M. R. Kalus, V. Reimer, S. Barcikowski and B. Gökce, Discrimination of effects leading to gas formation during pulsed laser ablation in liquids, *Appl. Surf. Sci.*, 2019, **465**, 1096–1102, DOI: **10.1016/j.apsusc.2018.09.224**.

156 M. R. Kalus, R. Lanyumba, S. Barcikowski and B. Gökce, Discrimination of ablation, shielding, and interface layer effects on the steady-state formation of persistent bubbles under liquid flow conditions during laser synthesis of colloids, *J. Flow Chem.*, 2021, **11**, 773–792, DOI: **10.1007/s41981-021-00144-7**.

157 R. Lahoz, A. Naghilou, W. Kautek and O. Bomati-Miguel, Study of the physicochemical surface alterations and incubation phenomena induced on iron targets by nanosecond pulsed laser ablation in liquids: effect on productivity and characteristics of the synthesized nanoscale zero-valent iron (nZVI) particles, *Appl. Surf. Sci.*, 2020, **511**, 145438, DOI: **10.1016/j.apsusc.2020.145438**.

158 R. Nadarajah, S. Barcikowski and B. Gökce, Picosecond laser-induced surface structures on alloys in liquids and their influence on nanoparticle productivity during laser ablation, *Opt. Express*, 2020, **28**(3), 2909, DOI: **10.1364/oe.28.002909**.

159 W. Charee, V. Tangwarodomnukun and C. Dumkum, Laser ablation of silicon in water under different flow rates, *Int. J. Adv. Des. Manuf. Technol.*, 2015, **78**(1–4), 19–29, DOI: **10.1007/s00170-014-6625-6**.

160 P. Nandini, K. Akash, G. Rohit, S. Vipul and I. A. Palani, Investigations on the Influence of Liquid-Assisted Laser Ablation of NiTi Rotating Target to Improve the Formation Efficiency of Spherical Alloyed NiTi Nanoparticles, *J. Mater. Eng. Perform.*, 2017, **26**(10), 4707–4717, DOI: **10.1007/s11665-017-2886-1**.

161 G. Marzun, A. Levish, V. Mackert, T. Kallio, S. Barcikowski and P. Wagener, Laser synthesis, structure and chemical properties of colloidal nickel-molybdenum nanoparticles for the substitution of noble metals in heterogeneous catalysis, *J. Colloid Interface Sci.*, 2017, **489**, 57–67, DOI: **10.1016/j.jcis.2016.09.014**.

162 Y. Jiang, P. Liu, Y. Liang, H. B. Li and G. W. Yang, Promoting the yield of nanoparticles from laser ablation in liquid, *Appl. Phys. A: Mater. Sci. Process.*, 2011, **105**(4), 903–907, DOI: **10.1007/s00339-011-6557-z**.

163 V. Piotto, L. Litti and M. Meneghetti, Synthesis and Shape Manipulation of Anisotropic Gold Nanoparticles by Laser Ablation in Solution, *J. Phys. Chem. C*, 2020, **124**(8), 4820–4826, DOI: **10.1021/acs.jpcc.9b10793**.

164 A. Syafiuddin, S. Salmiati, M. R. Salim, A. Beng Hong Kueh, T. Hadibarata and H. Nur, A Review of Silver Nanoparticles: Research Trends, Global Consumption, Synthesis, Properties, and Future Challenges, *J. Chin. Chem. Soc.*, 2017, **64**(7), 732–756, DOI: **10.1002/jccs.201700067**.

165 S. F. Wirtz, A. P. A. Cunha, M. Labusch, G. Marzun, S. Barcikowski and D. Söffker, Development of a low-cost FPGA-based measurement system for real-time processing of acoustic emission data: proof of concept using control of pulsed laser ablation in liquids, *Sensors*, 2018, **18**(6), 1–11, DOI: **10.3390/s18061775**.

166 S. Crivellaro, A. Guadagnini, D. M. Arboleda, D. Schinca and V. Amendola, A system for the synthesis of nanoparticles by laser ablation in liquid that is remotely controlled with PC or smartphone, *Rev. Sci. Instrum.*, 2019, **90**(3), 033902, DOI: **10.1063/1.5083811**.

167 M. Labusch, A. P. A. Cunha, S. F. Wirtz, S. Reichenberger, E. Cleve, D. Söffker and S. Barcikowski, Acoustic emission control avoids fluence shifts caused by target runaway during laser synthesis of colloids, *Appl. Surf. Sci.*, 2019, **479**, 887–895, DOI: **10.1016/j.apsusc.2019.02.080**.

168 B. Freeland, R. McCann, G. Alkan, B. Friedrich, G. Foley and D. Brabazon, Stable nano-silver colloid production via Laser Ablation Synthesis in Solution (LASiS) under laminar recirculatory flow, *Adv. Mater. Process. Technol.*, 2020, **6**(4), 677–685, DOI: **10.1080/2374068X.2020.1740877**.

169 S. Zhu, Y. F. Lu, M. H. Hong and X. Y. Chen, Laser ablation of solid substrates in water and ambient air, *J. Appl. Phys.*, 2001, **89**(4), 2400–2403, DOI: **10.1063/1.1342200**.

170 F. Waag, Y. Li, A.R. Ziefuß, E. Bertin, M. Kamp, V. Duppel, G. Marzun, L. Kienle, S. Barcikowski and B. Gökce, Kinetically-controlled laser-synthesis of colloidal high-entropy alloy nanoparticles, *RSC Adv.*, 2019, **9**(32), 18547–18558, DOI: **10.1039/c9ra03254a**.

171 C. Han, R. Wang, A. Pan, W. Wang, H. Huang, J. Zhang and C. Niu, Morphology-directing transformation of carbon nanotubes under the irradiation of pulsed laser with different pulsed duration, *Opt. Laser Technol.*, 2019, **109**, 27–32, DOI: **10.1016/j.optlastec.2018.07.058**.

172 M. Nazemi, S. R. Panikkanvalappil, C. K. Liao, M. A. Mahmoud and M. A. El-Sayed, Role of Femtosecond Pulsed Laser-Induced Atomic Redistribution in Bimetallic Au-Pd Nanorods on Optoelectronic and Catalytic Properties, *ACS Nano*, 2021, **15**(6), 10241–10252, DOI: **10.1021/acsnano.1c02347**.

173 K. Zhang, D. S. Ivanov, R. A. Ganeev, G. S. Boltaev, P. S. Krishnendu, S. C. Singh, M. E. Garcia, I. N. Zavestovskaya and C. Guo, Pulse duration and wavelength effects of laser ablation on the oxidation, hydrolysis, and aging of aluminum nanoparticles in water, *Nanomaterials*, 2019, **9**(5), 767, DOI: **10.3390/nano9050767**.

174 G. González-Rubio, P. Díaz-Núñez, A. Rivera, A. Prada, G. Tardajos, J. González-Izquierdo, L. Bañares, P. Llombart, L. G. Macdowel, M. A. Palafox, L. M. Liz-Marzán, O. Peña-Rodríguez and A. Guerrero-Martínez, Femtosecond laser reshaping yields gold nanorods with ultranarrow surface plasmon resonances, *Science*, 2017, **358**(6363), 640–644, DOI: **10.1126/science.aan8478**.

175 M. Curcio, A. De Bonis, A. Santagata, A. Galasso and R. Teghil, Effect of laser pulse duration on properties of metal and metal carbide nanoparticles obtained by laser in liquid synthesis, *Opt. Laser Technol.*, 2021, **138**, 106916, DOI: **10.1016/j.optlastec.2021.106916**.

176 J. Xiao, G. Ouyang, P. Liu, C. X. Wang and G. W. Yang, Reversible nanodiamond-carbon onion phase transformations, *Nano Lett.*, 2014, **14**(6), 3645–3652, DOI: **10.1021/nl5014234**.

177 Z. Wang, B. Xiao, Z. Lin, S. Shen, A. Xu, Z. Du, Y. Chen and W. Zhong, In situ surface decoration of RuO_2 nanoparticles by laser ablation for improved oxygen evolution reaction activity in both acid and alkali solutions, *J. Energy Chem.*, 2021, **54**, 510–518, DOI: **10.1016/j.jechem.2020.06.042**.

178 G. K. Yogesh, S. Shukla, D. Sastikumar and P. Koinkar, Progress in pulsed laser ablation in liquid (PLAL) technique for the synthesis of carbon nanomaterials: a review, *Appl. Phys. A: Mater. Sci. Process.*, 2021, **127**(11), 810, DOI: **10.1007/s00339-021-04951-6**.

179 M. Dell'Aglio, V. Motto-Ros, F. Pelascini, I. B. Gornushkin and A. De Giacomo, Investigation on the material in the plasma phase by high temporally and spectrally resolved emission imaging during pulsed laser ablation in liquid (PLAL) for NPs production and consequent considerations on NPs formation, *Plasma Sources Sci. Technol.*, 2019, **28**(8), 085017, DOI: **10.1088/1361-6595/ab369b**.

180 J. Johny, M. Kamp, O. Prymak, A. Tymoczko, U. Wiedwald, C. Rechbock, U. Schürmann, R. Popescu, D. Gerthsen, L. Kienle, S. Shaji and S. Barcikowski, Formation of Co–Au Core–shell nanoparticles with thin gold shells and soft magnetic ε-cobalt cores ruled by thermodynamics and kinetics, *J. Phys. Chem. C*, 2021, **125**(17), 9534–9549, DOI: **10.1021/acs.jpcc.1c02138**.

181 D. Spadaro, M. A. Iatì, M. G. Donato, P. G. Gucciardi, R. Saija, A. R. Cherlakola, S. Scaramuzza, V. Amendola and O. M. Maragò, Scaling of optical forces on Au–PEG core–shell nanoparticles, *RSC Adv.*, 2015, **5**(113), 93139–93146, DOI: **10.1039/c5ra20922f**.

182 X. Li, G. Zhang, L. Jiang, Z. Shi, K. Zhang, W. Rong, J. Duan and Y. Lu, Production rate enhancement of size-tunable silicon nanoparticles by temporally shaping femtosecond laser pulses in ethanol, *Opt. Express*, 2015, **23**(4), 4226–4232, DOI: **10.1364/OE.23.004226**.

183 M. Dell'Aglio, R. Gaudiuso, R. Elrashedy, O. De Pascale, G. Palazzo and A. De Giacomo, Collinear double pulse laser ablation in water for the production of silver nanoparticles, *Phys. Chem. Chem. Phys.*, 2013, **15**(48), 20868–20875, DOI: **10.1039/c3cp54194k**.

184 B. Liu, Z. Hu and Y. Che, *Nanoparticle production in liquid with multiple-pulse ultrafast laser ablation*, US 2011/0192714 A1, 2011.

185 G. Mínguez-Vega, J. Lancis, J. Caraquitena, V. Torres-Company and P. Andrés, High spatiotemporal resolution in multifocal processing with femtosecond laser pulses, *Opt. Lett.*, 2006, **31**(17), 2631–2633, DOI: **10.1364/ol.31.002631**.

186 O. Mendoza-Yero, G. Mínguez-Vega and J. Lancis, Encoding complex fields by using a phase-only optical element, *Opt. Lett.*, 2014, **39**(7), 1740, DOI: **10.1364/ol.39.001740**.

187 J. Cao, Q. Yang, Y. Miao, Y. Li, S. Qiu, Z. Zhu, P. Wang and Z. Chen, Enhance the delivery of light energy ultra-deep into turbid medium by controlling multiple scattering photons to travel in open channels, *Light: Sci. Appl.*, 2022, **11**(1), 108, DOI: **10.1038/s41377-022-00795-8**.

7.5 List of Publications

7.5.1 Published Peer-reviewed Articles

1. FeNi Nanoparticle-Modified Reduced Graphene Oxide as a Durable Electrocatalyst for Oxygen Evolution. **I. Y. Khairani**, B. Jin, S. M. Palardonio, U. Hagemann, B. Alonso, A. Ortega, C. Doñate-Buendía, J. Martorell, C. Ros, T. Kallio, B. Gökce. J. Catal. 2024, 439 (September), 115771, DOI: 10.1016/j.jcat.2024.115771. – *Original research article*
2. Parallel Diffractive Multi-Beam Pulsed-Laser Ablation in Liquids Toward Cost-Effective Gram Per Hour Nanoparticle Productivity. **I. Y. Khairani**, M. Spellauge, F. Riahi, H. P. Huber, B. Gökce, C. Doñate-Buendía. *Adv. Photonics Res.* 2024, 5, 5, 2300290, DOI: 10.1002/adpr.202300290. – *Original research article (featured as front cover page)*
3. 4D Printing of Magneto-Responsive Polymer Structures by Masked Stereolithography for Miniaturised Actuators. J.L. Kricke, **I. Y. Khairani**, B.B.J. Beele, N. Shkodich, M. Farle, A. Slabon, C. Doñate-Buendía, B. Gökce, *Virtual Phys. Prototyp*. 2023, 18 (1), DOI: 10.1080/17452759.2023.2251017. – *Original research article*
4. Green Nanoparticle Synthesis at Scale: A Perspective on Overcoming the Limits of Pulsed Laser Ablation in Liquids for High-Throughput Production. **I. Y. Khairani,** G. Mínguez-Vega, C. Doñate-Buendía, B. Gökce. *Phys. Chem. Chem. Phys.* 2023, DOI: 10.1039/D3CP01214J – *Perspective article*
5. Solvent Influence on the Magnetization and Phase of Fe-Ni Alloy Nanoparticles Generated by Laser Ablation in Liquids, **I.Y. Khairani**, Q. Lin, J. Landers, S. Salamon, C. Doñate-Buendía, E. Karapetrova, H. Wende, G. Zangari, B. Gökce. *Nanomaterials* 2023, *13*, 227, DOI: 10.3390/nano13020227 – *Original research article*
6. Fabrication, Structure, and Magnetic Properties of Pure-Phase $BiFeO_3$ and $MnFe_2O_4$ Nanoparticles and their Nanocomposites, **I.Y. Khairani**, A.N. Arifiadi, J.H. Lee, B. Bhoi, S.K.S. Patel, S.K. Kim. *Journal of Magnetics* 2020, 25, 2, pg. 140 – 149, DOI: 10.4283/JMAG.2020.25.2.140 – *Original research article*
7. Synthesis and multiferroic properties of high-purity $CoFe_2O_4$-$BiFeO_3$ nanocomposites, A. N. Arifiadi, K.T. Kim, **I. Y. Khairani**, C. B. Park, K. H. Kim, S. K. Kim, *Journal of Alloys and Compounds* 2021, 867, 159008, DOI: 10.1016/j.jallcom.2021.159008 – *Original research article*
8. The Effect of Alkaline Ratios of NaOH to NH_3 on the Formation of Nanostructured Titania, I. Kartini, **I.Y. Khairani**, S. Mustofa, S.J. Santosa, L.Z. Wang, *Materials Science Forum* 2017, 886, pg. 42 – 47. DOI: 10.4028/www.scientific.net/MSF.886.42 – *Original research article*
9. Nanostructured Titanium Dioxide for Functional Coatings, I. Kartini, **I.Y. Khairani**, K. Triyana, S. Wahyuni (2018). Titanium Dioxide: Material for a Sustainable Environment, pg. 45. DOI: 10.5772/intechopen.74555 – *Book chapter*

7.5.2 In preparation or Submitted

1. Energy-Efficient Nitrate-to-Ammonia Electrochemical Reduction in a Tandem Configuration, M.E. Chávez**, I. Y. Khairani**, M. Biset-Peiró, J.R. Morante, B. Gökce, S. Murcia-López*, J. Chem. Eng*. 2024 *– Original research article*

7.5.3 Presentations in International Conferences

- **Oral Presentation:** Beam splitting towards gram per hour productivity of iron-nickel nanocatalysts by laser ablation in water, *SPIE Photonics West 2024*, San Francisco, USA, 27 January – 2 February 2024
- **Oral Presentation:** Influence of the Ablation Liquid on the Phase and Magnetization of Laser-generated Fe-Ni Nanoparticles, *Nanospainconference 2023*, Tarragona, Spain, 25 – 28 April 2023.
- **Poster**: Solvent Influence on the Magnetization and Phase of Fe-Ni Alloy Nanoparticles generated by Pulsed Laser Ablation in Liquids, *International Conference on Magnetic and Superconducting Materials MSM22,* Duisburg, Germany, 28 August – 02 September 2022.
- **Poster**: Structural and Magnetic Properties of $MnFe_2O_4$ – $BiFeO_3$ Nanocomposites, *The Korean Magnetics Society 2019 Summer Conference*, Busan, South Korea, 22 – 24 May 2019.
- **Poster**: Study of Binary Alkaline Ratio on the Synthesis of Titania Nanostructured via Hydrothermal Method. *The 9th International Mesostructured Material Symposium (IMMS 9),* Brisbane, Australia, 17 – 20 August 2015.

7.6 Acknowledgement

First and foremost, I would like to thank God Almighty, Allah SWT, for granting me the opportunity and possibility to enrich my mind on the state-of-the-art topics I delved deeply into during this PhD study. I thank Allah for blessing me with people who have supported me throughout this journey over the years—their warmth, kindness, patience, and never-ending support have meant everything. There are many people in my thoughts, too many to mention one by one. Even if you are not on this list, please remember that everyone who has helped me from the day I was born until the day I wrote this paragraph deserves my heartfelt acknowledgement.

I would like to thank my husband, Haydar, for his support and motivation. He always knows how to cheer me up and lift my mood whenever I am feeling low. He always accompanies me wherever I go and sacrifices his needs for my sake. He is one of the biggest reasons I could finish my PhD. I will forever be grateful to my family: my mom, my dad, my sister, and my brother, for their unwavering love. I am grateful for their prayers, their genuine happiness at my happiness, and their enduring support. Without them, I would not be where I am today. I am also thankful to my mother-in-law, my father-in-law, and my sister-in-law, for being patient, loving, supportive, and genuinely proud of me. All of them have made countless sacrifices, their patience as vast as the ocean, and their warmth as gentle as sunshine in the morning. Despite being separated by thousands of kilometers, they are always there whenever I need them.

I am deeply grateful to my first supervisor, Bilal, for trusting me—even though my main motivation to join him was to be reunited with my husband, who was already in Germany at the time. Despite knowing this, he still accepted me as his PhD student and placed his trust in me. I am forever grateful for this chance, and I thank God I was able to fulfill my promise to complete my PhD. I also thank Bilal for entrusting me with the management of the LESGO Project, which allowed me to organize the research as I envisioned, develop it in my own way, and pursue it independently, while still receiving direction when I needed it. I had the opportunity to collaborate with project partners who were crucial in producing good results, and I was able to attend many conferences and workshops that will benefit my future. I am thankful that, together with him, we published four articles that will remain open access for the world to see and learn from. I am grateful to have had the chance to know and work with him.

I am also deeply grateful to my second supervisor and group leader in the polymer group, Carlos. Without him, I would have lost sight of my PhD journey. Without his expertise and guidance, I would not have published all those articles. His intelligent yet humble and gentle approach resonates deeply with me, making it very easy to work together. I truly appreciate his hands-on support, his willingness to listen, and the help he provided through my challenges. I especially appreciate how he always prioritized his group members and was always there for us. His ideas were always precise and well-considered, helping us avoid unnecessary effort and wasted time, which made our work efficient. I am forever grateful to have had him as my group leader and as the person who worked most closely with me during my PhD. Without him, I would not have finished my PhD as smoothly as I did.

I also thank the rest of my colleagues at MAM: Mareen, Claudia, Hamed, Shabbir, Jan, Farbod, Nikolas, Johanna, Silja, Abdel, Markus, Ingo, and many others whom I cannot mention individually. I am thankful for their kindness, warmth, and support during my time at MAM. I am especially grateful to Mareen for her positive energy, Claudia for her kindness, Hamed for his helpfulness, Shabbir for his friendliness, Jan for his perceptiveness, Nikolas and Johanna for their meticulous work, and Silja for her authenticity. Everyone possesses amazing traits from which I have learned so much. As someone who had mostly worked alone, I finally learned, thanks to the people at MAM, that if you want to go far, go together.

I am also thankful to my project partners and co-authors, especially Benjin, Sid, and Carles, for their help throughout my PhD journey. I would also like to thank my former supervisors, Prof. Kim Sang Koog (Materials Science and Engineering, Seoul National University) and Prof. Indriana Kartini (Chemistry, Universitas Gadjah Mada), for their outstanding support throughout my master's and bachelor's studies, and even afterwards. Without them, I would not be where I am now. I would also like to thank the committee of my PhD for the fruitful and engaging discussions during the defense, as well as Ms. Sabine Kranz for her support during my PhD and my defense.

Due to privacy concerns, CV is removed from the digital version of the dissertation.